



8-2013

Essentially Analytical Theory Closure for Space Filtered Thermal-Incompressible Navier-Stokes Partial Differential Equation System on Bounded Domains

Mikhail Alexandrovich Sekachev
University of Tennessee - Knoxville, mikhail@utk.edu

Recommended Citation

Sekachev, Mikhail Alexandrovich, "Essentially Analytical Theory Closure for Space Filtered Thermal-Incompressible Navier-Stokes Partial Differential Equation System on Bounded Domains." PhD diss., University of Tennessee, 2013.
https://trace.tennessee.edu/utk_graddiss/2479

This Dissertation is brought to you for free and open access by the Graduate School at Trace: Tennessee Research and Creative Exchange. It has been accepted for inclusion in Doctoral Dissertations by an authorized administrator of Trace: Tennessee Research and Creative Exchange. For more information, please contact trace@utk.edu.

To the Graduate Council:

I am submitting herewith a dissertation written by Mikhail Alexandrovich Sekachev entitled "Essentially Analytical Theory Closure for Space Filtered Thermal-Incompressible Navier-Stokes Partial Differential Equation System on Bounded Domains." I have examined the final electronic copy of this dissertation for form and content and recommend that it be accepted in partial fulfillment of the requirements for the degree of Doctor of Philosophy, with a major in Mechanical Engineering.

Allen J. Baker, Major Professor

We have read this dissertation and recommend its acceptance:

Kivanc Ekici, Ohannes Karakashian, Steven M. Wise, Kwai L. Wong

Accepted for the Council:

Dixie L. Thompson

Vice Provost and Dean of the Graduate School

(Original signatures are on file with official student records.)

**Essentially Analytical Theory Closure for Space Filtered Thermal-Incompressible Navier-Stokes Partial
Differential Equation System on Bounded Domains**

A Dissertation Presented for the
Doctor of Philosophy
Degree
The University of Tennessee, Knoxville

Mikhail Alexandrovich Sekachev

August 2013

Copyright © 2013 by Mikhail Alexandrovich Sekachev

All rights reserved

This dissertation is dedicated to my mother whose love and support became the main source of encouragement in pursuing my dreams

ACKNOWLEDGMENTS

It is with immense gratitude that I acknowledge the support and help of my academic advisor, Professor A. J. Baker, who gave me the freedom to explore on my own and at the same time the guidance to recover when my steps faltered. He has been always there to listen and give advice. His patience and support helped me overcome many crisis situations and finish this dissertation. His insightful comments were always thought-provoking thus helping me to move forward. I am also thankful to him for encouraging the use of correct grammar and consistent notation in my writings and for carefully reading and commenting on revisions of this manuscript.

This dissertation would not have been possible without the help and practical advice of Dr. Kwai Wong to whom I owe tremendous gratitude. His constructive criticisms at different stages of my research always helped me focus on what's important. His initial teachings of parallel computing and the long-lasting support in exploring this field are appreciated beyond measure. Dr. Wong's parallel code called PICMSS has been the most important computational tool of my research and I am deeply indebted for the countless hours of valuable discussion he spent with me while I was learning this tool. I am also thankful to him for the continuous help in finding financial support.

I further wish to acknowledge the faculty members of my doctoral committee, Professor Ohannes Karakashian, Dr. Kivanc Ekici and Dr. Steven Wise, for their support and encouragement during the course of this research.

I would like to acknowledge the financial and technical support of the Joint Institute for Computational Sciences and the National Center for Computational Sciences that have sponsored this study by offering me graduate assistantships.

ABSTRACT

Numerical simulation of turbulent flows is identified as one of the grand challenges in high-performance computing. The straight forward approach of solving the Navier-Stokes (NS) equations is termed Direct Numerical Simulation (DNS). In DNS the majority of computational effort is spent on resolving the smallest scales of turbulence, which makes this approach impractical for most industrial applications even on present-day supercomputers. A more feasible approach termed Large Eddy Simulation (LES) has evolved over the last five decades to facilitate turbulent flow predictions for reasonable Reynolds (Re) numbers and domain sizes. LES theory uses the concept of convolution with a spatial filter, which allows it to compute only the major scales of turbulence as determined by the diameter of the filter. The rest of the length scales are not resolved posing the so-called closure problem of LES. For bounded domains, besides the closure problem, an equally challenging issue of LES is that of prescribing the suitable boundary conditions for the resolved-scale state variables. Additional problems arise because the convolution operation does not generally commute with differentiation in the presence of boundaries.

This dissertation details derivation of an essentially analytical closure theory for the unsteady three-dimensional space filtered thermal-incompressible NS partial differential equation (PDE) system on bounded domains. This is accomplished by the union of rational LES theory, Galdi and Layton, with modified continuous Galerkin theory of Kolesnikov with specific focus on correct adaptation of a constant measure filter near the Dirichlet type boundary. The analytical closure theory state variable organization is guided by classic fluid mechanics perturbation theory. Derivation and implementation of suitable boundary conditions (BCs) as well as the boundary commutation error (BCE) integral is accomplished using the ideas of approximate deconvolution (AD) theory. Non-homogeneous BCs for the auxiliary problem of *arLES* theory are derived.

TABLE OF CONTENTS

1. Introduction.....	1
1.1 Brief History and Challenges in LES	3
1.2 This Dissertation	5
2. Large Eddy Simulation	6
2.1 Conservation Principles	7
2.2 Space Filtering Concepts.....	9
2.3 Space Filtered Navier-Stokes Equations	11
2.4 Reynolds Averaged Navier-Stokes.....	13
2.5 SGS Tensor Closure Modeling for LES.....	15
2.6 The Rational LES Closure Formulation.....	18
2.7 Analytical SFS Tensor/Vector Closures	23
2.8 The Auxiliary Problem.....	25
3. Space Filtering on Bounded Domains	30
3.1 Near Wall Resolution and Near Wall Modeling.....	31
3.2 The Boundary Commutation Error Integral.....	33
3.3 Approximate Deconvolution Boundary Conditions.....	35
3.4 Modified ADBC Formulation.....	38
3.5 Boundary Conditions for the Auxiliary Problem.....	39
4. Essentially Analytical Rational LES Theory CFD Algorithm	42
4.1 Space Filtered CCM.....	42
4.2 Error Analysis.....	43
4.3 Poisson Equation for ϕ	48
4.4 Pressure Poisson Equation	49
4.5 Space Filtered CCM Solution Strategy Overview.....	53

5. <i>ar</i> LES Weak Form FE Implementation.....	56
5.1 Galerkin Weak Statement	59
5.2 Finite Element Template Statement	63
5.3 The GWS and Template for the SFS Closure.....	67
5.4 Finite Element AD Formula Implementation.....	71
6. Discussion and Results	73
6.1 Non-steady Heat Conduction Problem.....	74
6.1.1 One-Dimensional Analysis.....	74
6.1.2 Two-Dimensional Analysis	77
6.1.3 Asymptotic Convergence, Error Quantification	89
6.1.4 Summary and Conclusions	91
6.2 Two-Dimensional Channel Flow	92
6.2.1 Time-Averaged Boundary Layer Profile	92
6.2.2 Space Filtered Boundary Layer Profile	96
6.2.3 Diagnostics of Space-Filtering	98
6.2.4 Solution Adaptive Mesh Refinement	100
6.2.5 Optimal Mesh Construction and Final Tests	102
6.3 Three-Dimensional Flow Over a Flat Plate	103
6.3.1 Establishing a Benchmark Problem.....	103
6.3.2 Dispersion Error Control for $Re=1E5$	105
6.3.3 AD Formulation Verification.....	105
6.4 Three-Dimensional Buoyancy-Driven Cavity Flow	107
6.4.1 Problem Statement	107
6.4.2 Effects of Non-Dimensionalization on Pressure Distribution.....	110
6.4.3 Modified CCM θ -Implicit Procedure	112

6.4.4 Template Statement	112
6.4.5 Thermal Cavity at $Ra=10^8$	116
7. Summary and Conclusions	121
Bibliography	123
Appendices.....	130
Appendix A	131
Appendix B	142
Appendix C	214
Vita	221

LIST OF TABLES

Table A.1: Convergence data under uniform mesh refinement	132
Table A.2: Analytical values and the slopes of \bar{u} at the wall	133
Table A.3: Computed values and the slopes of u at the wall	134
Table A.4: Comparison of computed space-filtered velocity slopes at the wall.....	135
Table A.5: Uniform mesh refinement study for a constant filter measure $\delta^+ = 36$	136
Table A.6: Uniform mesh refinement study for a constant filter measure $\delta^+ = 18$	137
Table A.7: Uniform mesh refinement study for a constant filter measure $\delta^+ = 9$	138
Table A.8: Uniform mesh refinement study for a constant filter measure $\delta^+ = 4.5$	139
Table A.9: Uniform mesh refinement study for a constant filter measure $\delta^+ = 2.25$	140
Table A.10: Thermal cavity problem parameters for $Pr = 0.7$ and $C_s = \delta = 0.05$	141

LIST OF FIGURES

Figure B.1: A sample of the velocity field u and the corresponding space filtered velocity \bar{u} (bold line, top). The unresolved velocity field u' , and the corresponding space filtered unresolved velocity \bar{u}' (bold line, bottom) (Pope, 2000)	143
Figure B.2: Polynomial interpolation of $\mathcal{F}(g_\delta)$. Top, 2 nd order Taylor series; middle, 2 nd order Padé; bottom, 4 th order Padé	144
Figure B.3: Vorticity distributions from level 5 GWS ^h + θ TS rLES solutions \bar{u}^h , at times $n\Delta t = 50, 70, 80$ s (left to right) corresponding to (top to bottom): benchmark, auxiliary problem direct solution, auxiliary problem via convolution (John, 2004)	145
Figure B.4: Domain of integration for $\bar{u}^{n+1}(\mathbf{x}_b)$	146
Figure B.5: Filtering through the wall with extended q	147
Figure B.6: Errors in \bar{q} (Borggaard and Iliescu, 2006).....	148
Figure B.7: Errors in \bar{q} (this study).....	149
Figure B.8: Test 1a - Exact boundary conditions (q is not extended outside of Ω), exact BCE integral.....	150
Figure B.9: Test 1b - Exact boundary conditions (q is extended outside of Ω), exact BCE integral.....	151
Figure B.10: Test 2 - Exact boundary conditions, no BCE integral	152
Figure B.11: Test 1b - Absolute error in approximating q using the AD formula.....	153
Figure B.12: Test 3 - Exact boundary conditions, approximate BCE integral.....	154
Figure B.13: Test4 - Approximate boundary conditions, approximate BCE integral	155
Figure B.14: Comparison of the computed and DNS solutions for $Re^+ = 180$	156
Figure B.15: Similarity space (top) and physical space (bottom) velocity profiles	157

Figure B.16: Shear stress profiles for $Re^+ = 180$	158
Figure B.17: Comparison of computed (PICMSS) and reference (WILCOX) velocity profiles in similarity space (top) and physical space (bottom).....	159
Figure B.18: Action of space filtering on the velocity profile with $\delta = 0.001$	160
Figure B.19: Action of space filtering on the Reynolds stress profile with $\delta = 0.001$	161
Figure B.20: Action of space filtering on the constant pressure gradient profile, $\partial p / \partial x = -32.595$, with $\delta = 0.001$	162
Figure B.21: The BCE integral as a function of filter measure	163
Figure B.22: The importance of the BCE term. Solid line – analytical \bar{u}^+ , circle – computed \bar{u}^+ with BCE term, diamond – computed \bar{u}^+ without BCE term.....	164
Figure B.23: Comparison of a time-averaged velocity profile with four space-filtered velocity profiles for different filter measures: (a) full-size profile with logarithmic scale; (b) close-up of the viscous sublayer without the logarithmic scale.....	165
Figure B.24: Comparison of a time-averaged velocity profile with the unfiltered velocity profiles for different filter measures: (a) full-size profile with logarithmic scale; (b) close-up of the viscous sublayer without a logarithmic scale.....	166
Figure B.25: Optimal mesh construction	167
Figure B.26: Evolution of the space-filtered velocity profile for $Re^+ = 180$ (exact BCs, exact BCE).....	168
Figure B.27: Computed solutions for three case studies.....	169
Figure B.28: Error analysis: solid line – exact BCs and BCE; dashed line – approximate BCs and BCE	170
Figure B.29: Boundary layer development for flow over a flat plate. Free stream velocity $u = 1$ m/s	171
Figure B.30: Dirichlet boundary conditions for a flat plate with symmetry plane. Empty cells in the table imply zero Neumann, or do-nothing BCs	172

Figure B.31: Computational mesh for flow over a flat plate	173
Figure B.32: Flat-plate computed and similarity solutions for $Re = 1E3$	174
Figure B.33: Flat-plate computed and similarity solutions for $Re = 1E4$	175
Figure B.34: Flat-plate computed and similarity solutions for $Re = 1E5$	176
Figure B.35: Flat-plate second velocity component distribution for $Re = 1E3$	177
Figure B.36: Flat-plate second velocity component distribution for $Re = 1E4$	178
Figure B.37: Flat-plate second velocity component distribution for $Re = 1E5$	179
Figure B.38: Flat-plate third velocity component distribution for $Re = 1E3$	180
Figure B.39: Flat-plate third velocity component distribution for $Re = 1E4$	181
Figure B.40: Flat-plate third velocity component distribution for $Re = 1E5$	182
Figure B.41: Dispersion error distribution caused by the leading edge BC singularity, $Re = 1E5$	183
Figure B.42: Dispersion error control using Kolesnikov's theory, $Re = 1E5$	184
Figure B.43: Comparison of the Blasius and two computed solutions for $Re=1E6$. The profiles are extracted from the trailing edge of the flat plate ($x=0.01, y=0$).....	185
Figure B.44: Computed velocity profiles with and without ADBC formulation.....	186
Figure B.45: Differentially heated enclosure with 1:8:8 aspect ratio (not to scale).....	187
Figure B.46: Pressure contours for square thermal cavity at $Ra = 10^4$. The choice of reference temperature, i.e. $T_{ref} = T_c$ (left) and $T_{ref} = (T_H + T_C) / 2$ (right), significantly affects the pressure distribution.	188
Figure B.47: Temperature distribution at $t=80, 120$ and 217.5 seconds for an incipient non-steady laminar flow at $Ra = 4 \times 10^5, Re = 756$	189

Figure B.48: Temperature samples in the upper-right corner of the cavity at $t=172.5, 177.5, 182.5$ and 187.5 seconds indicating an incipient non-steady laminar flow at $Ra = 4 \times 10^5$, $Re = 756$	190
Figure B.49: Velocity vectors directly on the surface (top and right planes). Symmetry plane is shown in front ($z=8$).....	191
Figure B.50: Iso-surfaces of temperature. Solid wall is shown in front ($z=0$)	192
Figure B.51: Iso-surfaces of velocity magnitude. Symmetry plane is shown in front ($z=8$).....	193
Figure B.52: Iso-surfaces of velocity magnitude. Solid wall is shown in front ($z=0$)	194
Figure B.53: Temperature contours.....	195
Figure B.54: Velocity magnitude contours.....	196
Figure B.55: Iso-surfaces of velocity magnitude. Comparison of the filtered (left) and AD (right) velocity fields. Symmetry plane is shown in front ($z=8$).....	197
Figure B.56: Comparison of laminar and turbulent velocity profiles.....	198
Figure B.57: Comparison of laminar and turbulent velocity profiles (viscous sublayer)	199
Figure B.58: Thermal cavity V-velocity profiles extracted from the symmetry plane ($z=8$) at different heights	200
Figure B.59: Thermal cavity V-velocity profiles extracted from the symmetry plane ($z=8$) at different heights	201
Figure B.60: Interpolated thermal cavity V-velocity profiles extracted from the symmetry plane ($z=$ 8) at $y=1$ and $y=5$	202
Figure B.61: Thermal cavity symmetry plane unitized scale temperature flood with velocity vector overlay. Dashed circles highlight the traversing vortex entities at hot/cold walls.....	203

Figure B.62: Thermal cavity symmetry plane *arLES* theory close-up flood with velocity vector

overlay, $Ra = 10^8$, $t=382.1s$. Left to right, top to bottom: $\bar{\Theta}$, $\overline{u_2\Theta'} + u_2'\bar{\Theta}$, $\bar{u}_1\bar{u}_2$,

$\overline{u_1u_2'} + u_1'\bar{u}_2$, $\overline{u_1'u_2'}$ 204

Figure B.63: The *arLES* statistics – C_{11} component 205

Figure B.64: The *arLES* statistics – C_{12} component 206

Figure B.65: The *arLES* statistics – C_{13} component 207

Figure B.66: The *arLES* statistics – C_{22} component 208

Figure B.67: The *arLES* statistics – C_{23} component 209

Figure B.68: The *arLES* statistics – C_{33} component 210

Figure B.69: The *arLES* statistics – V_1^\ominus component..... 211

Figure B.70: The *arLES* statistics – V_2^\ominus component..... 212

Figure B.71: The *arLES* statistics – V_3^\ominus component..... 213

NOMENCLATURE

$[A]$	matrix inverse differential operator in $rLES$
$A_\delta(\dots)$	boundary commutation error integral
c_{ij}	cross-stress tensor pair, unfiltered
\bar{c}_{ij}	cross-stress tensor pair
C	continuity constraint variable
C_{ij}	cross-stress tensor from triple decomposition
C_s	Smagorinsky constant and SFS constant
D	depth of a thermal cavity
\mathbb{D}	deformation (or strain rate) tensor
$\mathcal{D}(\dots)$	differential definition
DE	conservation of energy principle
DM	conservation of mass principle
DP	conservation of momentum principle
f	source function and a general function placeholder
$F(\dots)$	filter function
$\mathcal{F}(\dots)$	Fourier transform
f_j	kinematic flux vector
f_j^d	dissipative flux vector
g	constant of gravitational acceleration
g_i	gravity vector components
\hat{g}_i	gravity unit vector components
g_δ	Gaussian filter function
h	finite element mesh measure
H	channel's half-width and height of a thermal cavity
H^+	dimensionless half-width of a channel in similarity coordinates
i	coordinate direction subscript
$[I]$	identity matrix
\mathbb{I}	unit tensor
j	coordinate direction subscript
k	coordinate direction subscript
$\mathcal{L}(\dots)$	conservation principle and PDE system
L_{ij}	Leonard stress tensor from triple decomposition
L_{ref}	reference length
n	dimension of the problem
n	superscript/subscript indicating time discretization level
n	normal vector component
\hat{n}	unit normal vector component
N	Newton-Cotes degree

N	superscript indicating approximate solution via inner product
N_k	finite element basis function set
$\mathcal{O}(\dots)$	order of approximation
p	pressure
p	superscript indicating iteration index
\bar{p}	space filtered pressure
\bar{p}^*	space filtered pressure, not satisfying continuity
\hat{p}	time-averaged pressure
p'	residual pressure and non-dimensional pressure
p_{ref}	reference pressure
q, q_α	state-variable placeholder
Q	expansion coefficients from a weak statement
$\mathbb{R}^d, \mathbb{R}^n$	Euclidean space
R	height aspect ratio of a thermal cavity
R_{ij}	Reynolds subgrid-scale tensor from triple decomposition
s	coordinate direction
s, s_α	source function
\mathbb{S}	full Navier-Stokes stress tensor
$ \bar{\mathbb{S}} $	Galilean invariant in Smagorinsky model
t	time
t'	non-dimensional time
t_{ref}	reference time
T	dimensional temperature and total/final time
T_C	temperature of the “cold” wall in thermal cavity
T_H	temperature of the “hot” wall in thermal cavity
T_{ref}	reference temperature
u	velocity component in x-direction
\mathbf{u}	velocity vector
\bar{u}	space filtered velocity
\bar{u}^*, \tilde{u}	space filtered velocity, not satisfying continuity
\hat{u}	time-averaged velocity
\tilde{u}	space filtered velocity of RaNS time-average velocity
u'	residual velocity and non-dimensional velocity
u_{AD}	velocity calculated via approximate deconvolution formula
u_{ave}	averaged velocity
u_τ	friction velocity
u^+	dimensionless velocity in similarity coordinates
U_{ref}	reference velocity
v	velocity component in y-direction
v_j^\ominus	cross-thermal vector pair, unfiltered

\bar{v}_j^\ominus	cross-thermal vector pair
w	velocity component in z-direction and quadrature weights
W	width of a thermal cavity
x	coordinate direction and subscript
x'	non-dimensional coordinate direction
\mathbf{x}	vector of spatial coordinates
y	coordinate direction and subscript
y^+	dimensionless normal distance in similarity coordinates
z	coordinate direction and subscript

Greek symbols

α	coefficient of thermal diffusivity
β	coefficient of thermal expansion
γ	shape factor in rLES, $\gamma = 6$
Γ	boundary of Ω
δ	filter measure
δ^+	dimensionless filter measure in similarity coordinates
δ_{ij}	Kronecker delta function
Δ	local grid size in Smagorinsky model
Δt	time discretization step
ΔT_{ref}	reference temperature gradient
ε	convergence tolerance
ε_i	commutation error
ζ	coordinate direction
λ	constant from linearity property
θ	implicitness factor
Θ	non-dimensional temperature
$\bar{\Theta}$	space filtered non-dimensional temperature
Θ'	residual non-dimensional temperature
μ	dynamic viscosity
μ^+	dimensionless dynamic viscosity in similarity coordinates
ν	kinematic viscosity
ν^t	turbulent eddy viscosity
ξ	vector of spatial coordinates
ρ_0	constant density
τ_{ij}	subgrid-scale tensor
τ_w	wall shear stress
ϕ	continuity constraint function
ϕ_{ref}	reference continuity constraint function
Φ	weak statement test space function
Ψ	weak statement trial space function
Ω	spatial domain

Ω_e	finite element domain
Ω^h	spatial discretization of Ω

Dimensionless groups

Bo	Boussinesq number
Gr	Grashof number
Pe	Peclet number
Pr	Prandtl number
Ra	Rayleigh number
Re	Reynolds number
Re_H	Reynolds number based on the averaged velocity and channel's width
Re_L	Reynolds number based on flat plate's length
Re^t	Turbulent Reynolds number
Re^+	Reynolds number based on friction velocity u_τ

LIST OF ABBREVIATIONS

<i>ar</i> LES	Analytical rational large eddy simulation
AD	Approximate deconvolution
ADBC	Approximate deconvolution boundary conditions
BC	Boundary condition
BCE	Boundary commutation error
BCs	Boundary conditions
BL	Boundary layer
CCM	Continuity constraint method
CFD	Computational fluid dynamics
DNS	Direct numerical simulation
EBV	Elliptic boundary value
FCT	Flux-corrected transport
FD	Finite difference
FE	Finite element
FEM	Finite element method
GMRES	Generalized minimal residual method
GWS	Galerkin weak statement
IBV	Initial boundary value
IC	Initial condition
ILES	Implicit large eddy simulation
INS	Incompressible Navier-Stokes
LES	Large eddy simulations
MILES	Monotone integrated large eddy simulation
MLT	Mixing length theory
NS	Navier-Stokes
NWM	Near-wall model
NWR	Near-wall resolution
PDE	Partial differential equation
PICMSS	Parallel interoperable computational mechanics system simulator
PPE	Pressure Poisson equation
PPM	Piecewise parabolic method
RaNS	Reynolds-averaged Navier-Stokes
<i>r</i> LES	Rational large eddy simulation
SFS	Subfilter scale
SGS	Subgrid-scale
SGSE	Subgrid-scale estimation
SMAC	Simplified marker and cell
TS	Taylor series
TVD	Total variation diminishing
WS	Weak statement

1. INTRODUCTION

Turbulent flows are omnipresent in nature and are an integral part of our everyday life. The variety of turbulent flows is probably as diverse as the number of length scales they possess. The examples range from streams in small creeks to gigantic atmosphere and ocean currents, from blood stream in arteries to water torrents through Francis turbines used in dams, from flows over a golf ball to flows around aircraft wing tips. A wide variety of other examples of turbulence can be found in a book by Marcel Lesieur (2008).

Numerical simulation of turbulent flows is required to gain better understanding of many processes in nature and in industry. Turbulence is made of an entire hierarchy of eddies over a wide range of length scales. The Navier-Stokes equations that describe turbulent incompressible flows can in general be used unaltered in order to resolve all details and scales of turbulence, i.e. the spatial and temporal evolution of the entire range of eddies. This straight forward approach of solving the Navier-Stokes equations is termed *direct numerical simulation* (DNS). The DNS approach is so computationally expensive that it is currently not feasible for Reynolds (Re) numbers encountered in most industrial applications and for reasonable domain sizes. To capture the smallest dissipative Kolmogorov's scales using a 3D Cartesian uniform mesh an estimation of mesh cells required is given by $N \approx Re^{9/4}$ (John, 2004). In addition, one can estimate that the number of floating point operations required to complete the simulation is proportional to the number of mesh points and the number of time steps. A good discussion of the computational cost of DNS is provided by Pope (2000), who concludes that the cost increases as the cube of the Reynolds number. In those applications for which DNS is currently feasible more difficulties arise from the fact that the boundary and initial conditions must have the precision which is required by the smallest scales of the flow. The conditions which are that precise seem to be impossible to provide

for most geophysical flows for instance. And even for smaller problems, surface roughness might significantly degrade the solution accuracy.

While the direct numerical simulation approach of solving turbulent flows is still facing many issues even on present-day computers, two major alternatives exist. The *Reynolds-averaged Navier-Stokes* (RaNS) theory avoids full resolution of time and space evolution of turbulence by using the concept of time averaging. In RaNS every flow property is decomposed into its time-mean and fluctuating components. Applying time averaging to conservation principles yields a set of Reynolds-averaged Navier-Stokes equations that describe the spatial variations of time-averaged flow quantities. The consequence of applying this operation to non-linear NS equations is the appearance of an unknown turbulent inertia tensor for which no physical laws exist. A statistical or semi-empirical *closure model* is required to resolve this dilemma. Many different models have been proposed to resolve the *closure problem*, most of which are based on the Boussinesq eddy-viscosity approximation. A good discussion of these candidates is provided in a book by Wilcox (2006). Despite much success in using this approach for certain types of turbulent flows it shows very little applicability to most problems of interest. However it must be noted that although RaNS may now be yielding diminishing returns it is still far from obsolete as it is used in most of engineering analysis (White, 2006).

The second alternative is termed Large Eddy Simulation (LES), the computational cost of which is generally placed somewhere in between the RaNS and DNS approaches. In LES the larger unsteady motions are directly resolved, while smaller ones require closure. Unlike RaNS where the flow quantities are averaged in time, the LES theory uses the concept of convolution with a spatial filter. The goal of LES is to compute only the scales defined by the diameter of the filter. Thus the flow quantities are decomposed into two parts, viz., the resolved scales and the unresolved scales. Filtering operation (generally defined via convolution) is applied to the conservation principles PDE system yielding a set of

Space Filtered Navier-Stokes equations. Unlike RANS where time-averaging process generates only one turbulent inertia tensor in each equation, filtering operation in LES generates a quadruple of tensors a priori unknown.

This dissertation focuses strictly on Large Eddy Simulation approach, while RANS and DNS methods are only mentioned occasionally.

1.1 BRIEF HISTORY AND CHALLENGES IN LES

The Large Eddy Simulation concept was originally introduced in the pioneering work of Joseph Smagorinsky (1963) and the unique features of LES were first explored by James Deardorf (1970). In his work Smagorinsky introduced the concept of *eddy viscosity*, which is now known as the *Smagorinsky model*. To resolve the closure problem the eddy viscosity parameter was defined as a function of the filter radius, the magnitude of the resolved velocity gradient and a global constant. The Smagorinsky model is the first and the simplest subgrid-scale (SGS) model, the drawbacks of which are now well known and documented, e.g., see Zang et al. (1993). For example, the global constant used in this model cannot be uniquely determined and used in various turbulent flows. Also, it is easily identified that the backscatter of energy is completely prevented since the eddy viscosity is always positive. Finally, the Smagorinsky model generally provides too much diffusion and the eddy viscosity does not vanish for laminar flows.

An improvement to the original Smagorinsky model is proposed by Germano et al. (1991) and their *dynamic SGS model*. The improved approach allows computing the unknown constant dynamically as a function of space and time. This means that the constant is no longer a global parameter specified a priori, but is instead computed internally by the program depending on the local flow conditions. In contrast to the Smagorinsky model the dynamic SGS model does allow backscatter of energy due to its

ability to predict negative values of the unknown constant. However, numerical tests show that this constant can vary significantly in space and time, i.e., it may become a very non-smooth function (John, 2004). Other improvements to the dynamic SGS model have been proposed with varying levels of success, e.g. see Ghosal et al. (1995), Yang and Ferziger (1993), Carati and Eijnden (1997) .

It is now evident that the fundamental challenge in LES is to provide a satisfactory closure to the four unknown tensor fields that appear in the resolved-scale conservation principles. As just described, there exists a range of *deviatoric* SGS tensor model definitions which provide closure based entirely on the empirical insight. In distinction to a model, Galdi and Layton (2000) introduced a fundamentally new approach in LES which provides a mathematically elegant closure based strictly on analytical considerations. This approach is now known as the *rational LES* (*rLES*) theory. The second order *rLES* formulation is based on approximations in wave number space and computes the Fourier transform of the Gaussian filter using the *rational* subdiagonal Padé approximation. A good mathematical as well as numerical analysis of *rLES* can be found in a book by Berselli et al. (2006). In this dissertation the rational LES theory is used as the base approach in deriving a new essentially analytical rational LES (*arLES*) formulation.

For bounded domains, besides the closure problem, an equally challenging issue of LES is that of prescribing suitable boundary conditions for the resolved-scale state variables. Two major approaches to tackle this problem include either using a constant filter measure throughout the computational domain or a filter of spatially non-uniform which vanishes at the boundary. A constant filter measure approach is used throughout this dissertation while the appropriate formulation to face the challenges incurred by making this choice is derived.

1.2 THIS DISSERTATION

This dissertation details derivation of an essentially analytical rational LES (*arLES*) theory closure for unsteady three-dimensional space filtered thermal-incompressible NS PDE system, well-posed for bounded domains. Original contributions of this work include

1. Resolution of the problem of correctly adapting a filter of constant measure near the Dirichlet boundary through design of suitable boundary conditions based on *Approximate Deconvolution* (AD) combined with Galerkin weak forms.
2. Derivation of an approximate solution for the *Boundary Commutation Error* (BCE) integral when filtering through a non-homogeneous Dirichlet boundary via *Approximate Deconvolution Boundary Conditions* (ADBC) methodology.
3. Derivation of the suitable non-homogeneous Dirichlet boundary conditions for the *auxiliary problem* of *arLES* theory organized via perturbation theory. The BC closure of $\mathcal{O}(\delta^2)$ is derived via direct evaluation of unfiltered tensors followed by the application of ADBC methodology.
4. Assessment of *arLES* theory proper order *subfilter scale* (SFS) tensor implementation based on weak form CFD error annihilation theory.
5. Extension of the *arLES* theory to the thermal NS with focus on BCs suitable for bounded domains.

2. LARGE EDDY SIMULATION

Large eddy simulation (LES) has a five decade history in numerical simulation of turbulent flows. In LES the larger unsteady motions are directly resolved, while the action of smaller scales is modeled. The key hypothesis states that the large-scale motions are affected by the flow geometry and are not universal, whereas the small-scale motions are nearly isotropic and have a universal character.

The computational cost of direct numerical simulation (DNS) is extremely high. A solution obtained by DNS requires a complete three-dimensional, time-dependent solution of the Navier-Stokes equations. However, over 99% of the computational effort in DNS is devoted to the smallest, dissipative scales, whereas the energy and anisotropy are contained predominantly in the larger scales of motion (Pope, 2000). In LES, only the large-scale eddies are computed directly. The action of small-scale motions is represented by simple models. This allows having computational grids with cells that are much larger than the smallest scales of turbulence, viz., eddies of Kolmogorov scale (Kolmogorov, 1941). Additionally, much larger time steps can be taken in LES as compared to DNS. As a result, obtaining a solution at a given Reynolds number is much cheaper using LES as opposed to DNS. Conversely, for a given computational cost one can achieve a much higher Reynolds number solution with LES than with DNS.

The approach of LES can be summarized in six steps:

- i. Define a filtering operation that will decompose every state-variable (velocity, pressure etc) into the sum of resolved and unresolved components.
- ii. Derive the equations for filtered quantities from the original conservation principles. This operation applied to the momentum equation generates a quadruple of unknown tensors which describe interactions between resolved and unresolved scales.

- iii. Obtain a closure by modeling the four unknown tensor fields. This yields an LES subgrid-scale (SGS) model.
- iv. Provide the boundary conditions for space-filtered state variables, or a so-called Near Wall Model (NWM) in LES
- v. Discretize the domain appropriately. One may opt to resolve most of the scales in the near wall region directly instead of modeling them. This is called LES with Near-Wall Resolution (NWR)
- vi. Perform a simulation by solving the filtered equations numerically.

2.1 CONSERVATION PRINCIPLES

The PDE system of continuum mechanics conservation principles describing viscous thermal flow of an incompressible Newtonian fluid is collectively termed the Navier-Stokes equations, complemented with a temperature-driven body force and the energy equation. This system of closely coupled PDEs for mass, momentum and energy transport written in dimensional form is

$$\text{DM: } \mathcal{L}(\rho_0) = \text{div}(\mathbf{u}) = \frac{\partial u_i}{\partial x_i} = 0 \quad (2.1)$$

$$\text{DP: } \mathcal{L}(u_i) = \frac{\partial u_i}{\partial t} + \frac{\partial}{\partial x_j} \left(u_j u_i - \nu \frac{\partial u_i}{\partial x_j} + \frac{1}{\rho_0} p \delta_{ij} \right) + \beta (T - T_{ref}) g_i = 0 \quad (2.2)$$

$$\text{DE: } \mathcal{L}(T) = \frac{\partial T}{\partial t} + \frac{\partial}{\partial x_j} \left(u_j T - \alpha \frac{\partial T}{\partial x_j} \right) = 0 \quad (2.3)$$

where u_i are components of the velocity vector \mathbf{u} , p is the pressure, T is the temperature, T_{ref} is some reference temperature, t is the time, x_j are the space coordinates, g_i are components of the gravity vector, ρ_0 is the density, ν is the coefficient of kinematic viscosity, β is the coefficient of thermal expansion, α is the coefficient of thermal diffusivity, δ_{ij} is the Kronecker delta.

The indices range $1 \leq i, j \leq n$, where n is the dimension of the problem. The Boussinesq approximation (Boussinesq, 1987) derives the thermal body force in the momentum equation (2.2).

To non-dimensionalize equations (2.1) through (2.3) the following scales are introduced

- L_{ref} – a characteristic length scale
- U_{ref} - a characteristic velocity scale
- T_{ref} - a characteristic temperature scale
- $t_{ref} = L_{ref} / U_{ref}$ - a characteristic time scale for the problem

The following non-dimensional (non-D) groups are then used to rewrite equations (2.1) through (2.3) in non-D form

$$\begin{aligned} x'_j &= \frac{x_j}{L_{ref}}; & u'_j &= \frac{u_j}{U_{ref}}; & t' &= \frac{t}{L_{ref} / U_{ref}} \\ p' &= \frac{p}{\rho_0 U_{ref}^2}; & \Theta &= \frac{T - T_{ref}}{\Delta T_{ref}} \end{aligned} \quad (2.4)$$

Dropping the primes non-D equations (2.1) through (2.3) become

$$DM': \mathcal{L}(\rho_0) = \nabla \cdot \mathbf{u} = \text{div}(\mathbf{u}) = 0 \quad (2.5)$$

$$DP': \mathcal{L}(u_i) = \frac{\partial u_i}{\partial t} + \frac{\partial}{\partial x_j} \left(u_j u_i - \frac{1}{Re} \frac{\partial u_i}{\partial x_j} + p \delta_{ij} \right) + \frac{Gr}{Re^2} \Theta \hat{g}_i = 0 \quad (2.6)$$

$$DE': \mathcal{L}(\Theta) = \frac{\partial \Theta}{\partial t} + \frac{\partial}{\partial x_j} \left(u_j \Theta - \frac{1}{Pe} \frac{\partial \Theta}{\partial x_j} \right) = 0 \quad (2.7)$$

where Reynolds, Peclet and Grashof numbers are defined as

$$Re = \frac{U_{ref} L_{ref}}{\nu}; \quad Pe = \frac{U_{ref} L_{ref}}{\alpha} = Re \cdot Pr; \quad Gr = \frac{g \beta \Delta T_{ref} L_{ref}^3}{\nu^2}; \quad (2.8)$$

2.2 SPACE FILTERING CONCEPTS

Unlike DNS, which resolves all scales in the flow, the goal of LES is to compute only the scales defined by the diameter of the filter. The principal operation of LES is low-pass filtering, i.e., the scales associated with high frequencies are filtered out and scales associated with low frequencies are retained. The flow quantities which describe the flow (velocity, pressure etc.) are therefore decomposed into two parts, namely, the resolved scales and the resultant unresolved scales.

In classical LES, the convolution operation defines the resolved larger scale motion. During the filtering operation, the conservation principles are convolved with a spatial filter function and the result is the space filtered conservation equations. Leonard (1974) defined a generalized filter as a convolution integral, hence

$$\bar{u}_i(\mathbf{x}, t) \equiv \int F(\mathbf{x} - \boldsymbol{\xi}) u_i(\boldsymbol{\xi}, t) d\boldsymbol{\xi} \quad (2.9)$$

where the integration is performed over the entire domain, and the filter function, F , is normalized by requiring that

$$\int F(\mathbf{x} - \boldsymbol{\xi}) d\boldsymbol{\xi} = 1 \quad (2.10)$$

The difference between the actual solution, $u_i(\mathbf{x}, t)$, and the space filtered quantity, $\bar{u}_i(\mathbf{x}, t)$, forms the residual field, $u'_i(\mathbf{x}, t)$, thus defined by

$$u'_i(\mathbf{x}, t) \equiv u_i(\mathbf{x}, t) - \bar{u}_i(\mathbf{x}, t) \quad (2.11)$$

There are many kinds of filter kernels available. Filters can be isotropic or non-isotropic, homogeneous or non-homogeneous. Despite of the specific choice the filter must always provide a measure (size of

the filter) which defines the smallest resolvable scales of the flow. The Gaussian filter is used throughout this dissertation.

A visualization of how filtering works is shown in Figure B.1. All figures used in this manuscript are placed in Appendix B. Consider a random scalar one-dimensional function $u(x)$ that represents a sample velocity field and the corresponding filtered field $\bar{u}(x)$ obtained using the Gaussian filter with $\delta \approx 0.35$. As can be seen the filtered velocity $\bar{u}(x)$ follows the same pattern as the original unfiltered velocity field $u(x)$. This simply shows that the longer lengthscale fluctuations have been preserved. The shorter lengthscale fluctuations, however, have been removed. Figure B.1 shows the essence of how turbulent flows can be accurately approximated without resolving all the scales in the flow. The bottom part of the figure shows the LES theory residual $u'(x)$ which has also been filtered. It is important to notice that the filtered unresolved field is in general not zero, i.e., $\overline{u'(x)} \neq 0$.

After an appropriate filtering operator is chosen, a space filtered velocity \bar{u}_i , and a space filtered pressure \bar{p} can be defined. The filtering operator is assumed to have the following two properties:

- 1) The filter is a linear operator

$$\overline{\mathbf{u} + \lambda \mathbf{v}} = \bar{\mathbf{u}} + \lambda \bar{\mathbf{v}} \quad (2.12)$$

- 2) The filter is spatially uniform, so that filtering and differentiation commute

$$\overline{\left(\frac{\partial \mathbf{u}}{\partial x_i} \right)} = \left(\frac{\partial \bar{\mathbf{u}}}{\partial x_i} \right) \quad (2.13)$$

The LES filtering operator, as defined by Leonard (1974), uses convolution with an appropriate filter function F , i.e., the space filtered velocity and pressure (\bar{u}_i, \bar{p}) are defined by convolving the NS primitive variables (u_i, p) with a filter function

$$\bar{u}_i(\mathbf{x}, t) \equiv (F * u_i)(\mathbf{x}, t) = \int_{\mathbb{R}^d} F(\mathbf{x} - \boldsymbol{\xi}) u_i(\boldsymbol{\xi}, t) d\boldsymbol{\xi} \quad (2.14)$$

$$\bar{p}(\mathbf{x}, t) \equiv (F * p)(\mathbf{x}, t) = \int_{\mathbb{R}^d} F(\mathbf{x} - \boldsymbol{\xi}) p(\boldsymbol{\xi}, t) d\boldsymbol{\xi} \quad (2.15)$$

Linearity of integration property applied to (2.14) and (2.15) immediately proves that Leonard's filtering operator is linear and property (2.12) is satisfied. If domain is unbounded and the functions (u_i, p) are sufficiently smooth in space and time, filtering and differentiation commute and property (2.13) is also satisfied. As will be shown later, this is not the case for bounded domains.

With space filtered velocity and pressure (\bar{u}_i, \bar{p}) clearly defined in (2.14)-(2.15) the equations for these new variables are needed. These equations are derived in the next section.

2.3 SPACE FILTERED NAVIER-STOKES EQUATIONS

Space filtered conservation principles for mass, momentum and energy transport are derived by applying a filtering operation to equations (2.5)-(2.7).

The continuity equation is filtered first. Using the assumption that filtering and differentiation commute the space filtered continuity equation is

$$\overline{DM}: \mathcal{L}(\bar{\rho}_0) = \frac{\partial \bar{u}_i}{\partial x_i} = \frac{\partial \bar{u}_i}{\partial x_i} = 0 \quad (2.16)$$

Being linear, the continuity equation does not change after filtering. Notice also that if \bar{u}_i in (2.16) is replaced by $u_i - u'_i$ the following manipulations can be performed

$$\frac{\partial \bar{u}_i}{\partial x_i} = \frac{\partial (u_i - u'_i)}{\partial x_i} = \frac{\partial (u_i)}{\partial x_i} - \frac{\partial (u'_i)}{\partial x_i} = -\frac{\partial (u'_i)}{\partial x_i} = 0 \quad (2.17)$$

showing that the unresolved field is also solenoidal.

Filtering of the momentum equation is performed in like manner. A filtering operator is applied to both sides of equation (2.6). Using properties (2.12) and (2.13) the space filtered momentum equation takes the form

$$\mathbf{DP} : \mathcal{L}(\bar{u}_i) = \frac{\partial \bar{u}_i}{\partial t} + \frac{\partial}{\partial x_j} \left(\overline{u_j u_i} - \frac{1}{Re} \frac{\partial \bar{u}_i}{\partial x_j} + \bar{p} \delta_{ij} \right) + \frac{Gr}{Re^2} \bar{\Theta} \hat{g}_i = 0 \quad (2.18)$$

Unlike the continuity equation which does not change after filtering, the filtered nonlinear momentum equation (2.18) is not the same as its non-filtered counterpart (2.6), because of the following inequality

$$\overline{u_j u_i} \neq \bar{u}_j \bar{u}_i. \quad (2.19)$$

Finally, space filtering of the energy equation yields

$$\mathbf{DE} : \mathcal{L}(\bar{\Theta}) = \frac{\partial \bar{\Theta}}{\partial t} + \frac{\partial}{\partial x_j} \left(\overline{u_j \Theta} - \frac{1}{Pe} \frac{\partial \bar{\Theta}}{\partial x_j} \right) = 0 \quad (2.20)$$

The irreversible work viscous dissipation term in (2.20) is ignored.

As can be seen from (2.18) and (2.20) these equations are very similar to their non-filtered counterparts with exception that they poses new unknown quantities, namely $\overline{u_j u_i}$ and $\overline{u_j \Theta}$. Using linearity of the filter property (2.12) these terms can be expanded as

$$\overline{u_j u_i} = \overline{(\bar{u}_j + u'_j)(\bar{u}_i + u'_i)} = \bar{u}_j \bar{u}_i + \overline{u'_j \bar{u}_i} + \overline{\bar{u}_j u'_i} + \overline{u'_j u'_i} \quad (2.21)$$

$$\overline{u_j \Theta} = \overline{(\bar{u}_j + u'_j)(\bar{\Theta} + \Theta')} = \bar{u}_j \bar{\Theta} + \overline{u'_j \bar{\Theta}} + \overline{\bar{u}_j \Theta'} + \overline{u'_j \Theta'} \quad (2.22)$$

Thus, instead of just one convective term in each momentum equation there is now a quadruple of tensors associated with convection processes in the flow. The first term in (2.21) is the resolved scale

tensor which describes convection processes of the large-scale motions. The second and third terms are the cross tensors which involve resolved and unresolved scale interactions. Finally, the last term is the unresolved subfilter scale tensor.

Filtering of the Navier-Stokes equations generates four unknown tensors involving resolved and unresolved scale tensor products. The energy equation generates a system of four similarly unknown vector fields, as shown in (2.22). In order to close the system of space filtered NS equations the unknown tensors (and vectors) must be expressed in terms of the resolved scale state variable. Replacement of $\overline{u_j u_i}$ in terms of \bar{u}_i and \bar{u}_j (also $\overline{u_j \Theta}$ in terms of \bar{u}_j and $\bar{\Theta}$) is the closure challenge in large eddy simulation.

2.4 REYNOLDS AVERAGED NAVIER-STOKES

The Reynolds averaged Navier-Stokes equations (RaNS) are derived by *time averaging* the conservation principle PDEs (as opposed to *space filtering* in LES) using *Reynolds decomposition* whereby the instantaneous velocity u_i is expressed as the sum of a mean, \hat{u}_i , and a fluctuating part, u'_i , so that

$$u_i = \hat{u}_i + u'_i \quad (2.23)$$

In equation (2.23), the quantity \hat{u}_i is the time-averaged, or mean, velocity defined by

$$\hat{u}_i = \lim_{T \rightarrow \infty} \frac{1}{T} \int_t^{t+T} u_i dt \quad (2.24)$$

Since the time-average of the mean velocity is again the same time-averaged value, the time average of the fluctuating part of the velocity is zero, hence

$$\hat{u}'_i = \lim_{T \rightarrow \infty} \frac{1}{T} \int_t^{t+T} (u_i - \hat{u}_i) dt = \hat{u}_i - \hat{u}_i = 0 \quad (2.25)$$

For incompressible flows the time-averaged isothermal DP PDE in non-dimensional form is

$$\mathbf{DP} : \mathcal{L}(\hat{u}_i) = \frac{\partial \hat{u}_i}{\partial t} + \frac{\partial}{\partial x_j} \left(\hat{u}_j \hat{u}_i + \widehat{u'_j u'_i} - \frac{1}{Re} \frac{\partial \hat{u}_i}{\partial x_j} + \hat{p} \delta_{ij} \right) = 0 \quad (2.26)$$

The only difference between RaNS and NS equations is the generated single unknown Reynolds stress tensor $\widehat{u'_j u'_i}$ in (2.26). A wide range of theoretical frameworks generate closure models for $\widehat{u'_j u'_i}$. The pervasive basis is variations on mixing length theory leading to an *eddy viscosity* hypothesis of dimensionality $L^2 t^{-1}$. The assumption pervading RaNS closure models is existence of a *turbulent eddy viscosity* ν^t multiplying the Stokes strain rate tensor based on time averaged velocity

$$\widehat{u'_j u'_i} \equiv \tau_{ij} \propto -\nu^t \hat{S}_{ij} \quad (2.27)$$

Eddy viscosity non-dimensionalized by kinematic viscosity defines the *turbulent Reynolds number* Re^t

$$Re^t = \nu^t / \nu \quad (2.28)$$

and the resultant non-D isothermal RaNS DP is

$$\mathbf{DP} : \mathcal{L}(\hat{u}_i) = \frac{\partial \hat{u}_i}{\partial t} + \frac{\partial}{\partial x_j} \left(\hat{u}_j \hat{u}_i - \frac{1 + Re^t}{Re} \frac{\partial \hat{u}_i}{\partial x_j} + \hat{p} \delta_{ij} \right) = 0 \quad (2.29)$$

When Re^t becomes very high, transparent in (2.29), the eddy viscosity closure modeling significantly augments the diffusion level in RaNS DP compared to NS, the “1” in $1 + Re^t$. The computational benefit to RaNS algorithm performance is substantial diffusive moderation of the dispersion error mode intrinsic to discrete CFD algorithms addressing NS at large Re numbers.

2.5 SGS TENSOR CLOSURE MODELING FOR LES

In distinction to RaNS, space filtering the NS PDEs generates a convective term $\overline{u_j u_i}$ composed of the quadruple of tensors (2.21). One of the standard approaches to LES closure for DP is termed *triple decomposition*, well detailed in Sagaut (2004). This approach assumes all terms in (2.21) are expressible in the resolved scale variable, leading to the resultant SGS tensor closure model

$$\begin{aligned}\tau_{ij} &\equiv \overline{u_j u_i} - \overline{u_j} \overline{u_i} \\ &= L_{ij} + C_{ij} + R_{ij}\end{aligned}\tag{2.30}$$

where Leonard, cross-stress and Reynolds subgrid tensors are defined as

$$\begin{aligned}L_{ij} &\equiv \overline{\overline{u_j} \overline{u_i}} - \overline{u_j} \overline{u_i} \\ C_{ij} &\equiv \overline{\overline{u_j} u'_i} + \overline{u'_j \overline{u_i}} \\ R_{ij} &\equiv \overline{u'_j u'_i}\end{aligned}\tag{2.31}$$

Rearranging (2.30) defines the unknown $\overline{u_j u_i} = \tau_{ij} + \overline{u_j} \overline{u_i}$ which inserted into space filtered DP NS (2.18) gives

$$\text{DP} : \mathcal{L}(\overline{u_i}) = \frac{\partial \overline{u_i}}{\partial t} + \frac{\partial}{\partial x_j} \left(\overline{u_j} \overline{u_i} + \tau_{ij} - \frac{1}{Re} \frac{\partial \overline{u_i}}{\partial x_j} + \overline{p} \delta_{ij} \right) = 0\tag{2.32}$$

Note that (2.32) is *absolutely identical* with RaNS DP PDE (2.26).

The pioneering spatial filtered NS DP isothermal turbulent flow simulation publication is Smagorinsky (1963). The single tensor model based *only* on the resolved scale velocity attempts to estimate the action of the LES dual resolved-unresolved scale plus strictly unresolved scale *tensor triple* in (2.21). This ends up placing the entire burden of prediction fidelity on physical insight. The Smagorinsky closure model is of mixing length theory (MLT) *eddy viscosity* hypothesis with a single model constant. It is

distinguishable from the RaNS MLT closure *only* by this constant replacing the Prandtl MLT definition with van Driest wall proximity damping function. The turbulent viscosity parameter in the Smagorinsky model is

$$\nu^t = C_s \Delta^2 |\bar{\mathbb{S}}| \quad (2.33)$$

where C_s is the Smagorinsky constant, Δ is the local grid size, and $|\bar{\mathbb{S}}| = \sqrt{2\bar{\mathbb{S}}_{ij}\bar{\mathbb{S}}_{ij}}$.

This ultimately simple Smagorinsky closure model soon proved inadequate, prompting numerous alterations catalyzed by the *Leonard stress* manipulation of resolved scale tensor equating to the resolved/unresolved scale interaction tensor field triple, Leonard (1974). The principally successful modifications, Germano et al. (1991), Lilly (1992), are termed *dynamic subgrid-scale* models which replace the Smagorinsky constant with *distributions* computed on the fly using dynamic solution-adaptive mesh refinement processes. The excessive contribution of diffusion $\mathcal{O}(h^2)$ by these SGS models is attempted corrected via alteration of numerics to locally monotone FD schemes (Boris, 1990), (Boris et al., 1992). Monotone integrated LES (MILES), the original implicit LES (ILES) algorithm further alters the SGS model resolved scale velocity prediction via approximate deconvolution (AD) onto a finer mesh (Shah and Ferziger, 1995). AD augmented with a subgrid-scale estimation (SGSE) model is reported (Domaradzki and Saiki, 1997), (Domaradzki and Yee, 2000).

AD utilization in the fully turbulent regime has generated *a posteriori* data in quantitative agreement with DNS data, c.f., (Stolz and Adams, 1999), (Stolz et al., 2001). An alternate ILES theorization addresses diffusive deficiencies via *high resolution* flux vector differencing schemes, (Grinstein and Fureby, 2004), (Margolin et al., 2006), (Grinstein et al., 2007). Numerics of this genre include flux-corrected transport

(FCT), the piecewise parabolic method (PPM), and total variation diminishing (TVD) differencing, c.f., (Harten, 1983).

At transitional Re original Smagorinsky (1963) and the filtered structure function SGS tensor model (Metais and Lesieur, 1992) proved excessively diffusive. SGS tensor alterations seeking improved transitional Re fidelity include insertion of van Driest wall-damping and a Klebanoff-type intermittency correction (Piomelli et al., 1990), dynamic SGS model alterations (Germano et al., 1991), (Lilly, 1992), low Re corrections (Voke and Yang, 1995), high-pass filtered eddy viscosity models (Stolz et al., 2004). Schlatter et al. (2004) document *a posteriori* data validation for a transitional Re specification on rather coarse meshes using AD.

Despite the truly consequential simplifications leading to DP (2.32), hence SGS tensor models based on MLT, the LES literature documents considerable success for a range of fully turbulent and select transitional Re simulations. Via the assumptions generating (2.32) the omission of the BCE integrals in (2.18) and (2.20), hence identification of resolved scale velocity *genuine* no-slip wall BCs, is of no consequence. As with RaNS closure modeling, usage of MLT based closure models in LES to state variable scalar members, if considered, requires *turbulent* Prandtl number hypothesis.

The algorithm implementation of an SGS tensor model in LES presents no fundamental challenge. In fact, if there was no alternative to an SGS tensor model this section would not have been written. Fortunately mathematically rigorous convolution/deconvolution operations for (2.21)-(2.22) are identified leading to the opportunity to derive an *essentially analytical* LES closure as described in the next section.

2.6 THE RATIONAL LES CLOSURE FORMULATION

The rational LES (*rLES*) theory closure of Galdi and Layton (2000) is based strictly on analytical considerations. It derives its name from the fact that the Fourier transform of the Gaussian filter is evaluated by the rational subdiagonal Padé approximation. The *rLES* theory closure provides analytical determination of the first three of the quadruple of stress tensors (2.21).

Progressively higher order polynomial interpolations of the Gaussian Fourier transform are compared in Figure B.2, Gaussian the solid lines and interpolation the dashed lines. The second order Taylor series (TS), which leads to the SGS tensor *gradient model* closure, generates a truly poor approximation to the Gaussian distribution, becoming non-positive at roughly filter measure half-span. Therefore, the TS approximation is only good for small wave numbers and fails completely for high wave numbers. Since dumping of scales associated with high frequencies is the primary property of the Gaussian filter the Taylor polynomial approximation is inadequate. Second and fourth order rational polynomial interpolations are significant improvements. The polynomial definitions are

$$2^{\text{nd}} \text{ order Taylor: } e^{ax_i} = 1 + ax_i + \mathcal{O}(a^2 x_i^2) \quad (2.34)$$

$$2^{\text{nd}} \text{ order Padé: } e^{ax_i} = \frac{1}{1 + ax_i} + \mathcal{O}(a^2 x_i^2) \quad (2.35)$$

$$4^{\text{th}} \text{ order Padé: } e^{ax_i} = \frac{1}{1 + ax_i + a^2 x_i^2} + \mathcal{O}(a^4 x_i^4) \quad (2.36)$$

For reference, the Gaussian filter is defined as

$$g_\delta(\mathbf{x}) \equiv \left(\frac{\gamma}{\pi \delta^2} \right)^{n/2} \exp\left(-\frac{\gamma}{\delta^2} \|\mathbf{x}\|_2^2 \right) \quad (2.37)$$

Using the convolution theorem the Fourier transforms of the large scale and cross terms in (2.21) are

$$\begin{aligned}
\mathcal{F}(\overline{u_j u_i}) &= \mathcal{F}(g_\delta) \mathcal{F}(\overline{u_j u_i}) \\
\mathcal{F}(\overline{u_j u'_i}) &= \mathcal{F}(g_\delta) (\mathcal{F}(\overline{u_j}) * \mathcal{F}(u'_i)) \\
\mathcal{F}(\overline{u'_j u_i}) &= \mathcal{F}(g_\delta) (\mathcal{F}(u'_j) * \mathcal{F}(\overline{u_i}))
\end{aligned} \tag{2.38}$$

Since $\mathcal{F}(g_\delta) \neq 0$, the Fourier transforms of u_i and u'_i are

$$\mathcal{F}(u_i) = \frac{\mathcal{F}(g_\delta) \mathcal{F}(u_i)}{\mathcal{F}(g_\delta)} = \frac{\mathcal{F}(\overline{u_i})}{\mathcal{F}(g_\delta)} \tag{2.39}$$

$$\mathcal{F}(u'_i) = \left(\frac{1}{\mathcal{F}(g_\delta)} - 1 \right) \mathcal{F}(\overline{u_i}) \tag{2.40}$$

Inserting (2.39) and (2.40) into (2.38) gives

$$\begin{aligned}
\mathcal{F}(\overline{u_j u_i}) &= \mathcal{F}(g_\delta) \mathcal{F}(\overline{u_j u_i}) \\
\mathcal{F}(\overline{u_j u'_i}) &= \mathcal{F}(g_\delta) \left(\mathcal{F}(\overline{u_j}) * \left(\frac{1}{\mathcal{F}(g_\delta)} - 1 \right) \mathcal{F}(\overline{u_i}) \right) \\
\mathcal{F}(\overline{u'_j u_i}) &= \mathcal{F}(g_\delta) \left(\left(\frac{1}{\mathcal{F}(g_\delta)} - 1 \right) \mathcal{F}(\overline{u_j}) * \mathcal{F}(\overline{u_i}) \right)
\end{aligned} \tag{2.41}$$

In (2.41) the Fourier transform of the Gaussian $\mathcal{F}(g_\delta)$ needs to be approximated by a simpler function.

The Taylor LES legacy approach utilizes a second-order Taylor series interpolation of the Gaussian of measure δ and shape factor γ . The required approximations for $\mathcal{F}(g_\delta)$ and $1/\mathcal{F}(g_\delta)$ are given in the form of quadratic polynomials, hence

$$\begin{aligned}
\mathcal{F}(g_\delta(\delta, \boldsymbol{\gamma})) &= 1 - \frac{\|\boldsymbol{\gamma}\|_2^2}{4\gamma} \delta^2 + \mathcal{O}(\delta^4) \\
\frac{1}{\mathcal{F}(g_\delta(\delta, \boldsymbol{\gamma}))} &= 1 + \frac{\|\boldsymbol{\gamma}\|_2^2}{4\gamma} \delta^2 + \mathcal{O}(\delta^4)
\end{aligned} \tag{2.42}$$

Inserting (2.42) into (2.41) and using well known properties of Fourier transformations results in

$$\begin{aligned}
\mathcal{F}(\overline{\bar{u}_j \bar{u}_i}) &= \mathcal{F}(\bar{u}_j \bar{u}_i) + \frac{\delta^2}{4\gamma} \mathcal{F}\left(\frac{\partial^2(\bar{u}_j \bar{u}_i)}{\partial x_k \partial x_k}\right) + \mathcal{O}(\delta^4) \\
\mathcal{F}(\overline{\bar{u}_j u'_i}) &= -\frac{\delta^2}{4\gamma} \mathcal{F}\left(\bar{u}_j \frac{\partial^2 \bar{u}_i}{\partial x_k \partial x_k}\right) + \mathcal{O}(\delta^4) \\
\mathcal{F}(\overline{u'_j \bar{u}_i}) &= -\frac{\delta^2}{4\gamma} \mathcal{F}\left(\frac{\partial^2 \bar{u}_j}{\partial x_k \partial x_k} \bar{u}_i\right) + \mathcal{O}(\delta^4)
\end{aligned} \tag{2.43}$$

Applying the inverse Fourier transform, closures for the lead three tensors in (2.21) are

$$\begin{aligned}
\overline{\bar{u}_j \bar{u}_i} &= \bar{u}_j \bar{u}_i + \frac{\delta^2}{4\gamma} \frac{\partial^2(\bar{u}_j \bar{u}_i)}{\partial x_k \partial x_k} + \mathcal{O}(\delta^4) \\
\overline{\bar{u}_j u'_i} &= -\frac{\delta^2}{4\gamma} \bar{u}_j \frac{\partial^2 \bar{u}_i}{\partial x_k \partial x_k} + \mathcal{O}(\delta^4) \\
\overline{u'_j \bar{u}_i} &= -\frac{\delta^2}{4\gamma} \frac{\partial^2 \bar{u}_j}{\partial x_k \partial x_k} \bar{u}_i + \mathcal{O}(\delta^4)
\end{aligned} \tag{2.44}$$

Combining the terms in (2.44) and using well known kinematic relations generates the analytical closure

$$\overline{\bar{u}_j \bar{u}_i} + \overline{\bar{u}_j u'_i} + \overline{u'_j \bar{u}_i} = \bar{u}_j \bar{u}_i + \frac{\delta^2}{2\gamma} \frac{\partial \bar{u}_j}{\partial x_k} \frac{\partial \bar{u}_i}{\partial x_k} + \mathcal{O}(\delta^4) \tag{2.45}$$

For isothermal ($Gr = 0$) flow and omitting the Re^{-1} term in (2.18), (2.45) inserted therein produces the *gradient model* reported in the LES literature. In *a priori* testing for isotropic decaying turbulence, comparison with experiment showed quality correlations (Winckelmans et al., 2001). Conversely, numerous reported *a posteriori* CFD data confirm the gradient model does not dissipate sufficient energy yielding an unstable algebraic solution process (Vreman, 1995). Stabilizing the algorithm via Smagorinsky model insertion generates excessive diffusion (Clark et al., 1979).

The rLES theory resolution replaces TS interpolation with compact *rational* Padé polynomials, a formulation possessing ready extension to higher order approximations which are monotone and *non-negative*, Figure B.2.

The *rational* Padé approximations of the exponential reads as

$$e^{-\alpha x} = \frac{1}{1 + \alpha x} + \mathcal{O}(\alpha^2 x^2) \quad (2.46)$$

Using (2.46) to approximate $\mathcal{F}(g_\delta)$ and $1/\mathcal{F}(g_\delta)$ gives

$$\begin{aligned} \mathcal{F}(g_\delta(\delta, \mathbf{y})) &= \frac{1}{1 + \frac{\|\mathbf{y}\|_2^2}{4\gamma}} + \mathcal{O}(\delta^4) \\ \frac{1}{\mathcal{F}(g_\delta(\delta, \mathbf{y}))} &= 1 + \frac{\|\mathbf{y}\|_2^2}{4\gamma} \delta^2 + \mathcal{O}(\delta^4) \end{aligned} \quad (2.47)$$

Inserting (2.47) into (2.41) and taking the inverse Fourier transform produces

$$\begin{aligned} \overline{\overline{u_j u_i}} &= \left[\delta_{ij} - \frac{\delta^2}{4\gamma} \nabla^2 \right]^{-1} (\overline{u_j u_i}) + \mathcal{O}(\delta^4) \\ \overline{\overline{u_j u'_i}} &= -\frac{\delta^2}{4\gamma} \left[\delta_{ij} - \frac{\delta^2}{4\gamma} \nabla^2 \right]^{-1} \left(\overline{u_j} \frac{\partial^2 \overline{u_i}}{\partial x_k \partial x_k} \right) + \mathcal{O}(\delta^4) \\ \overline{\overline{u'_j u_i}} &= -\frac{\delta^2}{4\gamma} \left[\delta_{ij} - \frac{\delta^2}{4\gamma} \nabla^2 \right]^{-1} \left(\frac{\partial^2 \overline{u_j}}{\partial x_k \partial x_k} \overline{u_i} \right) + \mathcal{O}(\delta^4) \end{aligned} \quad (2.48)$$

Finally, (2.45) is replaced by the analytical closure

$$\overline{\overline{u_j u_i}} + \overline{\overline{u_j u'_i}} + \overline{\overline{u'_j u_i}} = \overline{u_j u_i} + \frac{\delta^2}{2\gamma} \left[\mathbf{I} - \frac{\delta^2}{4\gamma} \nabla^2 \right]^{-1} \left(\frac{\partial \overline{u_j}}{\partial x_k} \frac{\partial \overline{u_i}}{\partial x_k} \right) + \mathcal{O}(\delta^4) \quad (2.49)$$

Similarly, the rLES theory second order Padé closure for the lead triple in (2.22) is

$$\overline{\overline{u_j \Theta}} + \overline{\overline{u_j \Theta'}} + \overline{\overline{u'_j \Theta}} = \overline{u_j \Theta} + \frac{\delta^2}{2\gamma} \left[\mathbf{I} - \frac{\delta^2}{4\gamma} \nabla^2 \right]^{-1} \frac{\partial \overline{u_j}}{\partial x_k} \frac{\partial \overline{\Theta}}{\partial x_k} + \mathcal{O}(\delta^4) \quad (2.50)$$

The 2nd order Padé closure (2.49) for the lead three tensors in (2.21) involves the *matrix inverse differential operator*

$$[A] \equiv \left[I - \frac{\delta^2}{4\gamma} \nabla^2 \right]^{-1} \quad (2.51)$$

for I the identity matrix.

Equation (2.51) constitutes a second order elliptic boundary value (EBV) operator via the Laplacian on resolved scale velocity strain rate tensor product. The r LES literature references (2.51) as the *auxiliary problem*, detailed in section 2.8.

The closure requirement remaining is the fourth tensor in (2.21), LES theory predicted as the *dissipation* mechanism at the *unresolved scale threshold* replacing unfiltered NS viscous dissipation at molecular scale. Although the closure predicted via 2nd order Padé interpolations is formally negligible, the theory does predict a useful bound, i.e., $\mathcal{O}(\delta^4) \leq \mathcal{O}(\overline{u'_j u'_i}) \leq \mathcal{O}(\delta^2)$. Section 0 illustrates this fact as well as details the SFS tensor and vector closures used in this dissertation.

Of truly substantial theoretical significance the r LES theory closure is absent the word *turbulent*! All manipulations are rigorous mathematical operations defined for/by NS PDE system convolution. Consequently, (2.18) with (2.21) replaced by closure (2.49) is Reynolds number *unconstrained*, hence potentially pertinent to prediction of laminar, transitional and/or fully turbulent resolved scale velocity vector distributions.

2.7 ANALYTICAL SFS TENSOR/VECTOR CLOSURES

The remaining closure requirement is the fourth tensor in (2.21), also the fourth vector in (2.22), LES theory predicted as the *dissipation* mechanism at the *unresolved scale threshold* replacing unfiltered NS viscous dissipation at molecular scale.

The SFS closures predicted by the 2nd order Taylor and 2nd order rational approximations of the Gaussian Fourier transform are, respectively

$$\overline{u'_j u'_i} = \frac{\delta^4}{16\gamma^2} [\nabla^2 \bar{u}_j \nabla^2 \bar{u}_i] + \mathcal{O}(\delta^6) \quad (2.52)$$

$$\overline{u'_j u'_i} = \frac{\delta^4}{16\gamma^2} \left[I - \frac{\delta^2}{4\gamma} \nabla^2 \right]^{-1} [\nabla^2 \bar{u}_j \nabla^2 \bar{u}_i] + \mathcal{O}(\delta^6) \quad (2.53)$$

Both determinations are formally negligible since the lead term multiplier δ^4 is the truncation order in (2.45) and (2.49). This prediction is not trivial however, as rLES theory has *analytically* predicted the requirement $\mathcal{O}(\delta^4) < \mathcal{O}(\overline{u'_j u'_i}) < \mathcal{O}(\delta^2)$. Thereby, LES closure deviatoric SGS tensor models, universally of $\mathcal{O}(\delta^2)$, are too significant to theoretically address LES dissipation at the unresolved scale threshold.

A totally analytical space filtered Navier-Stokes closure is obtained by identifying the SFS tensor based on the weak form CFD theory for error annihilation. The companion SFS *vector* $\overline{u'_j \Theta}$ appearing in the energy equation (2.20) is also provided.

The CFD literature amply identifies discretization-induced *dispersion error* as the *energetic mechanism* requiring dissipation at the unresolved scale threshold. Since an LES SGS model in principle adds diffusion, the hypothesis is proposed stating that it should be possible to directly use numerical diffusion

supplied by a CFD algorithm in order to provide sufficient dissipation of mechanical energy at the unresolved scale threshold.

Three decades of extensive research at the University of Tennessee’s CFD Laboratory generated various modifications to the NS conservation system via Taylor series manipulations (Kolesnikov, 2000),(Chaffin, 1997), (Kim, 1988). Theory-generated analytical expressions augment the NS PDE system with dissipative flux terms that help increase stability and error control of finite element CFD algorithms. Following the idea of direct use of algorithm’s numerical diffusion an analytically-derived SFS tensor candidate is

$$-\overline{u'_j u'_i} \equiv C_s(\delta) \frac{h^2 Re}{6} \left[\overline{u}_j \overline{u}_k \frac{\partial \overline{u}_i}{\partial x_k} + \overline{u}_i \overline{u}_k \frac{\partial \overline{u}_j}{\partial x_k} \right] \quad (2.54)$$

for some constant $C_s(\delta)$ to be determined.

Interpretation of closure (2.54) as eddy viscosity type with dimensionality $L^2 t^{-1}$ “viscosity coefficient”

$\frac{h^2 Re}{6} \overline{u}_j \overline{u}_k$ is inaccurate, as the resolved scale velocity tensor products $\overline{u}_j \overline{u}_k$ and $\overline{u}_i \overline{u}_k$ therein are *non-positive definite*. The fact that (2.54) can promote anti-diffusion matches theoretically with the LES theory requirement of closure admitting *backscatter*, the energetic cascade from smaller to larger scales.

Adequate energetic capture requires $\delta \geq 2h$ and defining a non-constant δ induces commutation error, detailed in section 3.2. Altering the capture constraint to an equality confirms the scalar multiplier on tensor product coefficients in (2.54) are $\mathcal{O}(\delta^2)$. Hence inserted C_s cannot exceed $\mathcal{O}(\delta)$ for this analytical SFS tensor closure candidate to be rLES theory admissible. Specifically, for any $\mathcal{O}(\delta) < C_s \leq 1.0$ (2.54) exhibits the excessive $\mathcal{O}(\delta^2)$ inherent in SGS tensor models of MLT type.

For thermal problems analytical derivation of the companion SFS vector closure candidate for the temperature equation is (Grubert, 2006)

$$-\overline{u'_j \Theta'} \equiv C_s(\delta) \frac{h^2 RePr}{12} \left[\bar{u}_j \bar{u}_k \frac{\partial \bar{\Theta}}{\partial x_j} \right] \quad (2.55)$$

2.8 THE AUXILIARY PROBLEM

The rational LES closure (2.49) and (2.50) involves the matrix inverse differential operator

$$[A] \equiv \left[I - \frac{\delta^2}{4\gamma} \nabla^2 \right]^{-1} \quad (2.56)$$

The operator in (2.56) describes an elliptic second order boundary value problem which in *rLES* literature is referenced as the *auxiliary problem*.

John (2004) identifies two strategies for handling the auxiliary problem inverse differential operator $[A]$ in (2.56). From well-known properties of Fourier transformation and using the rational approximation (2.47) of $\mathcal{F}(g_\delta)$ a simple computation yields

$$\mathcal{F}(g_\delta * \bar{u}_i) = \mathcal{F}(g_\delta) \mathcal{F}(\bar{u}_i) \approx \frac{1}{1 + \frac{\|y_j\|_2^2}{4\gamma} \delta^2} \mathcal{F}(\bar{u}_i) = \mathcal{F} \left(\left[I - \frac{\delta^2}{4\gamma} \nabla^2 \right]^{-1} \bar{u}_i \right), \quad (2.57)$$

from what follows

$$g_\delta * \bar{u}_i = \left[I - \frac{\delta^2}{4\gamma} \nabla^2 \right]^{-1} \bar{u}_i \quad (2.58)$$

Thus the auxiliary problem is an approximation to convolution leading to the replacement of (2.49) with

$$\overline{\bar{u}_j \bar{u}_i} + \overline{\bar{u}_j u'_i} + \overline{u'_j \bar{u}_i} = \bar{u}_j \bar{u}_i + \frac{\delta^2}{2\gamma} g_\delta * \left(\frac{\partial \bar{u}_j}{\partial x_k} \frac{\partial \bar{u}_i}{\partial x_k} \right) \quad (2.59)$$

The alternative is an interpretation of the auxiliary problem as a backward Euler time integration algorithm for the IBV PDE statement

$$\begin{aligned} \frac{\partial q}{\partial t} - \nabla^2 q &= \frac{4\gamma}{\delta^2} f && \text{in } \Omega \times (0, T], \\ (\hat{n} \bullet \nabla) q &= 0 && \text{on } \partial\Omega \times [0, T], \\ q(0, \cdot) &= 0 && \text{in } \Omega, \end{aligned} \quad (2.60)$$

which for a single time step $\Delta t_1 = \delta^2 / 4\gamma$, and therefore the same final time $T = \delta^2 / 4\gamma$ lead to EBV PDE

$$\begin{aligned} \left[\mathbf{I} - \frac{\delta^2}{4\gamma} \nabla^2 \right] q(t_1) &= f(t_1) && \text{in } \Omega, \\ (\hat{n} \bullet \nabla) q &= 0 && \text{on } \partial\Omega. \end{aligned} \quad (2.61)$$

The performance of these two approaches for handling the auxiliary problem was evaluated in (John, 2004) using a mixing layer problem on an unbounded domain with initial condition (IC) characterized by a shear thickness σ_0 . Homogeneous Neumann, the *natural* BC for a weak formulation, is the precisely appropriate global BC, stated as appropriate for the auxiliary problem as well.

The vorticity distributions at times $n\Delta t = 50, 70, 80$ seconds are plotted in Figure B.3 comparing the performance of the auxiliary problem direct solution (2.61) and via convolution (2.59) with the benchmark. The results shown in Figure B.3 suggest that the solution of the auxiliary problem via convolution might be preferable to a direct process.

An alternative theoretical resolution of the auxiliary problem is derived in this dissertation. It accrues to CFD discrete theory mesh measure h connection to the fundamental LES precept of *resolved-unresolved*

scales. From classic fluid mechanics *perturbation theory*, “Most useful approximations (in fluid mechanics theory) are valid when one or more of the parameters or variables in the problem is small (or large)”, Van Dyke (1975). This quotation correlates precisely with the filter measure δ exponentiations in the rLES theory closure (2.49).

The resolved scale velocity \bar{u}_i is by definition $\mathcal{O}(1)$, which is valid as well for the convection tensor product second filtering $\overline{\bar{u}_j \bar{u}_i}$. By definition the unresolved scale velocity u'_i cannot exceed $\mathcal{O}(h)$ since spectral content is not resolvable on a mesh of measure $2h$. Via the constraint $\delta \geq 2h$ for adequate energetic capture u'_i is thus of $\mathcal{O}(\delta)$.

The rLES theory predicts $\overline{u'_j u'_i}$ is $\mathcal{O}(\delta^3)$, two orders smaller than that for u'_i . Thus $\mathcal{O}(\delta)$ and $\mathcal{O}(\delta^3)$ must bound $\overline{\bar{u}_j u'_i} + \overline{u'_j \bar{u}_i}$ hence the order cannot be other than nominally $\mathcal{O}(\delta^2)$. Therefore, via classic fluid mechanics perturbation theory (2.49) predicts

$$\overline{\bar{u}_j \bar{u}_i} = \bar{u}_j \bar{u}_i + \mathcal{O}(\delta^2) \quad (2.62)$$

Extracting (2.62) in the rLES theory second order Padé closure (2.49)

$$\overline{\bar{u}_j u'_i} + \overline{u'_j \bar{u}_i} = \frac{\delta^2}{2\gamma} \left[I - \frac{\delta^2}{4\gamma} \nabla^2 \right]^{-1} \left(\frac{\partial \bar{u}_j}{\partial x_k} \frac{\partial \bar{u}_i}{\partial x_k} \right) + \mathcal{O}(\delta^4) \quad (2.63)$$

So *indeed* the cross stress tensor pair is rLES theory confirmed $\mathcal{O}(\delta^2)$.

This combination of CFD theory with classic fluid mechanics perturbation theory generates precise resolution of the arLES theory auxiliary problem for the 2nd order Padé closure. Multiplying (2.63) through by $[A]$ yields

$$\left[I - \frac{\delta^2}{4\gamma} \nabla^2 \right] (\overline{u_j u'_i} + \overline{u'_j u_i}) = \frac{\delta^2}{2\gamma} \left(\frac{\partial \overline{u_j}}{\partial x_k} \frac{\partial \overline{u_i}}{\partial x_k} \right) + \mathcal{O}(\delta^4) \quad (2.64)$$

Denoting the *cross stress tensor pair* as

$$\overline{c}_{ij}(\mathbf{x}, t) \equiv \overline{u_j u'_i} + \overline{u'_j u_i} \quad (2.65)$$

and coalescing coefficients in (2.64) generates the *harmonic* Poisson EBV PDE system characterization of the classic LES theory identification of the *resolved-unresolved scale* tensor pair

$$\mathcal{L}(\overline{c}_{ij}) = -\nabla^2 \overline{c}_{ij} + \frac{4\gamma}{\delta^2} \overline{c}_{ij} - 2 \frac{\partial \overline{u_i}}{\partial x_k} \frac{\partial \overline{u_j}}{\partial x_k} = 0 \quad (2.66)$$

Note that (2.61) does bear functional resemblance to (2.64). Identification of suitable encompassing BCs for (2.66) is required. The proper boundary conditions for (2.66) are originally derived in this work and described in section 3.5.

Returning to the space filtered energy equation (2.20), *arLES* closure auxiliary problem resolution for scalar state variable member $\overline{\Theta}$ is the direct extension. The perturbation theory argument leads to

$$\overline{u_j \overline{\Theta}} = \overline{u_j} \overline{\Theta} + \mathcal{O}(\delta^2) \quad (2.67)$$

and substitution into (2.50) generates

$$\overline{u_j \overline{\Theta}'} + \overline{u'_j \overline{\Theta}} = \frac{\delta^2}{2\gamma} \left[I - \frac{\delta^2}{4\gamma} \nabla^2 \right]^{-1} \frac{\partial \overline{u_j}}{\partial x_k} \frac{\partial \overline{\Theta}}{\partial x_k} + \mathcal{O}(\delta^4) \quad (2.68)$$

Denoting the theory resolved-unresolved scale interaction *vector pair* as

$$\overline{v}_j^\ominus \equiv \overline{u_j \overline{\Theta}'} + \overline{u'_j \overline{\Theta}} \quad (2.69)$$

generates the *harmonic* Poisson EBV PDE system characterization of the *resolved-unresolved scale* vector pair

$$\mathcal{L}(\bar{\mathbf{v}}_j^\ominus) = -\nabla^2 \bar{\mathbf{v}}_j^\ominus + \frac{4\gamma}{\delta^2} \bar{\mathbf{v}}_j^\ominus - 2 \frac{\partial \bar{u}_j}{\partial x_k} \frac{\partial \bar{\Theta}}{\partial x_k} = 0 \quad (2.70)$$

As for (2.66), appropriate BCs for (2.70) are required. The development of suitable Dirichlet boundary conditions for (2.70) is presented in section 3.5.

3. SPACE FILTERING ON BOUNDED DOMAINS

“LES continues to have difficulties predicting near wall turbulence and to have still more difficulties predicting turbulence driven by flow/boundary interactions.”

(Berselli et al., 2006)

“One would like to believe that the commutation error would be small for some reasonable class of non-uniform filters, but this has never been conclusively demonstrated . . .”

(Ghosal and Moin, 1995)

A truly significant challenge in large eddy simulation (LES) is obtaining a closure theory for bounded domains. Despite a five decades literature this research topic is still far from being closed. During the filtering operation, the conservation principle PDEs are convolved with a spatial filter function resulting in the space filtered PDE system, referenced in the literature as the LES PDE form of NS. The final form of the space filtered PDE system is obtained under the assumption that differentiation and filtering operations commute. It is this assumption that is precisely considered herein since filtering and differentiation operations do not generally commute in the presence of domain boundaries even for functions that are sufficiently smooth in space and time (Dunca et al., 2003).

Besides the questionable assumption that differentiation and filtering operations commute, LES of bounded domain flows encounters yet another equally important problem. In order to fully describe the system and obtain a mathematically well-posed problem statement LES requires knowledge of suitable encompassing boundary conditions, as LES PDEs represent an elliptic boundary value problem. The presence of solid boundaries makes determining the proper boundary conditions a challenge.

3.1 NEAR WALL RESOLUTION AND NEAR WALL MODELING

One approach to wall boundary conditions in LES consists in using spatially non-uniform filter measure $\delta(\mathbf{x})$ which tends to zero at the boundary.

$$\delta = \delta(\mathbf{x}) \rightarrow 0 \quad \text{as} \quad \mathbf{x} \rightarrow \partial\Omega. \quad (3.1)$$

This approach is termed Near Wall Resolution (NWR). The main advantage of NWR is that the homogeneous Dirichlet boundary conditions for the resolved-scale velocity $\bar{\mathbf{u}}$ can be retained

$$\bar{\mathbf{u}}(\mathbf{x}) = 0 \quad \text{for} \quad \mathbf{x} \in \partial\Omega \quad (3.2)$$

However, it is intuitive that by considering a variable filter measure $\delta(\mathbf{x})$, the commutation errors ε_i are introduced since,

$$\varepsilon_i \equiv \overline{\left(\frac{\partial \mathbf{u}}{\partial x_i}\right)} - \left(\frac{\partial \bar{\mathbf{u}}}{\partial x_i}\right) \neq 0 \quad \text{for} \quad i = 1 \dots n \quad (3.3)$$

Indeed, the flows in bounded domains are essentially nonhomogeneous and the required smallest resolved length scales vary throughout the flow field.

Analysis of the commutation error is reported in the literature Ghosal and Moin (1995), Fureby and Tabor (1997), Vasilyev et al. (1998). The analysis in these references is based on one-dimensional Taylor series expansions for very smooth functions, which generally is not applicable in practice. Using special filter kernels it is shown that the commutation error is $\mathcal{O}(\Delta^2)$, where Δ is the non-D grid spacing.

Besides commutation errors introduced by using a variable filter measure in bounded domains, there is an even more substantial drawback to the NWR approach. As the filter size is decreased near the wall, the numerical resolution needed is greatly increased. In order to resolve the near-wall region, so that

no-slip condition can be accurately employed, the mesh size must be reduced accordingly. The computational cost scales like $Re^{2.4}$ in the near wall region, which is very close to that of DNS, see Chapman (1979).

Another approach to treat the wall boundary conditions in LES, termed Near Wall Modeling (NWM), employs a constant measure filter throughout the entire domain and is said to filter through the boundary. The computational cost of this approach is greatly reduced because the filter measure is constant throughout the entire domain. The commutation error, however, is still present, but takes a different form.

In NWM specifying boundary conditions for filtered quantities requires special treatment since the boundary conditions become inherently non-local. This non-locality simply implies that the filtered velocity \bar{u} on the boundary depends non-locally on the non-filtered velocity u near the boundary. Besides the difficulty of setting the proper boundary conditions in NWM, the filtered equations possess an extra source term that also requires closure. This term is originally derived by Fureby and Tabor (1997) and comes from the fact that in the presence of boundaries filtering with a constant filter does not commute with differentiation. Therefore the term itself is referred to as the Boundary Commutation Error (BCE) term (Berselli et al., 2006), or simply the commutator error (Layton and Trenchea, 2011).

Although both approaches have their advantages and disadvantages, it is clear that due to the prohibitive computational cost of the near-wall resolution approach, the near-wall modeling is more feasible for practical applications.

The BCE integral closure identification along with boundary conditions specification in case of wall bounded flows is presented in this dissertation. Throughout this manuscript a constant measure $\delta(x)$ Gaussian filter is defined, unless noted otherwise.

3.2 THE BOUNDARY COMMUTATION ERROR INTEGRAL

The derivation of the BCE integral starts by noting that the convolution operator in a bounded domain can only be applied if all functions (such as \mathbf{u} , p , etc) are first extended outside of the domain. Upon this extension the functions begin to fulfill the NS system in a suitable *distributional* sense, c.f. (Kolmogorov and Fomin, 1975), (Schwartz, 1966). It can be shown that the first order weak derivatives of the extended velocity, i.e. \mathbf{u}_t , $\nabla \mathbf{u}$, $\nabla \cdot \mathbf{u}$ and $\nabla \cdot (\mathbf{u}\mathbf{u}^T)$, are well defined on \mathbb{R}^d , since the extended functions possess the following regularities

$$\begin{aligned} \mathbf{u} &\in (H_0^1(\mathbb{R}^d))^d, \quad p \in L_0^2(\mathbb{R}^d) \quad \text{for } t \in [0, T], \\ \mathbf{u} &\in (H^1(0, T))^d \quad \text{for } \mathbf{x} \in \mathbb{R}^d. \end{aligned} \tag{3.4}$$

Since $\mathbf{u} \notin (H^2(\mathbb{R}^d))^d$, $p \notin H^1(\mathbb{R}^d)$ the stress tensor terms $\nabla \cdot \mathbb{D}(\mathbf{u})$ and ∇p must be defined in the sense of distributions. It then follows that the extended functions (\mathbf{u}, p) fulfill the following distributional form for the NS system

$$\mathbf{u}_t - 2\nu \nabla \cdot \mathbb{D}(\mathbf{u}) + \nabla \cdot (\mathbf{u}\mathbf{u}^T) + \nabla p = \mathbf{f} + \int_{\partial\Omega} \mathbb{S}(\mathbf{u}, p)(\mathbf{s}) \mathbf{n}(\mathbf{s}) \varphi(\mathbf{s}) dS(\mathbf{s}) \tag{3.5}$$

where $\varphi(\mathbf{s}) \in C_0^\infty(\mathbb{R}^d)$ and $\mathbf{n}(\mathbf{s})$ is the outward unit vector normal to $\partial\Omega$.

Once the LES state variable is well defined in the sense of distributions the convolution and differentiation commute and the convolution operator generates the LES PDE form for DP

$$\bar{\mathbf{u}}_t - 2\nu \nabla \cdot \mathbb{D}(\bar{\mathbf{u}}) + \nabla \cdot (\overline{\mathbf{u}\mathbf{u}^T}) + \nabla \bar{p} = \bar{\mathbf{f}} + A_\delta(\mathbb{S}(\mathbf{u}, p)) \tag{3.6}$$

Herein $A_\delta(\mathbb{S}(\mathbf{u}, p))$ is the BCE integral

$$A_\delta(\mathbb{S}(\mathbf{u}, p))(t, \mathbf{x}) \equiv \int_{\tilde{\Omega}} g_\delta(\mathbf{x} - \mathbf{s}) \mathbb{S}(\mathbf{u}, p)(t, \mathbf{s}) \mathbf{n}(\mathbf{s}) dS(\mathbf{s}) \quad (3.7)$$

and the full NS stress tensor $\mathbb{S}(\mathbf{u}, p)$ is

$$\mathbb{S}(\mathbf{u}, p) \equiv 2\nu\mathbb{D}(\mathbf{u}) - p\mathbb{I} \quad (3.8)$$

Therefore the correct LES PDE arising from the NS PDE on a bounded domain possesses a boundary integral named the BCE. The BCE integrand contains unfiltered state variable members, with subsequent convolution with filter $g_\delta(\mathbf{x} - \mathbf{s})$ transforming the completed integral to filtered state variable members.

The BCE integral augmentation for the energy equation is a direct extension

$$\bar{T}_t + \nabla \cdot (-\alpha \nabla \bar{T} + \overline{uT}) = \bar{f}_\Theta + A_\delta(\nabla T) \quad (3.9)$$

where $A_\delta(\nabla T)$ is

$$A_\delta(\nabla T)(t, \mathbf{x}) \equiv \int_{\tilde{\Omega}} g_\delta(\mathbf{x} - \mathbf{s}) \alpha \nabla T(t, \mathbf{s}) \mathbf{n}(\mathbf{s}) dS(\mathbf{s}) \quad (3.10)$$

John (2004) shows that the boundary commutation error is asymptotically negligible in $\mathbb{L}^p(\mathbb{R}^n)$ norm as $\delta \rightarrow 0$ (not to be confused with a non-constant filter radius) if and only if the normal stress vanishes almost everywhere on the boundary (the fluid and the boundary exert exactly zero normal force on each other). Of course, for most turbulent flows of interest this condition is not satisfied. It is also observed that the commutation error is largest near the solid wall and decays rapidly away from the wall. Finally, John (2004) notices that if the BCE term is dropped and the space filtered Navier-Stokes equations are discretized, the error committed is $\mathcal{O}(1)$!

3.3 APPROXIMATE DECONVOLUTION BOUNDARY CONDITIONS

To this point the necessity of retaining the BCE integrals in the resulting filtered conservation equations on a bounded domain is obvious. A separate issue in NWM approach is the specification of proper boundary conditions wherein the no-slip Dirichlet BC is generally replaced by some solution-dependent Neumann BC model. This complicating issue arises because the no-slip BC is satisfied by the unfiltered velocity, not the filtered resolved scale velocity! Slip-with-drag formulations are proposed by Piomelli and Balaras (2002), John et al. (2004), Sagaut (2004), John and Liakos (2006).

One of the recent NWM advances is the derivation of boundary conditions that are based on an approximate deconvolution approach (Borggaard and Iliescu, 2006). The ADBC method is formulated using the same ideas of filtering and deconvolution that are used by Galdi and Layton (2000) for their rational LES closure. The derivation and mathematical analysis of three AD LES models can be found in Berselli et al. (2006). In short, the approximate deconvolution methodology uses an approximation for the filtered flow variables (such as \bar{u}) to recover an approximation for u . The AD formulae are derived using the mathematical properties of a particular spatial filter and are then applied to a numerical approximation of \bar{u} to recover an approximation for u . The pioneering AD LES model was proposed by Leonard (1974).

The authors of ADBC use an approximate deconvolution formula to approximate not only the unknown boundary conditions for filtered variables, but to also the boundary commutation error term. They consider a one-dimensional heat conduction problem with time dependent boundary conditions to demonstrate their approach. Linearity of the heat equation allows them to separate the boundary condition considerations from the closure problem associated with non-linear equations such as Navier-Stokes DP. The numerical analysis shows that the BCE term should not be dropped from the space

filtered equations and demonstrates appropriate numerical approximations for the BCE and the boundary conditions.

The results of Borggaard and Iliescu (2006) are encouraging and the algorithm itself is very attractive due to its simplicity and generality. However, the ADBC approach requires extension to full dimensionality, starting with two-dimensional linear problems and eventually advancing to realistic NS PDEs addressing turbulent flow prediction.

As stated, the problem of specifying boundary conditions for resolved scale variables (with constant radius) becomes complicated due to their non-local nature. The ADBC procedure can identify the unknown BCs for the resolved scale at the new time level $\bar{\mathbf{u}}^{n+1}$ from the known quantities $\bar{\mathbf{u}}^n$ inside the domain and \mathbf{u}^{n+1} on the boundary. The derivation starts by defining the unknown filtered flow quantities $\bar{\mathbf{u}}^{n+1}$ at $\mathbf{x}_b \in \partial\Omega$ via convolution with a spatial filter

$$\bar{\mathbf{u}}^{n+1}(\mathbf{x}_b) \equiv (\mathbf{g}_\delta * \mathbf{u}^{n+1})(\mathbf{x}_b) = \int_{\Omega} \mathbf{g}_\delta(\mathbf{x}_b - \mathbf{y}) \mathbf{u}^{n+1}(\mathbf{y}) d\mathbf{y}, \quad \mathbf{x}_b \in \partial\Omega \quad (3.11)$$

In order to approximate the integral in (3.11) on the entire domain Ω , \mathbf{u}^{n+1} has to be known everywhere inside Ω , as well as on the boundary $\partial\Omega$. The derivation is simplified by the fact that the Gaussian \mathbf{g}_δ decays rapidly to zero away from \mathbf{x}_b and can therefore be neglected outside of the effective range of filter measure δ . This observation suggests that (3.11) only needs be evaluated in δ vicinity of \mathbf{x}_b (shaded area in Figure B.4).

Numerical integration via quadrature is used to approximate the convolution integral in (3.11). The gray nodes in Figure B.4 are the nodes included into an approximation for $\bar{\mathbf{u}}^{n+1}(\mathbf{x}_b)$ and are therefore used in quadrature. The values of \mathbf{u}^{n+1} on the boundary are obtained from the given Dirichlet boundary

conditions, while an approximation to \mathbf{u}^{n+1} at the interior nodes is obtained using the approximate deconvolution

$$\mathbf{u}^{n+1}(\mathbf{x}) = \bar{\mathbf{u}}^n(\mathbf{x}) - \frac{\delta^2}{24} \Delta \bar{\mathbf{u}}^n(\mathbf{x}) + \mathcal{O}(\delta^4) \quad (3.12)$$

The Laplacian term $\Delta \bar{\mathbf{u}}^n(\mathbf{x})$ in (3.12) can be approximated by finite differences (FD) or finite element (FE) trial space bases. Note that the AD (3.12) lies at the heart of the rational LES (*rLES*) closure, Galdi and Layton (2000), and a higher-order version of it, Berselli and Iliescu (2003). For a good summary and discussion of *rLES* an interested reader is referred to (Berselli et al., 2006) and (John, 2004).

Using AD (3.12) and the integration methodology illustrated in Figure B.4, the numerical quadrature for approximating the convolution integral (3.11) is

$$\bar{\mathbf{u}}^{n+1}(\mathbf{x}_b) \approx \sum_{i \in \mathcal{I}} w_i g_\delta(\mathbf{x}_b - \mathbf{x}_i) \left(\bar{\mathbf{u}}^n(\mathbf{x}_i) - \frac{\delta^2}{24} \Delta \bar{\mathbf{u}}^n(\mathbf{x}_i) \right) + \sum_{i \in \mathcal{B}} w_i g_\delta(\mathbf{x}_b - \mathbf{x}_i) \mathbf{u}^{n+1}(\mathbf{x}_i), \quad (3.13)$$

where the index sets \mathcal{I} and \mathcal{B} represent interior and boundary points, respectively; \mathbf{x}_i represent quadrature points and w_i are the weights.

Numerical evaluation of the BCE integral (3.7) depends on the approximations for $\nabla \mathbf{u}^{n+1}(\mathbf{s})$ and $\rho^{n+1}(\mathbf{s})$. The approximate deconvolution formula (3.12) is again pertinent to generate needed approximations, along with standard FD techniques to approximate the derivatives. (Borggaard and Iliescu, 2006).

3.4 MODIFIED ADBC FORMULATION

An accurate way of constructing the boundary conditions of non-homogeneous Dirichlet type is developed by including a buffer layer outside of the computational domain. A generalization of the ADBC to two dimensions is derived with a possibility of straight forward extension three dimensions.

Consider an example of two-dimensional non-steady heat conduction problem described in section 6.1.2. The approximate boundary conditions for space filtered \bar{q} are constructed using approach similar Borggaard and Iliescu (2006). However, the implementation herein has two major improvements over the original ADBC. The first is fundamental as it changes the way non-homogeneous Dirichlet BCs are estimated. As described in section 3.3, the original ADBC approach suggests that only the nodes that lay inside the shaded area (Figure B.4) should be included in an approximation to the convolution integral (3.11). Therefore, no extension of q outside of Ω is considered. However, in Figure B.8 it is shown how this technique causes very large errors to occur near boundaries with non-homogeneous Dirichlet BCs. In Figure B.9 these errors are eliminated by extending the Gaussian filter outside Ω by adding the corresponding extension of q . A numerical implementation of this technique is shown in Figure B.5. The filled nodes are in the interior as well as on the boundary. The values of q at these nodes are obtained via AD in the interior and given BCs on the boundary. The hollow nodes constitute the buffer layer placed outside of Ω . The values of q at the hollow nodes are known a priori, they are prescribed according to the extension of q , which in turn is defined by the given Dirichlet boundary conditions. No buffer layer extension is necessary where the boundary condition is set to zero Dirichlet. This extension is trivial since $q(x,y) = b(x,y) = 0$ and does not make any contribution to the final result.

Simplified implementation constitutes the second aspect by which this approach is different from the original ADBC. Changing the number of nodes included in quadrature (3.13) makes implementation

much simpler and helps to generalize the approach to three dimensions. Consider a boundary node (x_b, y_b) at which q is prescribed non-homogeneous Dirichlet BC (Figure B.5). The space filtered \bar{q} at node (x_b, y_b) is defined via convolution with a spatial filter, hence

$$\bar{q}(x_b, y_b) \equiv \iint_{\Omega} g_{\delta}(x_b - \zeta_1, y_b - \zeta_2) q(\zeta_1, \zeta_2) d\zeta_1 d\zeta_2, \quad (x_b, y_b) \in \partial\Omega \quad (3.14)$$

When the domain of integration is square (instead of circular), as in Figure B.5, the convolution integral in (3.14) can be accurately evaluated using a combination of two Newton-Cotes rules (one for each spatial direction), hence

$$\bar{q}(x_b, y_b) \approx \sum_{i=1}^{N_x} \sum_{j=1}^{N_y} g_{\delta}(x_b - x_i, y_b - y_j) q(x_i, y_j) w_i w_j \quad (3.15)$$

where N_x and N_y are Newton-Cotes degrees in x and y direction respectively, (x_i, y_j) are the quadrature points, and w_i and w_j are the corresponding weights.

Since the Gaussian filter decays rapidly away from (x_b, y_b) the inclusion of extra nodes outside of the dotted circle (Figure B.5) will not affect the result. This technique makes the implementation direct and general. An extension to three dimensions is straight forward by utilizing the same Newton-Cotes approximation in the z -direction. Another advantage of using this technique is the ease of performing calculations near domain corners as detailed in section 6.1.2.

3.5 BOUNDARY CONDITIONS FOR THE AUXILIARY PROBLEM

In three dimensions the auxiliary problem of *arLES* has been converted to six Poisson equations for cross-stress tensor \bar{c}_{ij} (2.66) and three Poisson equations for cross-thermal vector \bar{v}_j^{\ominus} (2.70). Each of these equations is an elliptic boundary value problem requiring specification of proper boundary

conditions. Homogeneous Neumann boundary condition has been exclusively used in the literature, primarily for lack of a better idea. This type BC is appropriate only for unbounded domain flows, hence absolutely invalid for bounded domains. Herein derivation of the long-awaited non-homogeneous BCs of Dirichlet type for the auxiliary problem of *arLES* is presented for the first time.

The development starts with recognition that it is possible to derive an approximation for the unfiltered “physically unrealistic” quantity c_{ij} using the AD formula (3.12), hence

$$c_{ij}(\mathbf{x}) = \bar{c}_{ij}(\mathbf{x}) - \frac{\delta^2}{4\gamma} \nabla^2 \bar{c}_{ij}(\mathbf{x}) + \mathcal{O}(\delta^4) \quad (3.16)$$

Multiplying equation (2.66) through by $\frac{\delta^2}{4\gamma}$ yields

$$\bar{c}_{ij} - \frac{\delta^2}{4\gamma} \nabla^2 \bar{c}_{ij} = \frac{\delta^2}{2\gamma} \frac{\partial \bar{u}_i}{\partial x_k} \frac{\partial \bar{u}_j}{\partial x_k} \quad (3.17)$$

Substituting (3.17) into (3.16) yields the required approximation for unfiltered c_{ij}

$$c_{ij}(\mathbf{x}) = \frac{\delta^2}{2\gamma} \frac{\partial \bar{u}_i(\mathbf{x})}{\partial x_k} \frac{\partial \bar{u}_j(\mathbf{x})}{\partial x_k} + \mathcal{O}(\delta^4) \quad (3.18)$$

Identical analysis is performed to derive an approximation to the companion cross-thermal vector pair v_j^\ominus , yielding

$$(v_j^\ominus)(\mathbf{x}) = \frac{\delta^2}{2\gamma} \frac{\partial \bar{\Theta}(\mathbf{x})}{\partial x_k} \frac{\partial \bar{u}_j(\mathbf{x})}{\partial x_k} + \mathcal{O}(\delta^4) \quad (3.19)$$

Approximations (3.18) and (3.19) are differential definitions easily evaluated via the Galerkin weak statement, discussed in chapter 5. Determination of $c_{ij}(\mathbf{x})$ and v_j^\ominus depends strictly on solutions to the

space filtered velocity, $\bar{\mathbf{u}}$, and temperature, $\bar{\Theta}$, fields. These solutions are known on the entire domain including the boundary owing to the AD boundary condition specification described in section 3.4.

Upon successful calculation of unfiltered mathematical entities c_{ij} and v_j^\ominus using (3.18) and (3.19) respectively, determination of the required non-homogeneous Dirichlet boundary conditions for space filtered \bar{c}_{ij} and \bar{v}_j^\ominus becomes straight forward. Using the same ideas of BC specification described in section 3.4 the unknown filtered quantity \bar{c}_{ij}^{n+1} at $\partial\Omega$ is defined via convolution with a spatial filter as

$$\bar{c}_{ij}^{n+1}(x_b, y_b) \equiv (g_\delta * c_{ij}^{n+1})(\mathbf{x}_b) = \iint_{\Omega} g_\delta(x_b - \zeta_1, y_b - \zeta_2) c_{ij}^{n+1}(\zeta_1, \zeta_2) d\zeta_1 d\zeta_2, \quad (x_b, y_b) \in \partial\Omega \quad (3.20)$$

An identical definition for $(\bar{v}_j^\ominus)^{n+1}$ at $\partial\Omega$ reads

$$(\bar{v}_j^\ominus)^{n+1}(x_b, y_b) \equiv (g_\delta * (v_j^\ominus)^{n+1})(\mathbf{x}_b) = \iint_{\Omega} g_\delta(x_b - \zeta_1, y_b - \zeta_2) (v_j^\ominus)^{n+1}(\zeta_1, \zeta_2) d\zeta_1 d\zeta_2 \quad (3.21)$$

Using the integration methodology illustrated in Figure B.5 and employing numerical quadrature to approximate the convolution integral in (3.20) and (3.21) the a priori unknown BCs are approximated

$$\bar{c}_{ij}^{n+1}(x_b, y_b) \approx \sum_{i=1}^{N_x} \sum_{j=1}^{N_y} g_\delta(x_b - x_i, y_b - y_j) c_{ij}^{n+1}(x_i, y_j) w_i w_j, \quad (3.22)$$

$$(\bar{v}_j^\ominus)^{n+1}(x_b, y_b) \approx \sum_{i=1}^{N_x} \sum_{j=1}^{N_y} g_\delta(x_b - x_i, y_b - y_j) (v_j^\ominus)^{n+1}(x_i, y_j) w_i w_j \quad (3.23)$$

where N_x and N_y are Newton-Cotes degrees in x and y direction respectively, (x_i, y_j) are the quadrature points, and w_i and w_j are the corresponding weights.

4. ESSENTIALLY ANALYTICAL RATIONAL LES THEORY CFD ALGORITHM

Two very important conclusions can be made by analyzing the set of conservation principles (2.1)-(2.3). Firstly, the continuity equation (2.1) in its own glory states that the velocity vector field must be solenoidal, or divergence-free. Secondly, the system has five equations with five unknowns (namely u_x, u_y, u_z, p, T), but there is no equation for determining the pressure distribution. Instead, the mass conservation equation (2.1) acts as a differential constraint on the solution to **DP+DE** system of PDEs. This constraint requires any solution \mathbf{u} that is established to **DP+DE** system be divergence-free.

The absence of a conservation principle for pressure can be remedied with a number of approaches. One of them is a vector field theory approach where the mass conservation equation is enforced exactly by converting it to an equation for some vector potential. In two dimensions this vector potential becomes a streamfunction. The existence of pressure is then completely eliminated by taking curl of the momentum equation. Although very effective this approach has a number of limitations, for instance, it is not capable of handling problems of pressure driven flows. Also the generalization of, say, streamfunction-vorticity method to three dimensions makes it extremely difficult to implement due to substantially increased mathematical burden.

Another class of CFD algorithms is based on pressure-relaxation methods that produce an inexact enforcement of the continuity constraint, but can be easily extended to three dimensional implementations. The Continuity Constraint Method (CCM) (Williams, 1993) is the generalization of this idea and used for deriving the LES theory CFD algorithm.

4.1 SPACE FILTERED CCM

The LES theory CFD algorithm used in this dissertation is based on the CCM methodology and belongs to the class of “pressure relaxation” methods. The Continuity Constraint Method is a primitive-variable

FEM CFD algorithm developed by Williams (1993). The algorithm encompasses the original finite difference SMAC method (Amsden and Harlow, 1970), along with a classical finite element velocity-correction method (Schneider et al., 1978).

Space filtered incompressible Navier-Stokes equations accompanied by the *ar*LES closure theory Poisson equations are

$$\text{DM} : \mathcal{L}(\bar{\rho}_0) = \frac{\partial \bar{u}_i}{\partial x_i} = 0 \quad (4.1)$$

$$\text{DP} : \mathcal{L}(\bar{u}_i) = \frac{\partial \bar{u}_i}{\partial t} + \frac{\partial}{\partial x_j} \left(\bar{u}_j \bar{u}_i + \bar{c}_{ij} + \overline{u'_j u'_i} - \frac{1}{Re} \frac{\partial \bar{u}_i}{\partial x_j} + \bar{p} \delta_{ij} \right) + \frac{Gr}{Re^2} \bar{\Theta} \hat{g}_i = 0 \quad (4.2)$$

$$\text{DE} : \mathcal{L}(\bar{\Theta}) = \frac{\partial \bar{\Theta}}{\partial t} + \frac{\partial}{\partial x_j} \left(\bar{u}_j \bar{\Theta} + \bar{v}_j^\ominus + \overline{u'_j \Theta'} - \frac{1}{Pe} \frac{\partial \bar{\Theta}}{\partial x_j} \right) = 0 \quad (4.3)$$

$$\mathcal{L}(\bar{c}_{ij}) = -\nabla^2 \bar{c}_{ij} + \frac{4\gamma}{\delta^2} \bar{c}_{ij} - 2 \frac{\partial \bar{u}_i}{\partial x_k} \frac{\partial \bar{u}_j}{\partial x_k} = 0 \quad (4.4)$$

$$\mathcal{L}(\bar{v}_j^\ominus) = -\nabla^2 \bar{v}_j^\ominus + \frac{4\gamma}{\delta^2} \bar{v}_j^\ominus - 2 \frac{\partial \bar{u}_j}{\partial x_k} \frac{\partial \bar{\Theta}}{\partial x_k} = 0 \quad (4.5)$$

4.2 ERROR ANALYSIS

Denoting \bar{u}_i^n as a known vector of initial conditions at time t^n the Taylor series expansion is employed to find $\tilde{\bar{u}}_i^{n+1}$ at time t^{n+1} by marching one step forward, i.e.,

$$\tilde{\bar{u}}_i^{n+1} = \bar{u}_i^n + \Delta t \left. \frac{\partial \bar{u}_i}{\partial t} \right|_n + \mathcal{O}(\Delta t^2) \quad (4.6)$$

A tilde symbol “~” signifies the fact that the computed velocity vector \tilde{u}_i^{n+1} does not satisfy the continuity equation, thus $\nabla \cdot \tilde{u}_i^{n+1} \neq 0$.

Substituting an expression for time derivative $\left. \frac{\partial \bar{u}_i}{\partial t} \right|_n$ obtained from (4.2) into (4.6) yields

$$\tilde{u}_i^{n+1} = \bar{u}_i^n - \Delta t \left. \frac{\partial}{\partial x_j} \left(\bar{u}_j \bar{u}_i + \bar{c}_{ij} + \overline{u'_j u'_i} + \bar{p} \delta_{ij} - \frac{1}{Re} \frac{\partial \bar{u}_i}{\partial x_j} \right) \right|_n + \left(\frac{Gr}{Re^2} \bar{\Theta} \hat{g} \right) + \mathcal{O}(\Delta t^2) \quad (4.7)$$

It is then assumed that there exists a pressure correction to \bar{p}^n which can be identified such that the computed velocity field at t^{n+1} satisfies the continuity equation, i.e., $\nabla \cdot \bar{u}_i^{n+1} = 0$. Denoting the corrected pressure as \bar{p}^* and keeping in mind that \bar{p}^* cannot stay inside the brackets, as it is strictly hypothetical, yields

$$\bar{u}_i^{n+1} = \bar{u}_i^n - \Delta t \left. \frac{\partial}{\partial x_j} \left(\bar{u}_j \bar{u}_i + \bar{c}_{ij} + \overline{u'_j u'_i} - \frac{1}{Re} \frac{\partial \bar{u}_i}{\partial x_j} \right) \right|_n + \left(\frac{Gr}{Re^2} \bar{\Theta} \hat{g} \right) - \Delta t \frac{\partial \bar{p}^*}{\partial x_i} + \mathcal{O}(\Delta t^2) \quad (4.8)$$

Note that there is no tilde on \bar{u}_i^{n+1} .

Subtracting (4.7) from (4.8) defines the error, i.e., the difference between the right answer and the computed solution, which reads as

$$\bar{u}_i^{n+1} - \tilde{u}_i^{n+1} = -\Delta t \frac{\partial}{\partial x_i} (\bar{p}^* - \bar{p}^n) + \mathcal{O}(\Delta t^2) \quad (4.9)$$

Taking the curl of both sides of (4.9) and using the fact that curl of the gradient of any scalar field ϕ is the zero vector gives

$$\nabla \times (\bar{u}_i^{n+1} - \tilde{u}_i^{n+1}) = 0 \quad (4.10)$$

Equation (4.10) then implies that the difference $\bar{u}_i^{n+1} - \tilde{u}_i^{n+1}$ must be expressible in terms of some scalar potential function, namely

$$\bar{u}_i^{n+1} - \tilde{u}_i^{n+1} = -\nabla \phi \quad (4.11)$$

Therefore the error introduced in the explicit Taylor series approach is incurred only by lack of satisfaction of the continuity equation with measure scalar potential ϕ .

The corrected pressure \bar{p}^* is strictly hypothetical and cannot be established using an explicit Taylor series, correspondingly the forward Euler scheme (explicit). This means that \bar{p}^* cannot be some kind of pressure distribution at time t^n and somehow have information from time t^{n+1} . Instead one needs to use at least a semi-implicit scheme. Therefore a much more feasible methodology in estimating \bar{p}^* is to use a θ -implicit Taylor series

$$\bar{u}_i|_{n+1} = \bar{u}_i|_n + \Delta t \left(\theta \frac{\partial \bar{u}_i}{\partial t} \Big|_{n+1} + (1-\theta) \frac{\partial \bar{u}_i}{\partial t} \Big|_n \right) + \mathcal{O}(\Delta t^{f(\theta)}) \quad (4.12)$$

The order of approximation in (4.12) is a function of θ , i.e.

$$f(\theta) = \begin{cases} 1 & \text{if } \theta > 0.5 \\ 2 & \text{if } \theta = 0.5 \end{cases} \quad (4.13)$$

Substituting expressions for time derivatives $\frac{\partial \bar{u}_i}{\partial t} \Big|_{n+1}$ and $\frac{\partial \bar{u}_i}{\partial t} \Big|_n$ obtained from (4.2) into (4.12) yields

$$\begin{aligned} \bar{u}_i|_{n+1} - \bar{u}_i|_n = & -\theta \Delta t \left(\frac{\partial}{\partial x_j} \left(\bar{u}_j \bar{u}_i + \bar{c}_{ij} + \overline{u'_j u'_i} + \bar{p} \delta_{ij} - \frac{1}{Re} \frac{\partial \bar{u}_i}{\partial x_j} \right) + \frac{Gr}{Re^2} \bar{\Theta} \hat{g}_i \right) \Big|_{n+1} \\ & - (1-\theta) \Delta t \left(\frac{\partial}{\partial x_j} \left(\bar{u}_j \bar{u}_i + \bar{c}_{ij} + \overline{u'_j u'_i} + \bar{p} \delta_{ij} - \frac{1}{Re} \frac{\partial \bar{u}_i}{\partial x_j} \right) + \frac{Gr}{Re^2} \bar{\Theta} \hat{g}_i \right) \Big|_n + \mathcal{O}(\Delta t^{f(\theta)}) \end{aligned} \quad (4.14)$$

Integration of momentum equations with a guessed pressure field \bar{p}^* results in a velocity field \bar{u}_i^* that does not in general satisfy the continuity constraint. Equation (4.14) can then be rewritten using the guessed pressure and velocity fields. However the advection term for time t^{n+1} can no longer be expressed in the divergence form since that would imply satisfaction of the continuity equation, which is not true. Following this considerations equation (4.14) becomes

$$\begin{aligned} \bar{u}_i^*|_{n+1} - \bar{u}_i|_n = & -\theta\Delta t \left(\bar{u}_j^* \frac{\partial \bar{u}_i^*}{\partial x_j} + \frac{\partial}{\partial x_j} \left(\bar{c}_{ij}^* + \overline{u'_j u'_i}^* + \bar{p}^* \delta_{ij} - \frac{1}{Re} \frac{\partial \bar{u}_i^*}{\partial x_j} \right) + \frac{Gr}{Re^2} \bar{\Theta}^* \hat{g}_i \right) \Big|_{n+1} \\ & - (1-\theta)\Delta t \left(\frac{\partial}{\partial x_j} \left(\bar{u}_j \bar{u}_i + \bar{c}_{ij} + \overline{u'_j u'_i} + \bar{p} \delta_{ij} - \frac{1}{Re} \frac{\partial \bar{u}_i}{\partial x_j} \right) + \frac{Gr}{Re^2} \bar{\Theta} \hat{g}_i \right) \Big|_n + \mathcal{O}(\Delta t^{f(\theta)}) \end{aligned} \quad (4.15)$$

Subtracting (4.15) from (4.14) defines the error distribution as

$$\begin{aligned} \bar{e}|_i^{n+1} = & \bar{u}_i|_{n+1} - \bar{u}_i^*|_{n+1} \\ = & \theta\Delta t \left(\bar{u}_j^* \frac{\partial \bar{u}_i^*}{\partial x_j} - \frac{\partial(\bar{u}_j \bar{u}_i)}{\partial x_j} \right) \Big|_{n+1} + \theta\Delta t \left(\frac{\partial(\bar{c}_{ij}^* - \bar{c}_{ij})}{\partial x_j} \right) \Big|_{n+1} + \theta\Delta t \left(\frac{\partial(\overline{u'_j u'_i}^* - \overline{u'_j u'_i})}{\partial x_j} \right) \Big|_{n+1} \\ & + \theta\Delta t \left(\frac{\partial(\bar{p}^* - \bar{p})}{\partial x_i} \right) \Big|_{n+1} + \theta\Delta t \frac{\partial}{\partial x_j} \left(\frac{1}{Re} \frac{\partial \bar{u}_i}{\partial x_j} - \frac{1}{Re} \frac{\partial \bar{u}_i^*}{\partial x_j} \right) \Big|_{n+1} + \theta\Delta t \frac{Gr}{Re^2} (\bar{\Theta}^* - \bar{\Theta}) \Big|_{n+1} \hat{g}_i + \mathcal{O}(\Delta t^{f(\theta)}) \end{aligned} \quad (4.16)$$

Taking the curl of equation (4.16) confirms the error field of θ -implicit scheme is not irrotational, i.e., $curl(\bar{e}|_i^{n+1}) \neq 0$. Equation (4.16) has six modes of error generation for the velocity field at t^{n+1} , namely due to advection, cross-stress tensor pair, SFS tensor, pressure, diffusion, and the buoyancy body force. Since only the error component associated with pressure can be represented by the gradient of a scalar potential function, all other terms in (4.16) are considered mathematically intractable, in the manner of the original CCM theory (Williams, 1993). The error generated by the remaining term must be reduced by insuring that $\bar{u}_i^*|_{n+1} \rightarrow \bar{u}_i|_{n+1}$. This is done by employing an iterative cycling through momentum

equations and, in case of thermal flow, the energy equation. This approach is implied in most pressure correction methods, but is rarely stated. If a pressure correction can direct the solution to momentum equations towards satisfaction of the continuity equation then the scheme has to be not only implicit but also iterative.

An iteration strategy is devised to drive the divergence error to below some specified level. The first step is to assume that the divergence error at iteration $k + 1$ can be approximated by the gradient of a potential function, hence

$$\left(\bar{u}_i^* - \bar{u}_i\right)_{n+1}^{k+1} \approx -\left(\frac{\partial \phi}{\partial x_i}\right)_{n+1}^{k+1} \quad (4.17)$$

Using (4.17) and neglecting the intractable terms in (4.16) yields

$$\left(\frac{\partial \phi}{\partial x_i}\right)_{n+1}^{k+1} \approx \theta \Delta t \left(\frac{\partial (\bar{p}^* - \bar{p})}{\partial x_i}\right)_{n+1}^k \quad (4.18)$$

Equation (4.18) is integrated and the constant of integration is set to zero. This results in a pseudo-pressure correction equation of the form

$$(\bar{p})_{n+1}^k = (\bar{p}^*)_{n+1}^k + \frac{1}{\theta \Delta t} (\phi)_{n+1}^{k+1} \quad (4.19)$$

Equation (4.19) states that the pressure correction at iteration k depends on the unknown solution ϕ at iteration $k + 1$. To remedy this problem a computable strategy relies on accumulation of ϕ solutions over the iterative sequence, i.e.,

$$(\bar{p}^*)_{n+1}^k = (\bar{p})_n + \frac{1}{\theta \Delta t} \sum_{\alpha=1}^k (\phi)_{n+1}^\alpha \quad (4.20)$$

where $(\bar{p})|_n$ is the known, mass conserving kinematic pressure at the previous converged solution time station.

4.3 POISSON EQUATION FOR ϕ

The development of a Poisson equation for continuity constraint potential function ϕ proceeds as follows. Recall from (4.11) that the defining equation for ϕ is

$$-\frac{\partial \phi}{\partial x_i} \equiv (\bar{u}_i - \bar{u}_i^*) \quad (4.21)$$

where \bar{u}_i is the solenoidal velocity for which $\nabla \cdot \bar{u}_i = 0$, and \bar{u}_i^* is the computed velocity not satisfying the continuity equation, i.e., $\nabla \cdot \bar{u}_i^* \neq 0$. Using these two facts and taking the divergence of (4.21) results in the Poisson equation for ϕ of the form

$$\mathcal{L}(\phi) = \frac{\partial^2 \phi}{\partial x_i^2} - \frac{\partial \bar{u}_i^*}{\partial x_i} = 0 \quad (4.22)$$

Hence, the continuity constraint function ϕ is the solution to an elliptic boundary value problem (4.22).

The Galerkin weak statement for (4.22) reads

$$GWS^N = \int_{\Omega} \Psi_j \mathcal{L}(\phi^N) d\Omega = \int_{\Omega} \Psi_j \frac{\partial^2 \phi^N}{\partial x_i^2} d\Omega - \int_{\Omega} \Psi_j \frac{\partial \bar{u}_i^{N*}}{\partial x_i} d\Omega = 0 \quad (4.23)$$

Applying the Green-Gauss theorem to (4.23) the Galerkin weak statement for ϕ becomes

$$\begin{aligned}
0 &= \int_{\Omega} \Psi_j \frac{\partial^2 \phi^N}{\partial x_i^2} d\Omega - \int_{\Omega} \Psi_j \frac{\partial \bar{u}_i^{N*}}{\partial x_i} d\Omega \\
&= - \int_{\Omega} \frac{\partial \Psi_j}{\partial x_i} \left(\frac{\partial \phi^N}{\partial x_i} \right) - \int_{\Omega} \Psi_j \frac{\partial \bar{u}_i^{N*}}{\partial x_i} d\Omega + \oint_{\Gamma} \Psi_j \left(\frac{\partial \phi^N}{\partial x_i} \right) n_i d\Gamma \\
&= - \int_{\Omega} \frac{\partial \Psi_j}{\partial x_i} \left(\frac{\partial \phi^N}{\partial x_i} \right) - \int_{\Omega} \Psi_j \frac{\partial \bar{u}_i^{N*}}{\partial x_i} d\Omega + \oint_{\Gamma} \Psi_j \left(\frac{\partial \phi^N}{\partial n} \right) d\Gamma
\end{aligned} \tag{4.24}$$

In his dissertation Williams describes six types of boundary conditions, namely, inflow, outflow, entrainment, symmetry, no-slip, and free-slip. The natural boundary condition for (4.22) is the projection of the gradient of ϕ onto the outward-pointing normal at the boundary. From (4.21) this projection is related to the error in velocity field at the boundary as

$$- \frac{\partial \phi}{\partial x_i} n_i = (\bar{u}_i - \bar{u}_i^*) n_i \tag{4.25}$$

The analysis of five types of boundary conditions (leaving off the free-slip condition) can be summarized as follows.

For inflow, symmetry, and no-slip boundaries the homogeneous Neumann BC is valid, hence

$$\frac{\partial \phi}{\partial x_i} n_i = 0$$

For outflow and entrainment boundaries the homogeneous Dirichlet BC is prescribed, hence

$$\phi = 0$$

4.4 PRESSURE POISSON EQUATION

Although it appears that the method is now complete there is still no equation for calculating the pressure field. Thus derivation of a filtered pressure Poisson equation (PPE) is required. The PPE is

implied by the space-filtered INS equations and is derived from there by taking the divergence of momentum equation (4.2) and invoking the continuity equation, yielding

$$\mathcal{L}(\bar{p}) = \frac{\partial}{\partial x_i} (\mathcal{L}(\bar{u}_i)) = \frac{\partial}{\partial x_i} \left(\frac{\partial \bar{u}_i}{\partial t} - \frac{1}{Re} \frac{\partial^2 \bar{u}_i}{\partial x_j^2} \right) + \frac{\partial}{\partial x_i} \left(\bar{u}_j \frac{\partial \bar{u}_i}{\partial x_j} + \frac{\partial}{\partial x_j} (\bar{c}_{ij} + \overline{u'_j u'_i}) \right) + \frac{\partial \bar{p}}{\partial x_i} + \frac{Gr}{Re^2} \bar{\Theta} \hat{g}_i = 0 \quad (4.26)$$

Assuming sufficient regularity, the continuity equation $\nabla \cdot \bar{\mathbf{u}} = 0$ can be invoked in three places to simplify equation (4.26). Assuming that temporal and spatial derivatives commute, the first term in (4.26) associated with time derivative is simplified as

$$\frac{\partial}{\partial x_i} \left(\frac{\partial \bar{u}_i}{\partial t} \right) = \frac{\partial}{\partial t} \left(\frac{\partial \bar{u}_i}{\partial x_i} \right) = 0$$

Likewise, assuming that spatial derivatives commute and noticing that reference Reynolds number does not vary over the flow field, the diffusion term in (4.26) also vanishes, hence

$$\frac{\partial}{\partial x_i} \left(\frac{1}{Re} \frac{\partial^2 \bar{u}_i}{\partial x_j^2} \right) = \frac{1}{Re} \frac{\partial^2}{\partial x_j^2} \left(\frac{\partial \bar{u}_i}{\partial x_i} \right) = 0$$

Finally, the convective acceleration term can be further simplified upon the same assumption of commuting spatial derivatives. The continuity equation is used to rewrite convective acceleration term in its final simplified form as

$$\frac{\partial}{\partial x_i} \left(\bar{u}_j \frac{\partial \bar{u}_i}{\partial x_j} \right) = \frac{\partial \bar{u}_j}{\partial x_i} \frac{\partial \bar{u}_i}{\partial x_j} + \bar{u}_j \frac{\partial}{\partial x_i} \left(\frac{\partial \bar{u}_i}{\partial x_j} \right) = \frac{\partial \bar{u}_j}{\partial x_i} \frac{\partial \bar{u}_i}{\partial x_j} + \bar{u}_j \frac{\partial}{\partial x_j} \left(\frac{\partial \bar{u}_i}{\partial x_i} \right) = \frac{\partial \bar{u}_j}{\partial x_i} \frac{\partial \bar{u}_i}{\partial x_j}$$

Therefore the pressure Poisson equation for a divergence-free space-filtered velocity vector field is

$$\mathcal{L}(\bar{p}) = \frac{\partial^2 \bar{p}}{\partial x_i^2} + \frac{\partial \bar{u}_j}{\partial x_i} \frac{\partial \bar{u}_i}{\partial x_j} + \frac{\partial^2}{\partial x_i \partial x_j} (\bar{c}_{ij} + \overline{u'_j u'_i}) + \frac{Gr}{Re^2} \frac{\partial \bar{\Theta}}{\partial x_i} \hat{g}_i = 0 \quad (4.27)$$

The construction of Galerkin weak statement for PPE in the form presented in (4.27) poses two problems. The first problem is associated with appearance of a spatial derivative on temperature in the buoyancy term, which poses a real challenge to the GMRES solver. Secondly, the natural pressure boundary conditions are hard to define.

To solve both of these problems the PPE is rewritten by introducing a new quantity $\mathcal{L}^*(\bar{u}_i)$ as

$$\mathcal{L}(\bar{p}) = \frac{\partial}{\partial x_i} \left(\mathcal{L}^*(\bar{u}_i) \right) = \frac{\partial}{\partial x_i} \left(\bar{u}_j \frac{\partial \bar{u}_i}{\partial x_j} + \frac{\partial}{\partial x_j} (\bar{c}_{ij} + \overline{u'_j u'_i}) + \frac{\partial \bar{p}}{\partial x_i} + \frac{Gr}{Re^2} \bar{\Theta} \hat{g}_i \right) = 0, \quad (4.28)$$

where $\mathcal{L}^*(\bar{u}_i)$ is defined as

$$\begin{aligned} \mathcal{L}^*(\bar{u}_i) &= \bar{u}_j \frac{\partial \bar{u}_i}{\partial x_j} + \frac{\partial}{\partial x_j} (\bar{c}_{ij} + \overline{u'_j u'_i}) + \frac{\partial \bar{p}}{\partial x_i} + \frac{Gr}{Re^2} \bar{\Theta} \hat{g}_i \\ &= \mathcal{L}(\bar{u}_i) - \frac{\partial \bar{u}_i}{\partial t} + \frac{1}{Re} \frac{\partial^2 \bar{u}_i}{\partial x_j^2} \\ &= -\frac{\partial \bar{u}_i}{\partial t} + \frac{1}{Re} \frac{\partial^2 \bar{u}_i}{\partial x_j^2} \end{aligned} \quad (4.29)$$

Applying the Green-Gauss theorem to (4.28) the Galerkin weak statement for PPE becomes

$$\int_{\Omega} \Psi_j \frac{\partial}{\partial x_i} \left(\mathcal{L}^*(\bar{u}_i^N) \right) d\Omega = - \int_{\Omega} \frac{\partial \Psi_j}{\partial x_i} \mathcal{L}^*(\bar{u}_i^N) d\Omega + \oint_{\Gamma} \Psi_j \mathcal{L}^*(\bar{u}_i^N) n_i d\Gamma = 0 \quad (4.30)$$

Using the definition for $\mathcal{L}^*(\bar{u}_i)$ the Galerkin weak statement for pressure results in

$$\begin{aligned}
0 &= \int_{\Omega} \Psi_k \frac{\partial}{\partial x_i} (\mathcal{L}^* (\bar{u}_i^N)) d\Omega \\
&= - \int_{\Omega} \frac{\partial \Psi_k}{\partial x_i} \left(\bar{u}_j \frac{\partial \bar{u}_i}{\partial x_j} + \frac{\partial}{\partial x_j} (\bar{c}_{ij} + \overline{u'_j u'_i}) + \frac{\partial \bar{p}}{\partial x_i} + \frac{Gr}{Re^2} \bar{\Theta} \hat{g}_i \right)^N d\Omega \\
&\quad + \oint_{\Gamma} \Psi_k \left(\bar{u}_j \frac{\partial \bar{u}_i}{\partial x_j} + \frac{\partial}{\partial x_j} (\bar{c}_{ij} + \overline{u'_j u'_i}) + \frac{\partial \bar{p}}{\partial x_i} + \frac{Gr}{Re^2} \bar{\Theta} \hat{g}_i \right)^N n_j d\Gamma \\
&= - \int_{\Omega} \frac{\partial \Psi_k}{\partial x_i} \left(\bar{u}_j \frac{\partial \bar{u}_i}{\partial x_j} + \frac{\partial}{\partial x_j} (\bar{c}_{ij} + \overline{u'_j u'_i}) + \frac{\partial \bar{p}}{\partial x_i} + \frac{Gr}{Re^2} \bar{\Theta} \hat{g}_i \right)^N d\Omega \\
&\quad + \oint_{\Gamma} \Psi_k \left(\bar{u}_n \frac{\partial \bar{u}_i}{\partial n} + \frac{\partial}{\partial n} (\bar{c}_{ij} + \overline{u'_j u'_i}) + \frac{\partial \bar{p}}{\partial n} + \frac{Gr}{Re^2} \bar{\Theta} \hat{g}_n \right)^N d\Gamma
\end{aligned} \tag{4.31}$$

At this point the boundary conditions for the pressure must also be prescribed. The BCs are obtained by projecting momentum equations onto the boundary itself (Gresho and Sani (1987), Orszag et al. (1986)). This can be done in two ways: either using the normal projection, or using two tangential projections of momentum equation onto the boundary. Projection onto the normal direction (outward-pointing) produces genuine non-homogeneous Neumann boundary condition for PPE in (4.27) on those boundaries where the normal velocity is specified, hence

$$\frac{\partial \bar{p}}{\partial n} = \frac{\partial}{\partial n} \left(\frac{1}{Re} \frac{\partial \bar{u}_n}{\partial n} \right) - \frac{\partial \bar{u}_n}{\partial t} - \bar{u}_n \frac{\partial \bar{u}_n}{\partial n} - \frac{\partial}{\partial n} (\bar{c}_{ij} + \overline{u'_j u'_i}) - \frac{Gr}{Re^2} \bar{\Theta} \hat{g}_n \tag{4.32}$$

The tangential projection with subsequent integration over the boundary gives a Dirichlet pressure boundary condition. Gresho and Sani (1987) demonstrate that if Neumann BC (normal) is applied to the pressure Poisson equation, the solution to the pressure field will also satisfy the Dirichlet BC (tangential). However, unlike Neumann boundary condition that applies for both $t = 0$ and $t > 0$, the tangential momentum equation on the boundary only applies for $t > 0$.

Note that the Galerkin weak statement (4.31) by virtue of Green-Gauss theorem ‘automatically’ implied the Neumann boundary equations shown in (4.32). Indeed, using an alternative definition of $\mathcal{L}^*(\bar{u}_i)$,

namely $\mathcal{L}^*(\bar{u}_i) = -\frac{\partial \bar{u}_i}{\partial t} + \frac{1}{Re} \frac{\partial^2 \bar{u}_i}{\partial x_j^2}$ the Galerkin weak statement for pressure is

$$\begin{aligned}
0 &= \int_{\Omega} \Psi_k \frac{\partial}{\partial x_i} \left(\mathcal{L}^*(\bar{u}_i^N) \right) d\Omega = \\
& - \int_{\Omega} \frac{\partial \Psi_k}{\partial x_i} \left(\bar{u}_j \frac{\partial \bar{u}_i}{\partial x_j} + \frac{\partial}{\partial x_j} (\bar{c}_{ij} + \overline{u'_j u'_i}) + \frac{\partial \bar{p}}{\partial x_i} + \frac{Gr}{Re^2} \bar{\Theta} \hat{g}_i \right)^N d\Omega + \oint_{\Gamma} \Psi \left(-\frac{\partial \bar{u}_i}{\partial t} + \frac{1}{Re} \frac{\partial^2 \bar{u}_i}{\partial x_j^2} \right)^N n_i d\Gamma \quad (4.33) \\
& = - \int_{\Omega} \frac{\partial \Psi_k}{\partial x_i} \left(\bar{u}_j \frac{\partial \bar{u}_i}{\partial x_j} + \frac{\partial}{\partial x_j} (\bar{c}_{ij} + \overline{u'_j u'_i}) + \frac{\partial \bar{p}}{\partial x_i} + \frac{Gr}{Re^2} \bar{\Theta} \hat{g}_i \right)^N d\Omega + \oint_{\Gamma} \Psi \left(-\frac{\partial \bar{u}_n}{\partial t} + \frac{1}{Re} \frac{\partial^2 \bar{u}_n}{\partial x_j^2} \right)^N d\Gamma
\end{aligned}$$

The same result is obtained by substituting (4.32) in (4.31).

4.5 SPACE FILTERED CCM SOLUTION STRATEGY OVERVIEW

The solution strategy for LES theory CCM algorithm is now devised, recalling a θ -implicit scheme requirement for an iterative procedure within the time-step. During iteration, CCM replaces genuine pressure with a continuity constraint variable, C_{n+1}^p , where the superscript p denotes iteration index.

Therefore, the θ -implicit scheme for momentum equations is

$$\begin{aligned}
\bar{u}_i^*|_{n+1}^p &= \bar{u}_i|_n - \theta \Delta t \left(\bar{u}_j^* \frac{\partial \bar{u}_i^*}{\partial x_j} + \frac{\partial}{\partial x_j} \left(\bar{c}_{ij}^* + \overline{u'_j u'_i}^* - \frac{1}{Re} \frac{\partial \bar{u}_i^*}{\partial x_j} \right) + \frac{\partial C}{\partial x_j} \delta_{ij} + \frac{Gr}{Re^2} \bar{\Theta}^* \hat{g}_i \right) \Big|_{n+1}^p \\
& - (1-\theta) \Delta t \left(\frac{\partial}{\partial x_j} \left(\bar{u}_j \bar{u}_i + \bar{c}_{ij} + \overline{u'_j u'_i} - \frac{1}{Re} \frac{\partial \bar{u}_i}{\partial x_j} \right) + \frac{\partial \bar{p}}{\partial x_j} \delta_{ij} + \frac{Gr}{Re^2} \bar{\Theta} \hat{g}_i \right) \Big|_n + \mathcal{O}(\Delta t^{f(\theta)})
\end{aligned} \quad (4.34)$$

The CCM iterative solution strategy modified to include *ar*LES closure equations proceeds as follows

- (1) Initialize the constraint state variable by either $C_{n+1}^1 = C_n^{p+1}$ or $C_{n+1}^1 = p^n$, where p^n is the pressure from the previous time step converged solution

(2) Solve the momentum and energy equations implicitly for $\bar{u}^*|^p$ and $\bar{\Theta}^*|^p$:

$$\left\{ \begin{array}{l} \bar{u}_i^*|_{n+1}^p = \bar{u}_i|_n - \theta \Delta t \left(\bar{u}_j^* \frac{\partial \bar{u}_i^*}{\partial x_j} + \frac{\partial}{\partial x_j} \left(\bar{c}_{ij}^* + \overline{u'_j u'_i}^* - \frac{1}{Re} \frac{\partial \bar{u}_i^*}{\partial x_j} \right) + \frac{\partial C}{\partial x_j} \delta_{ij} + \frac{Gr}{Re^2} \bar{\Theta}^* \hat{g}_i \right) \Big|_{n+1}^p \\ \quad - (1-\theta) \Delta t \left(\frac{\partial}{\partial x_j} \left(\bar{u}_j \bar{u}_i + \bar{c}_{ij} + \overline{u'_j u'_i} - \frac{1}{Re} \frac{\partial \bar{u}_i}{\partial x_j} \right) + \frac{\partial \bar{p}}{\partial x_j} \delta_{ij} + \frac{Gr}{Re^2} \bar{\Theta} \hat{g}_i \right) \Big|_n + \mathcal{O}(\Delta t^{f(\theta)}) \\ \bar{\Theta}^*|_{n+1}^p = \bar{\Theta}|_n - \theta \Delta t \left(\bar{u}_j^* \frac{\partial \bar{\Theta}^*}{\partial x_j} + \frac{\partial}{\partial x_j} \left(\bar{v}_j^{\Theta^*} + \overline{u'_j \Theta'}^* - \frac{1}{Pe} \frac{\partial \bar{\Theta}^*}{\partial x_j} \right) \right) \Big|_{n+1}^p \\ \quad - (1-\theta) \Delta t \left(\frac{\partial}{\partial x_j} \left(\bar{u}_j \bar{\Theta} + \bar{v}_j^{\Theta} + \overline{u'_j \Theta'} - \frac{1}{Pe} \frac{\partial \bar{\Theta}}{\partial x_j} \right) \right) \Big|_n + \mathcal{O}(\Delta t^{f(\theta)}) \end{array} \right. \quad (4.35)$$

(3) Solve Poisson equation for ϕ^p :

$$0 = - \left(\frac{\partial^2 \phi}{\partial x_i^2} \right) \Big| + \left(\frac{\partial \bar{u}_i^*}{\partial x_i} \right) \Big| \quad (4.36)$$

(4) Update approximation for C_{n+1} by

$$C_{n+1}^{p+1} = C_{n+1}^1 + \left(\frac{1}{\theta \Delta t} \right) \sum_{k=1}^p \phi^k \quad (4.37)$$

(5) Repeat steps (2) – (4) until

$$\phi_{\epsilon}^p < \epsilon, \text{ convergence tolerance}$$

(6) Solve Poisson equations for \bar{c}_{ij} :

$$0 = - \frac{\partial^2 \bar{c}_{ij}}{\partial x_k^2} + \frac{4\gamma}{\delta^2} \bar{c}_{ij} - 2 \frac{\partial \bar{u}_i}{\partial x_k} \frac{\partial \bar{u}_j}{\partial x_k} \quad (4.38)$$

(7) Solve Poisson equations for \bar{v}_j^{Θ} :

$$0 = -\frac{\partial^2 \bar{v}_j^\ominus}{\partial x_k^2} + \frac{4\gamma}{\delta^2} \bar{v}_j^\ominus - 2 \frac{\partial \bar{u}_j}{\partial x_k} \frac{\partial \bar{\Theta}}{\partial x_k} \quad (4.39)$$

(8) Prior to advancing the time step, solve the PPE:

$$0 = -\frac{\partial^2 \bar{p}}{\partial x_i^2} - \frac{\partial}{\partial x_i} \left(\bar{u}_j \frac{\partial \bar{u}_i}{\partial x_j} + \frac{\partial}{\partial x_j} (\bar{c}_{ij} + \overline{u'_j u'_i}) + \frac{Gr}{Re^2} \bar{\Theta} \hat{g}_i \right) \quad (4.40)$$

5. ARLES WEAK FORM FE IMPLEMENTATION

The set of LES theory partial differential equations (PDEs) augmented with boundary commutation integrals and two Poisson equations generated by the continuity constraint algorithm is

$$\mathcal{L}(\bar{u}_i) = \frac{\partial \bar{u}_i}{\partial t} + \frac{\partial}{\partial x_j} \left(\bar{u}_j \bar{u}_i + \bar{c}_{ij} + \overline{u'_j u'_i} - \frac{1}{Re} \frac{\partial \bar{u}_i}{\partial x_j} + \bar{p} \delta_{ij} \right) + \frac{Gr}{Re^2} \bar{\Theta} \hat{g}_i - A_\delta(\mathbb{S}(u_i, p)) = 0 \quad (5.1)$$

$$\mathcal{L}(\bar{\Theta}) = \frac{\partial \bar{\Theta}}{\partial t} + \frac{\partial}{\partial x_j} \left(\bar{u}_j \bar{\Theta} + \bar{v}_j^\ominus + \overline{u'_j \Theta'} - \frac{1}{Pe} \frac{\partial \bar{\Theta}}{\partial x_j} \right) - A_\delta(\nabla \Theta) = 0 \quad (5.2)$$

$$\mathcal{L}(\bar{c}_{ij}) = -\nabla^2 \bar{c}_{ij} + \frac{4\gamma}{\delta^2} \bar{c}_{ij} - 2 \frac{\partial \bar{u}_i}{\partial x_k} \frac{\partial \bar{u}_j}{\partial x_k} = 0 \quad (5.3)$$

$$\mathcal{L}(\bar{v}_j^\ominus) = -\nabla^2 \bar{v}_j^\ominus + \frac{4\gamma}{\delta^2} \bar{v}_j^\ominus - 2 \frac{\partial \bar{u}_j}{\partial x_k} \frac{\partial \bar{\Theta}}{\partial x_k} = 0 \quad (5.4)$$

$$\mathcal{L}(\phi) = \frac{\partial^2 \phi}{\partial x_i^2} - \frac{\partial \bar{u}_i^*}{\partial x_i} = 0 \quad (5.5)$$

$$\mathcal{L}(\bar{p}) = \frac{\partial^2 \bar{p}}{\partial x_i^2} + \frac{\partial}{\partial x_i} \left[\bar{u}_j \frac{\partial \bar{u}_i}{\partial x_j} + \frac{\partial}{\partial x_j} (\bar{c}_{ij} + \overline{u'_j u'_i}) + \frac{Gr}{Re^2} \bar{\Theta} \hat{g}_i \right] = 0 \quad (5.6)$$

With BCE definitions

$$A_\delta(\mathbb{S}(u_i, p))(t, x_k) \equiv \int_{\partial\Omega} g_\delta(x_k - s_k) \left[-p \delta_{ij} + \frac{1}{Re} \left(\frac{\partial u_i}{\partial x_j} \right) \right] \hat{n}_j ds \quad (5.7)$$

$$A_\delta(\nabla \Theta)(t, x_k) \equiv \int_{\partial\Omega} g_\delta(x_k - s_k) \left[\frac{1}{Pe} \left(\frac{\partial \Theta}{\partial x_j} \right) \right] \hat{n}_j ds \quad (5.8)$$

The irreversible work viscous dissipation term in (5.2) is ignored.

The SFS tensor and vector closure candidates are, respectively

$$\begin{aligned} -\overline{u'_j u'_i} &\equiv C_s(\delta) \frac{h^2 Re}{6} \left[\bar{u}_j \bar{u}_k \frac{\partial \bar{u}_i}{\partial x_k} + \bar{u}_i \bar{u}_k \frac{\partial \bar{u}_j}{\partial x_k} \right] \\ -\overline{u'_j \Theta'} &\equiv C_s(\delta) \frac{h^2 Pe}{12} \left[\bar{u}_j \bar{u}_k \frac{\partial \bar{\Theta}}{\partial x_j} \right] \end{aligned} \quad (5.9)$$

The system of space filtered equations described in (5.1)-(5.2) constitutes a nonlinear set of coupled initial-value PDEs, whose solutions are constrained by the incompressibility condition. PDEs (5.1)-(5.2) can be expressed in the flux vector form

$$\mathcal{L}(q) = \frac{\partial q}{\partial t} + \frac{\partial}{\partial x_j} (f_j - f_j^d) - s = 0 \quad (5.10)$$

where q is a state-variable place-holder, f_j is the kinematic flux vector, f_j^d is the dissipative flux vector and s is the source term. For three-dimensional analysis the following definitions apply

$$q \equiv \begin{Bmatrix} \bar{u} \\ \bar{v} \\ \bar{w} \\ \bar{\Theta} \end{Bmatrix}; f_j \equiv \begin{Bmatrix} \bar{u}_j \bar{u} + \bar{c}_{1j} + \bar{p} \delta_{1j} \\ \bar{u}_j \bar{v} + \bar{c}_{2j} + \bar{p} \delta_{2j} \\ \bar{u}_j \bar{w} + \bar{c}_{3j} + \bar{p} \delta_{3j} \\ \bar{u}_j \bar{\Theta} + \bar{v}_j^\ominus \end{Bmatrix}; f_j^d \equiv \begin{Bmatrix} \frac{1}{Re} \frac{\partial \bar{u}}{\partial x_j} + \overline{u'_j u'} \\ \frac{1}{Re} \frac{\partial \bar{v}}{\partial x_j} + \overline{u'_j v'} \\ \frac{1}{Re} \frac{\partial \bar{w}}{\partial x_j} + \overline{u'_j w'} \\ \frac{1}{Pe} \frac{\partial \bar{\Theta}}{\partial x_j} + \overline{u'_j \Theta'} \end{Bmatrix}; s = \begin{Bmatrix} -\frac{Gr}{Re^2} \bar{\Theta} \hat{g}_1 + A_\delta(\mathbb{S}(u, p)) \\ -\frac{Gr}{Re^2} \bar{\Theta} \hat{g}_2 + A_\delta(\mathbb{S}(v, p)) \\ -\frac{Gr}{Re^2} \bar{\Theta} \hat{g}_3 + A_\delta(\mathbb{S}(w, p)) \\ A_\delta(\nabla \Theta) \end{Bmatrix} \quad (5.11)$$

The quasi-linear Poisson PDEs (5.3)-(5.6) for \bar{c}_{ij} , \bar{v}_j^\ominus , ϕ and \bar{p} all of general form

$$\mathcal{L}(q_\alpha) = \nabla^2 q_\alpha - s_\alpha(q_\alpha) = 0 \quad (5.12)$$

where q_α is a state-variable place-holder and s_α is the source term. In three dimensions the following definitions apply

$$q_\alpha \equiv \left. \begin{array}{c} \bar{c}_{11} \\ \bar{c}_{12} \\ \bar{c}_{13} \\ \bar{c}_{22} \\ \bar{c}_{23} \\ \bar{c}_{33} \\ \bar{v}_1^\ominus \\ \bar{v}_2^\ominus \\ \bar{v}_3^\ominus \\ \phi \\ \rho \end{array} \right\} \quad (5.13)$$

$$s_\alpha = \left. \begin{array}{l} \frac{4\gamma}{\delta^2} \bar{c}_{11} - 2 \left(\frac{\partial \bar{u}}{\partial x} \frac{\partial \bar{u}}{\partial x} + \frac{\partial \bar{u}}{\partial y} \frac{\partial \bar{u}}{\partial y} + \frac{\partial \bar{u}}{\partial z} \frac{\partial \bar{u}}{\partial z} \right) \\ \frac{4\gamma}{\delta^2} \bar{c}_{12} - 2 \left(\frac{\partial \bar{u}}{\partial x} \frac{\partial \bar{v}}{\partial x} + \frac{\partial \bar{u}}{\partial y} \frac{\partial \bar{v}}{\partial y} + \frac{\partial \bar{u}}{\partial z} \frac{\partial \bar{v}}{\partial z} \right) \\ \frac{4\gamma}{\delta^2} \bar{c}_{13} - 2 \left(\frac{\partial \bar{u}}{\partial x} \frac{\partial \bar{w}}{\partial x} + \frac{\partial \bar{u}}{\partial y} \frac{\partial \bar{w}}{\partial y} + \frac{\partial \bar{u}}{\partial z} \frac{\partial \bar{w}}{\partial z} \right) \\ \frac{4\gamma}{\delta^2} \bar{c}_{22} - 2 \left(\frac{\partial \bar{v}}{\partial x} \frac{\partial \bar{v}}{\partial x} + \frac{\partial \bar{v}}{\partial y} \frac{\partial \bar{v}}{\partial y} + \frac{\partial \bar{v}}{\partial z} \frac{\partial \bar{v}}{\partial z} \right) \\ \frac{4\gamma}{\delta^2} \bar{c}_{23} - 2 \left(\frac{\partial \bar{v}}{\partial x} \frac{\partial \bar{w}}{\partial x} + \frac{\partial \bar{v}}{\partial y} \frac{\partial \bar{w}}{\partial y} + \frac{\partial \bar{v}}{\partial z} \frac{\partial \bar{w}}{\partial z} \right) \\ \frac{4\gamma}{\delta^2} \bar{c}_{33} - 2 \left(\frac{\partial \bar{w}}{\partial x} \frac{\partial \bar{w}}{\partial x} + \frac{\partial \bar{w}}{\partial y} \frac{\partial \bar{w}}{\partial y} + \frac{\partial \bar{w}}{\partial z} \frac{\partial \bar{w}}{\partial z} \right) \\ \frac{4\gamma}{\delta^2} \bar{v}_1^\ominus - 2 \left(\frac{\partial \bar{u}}{\partial x} \frac{\partial \bar{\Theta}}{\partial x} + \frac{\partial \bar{u}}{\partial y} \frac{\partial \bar{\Theta}}{\partial y} + \frac{\partial \bar{u}}{\partial z} \frac{\partial \bar{\Theta}}{\partial z} \right) \\ \frac{4\gamma}{\delta^2} \bar{v}_2^\ominus - 2 \left(\frac{\partial \bar{v}}{\partial x} \frac{\partial \bar{\Theta}}{\partial x} + \frac{\partial \bar{v}}{\partial y} \frac{\partial \bar{\Theta}}{\partial y} + \frac{\partial \bar{v}}{\partial z} \frac{\partial \bar{\Theta}}{\partial z} \right) \\ \frac{4\gamma}{\delta^2} \bar{v}_3^\ominus - 2 \left(\frac{\partial \bar{w}}{\partial x} \frac{\partial \bar{\Theta}}{\partial x} + \frac{\partial \bar{w}}{\partial y} \frac{\partial \bar{\Theta}}{\partial y} + \frac{\partial \bar{w}}{\partial z} \frac{\partial \bar{\Theta}}{\partial z} \right) \\ \frac{\partial \bar{u}^*}{\partial x} + \frac{\partial \bar{v}^*}{\partial y} + \frac{\partial \bar{w}^*}{\partial z} \\ - \frac{\partial}{\partial x_i} \left(\bar{u}_j \frac{\partial \bar{u}_i}{\partial x_j} + \frac{\partial}{\partial x_j} (\bar{c}_{ij} + \overline{u'_j u'_i}) + \frac{Gr}{Re^2} \bar{\Theta} \hat{g}_i \right) \end{array} \right\} \quad (5.14)$$

5.1 GALERKIN WEAK STATEMENT

The implementation of *arLES* theory is performed via finite element spatial discretization of a Galerkin weak statement (GWS) for the LES theory-identified PDE system (5.1)-(5.6). The GWS FE approach is marvelously described in a book by Baker (1983), and more recently in Baker (2006) and Baker (2012). The FE discrete implementation is summarized in six steps.

Step 1. The analysis starts by constructing a continuous approximation of the state-variable q and q_α with an assumption that space and time can be separated, hence

$$q(x_j, t) \cong q^N \equiv \sum_{i=1}^N \Psi_i(x_j) Q_i(t) \quad (5.15)$$

where $\Psi_i(x_j)$ is the *trial space* function set and $Q_i(t)$ is the set of unknown expansion coefficients that are determined during the computations. The summation over N denotes the inner product of the known trial function set and the set of unknown coefficients.

Step 2. The difference between the exact and approximate solutions defines the error function. The minimization of approximation error is accomplished via forming a *weak statement* (*WS*) as

$$WS^N \equiv \int_{\Omega} \Phi_i(x_j, t) \mathcal{L}(q^N) d\Omega = 0 \quad (5.16)$$

The weak statement ensures that the error due to $\mathcal{L}(q^N) \neq 0$ is made orthogonal to a set of *test space* functions $\Phi_i(x_j, t)$. The optimal choice for the test space function set $\Phi_i(x_j, t)$ is the one that produces the absolute minimum approximation error. For a wide range of engineering problem statements this minimization is achieved when the trial and test space function sets are identical (Baker, 2006). This

choice yields what is historically called the Galerkin form for WS^N , or simply the *Galerkin weak statement* (GWS^N), hence

$$GWS^N \equiv \int_{\Omega} \Psi_i(x_j) \mathcal{L}(q^N) d\Omega = 0 \quad (5.17)$$

Using (5.17) the GWS^N form for the differential equation system (5.10) is

$$\begin{aligned} 0 &= \int_{\Omega} \Psi_i \left(\frac{\partial q^N}{\partial t} + \frac{\partial}{\partial x_j} (f_j - f_j^d)^N - s^N \right) d\Omega \\ &= \int_{\Omega} \Psi_i \left(\frac{\partial q^N}{\partial t} - s^N \right) d\Omega - \int_{\Omega} \frac{\partial \Psi_i}{\partial x_j} (f_j - f_j^d)^N d\Omega + \oint_{\partial\Omega_e \cap \partial\Omega} \Psi_i (f_j - f_j^d)^N n_j d\Gamma \end{aligned} \quad (5.18)$$

Similarly, the GWS^N form of (5.12)

$$\begin{aligned} 0 &= \int_{\Omega} \Psi_i \left(\frac{\partial^2 q_{\alpha}^N}{\partial x_j^2} - s_{\alpha}^N \right) d\Omega \\ &= - \int_{\Omega} \frac{\partial \Psi_i}{\partial x_j} \left(\frac{\partial q_{\alpha}^N}{\partial x_j} \right) d\Omega - \int_{\Omega} \Psi_i s_{\alpha}^N d\Omega + \oint_{\partial\Omega_e \cap \partial\Omega} \Psi_i \frac{\partial q_{\alpha}^N}{\partial x_j} n_j d\Gamma \end{aligned} \quad (5.19)$$

In (5.18) and (5.19) the Green-Gauss theorem is applied to lower the order of the flux term derivatives and the Laplacian operator, respectively. This process also produces a surface integral creating a placeholder for all *natural* boundary conditions in the GWS^N .

Step 3. The FE approach utilizes a spatial semi-discretization Ω^h of the continuum solution domain Ω .

This discretization represents a union of non-overlapping subdomains Ω_e or finite elements, such that

$$\Omega \cong \Omega^h = \bigcup_e \Omega_e \quad (5.20)$$

Step 4. The FE approximation q^N is then formed as the union of FE approximations q_e with local support on Ω_e , hence

$$q(x_j, t) \cong q^N(x_j, t) \equiv q^h(x_j, t) = \bigcup_e q_e(x_j, t) \quad (5.21)$$

Therefore for any FE domain Ω_e the approximate functions $q_e(x_j, t)$ can be expressed in the general form as

$$q_e(x_j, t) \equiv \{N_k\}^T \{Q\}_e \quad (5.22)$$

where $\{N_k\}^T$ is a vector of FE trial space basis functions, also called the FE *basis set*. The number of elements in the basis set corresponds to the number of nodes in Ω_e .

Step 5. All integrals in the GWS^N (5.18) are evaluated locally for each element, and the resulting element matrices are then assembled into a global matrix statement. For unsteady PDEs, GWS^h produces a set of ordinary differential equations, coupled via the mass matrix $[MASS]$, i.e.,

$$GWS^h = [MASS] \frac{d\{Q\}}{dt} + \{RES(Q)\} = \{0\} \quad (5.23)$$

where $[MASS]$ is a square matrix whose entries are evaluated during the integration and assembly processes, $\{RES\}$ is a residual column vector containing contributions from all terms in (5.18) except the time term, $\{Q\}$ is a column vector of state-variable approximation coefficients at every node of the mesh.

Step 6. The remaining time derivative in (5.23) is discretized using the θ -implicit scheme, resulting in an algebraic statement

$$\{FQ\} = [MASS](\{Q_{n+1}\} - \{Q_n\}) + \Delta t(\theta\{RES\}_{n+1} + (1-\theta)\{RES\}_n) = \{0\} \quad (5.24)$$

The FE implementation of (5.19) for $\bar{c}_{ij}, \bar{v}_j^\ominus$ directly produces an algebraic system

$$\{FQ^\alpha\} = [DIFF + MASS]\{Q^\alpha\} + \{s^\alpha\} = \{0\} \quad (5.25)$$

which for pure Poisson equations for ϕ and \bar{p} is reduced to

$$\{FQ^\alpha\} = [DIFF]\{Q^\alpha\} + \{s^\alpha\} = \{0\} \quad (5.26)$$

A coupled nonlinear system of algebraic equations (5.24) produced by the GWS^h must be solved iteratively. Constructing the Jacobian matrix $[JAC]_{n+1} \equiv \partial\{FQ\} / \partial\{Q\}_{n+1}$ the classic Newton method is used with the following iterative cycle

$$\begin{aligned} \{Q\}_{n+1}^0 &= \{Q\}_n; \quad \{FQ\}_{n+1}^0 = \{FQ\}_n \\ \text{for } p &= 0, 1, 2, \dots \text{ until convergence} \\ \left[MASS + \theta \Delta t \frac{\partial\{RES\}}{\partial\{Q\}} \right]_{n+1}^p &\{\delta Q\}_{n+1}^{p+1} = -\{FQ\}_{n+1}^p \\ \{Q\}_{n+1}^{p+1} &= \{Q\}_{n+1}^p + \{\delta Q\}_{n+1}^{p+1} \end{aligned} \quad (5.27)$$

The solution to (5.12) for $\bar{c}_{ij}, \bar{v}_j^\ominus$ is obtained directly via the matrix statement

$$[DIFF + MASS]\{Q^\alpha\} = -\{s^\alpha\} \quad (5.28)$$

and for ϕ and \bar{p} via

$$[DIFF]\{Q^\alpha\} = -\{s^\alpha\} \quad (5.29)$$

5.2 FINITE ELEMENT TEMPLATE STATEMENT

The finite element (FE) template concept described in Baker (2006) states that the FE implementation of a weak statement produces six types of data for each FE domain Ω_e . Removing two data types from the original description, namely *element average* and *metric data*, the remaining four types are used in this work to represent the weak statement in the template format as

$$\{WS\}_e = \begin{pmatrix} global \\ constant \end{pmatrix} \left\{ \begin{matrix} element \\ variable \end{matrix} \right\}_e \left[\begin{matrix} master \\ matrix \end{matrix} \right] \left\{ \begin{matrix} unknown \\ or data \end{matrix} \right\}_e \quad (5.30)$$

where e denotes element dependence.

The following matrix identification convention is used for the master matrix

$[Mbccc]$:

$M = A, B, \text{ or } C$. Denotes the dimension of the problem $n = 1, 2, \text{ or } 3$.

$b = \text{an integer}$. Denotes the number of FE basis $\{N_k\}$ in the $\{WS_e\}$ term.

$c = x, y, z, \text{ or } 0$ repeated b times. Indicates if the basis is differentiated.

Using this notation the weak forms of equations (4.35) can be expressed in the template format. To avoid cluttering the SFS tensor and vector contributions are not included herein. Their FE templates are discussed in section 5.3. Denoting $TDT = \theta \Delta t$, $TDT1 = (1 - \theta) \Delta t$, and the values of the state-variables at the previous time step as UL, VL, WL, TL etc., the momentum equation in the x-direction is

$$\begin{aligned}
\{FU\} = & (1)\{ \}[c200]\{U\} & -(\text{TDT})\{ \}[c200]\{UBCE\} \\
& -(1)\{ \}[c200]\{UL\} & -(\text{TDT1})\{ \}[c200]\{UBCEL\} \\
& +(\text{TDT})\{U\}[c300x]\{U\} & +(\text{TDT1})\{UL\}[c300x]\{UL\} \\
& +(\text{TDT})\{V\}[c300y]\{U\} & +(\text{TDT1})\{VL\}[c300y]\{UL\} \\
& +(\text{TDT})\{W\}[c300z]\{U\} & +(\text{TDT1})\{WL\}[c300z]\{UL\} \\
& +(\text{TDT})\{ \}[c20x]\{C11\} & +(\text{TDT1})\{ \}[c20x]\{C11L\} \\
& +(\text{TDT})\{ \}[c20y]\{C12\} & +(\text{TDT1})\{ \}[c20y]\{C12L\} \\
& +(\text{TDT})\{ \}[c20z]\{C13\} & +(\text{TDT1})\{ \}[c20z]\{C13L\} \\
& +(\text{TDT} \div Re)\{ \}[c2kk]\{U\} & +(\text{TDT1} \div Re)\{ \}[c2kk]\{UL\} \\
& +(\text{TDT})\{ \}[c20x]\{C\} & +(\text{TDT1})\{ \}[c20x]\{P\} \\
& +(\text{TDT} * Gr \div Re^2 * g1)\{ \}[c200]\{T\} & +(\text{TDT1} * Gr \div Re^2 * g1)\{ \}[c200]\{TL\}
\end{aligned} \tag{5.31}$$

Note that the diffusion matrix $[c2kk]$ includes all three second-order spatial derivatives with respect to x , y , and z . The sign of the diffusion term changed due to the application of Green-Gauss theorem. The templates for y - and z -momentum equations can be expressed in exactly the same manner

$$\begin{aligned}
\{FV\} = & (1) \{ \} [c200] \{V\} & \{FW\} = & (1) \{ \} [c200] \{W\} \\
& - (1) \{ \} [c200] \{VL\} & & - (1) \{ \} [c200] \{WL\} \\
& + (TDT) \{U\} [c300x] \{V\} & & + (TDT) \{U\} [c300x] \{W\} \\
& + (TDT) \{V\} [c300y] \{V\} & & + (TDT) \{V\} [c300y] \{W\} \\
& + (TDT) \{W\} [c300z] \{V\} & & + (TDT) \{W\} [c300z] \{W\} \\
& + (TDT) \{ \} [c20x] \{C12\} & & + (TDT) \{ \} [c20x] \{C13\} \\
& + (TDT) \{ \} [c20y] \{C22\} & & + (TDT) \{ \} [c20y] \{C23\} \\
& + (TDT) \{ \} [c20z] \{C23\} & & + (TDT) \{ \} [c20z] \{C33\} \\
& + (TDT \div Re) \{ \} [c2kk] \{V\} & & + (TDT \div Re) \{ \} [c2kk] \{W\} \\
& + (TDT) \{ \} [c20y] \{C\} & & + (TDT) \{ \} [c20z] \{C\} \\
& + (TDT * Gr \div Re^2 * g1) \{ \} [c200] \{T\} & & + (TDT * Gr \div Re^2 * g1) \{ \} [c200] \{T\} \\
& - (TDT) \{ \} [c200] \{VBCE\} & & - (TDT) \{ \} [c200] \{WBCE\} \\
& + (TDT1) \{UL\} [c300x] \{VL\} & & + (TDT1) \{UL\} [c300x] \{WL\} \\
& + (TDT1) \{VL\} [c300y] \{VL\} & & + (TDT1) \{VL\} [c300y] \{WL\} \\
& + (TDT1) \{WL\} [c300z] \{VL\} & & + (TDT1) \{WL\} [c300z] \{WL\} \\
& + (TDT1) \{ \} [c20x] \{C12L\} & & + (TDT1) \{ \} [c20x] \{C13L\} \\
& + (TDT1) \{ \} [c20y] \{C22L\} & & + (TDT1) \{ \} [c20y] \{C23L\} \\
& + (TDT1) \{ \} [c20z] \{C23L\} & & + (TDT1) \{ \} [c20z] \{C33L\} \\
& + (TDT1 \div Re) \{ \} [c2kk] \{VL\} & & + (TDT1 \div Re) \{ \} [c2kk] \{WL\} \\
& + (TDT1) \{ \} [c20y] \{P\} & & + (TDT1) \{ \} [c20z] \{P\} \\
& + (TDT1 * Gr \div Re^2 * g1) \{ \} [c200] \{TL\} & & + (TDT1 * Gr \div Re^2 * g1) \{ \} [c200] \{TL\} \\
& - (TDT1) \{ \} [c200] \{VBCEL\} & & - (TDT1) \{ \} [c200] \{WBCEL\}
\end{aligned} \tag{5.32}$$

Using the same notation the energy equation is expressed in the following template form

$$\begin{aligned}
\{FT\} = & (1) \{ \} [c200] \{T\} & + (TDT) \{U\} [c300x] \{T\} & + (TDT1) \{UL\} [c300x] \{TL\} \\
& - (1) \{ \} [c200] \{TL\} & + (TDT) \{V\} [c300y] \{T\} & + (TDT1) \{VL\} [c300y] \{TL\} \\
& & + (TDT) \{W\} [c300z] \{T\} & + (TDT1) \{WL\} [c300z] \{TL\} \\
& & + (TDT) \{ \} [c20x] \{V1\} & + (TDT1) \{ \} [c20x] \{V1L\} \\
& & + (TDT) \{ \} [c20y] \{V2\} & + (TDT1) \{ \} [c20y] \{V2L\} \\
& & + (TDT) \{ \} [c20z] \{V3\} & + (TDT1) \{ \} [c20z] \{V3L\} \\
& & + (TDT \div Pe) \{ \} [c2kk] \{T\} & + (TDT1 \div Pe) \{ \} [c2kk] \{TL\} \\
& & - (TDT) \{ \} [c200] \{TBCE\} & - (TDT1) \{ \} [c200] \{TBCEL\}
\end{aligned} \tag{5.33}$$

The Galerkin weak statements for ϕ and \bar{p} are given by equations (4.24) and (4.33), respectively.

Multiplying both equations through by -1, the resulting template forms are

$$\begin{aligned}
\{FPRES\} = & (1) \{ \} [c2kk] \{PRES\} & + (1) \{ \} [c2yx] \{C12\} \\
& + (1) \{U\} [c30xx] \{U\} & + (1) \{ \} [c2yy] \{C22\} \\
& + (1) \{U\} [c30yx] \{V\} & + (1) \{ \} [c2yz] \{C23\} \\
& + (1) \{U\} [c30zx] \{W\} & + (1) \{ \} [c2zx] \{C13\} \\
& + (1) \{V\} [c30xy] \{U\} & + (1) \{ \} [c2zy] \{C23\} \\
& + (1) \{V\} [c30yy] \{V\} & + (1) \{ \} [c2zz] \{C33\} \\
& + (1) \{V\} [c30zy] \{W\} & + (Gr \div Re^2 \times g1) \{ \} [c2x0] \{T\} \\
& + (1) \{W\} [c30xz] \{U\} & + (Gr \div Re^2 \times g2) \{ \} [c2y0] \{T\} \\
& + (1) \{W\} [c30yz] \{V\} & + (Gr \div Re^2 \times g3) \{ \} [c2z0] \{T\} \\
& + (1) \{W\} [c30zz] \{W\} & \\
\{FPHI\} = & (1) \{ \} [c2kk] \{PHI\} \\
& + (1) \{ \} [c20x] \{U\} \\
& + (1) \{ \} [c20y] \{V\} \\
& + (1) \{ \} [c20z] \{W\}
\end{aligned} \tag{5.34}$$

Note that the SFS tensor contribution to (5.34) consists of 54 differential terms. The remaining templates for \bar{c}_{ij} and \bar{v}_j^\ominus are (only \bar{c}_{12} and \bar{v}_2^\ominus are presented)

$$\begin{aligned}
\{FC12\} = & (1) \{ \} [c2kk] \{C12\} & \{FV2\} = & (1) \{ \} [c2kk] \{V2\} & (5.35) \\
& + (4\gamma / \delta^2) \{ \} [c200] \{C12\} & & + (4\gamma / \delta^2) \{ \} [c200] \{V2\} \\
& - (2) \{U\} [c3x0x] \{V\} & & - (2) \{V\} [c2x0x] \{T\} \\
& - (2) \{U\} [c3y0y] \{V\} & & - (2) \{V\} [c2y0y] \{T\} \\
& - (2) \{U\} [c3z0z] \{V\} & & - (2) \{V\} [c2z0z] \{T\}
\end{aligned}$$

Finally, the template for the continuity constraint variable C represents an algebraic update operation replacing the master matrix with an identity matrix, hence

$$\begin{aligned}
\{FC\} = & (1) \{ \} [I] \{C\} \\
& + (1 \div TDT) \{ \} [I] \{PHI\}
\end{aligned} \tag{5.36}$$

5.3 THE GWS AND TEMPLATE FOR THE SFS CLOSURE

Following the idea of direct use of algorithm's numerical diffusion an analytically-derived SFS tensor candidate is

$$-\overline{u'_j u'_i} \equiv C_s(\delta) \frac{h^2 Re}{6} \left[\bar{u}_j \bar{u}_k \frac{\partial \bar{u}_i}{\partial x_k} + \bar{u}_i \bar{u}_k \frac{\partial \bar{u}_j}{\partial x_k} \right] \quad (5.37)$$

For thermal problems analytical derivation of the companion SFS vector closure candidate for the temperature is

$$-\overline{u'_j \Theta'} \equiv C_s(\delta) \frac{h^2 Pe}{12} \left[\bar{u}_j \bar{u}_k \frac{\partial \bar{\Theta}}{\partial x_j} \right] \quad (5.38)$$

The SFS tensor and vector closures (5.37) and (5.38) are associated with convection processes in the flow. These terms appear in conservation principles (4.2) and (4.3) with a partial derivative $\partial/\partial x_j$.

Including this fact and expanding (5.37) and (5.38) written in index form, yields

$$\begin{aligned} \frac{\partial}{\partial x_j} (\overline{u'_j u'_i}) &= -C_s \frac{h^2 Re}{6} \frac{\partial}{\partial x_j} \left[\bar{u}_j \bar{u}_k \frac{\partial \bar{u}_i}{\partial x_k} + \bar{u}_i \bar{u}_k \frac{\partial \bar{u}_j}{\partial x_k} \right] \\ &= -C_s \frac{h^2 Re}{6} \left\{ \begin{aligned} &\left[\frac{\partial}{\partial x} \left[\bar{u}\bar{u} \frac{\partial \bar{u}_i}{\partial x} + \bar{u}\bar{v} \frac{\partial \bar{u}_i}{\partial y} + \bar{u}\bar{w} \frac{\partial \bar{u}_i}{\partial z} \right] + \frac{\partial}{\partial y} \left[\bar{v}\bar{u} \frac{\partial \bar{u}_i}{\partial x} + \bar{v}\bar{v} \frac{\partial \bar{u}_i}{\partial y} + \bar{v}\bar{w} \frac{\partial \bar{u}_i}{\partial z} \right] \right] \\ &+ \frac{\partial}{\partial z} \left[\bar{w}\bar{u} \frac{\partial \bar{u}_i}{\partial x} + \bar{w}\bar{v} \frac{\partial \bar{u}_i}{\partial y} + \bar{w}\bar{w} \frac{\partial \bar{u}_i}{\partial z} \right] + \frac{\partial}{\partial x} \left[\bar{u}_i \bar{u} \frac{\partial \bar{u}}{\partial x} + \bar{u}_i \bar{v} \frac{\partial \bar{u}}{\partial y} + \bar{u}_i \bar{w} \frac{\partial \bar{u}}{\partial z} \right] \\ &+ \frac{\partial}{\partial y} \left[\bar{u}_i \bar{u} \frac{\partial \bar{v}}{\partial x} + \bar{u}_i \bar{v} \frac{\partial \bar{v}}{\partial y} + \bar{u}_i \bar{w} \frac{\partial \bar{v}}{\partial z} \right] + \frac{\partial}{\partial z} \left[\bar{u}_i \bar{u} \frac{\partial \bar{w}}{\partial x} + \bar{u}_i \bar{v} \frac{\partial \bar{w}}{\partial y} + \bar{u}_i \bar{w} \frac{\partial \bar{w}}{\partial z} \right] \end{aligned} \right\} \quad (5.39) \end{aligned}$$

$$\begin{aligned}
\frac{\partial}{\partial x_j} (\overline{u'_j \Theta'}) &= -C_s \frac{h^2 Pe}{12} \frac{\partial}{\partial x_j} \left[\overline{u_j \bar{u}_k} \frac{\partial \bar{\Theta}}{\partial x_k} \right] \\
&= -C_s \frac{h^2 Pe}{12} \left\{ \begin{aligned} &\frac{\partial}{\partial x} \left[\overline{u\bar{u}} \frac{\partial \bar{\Theta}}{\partial x} + \overline{u\bar{v}} \frac{\partial \bar{\Theta}}{\partial y} + \overline{u\bar{w}} \frac{\partial \bar{\Theta}}{\partial z} \right] \\ &+ \frac{\partial}{\partial y} \left[\overline{v\bar{u}} \frac{\partial \bar{\Theta}}{\partial x} + \overline{v\bar{v}} \frac{\partial \bar{\Theta}}{\partial y} + \overline{v\bar{w}} \frac{\partial \bar{\Theta}}{\partial z} \right] \\ &+ \frac{\partial}{\partial z} \left[\overline{w\bar{u}} \frac{\partial \bar{\Theta}}{\partial x} + \overline{w\bar{v}} \frac{\partial \bar{\Theta}}{\partial y} + \overline{w\bar{w}} \frac{\partial \bar{\Theta}}{\partial z} \right] \end{aligned} \right\} \quad (5.40)
\end{aligned}$$

The Galerkin weak statement for (5.39) is readily identified as

$$\begin{aligned}
0 &= \int_{\Omega} \Psi_l \frac{\partial}{\partial x_j} (\overline{u'_j u'_i})^N d\Omega \\
&= C_s \frac{h^2 Re}{6} \int_{\Omega} \frac{\partial \Psi_l}{\partial x_j} \left[\overline{u_j \bar{u}_k} \frac{\partial \bar{u}_i}{\partial x_k} + \overline{u_i \bar{u}_k} \frac{\partial \bar{u}_j}{\partial x_k} \right]^N d\Omega - C_s \frac{h^2 Re}{6} \oint_{\Gamma} \Psi_l \left[\overline{u_j \bar{u}_k} \frac{\partial \bar{u}_i}{\partial x_k} + \overline{u_i \bar{u}_k} \frac{\partial \bar{u}_j}{\partial x_k} \right]^N n_j d\Gamma \\
&= C_s \frac{h^2 Re}{6} \times \\
&\quad \left\{ \begin{aligned} &\left(\overline{u\bar{u}} \frac{\partial \Psi_l}{\partial x} \frac{\partial \bar{u}_i}{\partial x} + \overline{u\bar{v}} \frac{\partial \Psi_l}{\partial x} \frac{\partial \bar{u}_i}{\partial y} + \overline{u\bar{w}} \frac{\partial \Psi_l}{\partial x} \frac{\partial \bar{u}_i}{\partial z} \right) + \left(\overline{v\bar{u}} \frac{\partial \Psi_l}{\partial y} \frac{\partial \bar{u}_i}{\partial x} + \overline{v\bar{v}} \frac{\partial \Psi_l}{\partial y} \frac{\partial \bar{u}_i}{\partial y} + \overline{v\bar{w}} \frac{\partial \Psi_l}{\partial y} \frac{\partial \bar{u}_i}{\partial z} \right) \\ &+ \left(\overline{w\bar{u}} \frac{\partial \Psi_l}{\partial z} \frac{\partial \bar{u}_i}{\partial x} + \overline{w\bar{v}} \frac{\partial \Psi_l}{\partial z} \frac{\partial \bar{u}_i}{\partial y} + \overline{w\bar{w}} \frac{\partial \Psi_l}{\partial z} \frac{\partial \bar{u}_i}{\partial z} \right) + \left(\overline{u_i \bar{u}} \frac{\partial \Psi_l}{\partial x} \frac{\partial \bar{u}}{\partial x} + \overline{u_i \bar{v}} \frac{\partial \Psi_l}{\partial x} \frac{\partial \bar{u}}{\partial y} + \overline{u_i \bar{w}} \frac{\partial \Psi_l}{\partial x} \frac{\partial \bar{u}}{\partial z} \right) \\ &+ \left(\overline{u_i \bar{v}} \frac{\partial \Psi_l}{\partial y} \frac{\partial \bar{v}}{\partial x} + \overline{u_i \bar{w}} \frac{\partial \Psi_l}{\partial y} \frac{\partial \bar{v}}{\partial y} + \overline{u_i \bar{w}} \frac{\partial \Psi_l}{\partial y} \frac{\partial \bar{v}}{\partial z} \right) + \left(\overline{u_i \bar{u}} \frac{\partial \Psi_l}{\partial z} \frac{\partial \bar{w}}{\partial x} + \overline{u_i \bar{v}} \frac{\partial \Psi_l}{\partial z} \frac{\partial \bar{w}}{\partial y} + \overline{u_i \bar{w}} \frac{\partial \Psi_l}{\partial z} \frac{\partial \bar{w}}{\partial z} \right) \end{aligned} \right\} d\Omega \\
&\quad - C_s \frac{h^2 Re}{6} \oint_{\Gamma} \Psi_l \left[\overline{u_j \bar{u}_k} \frac{\partial \bar{u}_i}{\partial x_k} + \overline{u_i \bar{u}_k} \frac{\partial \bar{u}_j}{\partial x_k} \right]^N n_j d\Gamma \quad (5.41)
\end{aligned}$$

Similarly the Galerkin weak statement for (5.40) reads as

$$\begin{aligned}
0 &= \int_{\Omega} \Psi_l \frac{\partial}{\partial x_j} \left(\overline{u'_j \Theta^N} \right) d\Omega \\
&= C_s \frac{h^2 Pe}{12} \int_{\Omega} \frac{\partial \Psi_l}{\partial x_j} \left[\overline{u_j \bar{u}_k} \frac{\partial \bar{\Theta}}{\partial x_k} \right]^N d\Omega - C_s \frac{h^2 Pe}{12} \oint_{\Gamma} \Psi_l \left[\overline{u_j \bar{u}_k} \frac{\partial \bar{\Theta}}{\partial x_k} \right]^N d\Gamma \\
&= C_s \frac{h^2 Pe}{12} \int_{\Gamma} \left\{ \begin{aligned} &\overline{uu} \frac{\partial \Psi_l}{\partial x} \frac{\partial \bar{\Theta}}{\partial x} + \overline{uv} \frac{\partial \Psi_l}{\partial x} \frac{\partial \bar{\Theta}}{\partial y} + \overline{uw} \frac{\partial \Psi_l}{\partial x} \frac{\partial \bar{\Theta}}{\partial z} \\ &+ \overline{vu} \frac{\partial \Psi_l}{\partial y} \frac{\partial \bar{\Theta}}{\partial x} + \overline{vv} \frac{\partial \Psi_l}{\partial y} \frac{\partial \bar{\Theta}}{\partial y} + \overline{vw} \frac{\partial \Psi_l}{\partial y} \frac{\partial \bar{\Theta}}{\partial z} \\ &+ \overline{wu} \frac{\partial \Psi_l}{\partial z} \frac{\partial \bar{\Theta}}{\partial x} + \overline{wv} \frac{\partial \Psi_l}{\partial z} \frac{\partial \bar{\Theta}}{\partial y} + \overline{ww} \frac{\partial \Psi_l}{\partial z} \frac{\partial \bar{\Theta}}{\partial z} \end{aligned} \right\}^N d\Omega - C_s \frac{h^2 Pe}{12} \oint_{\Gamma} \Psi_l \left[\overline{u_j \bar{u}_k} \frac{\partial \bar{\Theta}}{\partial x_k} \right]^N d\Gamma
\end{aligned} \tag{5.42}$$

In integral relations (5.41) and (5.42) the measure of the mesh, h , is assumed constant, which is only true for uniform meshes. For non-uniform meshes this measure is element dependent thus has to stay as part of the integrand. In FEM the determinant of the Jacobian of coordinate transformation in three dimensions is defined as

$$\det = \frac{V_e}{8} \tag{5.43}$$

where V_e is the element's volume.

Assuming that the element is not severely skewed, the following assumption is reasonable

$$h \approx \sqrt[3]{V_e} \tag{5.44}$$

Performing simple arithmetic manipulations the relation between the mesh measure (squared) and the determinant of the Jacobian of coordinate transformation is

$$h^2 \approx 4 \det^{2/3} \tag{5.45}$$

The differential terms constructing the SFS tensor and vector closures include two spatial derivatives, each contributing a factor of \det^{-1} into the *metric data* (Baker, 2006). Accounting for the coordinate

transformation itself (a factor of \det), the resulting exponent on the determinant is -1 . Including h^2 multiplier and using approximation (5.45) gives an algebraic alteration to the metric data as

$$\frac{h^2}{\det} = \frac{4}{\sqrt[3]{\det}} \quad (5.46)$$

instead of the original \det^{-1} .

The SFS tensor and vector weak form construction requires special treatment. To avoid higher order matrices like $[c40000]$ the two-variable products of velocity components (UU, UV, UW etc.) are treated as one variable, meaning that only one shape function is used in constructing the GWS.

The FE templates for the SFS tensor and vector closures are given below. For the SFS tensor only the terms contributing to the x-momentum equation are presented, i.e., $\overline{u'_j u'}$. The alteration to the metric data (5.46) is indicated by adding "h" symbol to the name of the matrix.

$$\begin{aligned} \{FUPVPX\} &= \{FUPVP1\} + \{FUPVP2\} + \{FUPVP3\} \\ &= (C_s Re / 6) \{UU\} [c30xxh] \{U\} && + (C_s Re / 6) \{UU\} [c30xxh] \{U\} \\ &+ (C_s Re / 6) \{UV\} [c30xyh] \{U\} && + (C_s Re / 6) \{UV\} [c30xxh] \{U\} \\ &+ (C_s Re / 6) \{UW\} [c30xzh] \{U\} && + (C_s Re / 6) \{UW\} [c30xxh] \{U\} \\ &+ (C_s Re / 6) \{VU\} [c30yxh] \{U\} && + (C_s Re / 6) \{UU\} [c30yyh] \{V\} \\ &+ (C_s Re / 6) \{VV\} [c30yyh] \{U\} && + (C_s Re / 6) \{UV\} [c30yyh] \{V\} \\ &+ (C_s Re / 6) \{VW\} [c30yzh] \{U\} && + (C_s Re / 6) \{UW\} [c30yyh] \{V\} \\ &+ (C_s Re / 6) \{WU\} [c30zjh] \{U\} && + (C_s Re / 6) \{UU\} [c30zzh] \{W\} \\ &+ (C_s Re / 6) \{WV\} [c30zyh] \{U\} && + (C_s Re / 6) \{UV\} [c30zzh] \{W\} \\ &+ (C_s Re / 6) \{WW\} [c30zzh] \{U\} && + (C_s Re / 6) \{UW\} [c30zzh] \{W\} \end{aligned} \quad (5.47)$$

$$\begin{aligned}
\{FUPTP1\} &= (C_s Pe / 12) \{UU\} [c30xxh] \{T\} \\
&+ (C_s Pe / 12) \{UV\} [c30xyh] \{T\} \\
&+ (C_s Pe / 12) \{UW\} [c30xzh] \{T\} \\
&+ (C_s Pe / 12) \{VU\} [c30yxh] \{T\} \\
&+ (C_s Pe / 12) \{VV\} [c30yyh] \{T\} \\
&+ (C_s Pe / 12) \{VW\} [c30yzh] \{T\} \\
&+ (C_s Pe / 12) \{WU\} [c30zxh] \{T\} \\
&+ (C_s Pe / 12) \{WV\} [c30zyh] \{T\} \\
&+ (C_s Pe / 12) \{WW\} [c30zzh] \{T\}
\end{aligned} \tag{5.48}$$

5.4 FINITE ELEMENT AD FORMULA IMPLEMENTATION

Determination of proper boundary conditions for space filtered state-variables \bar{u}_i , $\bar{\Theta}$, \bar{c}_{ij} and \bar{v}_j^\ominus via approximate deconvolution approach requires implementation of the AD formula, i.e.,

$$q(\mathbf{x}) = \bar{q}(\mathbf{x}) - \frac{\delta^2}{24} \nabla^2 \bar{q}(\mathbf{x}) \tag{5.49}$$

Equation (5.49) represents a differential definition involving Laplacian operator and requiring discretization. Finite element evaluation of the unfiltered quantity $q(\mathbf{x})$ is readily established via Galerkin weak statement for (5.49), hence

$$\begin{aligned}
GWS^N &= \int_{\Omega} \Psi_i \left(q^N - \bar{q}^N + \frac{\delta^2}{24} \frac{\partial^2 \bar{q}^N}{\partial x_j^2} \right) d\Omega \\
&= \int_{\Omega} \Psi_i (q^N - \bar{q}^N) d\Omega - \frac{\delta^2}{24} \int_{\Omega} \frac{\partial \Psi_i}{\partial x_j} \left(\frac{\partial \bar{q}^N}{\partial x_j} \right) d\Omega + \frac{\delta^2}{24} \oint_{\Gamma} \Psi_i \frac{\partial \bar{q}^N}{\partial x_j} n_j d\Gamma \\
&= 0
\end{aligned} \tag{5.50}$$

The FE template statement for (5.50) is

$$\begin{aligned}
\{FQAD\} &= (1)\{ \} [c200]\{QAD\} \\
&+ (-1)\{ \} [c200]\{Q\} \\
&+ (-\delta^2 / 24)\{ \} [c2kk]\{Q\}
\end{aligned}
\tag{5.51}$$

The application of the Green-Gauss theorem to the Laplacian term in (5.49) generates an efflux boundary integral (last term in (5.50)) which is not known a priori. These slopes are calculated using third order forward finite difference formula based on four nodal values, i.e.,

$$\left. \frac{dq}{dx} \right|_{x_0} = c_0 q(x_0) + c_1 q(x_1) + c_2 q(x_2) + c_3 q(x_3)$$

where (5.52)

$$\begin{aligned}
c_0 &= -\frac{(2h_1 + h_2)H + h_1(h_1 + h_2)}{h_1(h_1 + h_2)H}; & c_1 &= \frac{(h_1 + h_2)H}{h_1 h_2 (h_2 + h_3)}; \\
c_2 &= -\frac{h_1 H}{h_2 (h_1 + h_2) h_3}; & c_3 &= \frac{h_1 (h_1 + h_2)}{H (h_2 + h_3) h_3}; \\
h_1 &= x_1 - x_0; & h_2 &= x_2 - x_1; & h_3 &= x_3 - x_2; & H &= h_1 + h_2 + h_3
\end{aligned}$$

6. DISCUSSION AND RESULTS

Verification and validation of an essentially analytical rational LES (*arLES*) formulation with focus on bounded domains is established by conducting computational experiments for four pertinent benchmark problems.

First the feasibility of the ADBC formulation is examined for a two-dimensional non-steady heat conduction problem with known analytical solution. The linear problem is chosen to separate the boundary condition considerations from the closure problem associated with non-linear equations such as the Navier-Stokes PDE system. The AD approach is utilized to approximate the unknown boundary conditions, as well as the BCE term.

During the second computational experiment the ADBC theory implementation is closely examined using two-dimensional fully-developed flow in a channel with time-averaged turbulent boundary layer (BL). Proper filter measure specification along with appropriate mesh construction technique is sought utilizing a typical turbulent BL profile.

The third computational experiment is conducted for three-dimensional external laminar flow over a flat plate. Since the *arLES* theory closure is absent the word *turbulent* it is Reynolds number *unconstrained*. Therefore validation of *arLES* theory applicability in predicting laminar flows on bounded domains is pertinent. This three-dimensional benchmark also helps to set the stage for implementing a more complicated three-dimensional and thermal analysis of buoyancy driven flow in a cavity.

Finally the *arLES* theory closure is fully examined for a three-dimensional thermally driven flow in a differentially heated cavity of aspect ratio 1x8x8. The spatial structure of the flow includes such complexities as vertical and horizontal boundary layers, corner structures, stratified core and so on which sensitively depend on the aspect ratio, Rayleigh and Prandtl numbers and thermal boundary

conditions. The buoyancy-driven cavity flow exhibits a critical Rayleigh (Ra) number responsible for transition from steady to various modes of unsteady cyclic flow with subsequent generation of a significant range of eddy scales for progressively larger Ra number.

6.1 NON-STEADY HEAT CONDUCTION PROBLEM

The first computational experiment examines feasibility of the ADBC formulation using one- and two-dimensional non-steady heat conduction problems with known analytical solutions. Originally the ADBC approach is demonstrated using one-dimensional heat conduction problem with time dependent boundary conditions (Borggaard and Iliescu, 2006). The linear problem is chosen to separate the boundary condition considerations from the closure problem associated with non-linear equations such as the Navier-Stokes PDE system. In this dissertation the original one-dimensional analysis is repeated with almost identical results. A numerical validation of ADBC for two-dimensional heat conduction problem is sought next.

6.1.1 ONE-DIMENSIONAL ANALYSIS

One-dimensional heat equation accompanied by initial and boundary conditions reads as

$$\left\{ \begin{array}{ll} \frac{\partial q}{\partial t} - \frac{\partial^2 q}{\partial x^2} = f & \text{in } \Omega \times (0, T], \\ q = b & \text{in } \partial\Omega \times (0, T], \\ q(x, 0) = q_0(x) & \text{in } \Omega. \end{array} \right. \quad (6.1)$$

The source term f , the boundary condition b , and the initial condition q_0 are chosen such that the heat equation has an exact solution

$$q(x, t) = t + \sin(2\pi x) + \sin(8\pi x) \quad (6.2)$$

This yields $f(x,t)=1+4\pi^2 \sin(2\pi x)+64\pi^2 \sin(8\pi x)$, $b(t)=t$ and $q_0(x)=\sin(2\pi x)+\sin(8\pi x)$. The domain of interest is $\Omega=(0,1)$ and the final time is $T=0.05$. The above functions need to be extended outside $\Omega=(0,1)$ in order to convolve the heat equation with a spatial filter. Therefore, the exact solution for q is extended by its values at the boundary, thus $q(x,t)=t$ for $x \notin (0,1)$. This yields the following extensions for f and q_0 : $f(x,t)=1$, $q_0(x)=t$ for $x \notin (0,1)$. One-dimensional Gaussian filter function, $g_\delta(x)$, has the form

$$g_\delta(x)=\left(\frac{6}{\pi\delta^2}\right)^{0.5} \exp\left(-\frac{6x^2}{\delta^2}\right) \quad (6.3)$$

where the filter measure δ is chosen to be 0.2. The interval $(0,1)$ is divided into 20 equidistant subintervals ($\Delta x=0.05$). In order to compute the convolved functions, the computational domain $(0,1)$ is extended to the left and right by $\delta=0.2$. To eliminate the effects of time integration a very small time-step is used, i.e., $\Delta t=0.0001$.

The space filtered version of the heat equation is derived by extending q , f , b and u_0 to \mathbb{R}^1 , and then convolving the heat equation with a spatial filter, resulting in

$$\bar{q}_t - \Delta \bar{q} + g_\delta(x-0) \frac{\partial q(0,t)}{\partial x} - g_\delta(x-1) \frac{\partial q(1,t)}{\partial x} = \bar{f} \quad \text{in } \mathbb{R}^1 \times (0,T). \quad (6.4)$$

In (6.4) the boundary commutation error (BCE) integral is evaluated at two end points via direct multiplication of a Gaussian function with a spatial derivative. These derivatives are approximated via first order finite differences as

$$\frac{\partial q(0,t)}{\partial x} \approx \frac{q(\Delta x,t)-q(0,t)}{\Delta x} \quad \text{and} \quad \frac{\partial q(1,t)}{\partial x} \approx \frac{q(1,t)-q(1-\Delta x,t)}{\Delta x} \quad (6.5)$$

The unknown components $q(\Delta x, t)$ and $q(1-\Delta x, t)$ that lie strictly inside Ω are evaluated using an approximate deconvolution formula, hence

$$\begin{aligned} q(\Delta x, t) &\approx \bar{q}(\Delta x) - \left(\frac{\delta^2}{24}\right) \frac{\bar{q}(0) - 2\bar{q}(\Delta x) + \bar{q}(2\Delta x)}{\Delta x^2} \\ q(1-\Delta x, t) &\approx \bar{q}(1-\Delta x) - \left(\frac{\delta^2}{24}\right) \frac{\bar{q}(1-2\Delta x) - 2\bar{q}(1-\Delta x) + \bar{q}(1)}{\Delta x^2} \end{aligned} \quad (6.6)$$

Finally the boundary conditions for \bar{q} are established using the ADBC approach detailed in section 3.3.

Borggaard and Iliescu (2006) conducted a set of four numerical experiments as described below. Their results are provided in Figure B.6 showing the plots of error in approximating space-filtered \bar{q} (in the original paper \bar{u} was used instead of \bar{q}). The numerical experiments are summarized as

Test 1: *Exact BCE Terms, Exact Boundary Conditions* (Figure B.6, top left). This test represents the benchmark.

Test 2: *No BCE Terms, Exact Boundary Conditions* (Figure B.6, top right). This experiment was conducted to illustrate the importance of the BCE integral.

Test 3: *Approximate BCE Terms, Exact Boundary Conditions* (Figure B.6, bottom left). In this test the BCE integral is approximated using finite differences and the AD formula as described in (6.5)-(6.6).

Test 4: *Approximate BCE Terms, Approximate Boundary Conditions* (Figure B.6, bottom right). Both the BCE integral and the boundary conditions are approximated.

These four experiments are repeated herein achieving almost identical results. Unfortunately, the original paper does not specify how the error in \bar{q} is calculated, therefore there is a slight discrepancy in the results. In this study the error is defined as the difference between exact and computed solutions.

The plots of error in approximating \bar{q} as produced in this study are shown in Figure B.7. The results of both studies are now compared.

Our result of Test 1 is significantly different from the result of Borggaard and Iliescu. A possible explanation might be that the error for Test 1 is defined differently from Tests 2, 3 and 4. The fact that it is strictly negative for a solution that consists of two sine functions makes I think this could be the reason.

In Test 2 the error distributions look almost identical. Both figures indicate a huge increase in error as compared to the result of Test 1. This increase proves the utmost importance of the BCE term and suggests that it should never be dropped from the space filtered equations.

In Test 3 the maxima and minima of error are in very good agreement. Both studies indicate a fourfold reduction in error as compared to Test 2. These results indicate the correct and efficient implementation of the BCE integral approximation as described above.

Finally the results of Test 4 agree very well also. In this test the exact boundary condition is replaced by an approximation. Both studies show a slight decrease of accuracy on the boundary, as compared to Test 3, which does not degrade the overall solution accuracy.

6.1.2 TWO-DIMENSIONAL ANALYSIS

Two-dimensional heat equation is used to continue numerical validation of ADBC. As before, the linear problem is chosen to decouple the boundary treatment from the closure problem. The heat equation in two dimensions along with the boundary and initial conditions reads as

$$\begin{cases} \frac{\partial q}{\partial t} - \left(\frac{\partial^2 q}{\partial x^2} + \frac{\partial^2 q}{\partial y^2} \right) = f(x, y) & \text{in } \Omega \times [0, T], \\ q(x, y, t) = b(x, y) & \text{in } \partial\Omega \times (0, T], \\ q(x, y, 0) = u_0(x, y) & \text{in } \Omega, \end{cases} \quad (6.7)$$

where domain $\Omega = \{0 \leq x \leq 1; 0 \leq y \leq 1\}$.

The source function $f(x, y)$ is prescribed to be

$$f(x, y) = 2\pi^2 \sin(\pi x) \sin(\pi y) \quad (6.8)$$

To shorten the analytical solution a non-homogeneous boundary condition is prescribed only at $y = 0$.

The other three segments of the boundary are assigned homogeneous Dirichlet BCs, hence

$$b(x, y) = \begin{cases} 0, & \text{for } x = 0; x, y = 1 \\ \frac{\sin(\pi x)}{2\pi}, & \text{for } y = 0 \end{cases} \quad (6.9)$$

The initial condition is identified from the analytical solution by setting time to zero, hence

$$q_0(x, y) = \frac{\sin(\pi x) \sinh(\pi - \pi y)}{2\pi \sinh(\pi)} + \frac{1}{2\pi^2} \sin(\pi x) \sin(\pi y) \quad (6.10)$$

The analytical solution to (6.7) reads as

$$q(x, y, t) = \frac{\sin(\pi x) \sinh(\pi - \pi y)}{2\pi \sinh(\pi)} + \frac{1}{2\pi^2} e^{-2\pi^2 t} \sin(\pi x) \sin(\pi y) + (1 - e^{-2\pi^2 t}) \sin(\pi x) \sin(\pi y) \quad (6.11)$$

which satisfies the initial condition (6.10), as well as the boundary condition (6.9).

6.1.2.1 ANALYTICAL SOLUTION OF THE HEAT EQUATION

Derivation of the analytical solution (6.11) is presented next. The solution to an initial-boundary value problem (6.7) with nonhomogeneities in both the heat equation and the boundary condition is obtained

in two steps. First keeping the non-homogeneous BC while removing the source term $f(x,y)$ the solution to the homogeneous heat equation is sought, i.e., q_1 . This solution is further divided into a sum of steady and non-steady solutions using the following theorem

Theorem (Without proof): Let $w(x,y)$ be the solution to a Dirichlet problem

$$\begin{cases} \left(\frac{\partial^2 w}{\partial x^2} + \frac{\partial^2 w}{\partial y^2} \right) = 0 & \text{in } \Omega \times [0, T], \\ w(x,y) = b(x,y) & \text{in } \partial\Omega \times (0, T], \end{cases} \quad (6.12)$$

and let $v(x,y,t)$ be the solution to an IBVP

$$\begin{cases} \frac{\partial v}{\partial t} - \left(\frac{\partial^2 v}{\partial x^2} + \frac{\partial^2 v}{\partial y^2} \right) = 0 & \text{in } \Omega \times [0, T], \\ v(x,y,t) = 0 & \text{in } \partial\Omega \times (0, T], \\ v(x,y,0) = q_0(x,y) - w(x,y) & \text{in } \Omega, \end{cases} \quad (6.13)$$

Then $q_1(x,y,t)$ satisfies

$$\begin{aligned} q_1(x,y,t) &= v(x,y,t) + w(x,y) \\ \lim_{t \rightarrow \infty} q_1(x,y,t) &= w(x,y) \end{aligned} \quad (6.14)$$

□

The second part of the solution to (6.7) satisfies the following IBVP problem

$$\begin{cases} \frac{\partial q_2}{\partial t} - \left(\frac{\partial^2 q_2}{\partial x^2} + \frac{\partial^2 q_2}{\partial y^2} \right) = f(x,y) & \text{in } \Omega \times [0, T], \\ q_2(x,y,t) = 0 & \text{in } \partial\Omega \times (0, T], \\ q_2(x,y,0) = 0 & \text{in } \Omega, \end{cases} \quad (6.15)$$

The final solution is comprised of the individual solutions to problems (6.12), (6.13) and (6.15), hence

$$q(x,y,t) = q_1(x,y,t) + q_2(x,y,t) = v(x,y,t) + w(x,y) + q_2(x,y,t) \quad (6.16)$$

Solution to the Dirichlet problem (6.12) with boundary condition (6.9) can be established using the integral transform method, see Example 2.14 in Özişik (1968) and Example 5.8 in Mikhaïlov and Özişik (1984). The solution is written in its final form as

$$w(x,y) = \frac{\sin(\pi x) \sinh(\pi - \pi y)}{2\pi \sinh(\pi)} \quad (6.17)$$

The initial condition in (6.13) depends on $w(x,y)$ as well as the initial condition $q_0(x,y)$. The latter has not been chosen yet. To simplify the solution to (6.13) the initial condition $q_0(x,y)$ is chosen to be

$$q_0(x,y) = w(x,y) + \frac{1}{2\pi^2} \sin(\pi x) \sin(\pi y) = \frac{\sin(\pi x) \sinh(\pi - \pi y)}{2\pi \sinh(\pi)} + \frac{1}{2\pi^2} \sin(\pi x) \sin(\pi y) \quad (6.18)$$

This yields the following initial condition for (6.13)

$$v(x,y,0) = q_0(x,y) - w(x,y) = \frac{1}{2\pi^2} \sin(\pi x) \sin(\pi y) \quad (6.19)$$

Using the separation of variables method an analytical solution for $v(x,y,t)$ is obtained as

$$v(x,y,t) = \frac{1}{2\pi^2} e^{-2\pi^2 t} \sin(\pi x) \sin(\pi y) \quad (6.20)$$

Finally the solution to an IBVP (6.15) with zero boundary and initial conditions is obtained using either the integral transform method or the Duhamel's principle. The solution for $q_2(x,y,t)$ is

$$q_2(x,y,t) = \left(1 - e^{-2\pi^2 t}\right) \sin(\pi x) \sin(\pi y) \quad (6.21)$$

Combining all three intermediate solutions, namely (6.17), (6.20) and (6.21) the solution to the original problem stated in (6.7) is

$$q(x, y, t) = \frac{\sin(\pi x) \sinh(\pi - \pi y)}{2\pi \sinh(\pi)} + \frac{1}{2\pi^2} e^{-2\pi^2 t} \sin(\pi x) \sin(\pi y) + (1 - e^{-2\pi^2 t}) \sin(\pi x) \sin(\pi y) \quad (6.22)$$

satisfying the initial condition (6.18) and the boundary condition (6.9).

6.1.2.2 COMPUTATIONAL SETUP

The space-filtered version of the heat equation is obtained by extending q , f , b and q_0 to \mathbb{R}^3 . The

heat equation can then be convolved with a spatial filter resulting in

$$\bar{q}_t - \Delta \bar{q} - \int_{\partial\Omega} g_\delta(\mathbf{x} - \mathbf{s}) \nabla q(\mathbf{s}) \cdot \mathbf{n}(\mathbf{s}) d\mathbf{s} = \bar{f} \quad \text{in } \mathbb{R}^3 \times (0, T). \quad (6.23)$$

The solution u , the source term f , the boundary condition b , and the initial condition q_0 are extended outside of Ω by their values at the boundary, yielding the extensions

$$q^{\text{ext}}(x, y, t) = q_0^{\text{ext}}(x, y, t) = b^{\text{ext}}(x, y) = \begin{cases} 0, & \text{for } x, y \notin \Omega \cup \{0 \leq x \leq 1; y \leq 0\} \\ \frac{\sin(\pi x)}{2\pi}, & \text{for } \{0 \leq x \leq 1; y \leq 0\} \end{cases} \quad (6.24)$$

And the source term is extended by 0, hence

$$f^{\text{ext}} = 0, \text{ for } x, y \notin \Omega \quad (6.25)$$

In two dimensions the Gaussian filter $g_\delta(x, y)$ is constructed as a product of two one-dimensional

Gaussians defined in (6.3), one for each spatial direction, thus

$$g_\delta(x, y) = \left(\frac{6}{\pi \delta^2} \right) \exp\left(-\frac{6(x^2 + y^2)}{\delta^2} \right)$$

where the filter measure δ is chosen to be 0.2.

A two-dimensional mesh is constructed by uniformly placing 21 nodes in each spatial direction making it a total of 441 nodes with $\Delta x = \Delta y = 0.05 = \Delta h$. The explicit Euler scheme is used with $\Delta t = 0.001$ and final time $T = 0.05$.

A set of numerical experiments is conducted similar to that of Borggaard and Iliescu (2006). The ADBC analysis starts by establishing an analytical solution for space-filtered \bar{q} based on the exact solution for q shown in (6.11). The exact boundary conditions needed for the first three tests are extracted from the exact solution for \bar{q} . This solution is also used for measuring the error in approximating \bar{q} . The error is evaluated by subtracting the computed solution from the exact one. The BCE term $\int_{\partial\Omega} g_\delta(\mathbf{x}-\mathbf{s})\nabla q(\mathbf{s})\cdot\mathbf{n}(\mathbf{s})d\mathbf{s}$ is computed exactly using the analytical solution for q . Finally, the space-filtered version of the source term $\bar{f}(x,y)$ is calculated the same way as \bar{q} , i.e., analytically, using the convolution with a spatial filter formula, thus

$$\bar{q}(\mathbf{x}_0) \equiv \int_{\Omega} g_\delta(\mathbf{x}_0 - \mathbf{y})q(\mathbf{y})d\mathbf{y} \quad (6.26)$$

$$\bar{f}(\mathbf{x}_0) \equiv \int_{\Omega} g_\delta(\mathbf{x}_0 - \mathbf{y})f(\mathbf{y})d\mathbf{y} \quad (6.27)$$

where q is the exact solution (6.11), and f is a given source function (6.8).

Analytical evaluations of \bar{q} , \bar{f} and the BCE term are performed using Wolfram Mathematica® software (Wolfram Research Inc, 2008).

6.1.2.3 NUMERICAL ANALYSIS

The first attempt to calculate \bar{q} analytically was to evaluate the integral in (6.26) precisely on $\Omega = \{0 \leq x \leq 1; 0 \leq y \leq 1\}$, i.e., without extending q outside of Ω . The boundary conditions extracted from this solution are used during the first test, which is supposed to represent our benchmark problem. However, the error in approximating \bar{q} turns out to be unacceptable near the wall which has non-zero Dirichlet boundary condition, i.e., $y=0$. Figure B.8 illustrates this error at final time $T=0.05$ peaking at $4.9\text{E-}02$. As can be clearly seen the error is dominant near the boundary $y=0$, where the non-zero Dirichlet BC is prescribed.

We believe that this error is due to the fact that q has to remain smooth and continuous when filtering through the boundaries. When filtering operation is performed the Gaussian filter continues to operate outside of $\Omega = \{0 \leq x \leq 1; 0 \leq y \leq 1\}$ for a distance of at least the filter measure δ , and then decays rapidly to 0. It is this region outside of Ω that has to be included in the computation of \bar{q} . This region will be called an “outside buffer layer”. The size of the buffer layer is defined by the filter measure δ . For those boundaries with homogeneous Dirichlet BCs, the extension for q in the buffer layer is zero, thus no extra treatment is required. Conversely, if the boundary condition is non-homogeneous Dirichlet, the function q should be extended outside of the boundary and the limits of integration in (6.26) should be increased outside of Ω by δ . In our case, the non-homogeneous Dirichlet BC is prescribed at $y=0$, therefore the limits of integration should be changed from \int_0^1 to $\int_{-\delta}^1$ in the y -direction. No extension in the x -direction is necessary since $q=0$ at $x=0$ and $x=1$, and the extension is trivial. Figure B.9 shows the error in calculating \bar{q} at $T=0.05$ after the buffer layer is added. The error drops by one order of magnitude compared with the result shown in Figure B.8, with the peak of $4.3\text{E-}03$.

In Test 1b the exact boundary conditions at $y=0$ are different from those of Test 1a. They not only depend (non-locally) on the values of q inside Ω and on the boundary $\partial\Omega$, but they also depend on the fictitious values of q outside of Ω . As can be seen from Figure B.9, modified boundary conditions completely eliminate the dominant error mode shown in Figure B.8. Based on this observation, a new methodology for approximating space filtered boundary conditions is developed (see section 3.4). But before constructing and testing the new boundary conditions (Test 4), two more tests are performed focusing attention on the BCE term.

In Test 1a and Test 1b the boundary commutation error term is calculated analytically as a line integral along each of the four bounding line segments. It acts as an additional source term in the heat equation (6.23). Test 2 is performed to illustrate the importance of the BCE term by not including it into the formulation. The boundary conditions are kept the same as in Test 1b (Figure B.9) and are exact. The error in approximating \bar{q} is shown in Figure B.10 at final time $T=0.05$. As can be observed, the solution is severely polluted by the absence of the BCE term, especially near the boundaries. The error has increased by one order of magnitude compared with the results of Test 1b, peaking at an absolute of $2.7E-02$. This result once again suggests that the BCE term plays an important role in the LES formulation and cannot be omitted.

The next challenge in numerical implementation of (6.23) is the fact that the BCE integral therein is not known a priori. A numerical approximation is required to evaluate this term. Moreover, the integrand itself is also unknown as it depends on the normal component of the derivative of q at the boundary. For our two-dimensional problem the BCE integral consists of four line integrals, one for each boundary segment, i.e.,

$$\begin{aligned}
& \int_{\partial\Omega} g_\delta(\mathbf{x}-\mathbf{s})\nabla q(\mathbf{s})\cdot\mathbf{n}(\mathbf{s})d\mathbf{s} \\
&= \iint_{\partial\Omega} g_\delta(x-s_1,y-s_2)\nabla q(s_1,s_2)\cdot\mathbf{n}(s_1,s_2)ds_1ds_2 \\
&= -\int_0^1 g_\delta(x-0,y-s_2)\frac{\partial q}{\partial x}(0,s_2)ds_2 \\
&\quad + \int_0^1 g_\delta(x-1,y-s_2)\frac{\partial q}{\partial x}(1,s_2)ds_2 \\
&\quad - \int_0^1 g_\delta(x-s_1,y-0)\frac{\partial q}{\partial y}(s_1,0)ds_1 \\
&\quad + \int_0^1 g_\delta(x-s_1,y-1)\frac{\partial q}{\partial y}(s_1,1)ds_1
\end{aligned} \tag{6.28}$$

Note that each of the four line integrals in (6.28) is a function of x and y . The partial derivatives of q are approximated using a second-order 3-point forward (and backward) difference approximation

$$\begin{aligned}
F'(x) &= \frac{-F(x+2h)+4F(x+h)-3F(x)}{2h} + \mathcal{O}(h^2) \\
F'(x) &= \frac{3F(x)-4F(x-h)+F(x-2h)}{2h} + \mathcal{O}(h^2)
\end{aligned} \tag{6.29}$$

Unlike the original one-dimensional analysis, where the derivatives are approximated using the standard 2-point difference approximation of first-order $\mathcal{O}(h)$, the 3-point difference formula gives a much more accurate result. The 3-point difference approximation requires knowing values of unfiltered q on the boundary (first point) and inside the domain (the other two points). While q on the boundary is obtained from given Dirichlet boundary conditions (6.9), the values of q inside the domain are not known a priori. An approximate deconvolution formula is used to recover unfiltered q from \bar{q} , hence

$$q^{n+1}(x,y) \approx \bar{q}^n(x,y) - \frac{\delta^2}{24} \Delta \bar{q}^n(x,y) + \mathcal{O}(\delta^4) \tag{6.30}$$

The Laplacian in (6.30) is approximated using the 2nd-order FD approximation on a quincunx, commonly referred to as two-dimensional five-point stencil

$$\Delta F(x,y) = \frac{F(x-h,y) + F(x+h,y) + F(x,y-h) + F(x,y+h) - 4F(x,y)}{h^2} + \mathcal{O}(h^2) \quad (6.31)$$

To check the accuracy of the approximate deconvolution formula (6.30), the exact solution (6.11) is compared with an approximation of q recovered from \bar{q} using (6.30) and (6.31). For this comparison an approximation of \bar{q} is computed in Test 1b. As a reminder, in Test 1b the boundary conditions and the BCE term are evaluated exactly. The error mode should then be primarily associated with the error incurred from using the AD formula (6.30). The infinity norm of the pointwise absolute error is plotted in Figure B.11 and is defined as

$$e = \left| \frac{q_{exact} - q_{appr.deconv.}}{q_{exact}} 100\% \right|_{\infty} \quad (6.32)$$

As can be seen, the AD formula gives sufficiently accurate approximation of non-filtered q .

We proceed with establishment of an approximation to the BCE integral. The line integrals in (6.28) are numerically integrated using Newton-Cotes quadrature rules. These rules are based on the evaluation of the integrand at equally spaced points and are therefore a natural choice for uniform Cartesian mesh. Although the Newton-Cotes formulae can be constructed for any degree n , for large n these rules can sometimes suffer from catastrophic *Runge's phenomenon* (Runge, 1901) where the error grows exponentially. To avoid this problem the interval of integration $[0,1]$ is broken down into smaller subintervals so that a lower degree rule can be used on each of these segments. This technique is called a composite rule. A five-point Newton-Cotes formula of closed type, or the Boole's rule is used (Boole and Moulton, 1960). This requires breaking the original interval of 21 nodes into five subintervals of length 0.2 (5 points per interval) and then adding the results. The same technique is used to evaluate all four line integrals in (6.28).

Boole's rule :

$$\int_a^b F(x)dx = \frac{b-a}{90} [7F(x_0) + 32F(x_1) + 12F(x_2) + 32F(x_3) + 7F(x_4)] - \frac{(b-a)^7}{1935360} F^{(6)}(\zeta) \quad (6.33)$$

where $x_i = a + \frac{i(b-a)}{n}$, and ζ is between a and b .

In Test 3 the exact BCE integral is replaced by its approximation as described above, while the boundary conditions are kept exact. Figure B.12 illustrates the resulting error in approximating \bar{q} at the final time $T=0.05$. The result shows that the error is almost identical to that of Test 1b. A slight variation is noticeable near the boundaries where the BCE term has the greatest effect. This indicates the appropriateness of the BCE term approximation technique and advances the analysis to the final test where the exact boundary conditions are replaced by an approximation.

In Test 4 the approximate boundary conditions for space filtered \bar{q} are constructed using a similar approach to that presented in Borggaard and Iliescu (2006). However, the implementation presented herein has two major improvements over the original ADBC approach. The details of this implementation are presented in section 3.4.

In this test problem the calculation of \bar{q} at $y=0$ is performed using a square domain of integration as shown in Figure B.5. Considering that $\delta=0.2$ and $\Delta h=0.05$ this square is composed of $9 \times 9 = 81$ nodes. In order to evaluate the convolution integral (3.14) and to take advantage of the composite rule of numerical integration, this square is broken down into four subsquares ($5 \times 5 = 25$ nodes each). The double integral is then numerically evaluated in each quarter using the Boole's rule applied in both x and y directions.

The boundaries with homogeneous Dirichlet BCs are treated differently. Since no buffer layer is included, the shaded area in Figure B.5 is reduced to a rectangle that lies solely inside Ω . Again, in our

test case this rectangle is made up of $9 \times 5 = 45$ nodes. This time the rectangle is broken down into two (not four) identical squares ($5 \times 5 = 25$ nodes each) and the numerical integration proceeds as before.

Finally, the boundary nodes (x_b, y_b) that are less than δ away from corners require special attention.

The domain of integration becomes smaller near the corners. This fact poses no problem for this integration technique. Since the composite rule used to evaluate the convolution integral (3.14) combines regions of different sizes, 4-, 3-, and 2-point Newton-Cotes formulae are easily employed to perform the integration, hence

Trapezoid rule:

$$\int_a^b F(x) dx = \frac{b-a}{2} [F(x_0) + F(x_1)] - \frac{(b-a)^3}{12} F^{(2)}(\xi)$$

Simpson's rule:

$$\int_a^b F(x) dx = \frac{b-a}{6} [F(x_0) + 4F(x_1) + F(x_2)] - \frac{(b-a)^5}{2880} F^{(4)}(\xi) \quad (6.34)$$

Simpson's 3/8 rule:

$$\int_a^b F(x) dx = \frac{b-a}{8} [F(x_0) + 3F(x_1) + 3F(x_2) + F(x_3)] - \frac{(b-a)^5}{6480} F^{(4)}(\xi)$$

where $x_i = a + \frac{i(b-a)}{n}$, and ξ is between a and b .

The approximate boundary conditions along with an approximate BCE term are implemented and the resulting error in approximating \bar{q} at the final time $T = 0.05$ is shown in Figure B.13. The error at the boundary nodes is not zero. However, the error in approximating the boundary conditions is rather small and does not degrade the overall solution accuracy. This verifies the overall appropriateness of the ADBC approach and gives encouragement to continue to DP.

6.1.3 ASYMPTOTIC CONVERGENCE, ERROR QUANTIFICATION

The *energy norm* is an integral measure intrinsic to boundary value problems like the heat conduction PDE system studied herein. The energy norm definition for (6.7)-(6.10) is

$$\|q\|_E \equiv \frac{1}{2} \left(\int_{\Omega} \kappa \nabla q \nabla q d\tau \right) \quad (6.35)$$

where κ denotes the thermal conductivity.

Weak form theory, c.f., Baker (2012) enables *a posteriori* estimation of approximation error via a regular mesh refinement process generating the solution sequence.

$$\|q^{\Delta h}\|_E + \|e^{\Delta h}\|_E = \|q\|_E = \|q^{\Delta h/2}\|_E + \|e^{\Delta h/2}\|_E = \dots \quad (6.36)$$

where $e^{\Delta h}$ and $e^{\Delta h/2}$ represent the discrete approximation error fields for mesh levels $\Omega^{\Delta h}$ and $\Omega^{\Delta h/2}$ respectively.

The weak form intrinsic *asymptotic error estimate* for (6.7)-(6.10) is

$$\|e^{\Delta h}\|_E \leq C l_e^{2k} \max |\nabla^{k+1} q| \quad (6.37)$$

for C a constant and $\max |\nabla^{k+1} q|$ the extremum $(k+1)^{st}$ derivative of the exact solution q .

For FE basis completeness degree k , this Taylor series-analogous multiplier quantifies how *smooth* the solution to (6.7)-(6.10) must be for the k -dependent weak form algorithm error estimate (6.37) to be valid.

This apparent limitation to the theory, i.e., exact solution q extremum derivative, is eliminated by bound replacement with the *data* driving the problem statement (Baker, 2012). Everything provided

beforehand in the problem statement, e.g., boundary conditions, filter measure, domain span, conductivity constitutes data. The refinement of (6.37) is

$$\|e^{\Delta h}\|_E \leq C l_e^{2\gamma} \|data\|_{L^2}^2, \gamma \equiv \min(k+1-m, r-m) \quad (6.38)$$

with additional parameters m , the integer order (1 or 2) of the underlying variational principle, and r , the measure of solution differentiability domination by *non-smooth data*. Of importance replacing the TS derivative with the *data* L2 norm generates a quantitative measure of error “size.”

Using equalities in (6.38) for $\|e^{\Delta h}\|_E$ and $\|e^{\Delta h/2}\|_E$ while clearing C , noting $m=1$ for (6.7), assuming smooth data and that $\|data\|_{L^2}^2$ is mesh insensitive

$$\|e^{\Delta h}\|_E = 2^{2k} \|e^{\Delta h/2}\|_E \quad (6.39)$$

Substituting (6.39) into (6.36) leads to

$$\Delta \|q^{\Delta h/2}\|_E \equiv \|q^{\Delta h/2}\|_E - \|q^{\Delta h}\|_E = (2^{2k} - 1) \|e^{\Delta h/2}\|_E \quad (6.40)$$

The resultant error estimate for the finer mesh solution of regular mesh refinement is

$$\|e^{\Delta h/2}\|_E = \frac{\Delta \|q^{\Delta h/2}\|_E}{2^{2k} - 1} \quad (6.41)$$

Solution adherence to asymptotic error estimate (6.38) for the finer mesh solution is verifiable via the slope calculation

$$slope = \frac{\log \|e^{\Delta h}\|_E / \log \|e^{\Delta h/2}\|_E}{\log 2} \quad (6.42)$$

Table A.1 summarizes *a posteriori* data generated from a uniform mesh refinement convergence study. All tables used in this manuscript are placed in Appendix A. Asymptotic convergence is clearly confirmed and monotone, however it is predicted suboptimal at approximately linear. The likely cause for suboptimal convergence is the filter measure $\delta=0.5$ being reduced by a factor of two for each successive mesh refinement, which likely alters $\|data\|_{L^2}^2$ in (6.38) which thus does not cancel out in the process leading to (6.41).

6.1.4 SUMMARY AND CONCLUSIONS

The original one dimensional ADBC approach of Borggaard and Iliescu (2006) is tested using a one-dimensional heat conduction problem. After repeating the 1D analysis and getting almost identical results numerical validation of ADBC for a two-dimensional heat conduction problem is sought. The linear problem is chosen to separate the boundary condition considerations from the closure problem associated with non-linear equations such as the Navier-Stokes PDE system. The AD approach is utilized to approximate the unknown boundary conditions for filtered variables, as well as to approximate the boundary commutation error term. The finite element analysis is performed using piecewise linear basis functions. The significance of the BCE term is demonstrated by simply removing it from the formulation and measuring the resulting error. The analysis suggests that no accurate solution can be established if the BCE term is not included in the formulation. This result is in perfect agreement with the numerical analysis of Borggaard and Iliescu (2006). The significance of the BCE term is also shown in John (2004) by measuring the convergence rate of the weak form BCE as δ tends to zero. It is shown therein that the rate of convergence is almost of order one if the test function is sufficiently smooth. An accurate approximation of the BCE integral is also offered using standard Newton-Cotes quadrature rules. The implementation is straight forward and efficient, however, other methods of numerical integration can be used, if necessary. The approximate boundary conditions for space filtered \bar{q} are constructed using a

similar approach to that presented in Borggaard and Iliescu (2006). A modification to the original ADBC approach is proposed in case of non-homogeneous Dirichlet BCs. In conclusion, the 2D analysis presented herein extends and generalizes the original 1D study of (Borggaard and Iliescu, 2006) while providing encouraging results for further analysis of more realistic turbulent flows.

6.2 TWO-DIMENSIONAL CHANNEL FLOW

The second computational experiment is for two-dimensional fully-developed channel flow with time averaged turbulent boundary layer profile. The fundamental difference of the solution to this problem, as compared to the heat conduction problem, is that the typical turbulent boundary layer profile looks nothing like a sine function. Thorough understanding is required as to what filter measure and mesh resolution would be reasonable to use. With this in mind the experiment's objectives are

- Perform validation of the ADBC formulation on a typical turbulent BL profile
- Provide insight into the process of choosing the suitable filter measure
- Establish the appropriate meshing technique, especially near the boundaries

6.2.1 TIME-AVERAGED BOUNDARY LAYER PROFILE

The reference turbulent boundary layer profile is obtained from the "PIPE" program as part of the companion software supplied in Turbulence Modeling for CFD by Wilcox (2006). The program allows choosing between twelve different turbulence models and provides freedom in placing the first node of the wall. The boundary layer profile used in this dissertation is generated via $k-\omega$ two-equation turbulence model with Reynolds number based on the friction velocity, u_τ , and channel's half-width, H , set to

$$Re^+ = \frac{u_\tau H}{\nu} = 180 \quad (6.43)$$

The number of nodes used is 201 and the first node off the wall is placed at

$$y^+ = 0.1 \quad (6.44)$$

The velocity profile is determined by solving the following two-point boundary value problem

$$\frac{du^+}{dy^+} = \frac{1 - y^+ / H^+}{1 + \mu_\tau^+} \quad (6.45)$$

where $H^+ = u_\tau H / \nu$ and $\mu_\tau^+ = \mu_\tau / \mu$ are dimensionless half-width and dynamic viscosity, respectively.

The standard similarity coordinates for dimensionless velocity and normal distance are defined as

$$u^+ \equiv \frac{u}{u_\tau} \quad \text{and} \quad y^+ \equiv \frac{u_\tau y}{\nu} \quad (6.46)$$

where the *friction velocity* is defined as $u_\tau = \sqrt{\tau_w / \rho}$.

Figure B.14 illustrates a comparison between the computed solution and the DNS data of Mansour et al. (1988). The results show very good agreement in the velocity as well as shear stress distributions. The computed solution can therefore be regarded as experimental or reference solution for the purposes of this dissertation.

The established profiles are converted from the similarity space to physical space by specifying the following properties

$$\begin{aligned} H &= 0.01 \text{ [m]} \\ \nu &= 1.004 \times 10^{-6} \text{ [m}^2\text{/s]} \\ \rho &= 998.01 \text{ [kg/m}^3\text{]} \end{aligned} \quad (6.47)$$

where H is the channel's half-width, ν is the kinematic viscosity and ρ is the density.

A comparison between the similarity space and physical space representation is shown in Figure B.15 for three Reynolds numbers. Notice how all three solutions fall on the same curve in the similarity space coordinate system.

The physical space Reynolds number based on the averaged velocity and channel's width becomes

$$Re_H = \frac{u_{ave} \cdot (2H)}{\nu} = 5430 \quad (6.48)$$

where the averaged velocity is calculated as

$$u_{ave} = \frac{1}{2H} \int_0^{2H} u dy = \frac{1}{H} \int_0^H u dy \quad (6.49)$$

For fully developed channel flow time-averaged incompressible Navier-Stokes equations reduce to

$$\mathcal{L}(\hat{u}) = \frac{1}{\rho} \frac{\partial \hat{p}}{\partial x} - \frac{\partial}{\partial y} (\hat{\tau}_{lam} + \hat{\tau}_{trb}) = 0 \quad (6.50)$$

where the turbulent and laminar shear stresses (per density) are defined as

$$\begin{aligned} \hat{\tau}_{lam} &= \nu \frac{\partial \hat{u}}{\partial y} \\ \hat{\tau}_{trb} &= -u'v' \end{aligned} \quad (6.51)$$

The hat symbol designates time-averaging.

Since $\partial \hat{p} / \partial x$ is constant and therefore independent of y equation (6.50) can be integrated with respect to y , yielding

$$\hat{\tau}_{lam} + \hat{\tau}_{trb} = \left(\frac{1}{\rho} \frac{\partial \hat{p}}{\partial x} \right) y + C_{int} \quad (6.52)$$

The constant of integration is determined using the fact that $\hat{\tau}_{lam} + \hat{\tau}_{trb} = 0$ at $y = H$, hence

$$C_{\text{int}} = -H \left(\frac{1}{\rho} \frac{\partial \hat{p}}{\partial x} \right) \quad (6.53)$$

As a result, the sum of the shear stresses is determined to be a linear function of y , i.e.,

$$\hat{\tau}_{\text{lam}} + \hat{\tau}_{\text{trb}} = \left(\frac{1}{\rho} \frac{\partial \hat{p}}{\partial x} \right) (y - H) \quad (6.54)$$

where the constant slope is determined by

$$\left(\frac{1}{\rho} \frac{\partial \hat{p}}{\partial x} \right) = -3.264 \times 10^{-2} \quad (6.55)$$

Both laminar and turbulent shear stress profiles as well as their sum are plotted in Figure B.16. Note that $\hat{\tau}_{\text{lam}} + \hat{\tau}_{\text{trb}}$ is indeed a linear function of y as derived in (6.54) with a slope identified in (6.55).

Using the reference profiles for \hat{u} , $\hat{\tau}_{\text{trb}}$ and $\partial \hat{p} / \partial x$ in physical space a two-dimensional channel flow benchmark is set up in PICMSS environment. Predetermined Reynolds stress and pressure gradient distributions are imposed throughout the channel for all time steps with an idea to drive the problem to a steady-state solution \hat{u} also known a priori. The velocity field is initialized as zero. The pressure distribution is linear as determined from (6.55). The Reynolds stress distribution $\hat{\tau}_{\text{trb}}(y)$ is imposed for all x . The time-averaged Navier-Stokes equations solved in this problem reduce to

$$\begin{aligned} \mathcal{L}(\hat{u}) &= \frac{\partial \hat{u}}{\partial t} + \frac{1}{\rho} \frac{\partial \hat{p}}{\partial x} - \frac{\partial}{\partial y} \left(\nu \frac{\partial \hat{u}}{\partial y} - u'v' \right) = 0 \\ \mathcal{L}(\hat{v}) &= \frac{1}{\rho} \frac{\partial \hat{p}}{\partial y} = 0 \end{aligned} \quad (6.56)$$

with the second equation being trivial.

The solution to (6.56) as well as all of the channel flow solutions described in this dissertation are obtained using the backward Euler implicit scheme. The computational mesh is always 2-element long and only the number of elements across the channel is mentioned. For this benchmark the mesh is 150-element wide. The Reynolds stress distribution $\hat{\tau}_{trb}(y)$ originally obtained with 201 nodes to the mid-channel is interpolated to a new mesh of 75 nodes. Since the solution is axisymmetrical the 75-node profile is mirrored onto the other half of a 151-node profile. The channel flow benchmark is intentionally constructed for a full-width channel so that problems with space filtering across the line of symmetry can be avoided in further analysis.

After just a few time steps a fully developed turbulent velocity profile is established. The comparison between the computed and reference velocity profiles is shown in Figure B.17. The perfect agreement verifies the correctness of implementation and advances the analysis to the next step where the space filtered equations are solved.

6.2.2 SPACE FILTERED BOUNDARY LAYER PROFILE

Space filtered incompressible Navier-Stokes equations for fully developed channel flow simplify to

$$\begin{aligned}\mathcal{L}(\bar{u}) &= \frac{\partial \bar{u}}{\partial t} + \frac{1}{\rho} \frac{\partial \bar{p}}{\partial x} - \frac{\partial}{\partial y} \left(\nu \frac{\partial \bar{u}}{\partial y} + \bar{\tau}_{trb} \right) - A_\delta = 0 \\ \mathcal{L}(\bar{v}) &= \frac{1}{\rho} \frac{\partial \bar{p}}{\partial y} = 0\end{aligned}\tag{6.57}$$

where $A_\delta = \int_{\tilde{\Omega}} g(\mathbf{x}-\mathbf{s}) \left[\nu \frac{\partial u}{\partial y} \cdot \mathbf{n} - p \cdot \mathbf{n} \right] dS(\mathbf{s})$ is the BCE integral and $\bar{\tau}_{trb} = -\overline{u'v'}$ is the SFS tensor.

The goal here is the same as before, i.e., using predetermined solutions for shear stress and pressure gradient drive the problem to a steady-state solution. However, in equations (6.57) the BCE integral must also be included and non-homogeneous Dirichlet BCs must be prescribed. The computed steady-

state solution is then compared to the reference velocity solution. The five necessary components just described, namely space filtered velocity, Reynolds stress, pressure gradient, BCE integral and the boundary conditions are determined analytically via space filtering of time-averaged profiles obtained in the previous section. The analytical evaluations are performed using Wolfram Mathematica® software (Wolfram Research Inc, 2008). The computed solution is denoted as \bar{u} , while the reference solution obtained by space filtering the time-averaged profile is denoted as $\bar{\hat{u}}$. Filtered and non-filtered velocity, Reynolds stress and pressure gradient profiles are illustrated in Figure B.18, Figure B.19 and Figure B.20, respectively. In all three figures space filtering operation causes significant errors to occur near the boundaries. The boundary commutation error integral provides means to account for these errors. Realizing that $\frac{\partial u}{\partial y}$ is independent of x and assuming that pressure is zero at the boundary the BCE

integral simplifies to just two terms evaluated at the boundary nodes, hence

$$A_{\delta} = \nu g_{\delta} (y-0) \left. \frac{\partial \hat{u}}{\partial y} \right|_{y=0} - \nu g_{\delta} (y-0.02) \left. \frac{\partial \hat{u}}{\partial y} \right|_{y=0.02} \quad (6.58)$$

where the $\left. \frac{\partial \hat{u}}{\partial y} \right|_{y=0} = 325.115$ and $\left. \frac{\partial \hat{u}}{\partial y} \right|_{y=0.02} = -325.115$ are easily established analytical quantities.

Note that the BCE integral is a function of filter measure δ as illustrated in Figure B.21.

The importance of the BCE integral is illustrated in Figure B.22. Using analytically determined BCs and the BCE integral a steady state solution is obtained for different filter measures. Each test is performed twice, with and without the BCE term. The computed solutions are then compared to the reference velocity profile. As can be seen from Figure B.22 for all filter measures, the BCE term plays an extremely important role in obtaining an accurate solution.

6.2.3 DIAGNOSTICS OF SPACE-FILTERING

Moving away from the manual environments used in the previous two sections, the rest of section 6.2 is devoted to the question of identifying a suitable filter measure and appropriate meshing technique.

First of all, it is necessary to understand how the filter measure δ affects the original time-averaged velocity profile (\hat{u}) when the convolution operation is performed. With the time-averaged velocity profile at hand a mesh of 1,001 nodes (501 nodes to the mid-channel) with progression ratio of 1.00438 is constructed placing the first node off the wall at $y^+ = 0.1$. Using the definition of convolution the space-filtered velocity (\bar{u}) is obtained by performing numerical integration of the time-averaged velocity distribution, hence

$$\bar{u}(y) \equiv (g_\delta * u)(y) = \int_{\Omega} g_\delta(y - \xi) u(\xi) d\xi \quad (6.59)$$

Six filter measures are selected to perform the analysis, namely $\delta^+ = 36; 18; 9; 4.5; 2.25; 1.125$. The resulting space-filtered velocity profiles (\bar{u}) are compared with the time-averaged velocity distribution (\hat{u}). Figure B.23 illustrates the first four profiles of \bar{u}^+ and compares them with the original time-averaged \hat{u}^+ . As can be clearly seen depending on the filter measure δ space-filtered \bar{u}^+ attains different non-zero values at the solid wall. The wall slopes of \bar{u} are calculated using a third-order forward FD formula at nodes 1 through 4 and are summarized in Table A.2. The values of \bar{u} at the wall presented in Table A.2 and the overall behavior of \bar{u} shown in Figure B.23 lead to an expected conclusion about the action of space-filtering operation, i.e. the smaller the filter measure, the better \bar{u} approximates \hat{u} . As can be seen from Table A.2 the value of $d\bar{u}/dy$ has approached a constant value of approximately 162. This behavior is caused by the fact that for all $\delta^+ < 5$ the filter is operating in the *viscous sublayer* where the velocity is linear.

Before the boundary commutation error integral (6.58) can be evaluated the unfiltered velocity field has to be computed first. Indeed, to evaluate the derivatives in (6.58) the unfiltered velocity (u) is computed from the analytically determined \bar{u} using the approximate deconvolution (AD) formula written in a homogeneous form as

$$\mathcal{D}(u_{AD}(y)) = u_{AD}(y) - \bar{u}(y) + \frac{\delta^2}{24} \Delta \bar{u}(y) = 0 \quad (6.60)$$

In what follows u and u_{AD} are used interchangeably. In order to compute, or recover u_{AD} from \bar{u} the linear differential equation (6.60) is implemented in the weak form as a differential definition as described in section 5.4. The application of the Green-Gauss theorem to the Laplacian term in (6.60) generates an efflux boundary integral (last term in (5.50)) that is not known a priori.

Using the same mesh of 1,001 nodes the unfiltered velocity (u_{AD}) is computed for each of the space-filtered velocity profiles shown in Figure B.23. The boundary integral in (5.50) is evaluated using analytical values of $d\bar{u}/dy$ presented in Table A.2. The resulting unfiltered velocity profiles (u_{AD}) are compared with the time-averaged velocity distribution (\hat{u}). Figure B.24 illustrates the first four profiles of u_{AD}^+ and compares them with the original time-averaged \hat{u}^+ .

The unfiltered velocity profiles, shown in Figure B.24, have very good agreement with the original time-averaged velocity profile except for the near wall region. Figure B.24b allows for a closer examination of the computed profiles near the wall. *The size of the error region can be approximately correlated with filter measure.* For all of the profiles the error region ends at approximately one-fourth of the filter measure, i.e. $y^+ < 0.25\delta^+$.

Figure B.24 also shows that similarly to the space-filtered \bar{u}^+ the unfiltered u_{AD}^+ has a non-zero slope at the wall. The wall values and the slopes of u are summarized in Table A.3. The wall slopes are calculated using third order forward FD formula at nodes 1 through 4.

6.2.4 SOLUTION ADAPTIVE MESH REFINEMENT

Gaining enough understanding of filtering effects the non-practical mesh of 1,001 nodes is replaced by a set of more reasonable ones. Defining the filter measure as $\delta = 2h$, where h is the element length, the six previously used values of δ correspond to six levels of uniform mesh refinement study, namely 11, 21, 41, 81, 161 and 321 nodes to the mid-channel. Indeed, the channel's half-width is defined as

$H^+ = 180$ (or $H = 0.01$). The element size is calculated as $h^+ = \frac{H^+}{nnodes-1}$ (or $h = \frac{H}{nnodes-1}$). If

$nnodes = 11$ then $h^+ = \frac{180}{11-1} = 18$ (or $h = \frac{0.01}{11-1} = 0.001$) and the filter measure is $\delta^+ = 2h^+ = 36$ (or

$\delta = 2h = 0.002$). Similarly, the other five filter measures of $\delta^+ = 18, 9, 4.5, 2.25$ and 1.125 correspond to the meshes of 21, 41, 81, 161 and 321 nodes, respectively.

The same analysis, as the one performed for the dense mesh of 1,001 nodes, is repeated for uniform meshes. An analytical profile of \bar{u} is first determined via numerical integration of the time-averaged data. The wall slopes are then calculated using third order forward FD formula at nodes 1 through 4. The results of the mesh refinement study are compared with the results obtained from a dense mesh of 1,001 nodes and summarized in Table A.4. Since all six profiles are determined analytically the nodal values of $\bar{u}(1)$ for all meshes including 1,001-node mesh are identical, these are the boundary conditions. The calculation of slopes $d\bar{u}/dy$, however, depends greatly on the mesh resolution. As can be seen from Table A.4 none of the six cases gave an adequate prediction of slope $d\bar{u}/dy$, which was obtained using 1,001-node mesh.

There are two *independent* factors that play an important role in predicting the slope accurately, i.e., the filter measure and the mesh resolution. By defining the filter measure as $\delta = 2h$ these two factors are kept dependent upon each other. The results of Table A.4 suggest that a uniform mesh refinement study needs to be performed for each of the chosen filter measures, while keeping it at a *constant* value. Note, however, that not all of the mesh levels can be used with any one of the chosen filter measures. In order to resolve the spectral content of a turbulent flow the filter measure must satisfy the condition

$$\delta \geq 2h \quad (6.61)$$

As can be seen from Table A.5 through Table A.9 for a uniform mesh the slope $d\bar{u}/dy$ can only be predicted accurately if the filter measure satisfies the following condition

$$\delta \geq 4h \quad (6.62)$$

If the mesh is not uniform the data suggests that placing the first node off the wall at $y \leq 0.25\delta$ will ensure an accurate prediction of $d\bar{u}/dy$. However, it is also observed that the region of $y \leq 0.25\delta$ corresponds to the region where u_{AD} does not agree with \hat{u} . Therefore placing the first node off the wall at exactly $y = 0.25\delta$ will allow accurate calculation of du_{AD}/dy as well. Of course, the first parasitic node $u_{AD}(1) \neq 0$ has to be excluded from the calculation of slope du_{AD}/dy . The calculation of du_{AD}/dy using second order forward FD formula at nodes 2 through 4 have also been included into the mesh refinement process presented in Table A.5 through Table A.9. The results indicate that for those cases where $\delta < 4h$ (in other words the first node off the wall is placed at $y < 0.25\delta$) the accuracy of predicting analytical slope $\frac{du_{AD}}{dy} = \frac{d\hat{u}}{dy} = 325.20$ drops. This is because the first node is placed inside the error region where u_{AD} does not agree with \hat{u} , shown in Figure B.24. On the other hand, if $\delta > 4h$, or simply $\delta = 2h$ (in other words the first node off the wall is placed at $y > 0.25\delta$) then the accuracy of

predicting the analytical slope also drops. This is not only because the mesh resolution becomes more coarse, but also because the 2nd, 3rd and 4th nodes are placed further away from the linear viscous sublayer where the slope $\frac{d\hat{u}}{dy} = 325.20$ is constant.

6.2.5 OPTIMAL MESH CONSTRUCTION AND FINAL TESTS

The optimal mesh construction consists in placing several auxiliary nodes in region $0 \leq y \leq \delta/4$ followed by a non-uniform mesh resolution with element sizes ranging from $\delta/4$ to $\delta/2$. Placement of the auxiliary nodes in a near-wall region allows for an accurate prediction of $d\bar{u}/dy$ with a third order forward FD approximation. The actual mesh construction for $0 \leq y \leq H$, where H is channel's half-width, is illustrated in Figure B.25 with three hollow nodes denoting the auxiliary nodes. Nodes 1, 2, 3 and 4 are used to calculate $d\bar{u}/dy$. Once this slope is computed it is then used in the Galerkin weak statement for the differential statement (6.60) to recover u_{AD} from \bar{u} . The slope of du_{AD}/dy necessary for evaluation of BCE is computed using nodes that lie in region $y \geq \delta/4$, i.e. nodes 5, 6 and 7.

The set of three final tests is performed with filter measure $\delta^+ = 16$ and a uniform mesh of 37 nodes across channel's half-width constructed in the manner shown in Figure B.25. The velocity is initialized by constant value $\bar{u} = 0.3$. In Test 1 the exact boundary conditions and exact BCE integral are used to establish the benchmark. The velocity time evolution is shown in Figure B.26. In Test 2 the BCs and the BCE integral are computed using approximate deconvolution. In Test 3 the BCE integral is removed to illustrate its importance. Figure B.27 shows the computed solutions for all three tests. The absence of the BCE integral clearly produces the erroneous result. A perfect agreement in velocity profiles between Test 1 and Test 2 validates the optimal mesh construction technique illustrated Figure B.25 as well as overall fidelity of the AD approach. The error distribution defined as the difference between the computed steady-state solution and the exact reference solution for Test 1 and Test 2 is shown in Figure

B.28. The error of Test 2 with approximations of BC and BCE is only slightly higher than that of Test 1 where the exact values are used.

6.3 THREE-DIMENSIONAL FLOW OVER A FLAT PLATE

The third computational experiment is conducted for three-dimensional external laminar flow over a flat plate. The *arLES* theory closure is absent the word *turbulent*. It is based on rigorous mathematical operations defined for/by NS PDE system convolution and is Reynolds number *unconstrained*. The theory is potentially pertinent to prediction of laminar, transitional and/or fully turbulent resolved scale velocity vector distributions. A successful solution to the laminar flat plate problem is pertinent to validating Reynolds unconstrained applicability of the essentially analytical rational LES closure theory for bounded domain flows. The benchmark considered herein also helps to set the stage for implementing a more complicated three-dimensional and thermal analysis described in section 0.

6.3.1 ESTABLISHING A BENCHMARK PROBLEM

Three-dimensional laminar flow over a flat plate is described by incompressible Navier-Stokes equations (2.1)-(2.2) absent the buoyancy body force term. The NS equations are solved in dimensional form with Reynolds number based on the plate's length. The coordinate system is arranged such that the fluid flows in the x-direction with a boundary layer developing in the y-direction, as illustrated in Figure B.29. A symmetry plane is imposed at $z=0$ to initialize the third component of the velocity.

The computational mesh is Cartesian with 101, 51 and 21 nodes in the x-, y- and z- direction, respectively. The flat plate is along the lower boundary of the domain ($y=0$) starting at $x=0$ m and is of length 0.1 m (0.3281 ft). The flow is initialized with a free-stream velocity of 1 m/s (3.2808 ft/s).

The domain extends a distance upstream of the plate's leading edge with a no-through-flow boundary condition simulating a free-stream approaching the plate. The domain also extends downstream of the

plate's trailing edge where similar no-through-flow boundary conditions apply. The detailed summary of the boundary conditions for u , v , w and ϕ are summarized in Figure B.30.

Axial stretching of the mesh is used to aid in resolving the region near the start and end of the plate, where the no-slip Navier-Stokes boundary condition begins at $x=0$ m and ends at $x=0.1$ m, as shown in Figure B.29. As usual for viscous flows, the mesh spacing at the wall is important, and an appropriate level of fineness is required to capture the viscous boundary layer.

Numerical solutions of the full NS equations are compared to the solution of the ordinary differential equation of Blasius (1908). H. Blasius found a celebrated solution for flat-plate flow based on boundary layer approximations, hence the solution is accurate for $Re_l \geq 1000$ (White, 2006). Three Reynolds numbers based on the plate's length are considered herein, i.e., $Re_l = 1E3$, $1E4$ and $1E5$. Computed velocity profiles obtained at the trailing edge of the plate in the symmetry plane ($x=0.1$, $z=0$) are compared against Blasius similarity solution. For $Re_l = 1E3$ the profiles vary slightly near the wall and close to the free stream, see Figure B.32. This result is expected since the boundary layer approximation is not fully applicable yet sufficiently accurate. Figure B.33 illustrates a much better agreement between computed and similarity solutions for $Re_l = 1E4$. Finally, Figure B.34 completes verification of the flat-plate benchmark exhibiting excellent agreement between computed and Blasius solutions.

Of particular interest are the second and third velocity component distributions since the full NS equations are solved. Figure B.35 through Figure B.37 illustrate distribution of v at the symmetry plane, $z=0$, for three selected Reynolds numbers. Figure B.38 through Figure B.40 illustrate distribution of w at the plane opposite to the symmetry plane, $z=0.05$, for all three Reynolds numbers. As expected the normal velocity v is not zero at the edge of the boundary layer. There must be a slight upwelling of flow because of the displacement of the outer stream (Panton, 1995). Qualitative similarity of v and w

velocity distributions, well-illustrated for $Re_L = 1E3$, confirms the action of continuity constraint as mass preserving.

6.3.2 DISPERSION ERROR CONTROL FOR $Re=1E5$

As Reynolds number increases the adverse effect caused by the leading edge BC singularity becomes more and more prominent. Figure B.41 illustrates this effect for $Re_L = 1E5$ where unphysical fluctuations in u (bottom plane, $y=0$) are caused by the well-known " $2\Delta x$ " dispersion error. While the maximum possible value of u is 1 m/s (free stream velocity), the legend of Figure B.41 indicates an unrealistic peak velocity of 1.4 m/s caused by these fluctuations. This problem is solved by adding additional terms to the conservation principle PDEs as dictated by Kolesnikov's theory (Kolesnikov, 2000). Besides the higher order accuracy, namely $\mathcal{O}(h^4)$, new differential terms provide just enough artificial diffusion to prevent huge velocity gradients at the leading edge BC singularity. The resulting solution is smooth and monotonic as shown in Figure B.42. Notice also that the flow upstream of the leading edge is still able to "sense" the BC singularity caused by the leading edge, however no dispersion error is present.

6.3.3 AD FORMULATION VERIFICATION

Consider a laminar boundary layer flow past a flat plate with $Re_L = 1E6$. This problem identifies the main benchmark test considered herein. The computational grid is of $101 \times 69 \times 21$ nodes in the x -, y - and z -direction, respectively. The size of the domain $\Omega = \{-0.02 \leq x \leq 1.12; 0.0 \leq y \leq 0.001; 0.0 \leq z \leq 0.5\}$.

As before, the flat plate is along the lower boundary of Ω ($y=0$) starting at $x=0$ m and is of length 0.1 m.

While Kolesnikov's additional terms resolve BC singularity very well it is important to verify that the computed solution still agrees with Blasius similarity profile. The comparison between computed (with Kolesnikov theory) and Blasius solutions is illustrated in Figure B.43. The agreement is very good with an

average absolute error not exceeding 4%. The *arLES* terms are then added to the established INS formulation and the result is added to Figure B.43. Since C11 term from *arLES* formulation is significantly aggravated by the plate's leading edge BC singularity it is not included in the computation. Again the agreement between computed *arLES* and analytical Blasius solutions is excellent with an average absolute error not exceeding 3%.

Following the ideas of mesh construction and ADBC implementation outlined in section 6.2 the AD boundary conditions and the BCE integral are added to complete the flat-plate problem formulation. The filter measure used is $\delta^+ = 8$. The results of ADBC formulation implementation are illustrated in Figure B.44. First, the AD boundary conditions are added replacing the no-slip BCs for all three velocity components. The first profile in Figure B.44 (solid line) is a reference solution for which no-slip boundary conditions are used. This profile is exactly the same as the one shown in Figure B.43 (dashed line), which agrees with analytical Blasius solution extremely well. Again, for this reference solution only Kolesnikov's terms are implemented and no *arLES* terms are added yet. The second profile in Figure B.44 (dashed line) represents the solution where no-slip BCs are replaced with AD BCs. In the absence of BCE integral the usage of non-homogeneous Dirichlet boundary conditions results in significant deviation of the computed solution from the reference one. The result of adding the BCE term to the formulation is the third profile in Figure B.44 (dash-and-dot line). The computed solution agrees very well with the reference one except for a short region near the wall, i.e., $y^+ < 0.25\delta^+ = 2$. As described earlier for a channel flow problem this is the region where AD formula fails to provide adequate result while recovering u from \bar{u} . The fourth profile in Figure B.44 (dotted line) represents the result with *arLES* terms added to the formulation, which is virtually identical to the previous one. This validates Reynolds number unconstrained applicability of the essentially analytical rational LES closure theory.

6.4 THREE-DIMENSIONAL BUOYANCY-DRIVEN CAVITY FLOW

Thermally driven flow in a differentially heated cavity is a well-known benchmark problem for testing CFD algorithms. This model of convective heat transfer should not be underestimated in its complexity. The spatial structure of the flow includes such complexities as vertical and horizontal boundary layers, corner structures, stratified core and so on which sensitively depend on the aspect ratio, Rayleigh and Prandtl numbers and thermal boundary conditions. In many cases the sensitivity of buoyancy-driven cavity flows can be attributed to the presence of multiple bifurcation points that yield laminar thermal convective processes which can transit from steady to various modes of unsteady flow (Winters, 1988).

The buoyancy driven cavity flow problem is based upon the geometry shown in Figure B.45 where W is the width, D is the depth and H the height of the cavity. The enclosure aspect ratio can be quantified as the ratio of the height to width $R=H/W$ and in the present analysis takes on the value $R=8$. The depth of the cavity is $D=8$ with a symmetry plane imposed at $z=8$ and a solid insulated wall at $z=0$. The gravity vector is directed in the negative y -coordinate direction, and the Boussinesq approximation is assumed to be valid, i.e. only small temperature excursions from the mean temperature are admitted (Boussinesq, 1987).

6.4.1 PROBLEM STATEMENT

The partial differential equation (PDE) system of continuum mechanics conservation principles describing thermal viscous flow of an incompressible fluid in non-dimensional form are presented in (2.5)-(2.7). These equations contain three non-dimensional groups, namely Reynolds, Peclet and Grashof. The equations used herein are non-dimensionalized slightly differently, with reference velocity chosen such that the Grashof number is not present in the final form. The following non-dimensional groups are used to obtain a new non-dimensional form

$$\begin{aligned}
x'_j &= \frac{x_j}{L_{ref}}; & u'_j &= \frac{u_j}{U_{ref}}; & t' &= \frac{t}{L_{ref}/U_{ref}} \\
\rho' &= \frac{\rho}{\rho_{ref}}; & \Theta &= \frac{T - T_{ref}}{\Delta T_{ref}}; & \phi' &= \frac{\phi}{\phi_{ref}}
\end{aligned} \tag{6.63}$$

With reference quantities defined

$$\begin{aligned}
L_{ref} &= W; & \Delta T_{ref} &= T_H - T_C; & T_{ref} &= T_C; \\
U_{ref} &= \sqrt{g\beta L_{ref} \Delta T_{ref}} = \sqrt{g\beta W (T_H - T_C)}; \\
\rho_{ref} &= \rho_0 U_{ref}^2 = \rho_0 g\beta W (T_H - T_C) \\
\phi_{ref} &= L_{ref} U_{ref} = \sqrt{g\beta W^3 (T_H - T_C)}
\end{aligned} \tag{6.64}$$

Dropping the primes, equations (2.6) and (2.7) are rewritten in an alternative non-dimensional form

$$\mathcal{L}(u_i) = \frac{\partial u_i}{\partial t} + \frac{\partial}{\partial x_j} \left(u_j u_i - \sqrt{\frac{Pr}{Ra}} \frac{\partial u_i}{\partial x_j} + p \delta_{ij} \right) + \Theta \hat{g}_i = 0 \tag{6.65}$$

$$\mathcal{L}(\Theta) = \frac{\partial \Theta}{\partial t} + \frac{\partial}{\partial x_j} \left(u_j \Theta - \frac{1}{\sqrt{Ra \cdot Pr}} \frac{\partial \Theta}{\partial x_j} \right) = 0 \tag{6.66}$$

where Rayleigh and Prandtl numbers are defined as

$$Ra = \frac{g\beta \Delta T_{ref} L_{ref}^3}{\nu \alpha}; \quad Pr = \frac{\nu}{\alpha} \tag{6.67}$$

Using definition $U_{ref} = \sqrt{g\beta L_{ref} \Delta T_{ref}}$ non-dimensional parameters in (6.65) can also be expressed in terms

of Re and Pe numbers, which will become useful in defining subfilter scale entities

$$\begin{aligned}
\sqrt{\frac{Pr}{Ra}} &= \frac{1}{\sqrt{Gr}} = \frac{1}{Re} \\
\frac{1}{\sqrt{Ra \cdot Pr}} &= \frac{1}{\sqrt{Bo}} = \frac{1}{Pe}
\end{aligned} \tag{6.68}$$

where Grashof and Boussinesq numbers are defined as

$$Gr = \frac{Ra}{Pr} = \frac{g\beta\Delta T_{ref} L_{ref}^3}{\nu^2}$$

$$Bo = Ra \cdot Pr = \frac{g\beta\Delta T_{ref} L_{ref}^3}{\alpha^2}$$
(6.69)

Throughout the analysis of differentially heated cavity the Prandtl number is assumed $Pr = 0.7$ and the Rayleigh number range is $Ra = 10^4 \div 10^8$. The domain of interest is comprised of five solid walls with no-slip boundary conditions and one symmetry plane with no-through flow. Temperature BCs imposed at the “cold” and “hot” walls are, respectively

$$\Theta|_{x=0} = 0 \quad \text{and} \quad \Theta|_{x=1} = 1$$
(6.70)

Referring to Figure B.45, the “top”, “bottom” and “back” walls are insulated, hence

$$\left. \frac{\partial \Theta}{\partial y} \right|_{y=0} = 0; \quad \left. \frac{\partial \Theta}{\partial y} \right|_{y=8} = 0; \quad \left. \frac{\partial \Theta}{\partial z} \right|_{z=0} = 0$$
(6.71)

The symmetry plane is imposed at $z=8$, hence

$$\left. \frac{\partial u}{\partial z} \right|_{z=8} = 0; \quad \left. \frac{\partial v}{\partial z} \right|_{z=8} = 0; \quad w|_{z=8} = 0;$$

$$\left. \frac{\partial \Theta}{\partial z} \right|_{z=8} = 0$$
(6.72)

The boundary conditions for ϕ and p are vanishing Neumann everywhere.

The initial conditions for transient simulation describe an isothermal fluid initially at rest. To speed up computations the temperature is initialized via linear distribution between cold and hot walls, hence

$$\mathbf{u}(x, y, z, t = 0) = 0$$

$$\Theta(x, y, z, t = 0) = x$$

$$\phi(x, y, z, t = 0) = 0$$

$$p(x, y, z, t = 0) = 0$$
(6.73)

Considering air at room temperature and standard atmospheric pressure non-dimensional units can be readily converted to dimensional ones via identification of reference length and velocity defined as, respectively

$$L_{ref} = \sqrt[3]{\frac{\nu^2 Ra}{g\beta\Delta T_{ref} Pr}} \quad U_{ref} = \sqrt{g\beta L_{ref}\Delta T_{ref}} \quad (6.74)$$

The needed properties in BG units include

- Constant of gravitational acceleration, $g = 32.17405$ [ft/s²]
- Coefficient of thermal expansion (gas), $\beta = 531.67^{-1}$ [1/°R]
- Reference temperature gradient, $\Delta T_{ref} = 200$ [°F]
- Kinematic viscosity of air at 72 °F, $\nu = 1.6485 \cdot 10^{-4}$ [ft²/s]
- Prandtl number of air at 72 °F, $Pr = 0.71517$
- Rayleigh number, $Ra = 10^8$

Using these values the reference length and velocity are, respectively

$$L_{ref} = 0.6797 \text{ [ft]} \quad U_{ref} = 2.8681 \text{ [ft/s]} \quad (6.75)$$

For $Ra = 10^7$ and $\Delta T_{ref} = 20$ [°F] the reference velocity is $U_{ref} = 0.9070$ [ft/s].

6.4.2 EFFECTS OF NON-DIMENSIONALIZATION ON PRESSURE DISTRIBUTION

Preliminary computational experiments for square thermal cavity benchmark indicate that the genuine pressure distribution is significantly influenced by the choice of reference temperature used during non-dimensionalization. This effect appears to be significant only for the cases of low Ra numbers, well below the transitional specification. Defining non-dimensional temperature as $\Theta = (T - T_{ref}) / \Delta T_{ref}$ with

$\Delta T_{ref} = T_H - T_C$ and choosing the reference temperature as $T_{ref} = T_C$ the boundary conditions for T imposed at the “cold” and “hot” walls are

$$\Theta|_{cold} = 0 \quad \text{and} \quad \Theta|_{hot} = 1 \quad (6.76)$$

Similarly, if $T_{ref} = (T_H + T_C)/2$ these boundary conditions become

$$\Theta|_{cold} = -\frac{1}{2} \quad \text{and} \quad \Theta|_{hot} = \frac{1}{2} \quad (6.77)$$

Although the choice of reference temperature is not expected to play any role, the results of this preliminary study prove otherwise. A qualitative analysis of the laminar square thermal cavity at $Ra = 10^4$ is performed on a uniform mesh of 33x33 nodes. Figure B.46 illustrates the pressure contours generated using temperature variations (6.76) and (6.77). The main conceptual difference between these two results lies in the behavior of pressure distribution along the cold wall, i.e., pressure rise when (6.76) is used and pressure drop when (6.77) is used. It is worth noting that the continuity constraint potential function ϕ exhibits the same behavior.

It is then established that this discrepancy is solely due to $\Theta = 0$ specification at the cold wall, which is believed to be the only reasonable choice since non-positive temperature specifications are not natural. The pressure distribution, as well as ϕ , are affected by this temperature specification only because the buoyancy force is uni-directional, i.e., not symmetric. In case of $\Theta = 0$ the buoyancy is approximately equivalent to the adverse pressure gradient for flow moving downwards along the cold wall, while along the hot wall this gradient assists in moving the flow upwards. This effect disappears for higher Rayleigh numbers where the buoyancy effects become dominant rendering an almost linear pressure distribution for both definitions, (6.76) and (6.77).

6.4.3 MODIFIED CCM θ -IMPLICIT PROCEDURE

The requirement to solve a Poisson equation for the genuine kinematic pressure distribution can be eliminated by coupling the equation for the continuity constraint potential function ϕ with the set of four main equations, producing a 5 by 5 Jacobian matrix. This change will also free the algorithm from the outside iterative loop used in the original CCM formulation. Instead, the iterations will be embedded in the Newton's procedure by aptly modifying the update of the continuity constraint variable C_{n+1} .

As demonstrated earlier the original CCM formulation requires an iterative procedure within the time-step. During these iterations the CCM replaces genuine pressure with a continuity constraint variable, C_{n+1}^p , where p is an iteration index. The modified CCM formulation herein does not require an iterative procedure as the Poisson equation for ϕ is coupled with the Navier-Stokes and energy equations. The continuity constraint variable C_{n+1}^p is updated during the Newton's iterative procedure. The initial iterative value C_{n+1}^1 at every time step is defined as the global sum for ϕ solutions accumulated over time, hence

$$C_{n+1}^p = \frac{1}{\theta \Delta t} \left[\sum_{k=1}^n \phi^k + \sum_{j=1}^p \delta \phi^j \right] \quad (6.78)$$

The iteration index p represents Newton iterations within the time step.

6.4.4 TEMPLATE STATEMENT

Following the ideas of template construction and matrix identification conventions described in section 5.2 the FE template statement is developed herein for a thermally driven cavity.

Ignoring irreversible work viscous dissipation term, the set of five coupled LES theory PDEs describing buoyancy-driven flow in a differentially heated cavity in three dimensions is

$$\begin{cases}
\mathcal{L}(\bar{u}) = \frac{\partial \bar{u}}{\partial t} + \frac{\partial}{\partial x_j} \left(\bar{u}_j \bar{u} + \bar{c}_{1j} + \overline{u'_j u'} - \sqrt{\frac{Pr}{Ra}} \frac{\partial \bar{u}}{\partial x_j} + \bar{p} \delta_{1j} \right) + \bar{\Theta} \hat{g}_1 - A_\delta(\mathbb{S}(u, p)) = 0 \\
\mathcal{L}(\bar{v}) = \frac{\partial \bar{v}}{\partial t} + \frac{\partial}{\partial x_j} \left(\bar{u}_j \bar{v} + \bar{c}_{2j} + \overline{u'_j v'} - \sqrt{\frac{Pr}{Ra}} \frac{\partial \bar{v}}{\partial x_j} + \bar{p} \delta_{2j} \right) + \bar{\Theta} \hat{g}_2 - A_\delta(\mathbb{S}(v, p)) = 0 \\
\mathcal{L}(\bar{w}) = \frac{\partial \bar{w}}{\partial t} + \frac{\partial}{\partial x_j} \left(\bar{u}_j \bar{w} + \bar{c}_{3j} + \overline{u'_j w'} - \sqrt{\frac{Pr}{Ra}} \frac{\partial \bar{w}}{\partial x_j} + \bar{p} \delta_{3j} \right) + \bar{\Theta} \hat{g}_3 - A_\delta(\mathbb{S}(w, p)) = 0 \\
\mathcal{L}(\bar{\Theta}) = \frac{\partial \bar{\Theta}}{\partial t} + \frac{\partial}{\partial x_j} \left(\bar{u}_j \bar{\Theta} + \bar{v}_j^\ominus + \overline{u'_j \Theta'} - \frac{1}{\sqrt{Ra \cdot Pr}} \frac{\partial \bar{\Theta}}{\partial x_j} \right) - A_\delta(\nabla \Theta) = 0 \\
\mathcal{L}(\phi) = \frac{\partial^2 \phi}{\partial x_i^2} - \frac{\partial \bar{u}_i}{\partial x_i} = 0
\end{cases} \quad (6.79)$$

Augmented with nine *arLES* generated Poisson equations

$$\begin{aligned}
\mathcal{L}(\bar{c}_{ij}) &= -\nabla^2 \bar{c}_{ij} + \frac{4\gamma}{\delta^2} \bar{c}_{ij} - 2 \frac{\partial \bar{u}_i}{\partial x_k} \frac{\partial \bar{u}_j}{\partial x_k} = 0 \\
\mathcal{L}(\bar{v}_j^\ominus) &= -\nabla^2 \bar{v}_j^\ominus + \frac{4\gamma}{\delta^2} \bar{v}_j^\ominus - 2 \frac{\partial \bar{u}_j}{\partial x_k} \frac{\partial \bar{\Theta}}{\partial x_k} = 0
\end{aligned} \quad (6.80)$$

Ignoring the pressure contribution the BCE definitions are

$$\begin{aligned}
A_\delta(\mathbb{S}(u, p))(t, x_k) &\equiv \int_{\partial\Omega} g_\delta(x_k - s_k) \left[\sqrt{\frac{Pr}{Ra}} \left(\frac{\partial u_i}{\partial x_j} \right) \right] \hat{n}_j ds \\
A_\delta(\nabla \Theta)(t, x_k) &\equiv \int_{\partial\Omega} g_\delta(x_k - s_k) \left[\frac{1}{\sqrt{Ra \cdot Pr}} \left(\frac{\partial \Theta}{\partial x_j} \right) \right] \hat{n}_j ds
\end{aligned} \quad (6.81)$$

The SFS tensor and vector closure candidates are, respectively

$$\begin{aligned}
-\overline{u'_j u'_i} &\equiv C_s(\delta) \frac{h^2}{6} \sqrt{\frac{Ra}{Pr}} \left[\bar{u}_j \bar{u}_k \frac{\partial \bar{u}_i}{\partial x_k} + \bar{u}_i \bar{u}_k \frac{\partial \bar{u}_j}{\partial x_k} \right] \\
-\overline{u'_j \Theta'} &\equiv C_s(\delta) \frac{h^2 \sqrt{Ra \cdot Pr}}{12} \left[\bar{u}_j \bar{u}_k \frac{\partial \bar{\Theta}}{\partial x_j} \right]
\end{aligned} \quad (6.82)$$

Three velocity components, the temperature and the continuity constraint potential function are denoted as $\{U\}, \{V\}, \{W\}, \{TEMP\}$ and $\{PHI\}$, respectively. Multiplying equation (6.78) through by $\theta\Delta t$ the continuity constraint variable C is redefined as $C^{new} = C \cdot \theta\Delta t$ and then C^{new} is denoted as $\{SPHI\}$. Upon application of the Green-Gauss theorem the negative sign of these terms as well as the Laplacian terms in (6.79) and (6.80) switches to positive.

Denoting $TDELTA = \theta\Delta t$, $MTDELTA = -\theta\Delta t$, $ITDELTA = \frac{1}{\theta\Delta t}$, $PAR1 = \sqrt{\frac{Pr}{Ra}}$, $PAR2 = \frac{1}{\sqrt{Ra \cdot Pr}}$, $ONE = 1$, and state-variables at the previous time step as UL, VL, WL and $TEMP_L$, and assuming $\theta = 1.0$ for simplicity, the momentum equation in x-direction in template form is

$$\begin{aligned}
\{FU\} = & (ONE)\{ \}[c200]\{U\} & + (TDELTA)\{ \}[c20y]\{C12\} & (6.83) \\
& + (MONE)\{ \}[c200]\{UL\} & + (TDELTA)\{ \}[c20z]\{C13\} \\
& + (TDELTA)\{U\}[c300x]\{U\} & + (TDELTA*PAR1)\{ \}[c2kk]\{U\} \\
& + (TDELTA)\{V\}[c300y]\{U\} & + (ONE)\{ \}[c20x]\{SPHI\} \\
& + (TDELTA)\{W\}[c300z]\{U\} & + (ONE)\{ \}[c20x]\{PHI\} \\
& + (TDELTA)\{ \}[c20x]\{C11\} & + (MTDELTA)\{ \}[c200]\{UBCE\}
\end{aligned}$$

The SFS tensor contribution of eighteen terms to (6.83) is given by (5.47) with Re replaced by $\sqrt{Ra/Pr}$.

Note that the diffusion matrix $[c2kk]$ includes all three second-order derivatives with respect to x , y , and z coordinates. The templates for y - and z -momentum equations can be expressed in exactly the same manner. However the momentum equation in y -direction will also include the buoyancy term.

$$\begin{aligned}
\{FV\} &= (\text{ONE})\{ \} [c200]\{V\} & \{FW\} &= (\text{ONE})\{ \} [c200]\{W\} \\
&+ (\text{MONE})\{ \} [c200]\{VL\} & &+ (\text{MONE})\{ \} [c200]\{WL\} \\
&+ (\text{TDELTA})\{U\} [c300x]\{V\} & &+ (\text{TDELTA})\{U\} [c300x]\{W\} \\
&+ (\text{TDELTA})\{V\} [c300y]\{V\} & &+ (\text{TDELTA})\{V\} [c300y]\{W\} \\
&+ (\text{TDELTA})\{W\} [c300z]\{V\} & &+ (\text{TDELTA})\{W\} [c300z]\{W\} \\
&+ (\text{TDELTA})\{ \} [c20x]\{C12\} & &+ (\text{TDELTA})\{ \} [c20x]\{C13\} \\
&+ (\text{TDELTA})\{ \} [c20y]\{C22\} & &+ (\text{TDELTA})\{ \} [c20y]\{C23\} \\
&+ (\text{TDELTA})\{ \} [c20z]\{C23\} & &+ (\text{TDELTA})\{ \} [c20z]\{C33\} \\
&+ (\text{TDELTA*PAR1})\{ \} [c2kk]\{V\} & &+ (\text{TDELTA*PAR1})\{ \} [c2kk]\{W\} \\
&+ (\text{ONE})\{ \} [c20y]\{SPHI\} & &+ (\text{ONE})\{ \} [c20z]\{SPHI\} \\
&+ (\text{ONE})\{ \} [c20y]\{PHI\} & &+ (\text{ONE})\{ \} [c20z]\{PHI\} \\
&+ (\text{MTDELTA})\{ \} [c200]\{VBCE\} & &+ (\text{MTDELTA})\{ \} [c200]\{WBCE\} \\
&+ (\text{MTDELTA})\{ \} [c200]\{TEMP\} & &
\end{aligned} \tag{6.84}$$

Using the same notation the energy equation and the Poisson equation for θ are expressed in the FE template form. Note that the equation for θ is multiplied through by ITDELTA in order to improve the condition number of the final Jacobian matrix that is passed to the linear equation solver.

$$\begin{aligned}
\{FTEMP\} &= (\text{ONE})\{ \} [c200]\{TEMP\} & \{FPHI\} &= (\text{ITDELTA})\{ \} [c2kk]\{PHI\} \\
&+ (\text{MONE})\{ \} [c200]\{TEMPL\} & &+ (\text{ITDELTA})\{ \} [c20x]\{U\} \\
&+ (\text{TDELTA})\{U\} [c300x]\{TEMP\} & &+ (\text{ITDELTA})\{ \} [c20y]\{V\} \\
&+ (\text{TDELTA})\{V\} [c300y]\{TEMP\} & &+ (\text{ITDELTA})\{ \} [c20z]\{W\} \\
&+ (\text{TDELTA})\{W\} [c300z]\{TEMP\} & & \\
&+ (\text{TDT})\{ \} [c20x]\{V1\} & & \\
&+ (\text{TDT})\{ \} [c20y]\{V2\} & & \\
&+ (\text{TDT})\{ \} [c20z]\{V3\} & & \\
&+ (\text{TDELTA*PAR2})\{ \} [c2kk]\{TEMP\} & & \\
&+ (\text{MTDELTA})\{ \} [c200]\{TBCE\} & &
\end{aligned} \tag{6.85}$$

Finally, the template for the continuity constraint variable is

$$\begin{aligned}
\{FSPHI\} &= (\text{ONE})\{ \} [I]\{SPHI\} \\
&+ (\text{ONE})\{ \} [I]\{PHI\}
\end{aligned} \tag{6.86}$$

6.4.5 THERMAL CAVITY AT $RA=10^8$.

The objective of this benchmark is to examine the fidelity of the essentially analytical rational LES theory closure for a turbulent Rayleigh number specification, i.e., $Ra=10^8$. The transition from laminar to turbulent flow is facilitated via a sequence of numerical tests with increasing Rayleigh number, hence Reynolds number. The first computational experiment utilizes $Ra=10^4$ and a linear distribution of temperature (6.73) to start the simulation. The steady-state solution is then used as an initial condition for the next test with higher Rayleigh number, i.e., $Ra=10^5$. This sequence of Rayleigh numbers is continued until $Ra=10^8$ is reached. The Prandtl number for all numerical experiments is constant at $Pr=0.7$. The required parameters for each Rayleigh number specification are summarized in Table A.10.

The flow in a differentially heated cavity transitions from steady to multi-scale unsteady above some critical Rayleigh number (Le Quere, 1994). Numerical tests for two-dimensional 8x1 cavity mark the transition from steady to a time-dependent flow at $Ra_{crit} \approx 3.1 \times 10^5$ (Xin and Le Quere, 2002). This has been further verified by the FEM results provided by Salinger et al. (2002). In the present study a computational experiment at a slightly above-critical Rayleigh number of 4×10^5 is conducted, resulting in a Reynolds number of 756. Temperature profiles at $t=80, 120, 217.5$ seconds are illustrated in Figure B.47. At $t \approx 170$ seconds the flow becomes non-steady and cyclic clearly defining the incipient unsteady laminar flow. At the end of both vertical thermal boundary layers located at the top-right and bottom-left corners of the cavity, the flow starts to ripple continuously indicating transition to a non-steady regime. This is illustrated by taking four consecutive time samples of temperature distribution as shown in Figure B.48. The highlighted peaks of temperature change their position up-and-down, left-and-right in a sinusoid-like fashion. This experiment clearly verifies the correctness of algorithm implementation via establishment of a non-steady transitional flow for a slightly above-critical Rayleigh number.

Full implementation of *arLES* theory closure is enabled at $Ra = 10^8$. The flow is initialized using the INS algorithm solution for $Ra = 10^7$. The approximate deconvolution approach is used to determine the boundary conditions and the BCE integral as described in Chapter 3. Non-uniform mesh of 65x207x41 nodes is refined near the solid walls according to the optimal mesh construction technique described in section 6.2.5 and illustrated in Figure B.25. Again, this technique requires placing a total of eight nodes within distance δ from the wall. DNS data for a 4x1 thermal cavity at $Ra = 10^{10}$ is used for determining reasonable filter measure δ (Trias et al., 2010). Averaged temperature as well as vertical and horizontal velocity profiles extracted from the horizontal mid-height plane all indicate the existence of peaks some distance away from the wall. The filter measure used herein is chosen such that it does not exceed any of these three distances, hence the space-filtered profiles are not expected to change their convexity within distance δ off the wall. The chosen filter measure is

$$\delta = 0.05 \tag{6.87}$$

The AD boundary conditions for the velocity components are implemented everywhere except for the symmetry plane. The AD BCs for temperature are imposed only at the hot and cold walls. In order to conserve mass no flow should be allowed across the boundaries. With this in mind the AD BCs for the velocity are only implemented for the two tangential components, fixing the normal component at zero. Evidently, this approach of imposing non-homogeneous Dirichlet BCs creates vector fields directly on the boundary, as illustrated in Figure B.49.

The existence of three-dimensional thermal and momentum boundary layers is visualized by plotting iso-surfaces of temperature and velocity vector magnitude, respectively. Iso-surfaces of ten temperature levels are illustrated in Figure B.50. A clearly visible thermal boundary layer exhibits laminar to turbulent transition. In a similar fashion, fourteen iso-surfaces of the velocity vector

magnitude are illustrated in Figure B.51 (view from the symmetry plane) and Figure B.52 (view from the solid wall). Both views nicely illustrate the transition from laminar to turbulent regime in the momentum boundary layer.

Temperature and velocity vector distribution contours extracted from different depths, Figure B.53 and Figure B.54, respectively, provide an alternative view of a fully three-dimensional thermal and momentum boundary layers. The stratified core is clearly visible in Figure B.53.

Figure B.55 visually compares the filtered (left) and the AD (right) velocity fields. The AD-generated noise at the first four auxiliary nodes placed in region $y < 0.25\delta$ is clearly visible. However, as explained in section 6.2.5, these parasitic values of AD state-variable members are not included in computations of BCs or BCE. The auxiliary nodes aid only in determining the wall gradients of space filtered quantities.

An illustrative “velocity bound” between laminar and turbulent regimes is established by plotting laminar and turbulent boundary layer profiles on the same graph using the standard (y^+, u^+) similarity coordinates, as defined in (6.46). Figure B.56 illustrates this idea by combining a typical turbulent boundary layer profile obtained from RaNS solution (denoted here as Wilcox) with three Blasius solutions for different Re numbers. The data shows that all three Blasius profiles plotted using (y^+, u^+) similarity coordinates remain in very good agreement with $y^+ = u^+$ curve up to $y^+ \approx 0.5\delta_{99\%}$, or half-way through the boundary layer thickness. The laminar and turbulent boundary layer profiles remain almost identical in the viscous sublayer ($y^+ < 5$) as illustrated in Figure B.57.

To quantify the boundary layer behavior four V-velocity profiles are extracted from the thermal cavity symmetry plane ($z = 8$) at different heights, i.e., different locations along the boundary layer, Figure B.58. As can be seen, a very thin boundary layer characterizes the flow as an attached wall jet. These profiles are truncated at their peaks and scaled to fit onto the graph with Blasius and Wilcox solutions,

Figure B.59. As can be seen, the profiles extracted from $y=1$ and $y=3$ tend to lie closer to the Blasius laminar solution, whereas for $y=5$ and $y=7$ these profiles resemble the RaNS turbulent solution. The interpolated profiles for $y=1$ and $y=5$ are also illustrated in Figure B.60 visually quantifying the transition from laminar to turbulent regimes.

An interesting feature of the $Ra=10^8$ resolved scale velocity vector field is the hot/cold wall traversing vortex entities that generate translating thermal fingers protruding wall normal into the cavity, illustrated in the unitized scale temperature field with velocity vector overlay, Figure B.61. As can be seen, the central one-third of the cavity's symmetry plane is predicted isothermal. The *arLES* theory state variable diagnostics focus is the wall-normal thermal finger encircled on the right in the unitized scale graph, Figure B.61. The *arLES* theory solution state variable floods with velocity vector overlay, Figure B.62, illustrate:

- *Top left.* Resolved scale temperature $\bar{\Theta}$ is $\mathcal{O}(10^0)$. The wall normal thermal finger is generated by an attached eddy, as clearly identified from the velocity vector overlay.
- *Top right.* Resolved-unresolved scale interaction cross-thermal vector second component $\bar{v}_2^\Theta = \bar{u}_2\bar{\Theta}' + \overline{u_2'\Theta}$ is $\mathcal{O}(10^{-1})$. The value of \bar{v}_2^Θ is minimized towards the vertex center.
- *Middle left.* Resolved scale convection tensor $\bar{u}_1\bar{u}_2$ is $\mathcal{O}(10^{-1})$, the most significant of the closure tensor quadruple. The thermal finger region is only a fraction of the extrema.
- *Middle right.* Resolved-unresolved cross-stress tensor $\bar{c}_{12} = \overline{\bar{u}_1 u_2'} + \overline{u_1' \bar{u}_2}$ at $\mathcal{O}(10^{-2})$ is one order smaller than $\bar{u}_1\bar{u}_2$.
- *Bottom.* SFS tensor $\overline{u_1' u_2'}$ resolution extrema at $\mathcal{O}(10^{-2})$ is located above and below the thermal finger dissipating energy from large motions to this smaller eddy.

These $Ra = 10^8$ *arLES* solution data snapshots contribute to qualitative validation of *arLES* theory order predictions for tensor/vector quadruples (2.21)-(2.22), as well as classic fluid mechanics perturbation theory ordering underlying *arLES* theory state variable organization. The resolved scale velocity tensor product, $\overline{u_j u_i}$, should exceed $\mathcal{O}(\delta^2) \Rightarrow (0.05)^2 = 0.0025 \approx \text{E-02}$. Figure B.62 (middle left) graphs *arLES* theory convection tensor product, $\overline{u_1 u_2}$, with data range $\pm \text{E-01}$, hence exceeding E-02 by an order of magnitude. The *arLES* closure assumes the cross-stress tensor is $\mathcal{O}(\delta^2)$. Figure B.62 (middle right) indicates the data range $\pm \text{E-02}$ confirming quantitative agreement with $\mathcal{O}(\delta^2) \approx \text{E-02}$. The perturbation theory order requirement for the SFS term is $\mathcal{O}(\delta^3) \Rightarrow (0.05)^3 = 0.000125 \approx \text{E-04}$. The SFS tensor/vector uniform constant coefficient is therefore $\mathcal{O}(\delta)$. In this dissertation this constant is set identical to the filter measure $C_s = \delta = 0.05$. The *arLES* closure SFS tensor term, $\overline{u'_1 u'_2}$, illustrated in Figure B.62 (bottom) has the data range $\pm \text{E-02}$. These extrema exists in wall-adjacent roll vortex structures only, which is not surprising since this is where $\mathcal{O}(h^2)$ dissipation is principally required. Elsewhere throughout the cavity $\overline{u'_1 u'_2}$ ranges $\pm \text{E-04}$ in excellent quantitative agreement with perturbation theory ordering.

Finally, Figure B.63 through Figure B.71 illustrate thermal cavity's rich spectral content by plotting cross-stress tensor and cross-thermal vector pair distributions.

7. SUMMARY AND CONCLUSIONS

This dissertation details derivation of an essentially analytical rational LES (*arLES*) closure theory for the unsteady three-dimensional space filtered thermal-incompressible NS PDE system on bounded domains. This model-free approach is established by the union of 2nd order rational LES theory, Galdi and Layton, with modified continuous Galerkin theory of Kolesnikov. The *arLES* theory is successfully extended to the thermal NS with specific focus on correct adaptation of a constant measure filter near the Dirichlet type boundary. The analytical closure theory state variable organization is guided by classic fluid mechanics perturbation theory generating a well-posed EBV solution strategy for the LES tensor/vector quadruples.

Derivation and implementation of suitable boundary conditions as well as the boundary commutation error integral is accomplished using the ideas of approximate deconvolution theory. An accurate way of constructing the boundary conditions of non-homogeneous Dirichlet type is developed by including a buffer layer outside of the computational domain. The suitable non-homogeneous Dirichlet boundary conditions for the auxiliary problem of *arLES* theory are newly derived. This auxiliary problem BC closure of $\mathcal{O}(\delta^2)$ is derived via direct evaluation of unfiltered tensors followed by the application of an improved ADBC methodology. Finally, the correct implementation of the AD formula with proper non-homogeneous Neumann BCs completes this mathematically elegant *arLES* formulation.

Verification and validation of *arLES* theory closure is established by conducting computational experiments for four pertinent benchmark problems. All tests confirm that the BCE integral, universally omitted in SGS modeled LES, plays an essential role in establishing an accurate solution. Uniform mesh refinement process for a linear problem confirms monotone asymptotic convergence, as part of the verification process. Validation of an improved ADBC formulation for a typical turbulent BL profile

identifies an optimal mesh construction technique suitable for any constant filter measure. The resulting solution-adaptive mesh refinement process exhibits convergence completing validation analysis. The *arLES* theory closure is absent the word *turbulent*. It is based on rigorous mathematical operations defined for/by NS PDE system convolution and is Reynolds number unconstrained. Successful validation of *arLES* theory applicability in predicting laminar flows on bounded domains is performed herein as compared with the Blasius solution.

Thermally driven cavity solution provides turbulent flow validation of *arLES* theory order predictions for tensor/vector quadruples. The results are in excellent quantitative agreement with classic fluid mechanics perturbation theory ordering underlying *arLES* theory state variable organization. The transition from laminar to turbulent regimes in the momentum boundary layer is validated with laminar Blasius and turbulent RaNS boundary layer profiles, respectively.

In conclusion, the essentially analytical closure theory derived herein provides a model-free, Reynolds number unconstrained LES formulation fully closed with analytical BC and BCE integral derivations based strictly on rigorous mathematical considerations.

BIBLIOGRAPHY

- AMSDEN, A. A. & HARLOW, F. H. 1970. The SMAC Method: A Numerical Technique for Calculating Incompressible Fluid Flows.
- BAKER, A. J. 1983. *Finite element computational fluid mechanics*, Washington, Hemisphere Pub. Corp.
- BAKER, A. J. 2006. *The Computational Engineering Sciences*, j-Computek Press.
- BAKER, A. J. 2012. *Finite elements : computational engineering sciences*, Hoboken, Wiley.
- BERSELLI, L. C. & ILIESCU, T. 2003. A higher-order subfilter-scale model for large eddy simulation. *Journal of Computational and Applied Mathematics*, 159, 411-430.
- BERSELLI, L. C., ILIESCU, T. & LAYTON, W. J. 2006. *Mathematics of Large Eddy Simulation of Turbulent Flows*, Heidelberg, Springer.
- BLASIUS, H. 1908. Grenzschichten in Flüssigkeiten mit kleiner Reibung. *Z. Math. Phys.*, 56, 1-37.
- BOOLE, G. & MOULTON, J. F. 1960. *A Treatise on the Calculus of Finite Differences, 2nd rev. ed.*, New York, Dover.
- BORGGGAARD, J. & ILIESCU, T. 2006. Approximate Deconvolution Boundary Conditions for Large Eddy Simulation. *Appl. Math. Lett.*, 19, 735-740.
- BORIS, J. P. 1990. On Large Eddy Simulation Using Subgrid Turbulence Models - Comment. *Whither Turbulence, Turbulence at the Crossroads*, 357, 344-353.
- BORIS, J. P., GRINSTEIN, F. F., ORAN, E. S. & KOLBE, R. L. 1992. New Insights into Large Eddy Simulation. *Fluid Dynamics Research*, 10, 199-228.
- BOUSSINESQ, J. 1987. *Théorie de l'écoulement tourbillonnant et tumultueux des liquides dans les lits rectilignes a grande section*, Paris, Gauthier-Villars et fils.
- CARATI, D. & EIJDEN, E. V. 1997. On the self-similarity assumption in dynamic models for large eddy simulations. *Physics of Fluids*, 9, 2165-2167.
- CHAFFIN, D. J. 1997. A Taylor Weak Statement Finite Element Method for Computational Fluid Dynamics. Knoxville, TN.
- CHAPMAN, D. R. 1979. Computational aerodynamics development and outlook. *AIAA Journal*, 17, 1293-1313.
- CLARK, R. A., FERZIGER, J. H. & REYNOLDS, W. C. 1979. Evaluation of subgrid scale models using an accurately simulated turbulent flow. *J. Fl. Mech.*, 91, 1-16.

- DEARDORF, J. 1970. A Numerical Study of 3 Dimensional Turbulent Channel Flow at Large Reynolds Numbers. *Journal of Fluid Mechanics*, 41, 453-480.
- DOMARADZKI, J. A. & SAIKI, E. M. 1997. A subgrid-scale model based on the estimation of unresolved scales of turbulence. *Physics of Fluids*, 9, 2148-2164.
- DOMARADZKI, J. A. & YEE, P. P. 2000. The subgrid-scale estimation model for high Reynolds number turbulence. *Physics of Fluids*, 12, 193-196.
- DUNCA, A., JOHN, V. & LAYTON, W. J. 2003. The commutation error of the space averaged Navier-Stokes equations on a bounded domain. In: GALDI, H., RANNACHER (ed.) *Contributions to Current Challenges in Mathematical Fluid Mechanics*. Germany: Birkhauser Verlag.
- FUREBY, C. & TABOR, G. 1997. Mathematical and Physical Constraints on Large-Eddy Simulations. *J. Theor. Comp. Fluid Dyn.*, 9, 85-102.
- GALDI, G. P. & LAYTON, W. J. 2000. Approximation of the larger eddies in fluid motion II: A model for space filtered flow. *Math. Model. Meth. Appl. Sci.*, 10, 343-350.
- GERMANO, M., PIOMELLI, U., MOIN, P. & CABOT, W. 1991. A Dynamic subgrid-scale eddy viscosity model. *Phys. Fluids A*, 3, 1760-1765.
- GHOSAL, S., LUND, T. S., MOIN, P. & AKSELVOLL, K. 1995. A Dynamic Localization Model for Large-Eddy Simulation of Turbulent Flows. *Journal of Fluid Mechanics*, 286, 229-255.
- GHOSAL, S. & MOIN, P. 1995. The basic equations for the large eddy simulation of turbulent flows in complex geometry. *J. Comp. Phys.*, 118, 24-37.
- GRESHO, P. M. & SANI, R. L. 1987. On Pressure Boundary Conditions For The Incompressible Navier-Stokes Equations. *Int. J. Numer. Meth. Fl.*, 7, 1111-1145.
- GRINSTEIN, F. F. & FUREBY, C. 2004. From canonical to complex flows: Recent progress on monotonically integrated LES. *Computing in Science & Engineering*, 6, 36-49.
- GRINSTEIN, F. F., MARGOLIN, L. G. & RIDER, W. J. 2007. *Implicit Large Eddy Simulation: Computing Turbulent Fluid Dynamics*, England, Cambridge University Press.

- GRUBERT, M. 2006. Development of a Potentially Accurate and Efficient LES CFD Algorithm to Predict Heat and Mass Transport in Inhabited Spaces. Knoxville.
- HARTEN, A. 1983. High-Resolution Schemes for Hyperbolic Conservation-Laws. *Journal of Computational Physics*, 49, 357-393.
- JOHN, V. (ed.) 2004. *Large Eddy Simulation of Turbulent Incompressible Flows. Analytical and Numerical Results for a Class of LES Models.*, Berlin: Springer.
- JOHN, V., LAYTON, W. & SAHIN, N. 2004. Derivation and Analysis of Near Wall Models for Channel and Recirculating Flows. *Comp. Math Appl.*, 48, 1135-1151.
- JOHN, V. & LIAKOS, A. 2006. Time-dependent flow across a step: the slip with friction boundary condition. *J. Numer. Meth. Fl.*, 50, 713-731.
- KIM, J. W. 1988. On a Taylor Weak Statement for Finite Element Computations in Gas Dynamics. Knoxville, TN.
- KOLESNIKOV, A. 2000. Efficient implementation of high order methods in computational fluid dynamics. Knoxville, TN.
- KOLMOGOROV, A. N. 1941. Local Structure of Turbulence in an Incompressible Viscous Fluid at Very High Reynolds Numbers. *Doklady Akademiya Nauk SSSR*, 30, 299-303.
- KOLMOGOROV, A. N. & FOMIN, S. V. 1975. *Introductory real analysis*, New York, Dover Publications.
- LAYTON, W. & TRENCH, C. 2011. The Das-Moser commutator closure for filtering through a boundary is well-posed. *Mathematical and Computer Modelling*, 53, 566-573.
- LE QUERE, P. 1994. Onset of Unsteadiness, Routes to Chaos and Simulations of Chaotic Flows in Cavities Heated from the Side - a Review of Present Status. *Heat Transfer 1994 - Proceedings of the Tenth International Heat Transfer Conference, Vol 1*, 281-296.
- LEONARD, A. 1974. Energy Cascade in Large-eddy Simulations of Turbulent Fluid Flows. *Adv. Geophys. A*, 18, 237-248.
- LESIEUR, M. 2008. *Turbulence in fluids*, New York, Springer.
- LILLY, D. K. 1992. A proposed modification of the Germano subgrid-scale closure method. *Phys. Fluids A*, 4, 663-635.

- MANSOUR, N. N., KIM, J. & MOIN, P. 1988. Reynolds-Stress and Dissipation-Rate Budgets in a Turbulent Channel Flow. *Journal of Fluid Mechanics*, 194, 15-44.
- MARGOLIN, L. G., RIDER, W. J. & GRINSTEIN, F. F. 2006. Modeling turbulent flow with implicit LES. *Journal of Turbulence*, 7, 1-27.
- METAIS, O. & LESIEUR, M. 1992. Spectral Large-Eddy Simulation of Isotropic and Stably Stratified Turbulence. *Journal of Fluid Mechanics*, 239, 157-194.
- MIKHAĬLOV, M. D. & ÖZİŞİK, M. N. 1984. *Unified analysis and solutions of heat and mass diffusion*, New York, Wiley.
- ORSZAG, S. A., ISRAELI, M. & DEVILLE, M. O. 1986. Boundary Conditions for Incompressible Flows. *J. Sci. Comp.*, 1, 75-111.
- ÖZİŞİK, M. N. 1968. *Boundary value problems of heat conduction*, Scranton, International Textbook Co.
- PANTON, R. L. 1995. *Incompressible flow*, New York, Wiley.
- PIOMELLI, U. & BALARAS, E. 2002. Wall-Layer Models for Large-Eddy Simulations. *Annual Rev. Fl. Mech.*, 34, 349-374.
- PIOMELLI, U., ZANG, T. A., SPEZIALE, C. G. & HUSSAINI, M. Y. 1990. On the Large-Eddy Simulation of Transitional Wall-Bounded Flows. *Physics of Fluids a-Fluid Dynamics*, 2, 257-265.
- POPE, S. B. 2000. *Turbulent Flows*, Cambridge, Cambridge University Press.
- RUNGE, C. 1901. Über empirische Funktionen und die Interpolation zwischen äquidistanten Ordinaten. *Zeitschrift für Mathematik und Physik*, 46, 224–243.
- SAGAUT, P. 2004. *Large Eddy Simulation for Incompressible Flows*, Berlin, Springer.
- SALINGER, A. G., LEHOUCQ, R. B., PAWLOWSKI, R. P. & SHADID, J. N. 2002. Computational bifurcation and stability studies of the 8 : 1 thermal cavity problem. *International Journal for Numerical Methods in Fluids*, 40, 1059-1073.
- SCHLATTER, P., STOLZ, S. & KLEISER, L. 2004. LES of transitional flows using the approximate deconvolution model. *International Journal of Heat and Fluid Flow*, 25, 549-558.

- SCHNEIDER, G. E., RAITBY, G. D. & YOVANOVICH, M. M. 1978. Finite element analysis of incompressible flow incorporating equal order pressure and velocity interpolation. *Numerical Heat Transfer*, 1, 433 - 451.
- SCHWARTZ, L. 1966. *Théorie des distributions*, Paris, Hermann.
- SHAH, K. B. & FERZIGER, J. H. 1995. A New Non-Eddy Viscosity Subgrid-Scale Model and Its Application to Channel Flow. *CTR Annual Research Briefs*. Stanford University.
- SMAGORINSKY, J. 1963. General Circulation Experiments with the Primitive Equations. I. The Basic Experiments. *Monthly Weather Review*, 91, 99-164.
- STOLZ, S. & ADAMS, N. A. 1999. An approximate deconvolution procedure for large-eddy simulation. *Physics of Fluids*, 11, 1699-1701.
- STOLZ, S., ADAMS, N. A. & KLEISER, L. 2001. An approximate deconvolution model for large-eddy simulation with application to incompressible wall-bounded flows. *Physics of Fluids*, 13, 997-1015.
- STOLZ, S., SCHLATTER, P., MEYER, D. & KLEISER, L. 2004. High-pass filtered eddy-viscosity models for LES. *Direct and Large-Eddy Simulation V, Proceedings*, 9, 81-88.
- TRIAS, F. X., VERSTAPPEN, R. W. C. P., GOROBETS, A., SORIA, M. & OLIVA, A. 2010. Parameter-free symmetry-preserving regularization modeling of a turbulent differentially heated cavity. *Computers & Fluids*, 39, 1815-1831.
- VAN DYKE, M. 1975. *Perturbation methods in fluid mechanics*, Stanford, Calif., Parabolic Press.
- VASILYEV, O. V., LUND, T. S. & MOIN, P. 1998. A General Class of Commutative Filters for LES in Complex Geometries. *J. Comp. Phys.*, 146, 82-104.
- VOKE, P. R. & YANG, Z. Y. 1995. Numerical Study of Bypass Transition. *Physics of Fluids*, 7, 2256-2264.
- VREMAN, B. 1995. Direct and large-eddy simulation of the compressible turbulent mixing layer. Netherlands.
- WHITE, F. M. 2006. *Viscous fluid flow*, New York, NY, McGraw-Hill Higher Education.
- WILCOX, D. C. 2006. *Turbulence modeling for CFD*, La Cãnada, Calif., DCW Industries.
- WILLIAMS, P. T. 1993. A three-dimensional, time-accurate, incompressible, Navier-Stokes, finite element CFD algorithm. Knoxville.

- WINCKELMANS, G. S., WRAY, A. A., VASILYEV, G. V. & JEANMART, H. 2001. Explicit filtering large-eddy simulations using the tensor-diffusivity model supplemented by a dynamic Smagorinsky term. *Phys. Fl.*, 13, 1385-1403.
- WINTERS, K. H. 1988. Hopf bifurcation in the double-glazing problem with conducting boundary. *J. Heat Trans.*, 109, 894–898.
- WOLFRAM RESEARCH INC 2008. Mathematica. 7.0 ed. Champaign, IL: Wolfram Research, Inc.
- XIN, S. & LE QUERE, P. 2002. An extended Chebyshev pseudo-spectral benchmark for the 8 : 1 differentially heated cavity. *International Journal for Numerical Methods in Fluids*, 40, 981-998.
- YANG, K. S. & FERZIGER, J. H. 1993. Large-Eddy Simulation of Turbulent Obstacle Flow Using a Dynamic Subgrid-Scale Model. *AIAA Journal*, 31, 1406-1413.
- ZANG, Y., STREET, R. L. & KOSEFF, J. R. 1993. A Dynamic Mixed Subgrid-Scale Model and Its Application to Turbulent Recirculating-Flows. *Physics of Fluids a-Fluid Dynamics*, 5, 3186-3196.

APPENDICES

APPENDIX A

TABLES

Table A.1: Convergence data under uniform mesh refinement

Mesh	$\ \bar{q}\ _E$	$\Delta\ \bar{q}^{\Delta h/2}\ _E$	$\ e^{\Delta h/2}\ _E$	<i>slope</i>
8x8	0.4359	-	-	-
16x16	0.7558	0.3199	0.1066	-
32x32	0.9174	0.1615	0.0538	0.9857
64x64	0.9875	0.0702	0.0234	1.2033

Table A.2: Analytical values and the slopes of \bar{u} at the wall

δ^+	δ	$\bar{u}(1)$	$d\bar{u}/dy$
36	2.0E-03	0.0563	108.64
18	1.0E-03	0.0344	142.23
9	5.0E-04	0.0184	158.36
4.5	2.5E-04	0.0093	161.53
2.25	1.25E-04	0.0047	162.25
1.125	6.25E-05	0.0023	161.62

Table A.3: Computed values and the slopes of u at the wall

δ^+	δ	$u_{AD}(1)$	du_{AD} / dy
36	2.0E-03	0.0392	137.28
18	1.0E-03	0.0203	164.53
9	5.0E-04	0.0096	170.09
4.5	2.5E-04	0.0047	174.12
2.25	1.25E-04	0.0023	184.58
1.125	6.25E-05	0.0011	198.26

Table A.4: Comparison of computed space-filtered velocity slopes at the wall

δ^+	δ	<i>n</i> nodes (to mid-channel)	$h^+(1)$	$\bar{u}(1)$	$d\bar{u}/dy$ (uniform)	$d\bar{u}/dy$ (1,001 nodes)	<i>Factor</i> *
36	2.0E-03	11	18	0.0563	159.35	108.64	0.682
18	1.0E-03	21	9	0.0344	209.51	142.23	0.678
9	5.0E-04	41	4.5	0.0184	206.42	158.36	0.767
4.5	2.5E-04	81	2.25	0.0093	192.49	161.53	0.839
2.25	1.25E-04	161	1.125	0.0047	196.59	162.25	0.822
1.125	6.25E-05	321	0.5625	0.0023	197.31	161.62	0.819

* $Factor = \frac{d\bar{u}/dy (1,001 \text{ nodes})}{d\bar{u}/dy (\text{uniform})}$

Table A.5: Uniform mesh refinement study for a constant filter measure $\delta^+ = 36$

δ^+	n_{nodes}	$h^+(1)$	δ definition	$\left(\frac{du_{AD}}{dy}\right)_{2-3-4}$	$\bar{u}(1)$	$d\bar{u}/dy$ (uniform)	$d\bar{u}/dy$ (1,001 nodes)	Factor	Abs.Err(%)
36	11	18	2h	77.10	0.0563	159.35	108.64	0.682	46.68
36	21	9	4h	192.44	0.0563	117.82	108.64	0.922	8.45
36	41	4.5	8h	184.00	0.0563	108.31	108.64	1.003	0.30
36	81	2.25	16h	157.64	0.0563	108.46	108.64	1.002	0.17
36	161	1.125	32h	146.02	0.0563	108.61	108.64	1.000	0.03
36	321	0.5625	64h	140.87	0.0563	108.64	108.64	1.000	0.00

Table A.6: Uniform mesh refinement study for a constant filter measure $\delta^+ = 18$

δ^+	<i>nnodes</i>	$h^+(1)$	δ definition	$\left(\frac{du_{AD}}{dy}\right)_{2-3-4}$	$\bar{u}(1)$	$d\bar{u}/dy$ (uniform)	$d\bar{u}/dy$ (1,001 nodes)	<i>Factor</i>	<i>Abs.Err</i> (%)
18	11	18	-	-	-	-	-	-	-
18	21	9	2h	179.28	0.0344	209.51	142.23	0.678	47.30
18	41	4.5	4h	291.39	0.0344	146.51	142.23	0.970	3.01
18	81	2.25	8h	234.18	0.0344	140.77	142.23	1.010	1.03
18	161	1.125	16h	193.16	0.0344	141.92	142.23	1.002	0.22
18	321	0.5625	32h	176.23	0.0344	142.43	142.23	0.998	0.14

Table A.7: Uniform mesh refinement study for a constant filter measure $\delta^+ = 9$

δ^+	n_{nodes}	$h^+(1)$	δ definition	$\left(\frac{du_{AD}}{dy}\right)_{2-3-4}$	$\bar{u}(1)$	$d\bar{u}/dy$ (uniform)	$d\bar{u}/dy$ (1,001 nodes)	Factor	Abs.Err(%)
9	11	18	-	-	-	-	-	-	-
9	21	9	-	-	-	-	-	-	-
9	41	4.5	2h	316.90	0.0184	206.42	158.36	0.767	30.35
9	81	2.25	4h	329.60	0.0184	156.31	158.36	1.013	1.29
9	161	1.125	8h	245.29	0.0184	156.48	158.36	1.012	1.19
9	321	0.5625	16h	200.13	0.0184	158.03	158.36	1.002	0.21

Table A.8: Uniform mesh refinement study for a constant filter measure $\delta^+ = 4.5$

δ^+	n_{nodes}	$h^+(1)$	δ definition	$\left(\frac{du_{AD}}{dy}\right)_{2-3-4}$	$\bar{u}(1)$	$d\bar{u}/dy$ (uniform)	$d\bar{u}/dy$ (1,001 nodes)	Factor	Abs.Err(%)
4.5	11	18	-	-	-	-	-	-	-
4.5	21	9	-	-	-	-	-	-	-
4.5	41	4.5	-	-	-	-	-	-	-
4.5	81	2.25	2h	350.59	0.0093	192.49	161.53	0.839	19.17
4.5	161	1.125	4h	325.34	0.0093	160.07	161.53	1.009	0.90
4.5	321	0.5625	8h	244.73	0.0093	159.90	161.53	1.010	1.01

Table A.9: Uniform mesh refinement study for a constant filter measure $\delta^+ = 2.25$

δ^+	n_{nodes}	$h^+(1)$	δ definition	$\left(\frac{du_{AD}}{dy}\right)_{2-3-4}$	$\bar{u}(1)$	$d\bar{u}/dy$ (uniform)	$d\bar{u}/dy$ (1,001 nodes)	Factor	Abs.Err(%)
2.25	11	18	-	-	-	-	-	-	-
2.25	21	9	-	-	-	-	-	-	-
2.25	41	4.5	-	-	-	-	-	-	-
2.25	81	2.25	-	-	-	-	-	-	-
2.25	161	1.125	2h	342.68	0.0047	196.59	161.53	0.822	21.70
2.25	321	0.5625	4h	325.73	0.0047	161.12	161.53	1.003	0.25

Table A.10: Thermal cavity problem parameters for $Pr = 0.7$ and $C_s = \delta = 0.05$

Ra	Re (TTTT97)	Pe (TTTT99)	$\sqrt{\frac{Pr}{Ra}}$ (TTTT29)	$\frac{1}{\sqrt{Ra \cdot Pr}}$ (TTTT47)	$\frac{C_s \cdot Re}{24}$ (TTTT58)	$\frac{C_s \cdot Pe}{12}$ (TTTT88)	$\frac{24}{\delta^2}$ (TTTT54)	$\frac{\delta^2}{24}$ (CE1)
1.0E+04	1.195E+02	8.367E+01	8.367E-03	1.195E-02	2.490E-01	3.486E-01	9.600E+03	1.042E-04
1.0E+05	3.780E+02	2.646E+02	2.646E-03	3.780E-03	7.874E-01	1.102E+00		
4.0E+05	7.559E+02	5.292E+02	1.323E-03	1.890E-03	1.575E+00	2.205E+00		
1.0E+06	1.195E+03	8.367E+02	8.367E-04	1.195E-03	2.490E+00	3.486E+00		
1.0E+07	3.780E+03	2.646E+03	2.646E-04	3.780E-04	7.874E+00	1.102E+01		
1.0E+08	1.195E+04	8.367E+03	8.367E-05	1.195E-04	2.490E+01	3.486E+01		

APPENDIX B

FIGURES

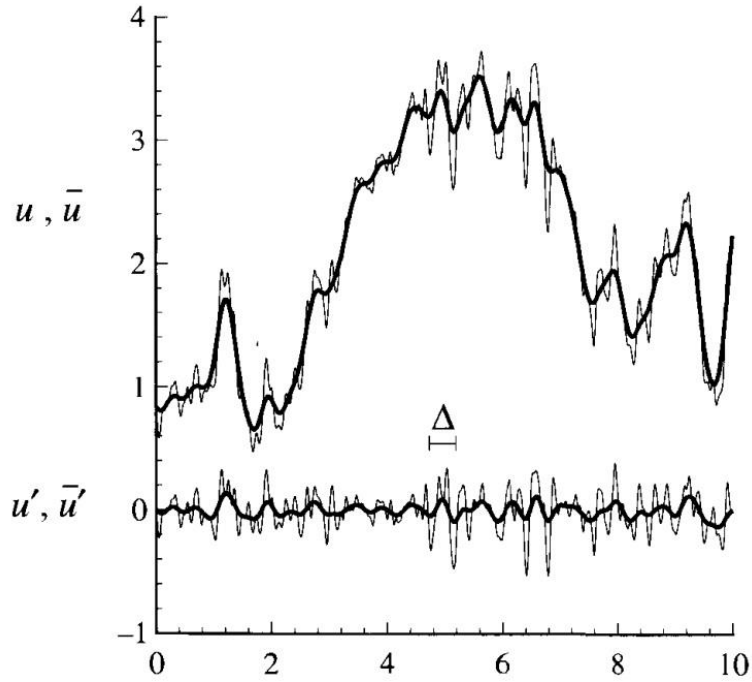


Figure B.1: A sample of the velocity field u and the corresponding space filtered velocity \bar{u} (bold line, top). The unresolved velocity field u' , and the corresponding space filtered unresolved velocity \bar{u}' (bold line, bottom) (Pope, 2000)

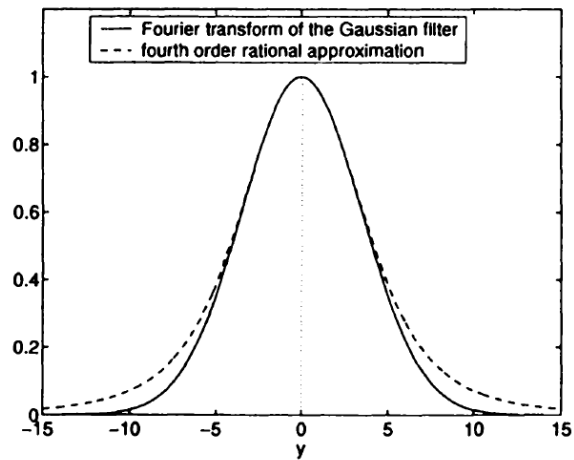
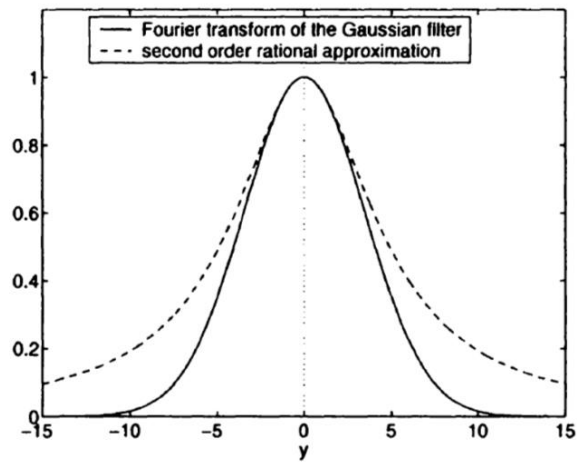
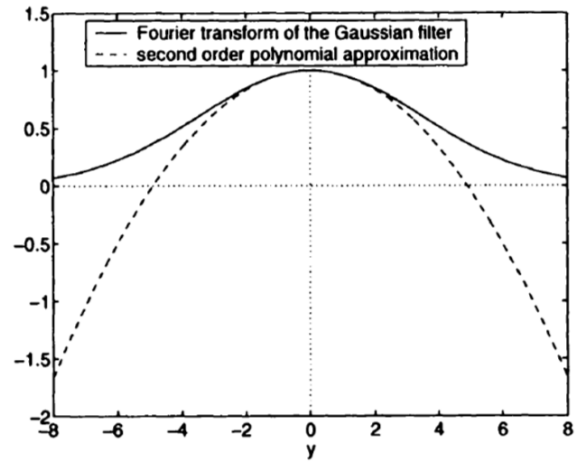


Figure B.2: Polynomial interpolation of $\mathcal{F}(g_\delta)$. Top, 2nd order Taylor series; middle, 2nd order Padé; bottom, 4th order Padé

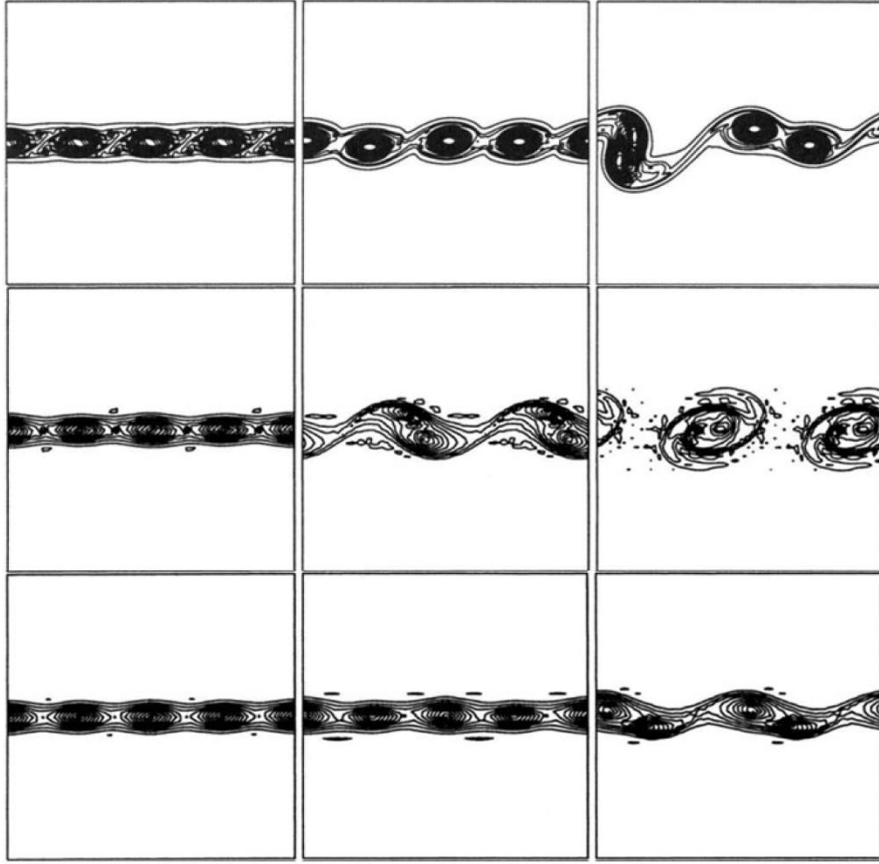


Figure B.3: Vorticity distributions from level 5 $GWS^h + \theta TS$ $rLES$ solutions \bar{u}^h , at times $n\Delta t = 50, 70, 80$ s (left to right) corresponding to (top to bottom): benchmark, auxiliary problem direct solution, auxiliary problem via convolution (John, 2004)

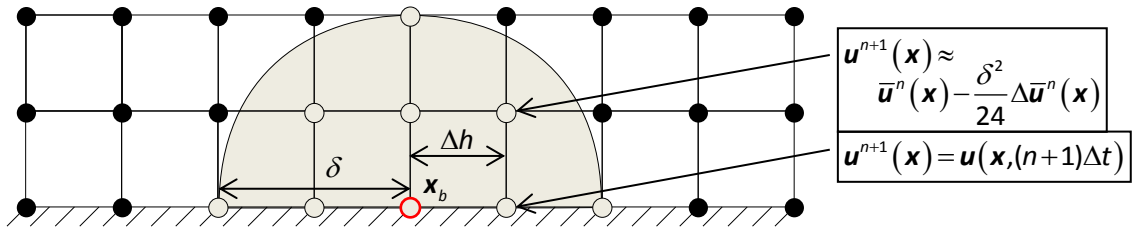


Figure B.4: Domain of integration for $\bar{u}^{n+1}(\mathbf{x}_b)$

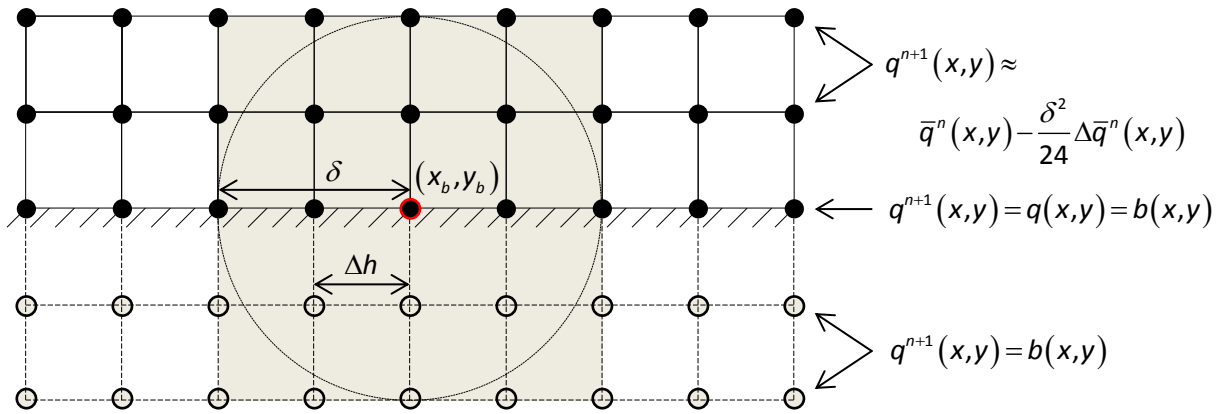


Figure B.5: Filtering through the wall with extended q

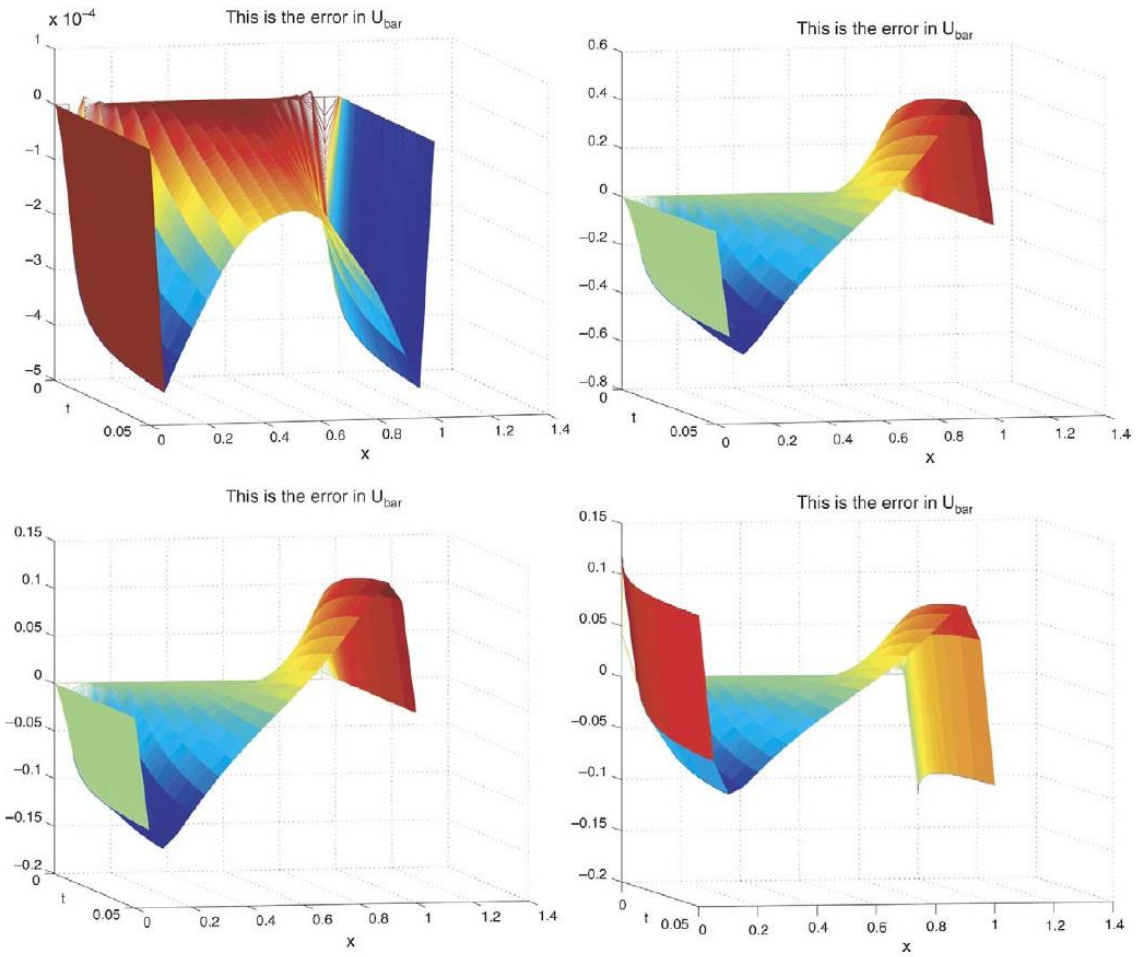


Figure B.6: Errors in \bar{q} (Borggaard and Iliescu, 2006)

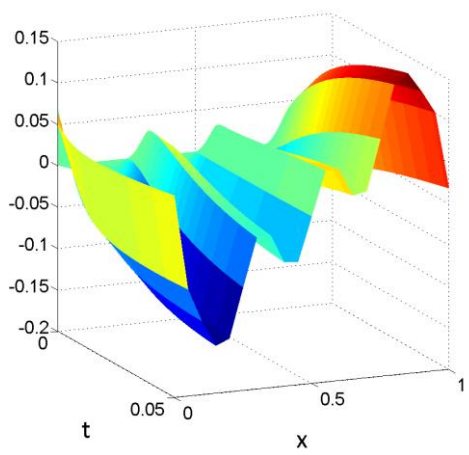
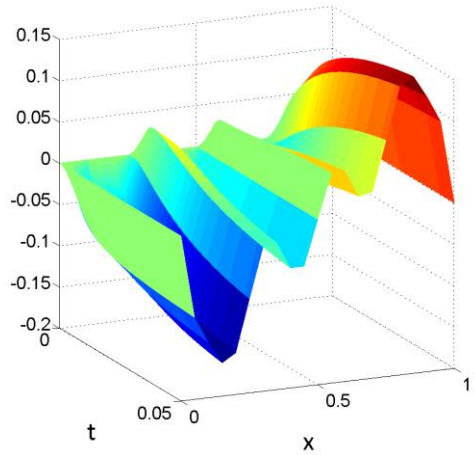
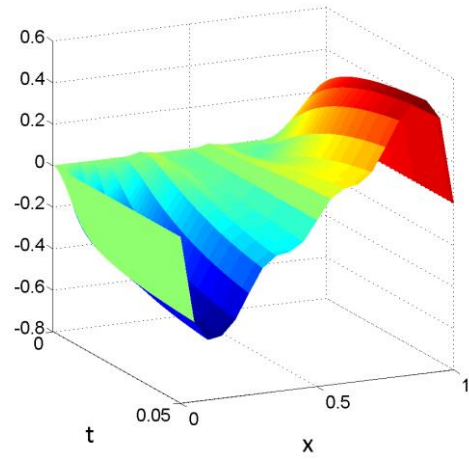
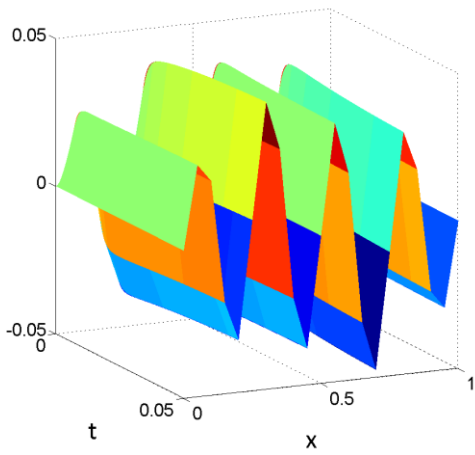


Figure B.7: Errors in \bar{q} (this study)

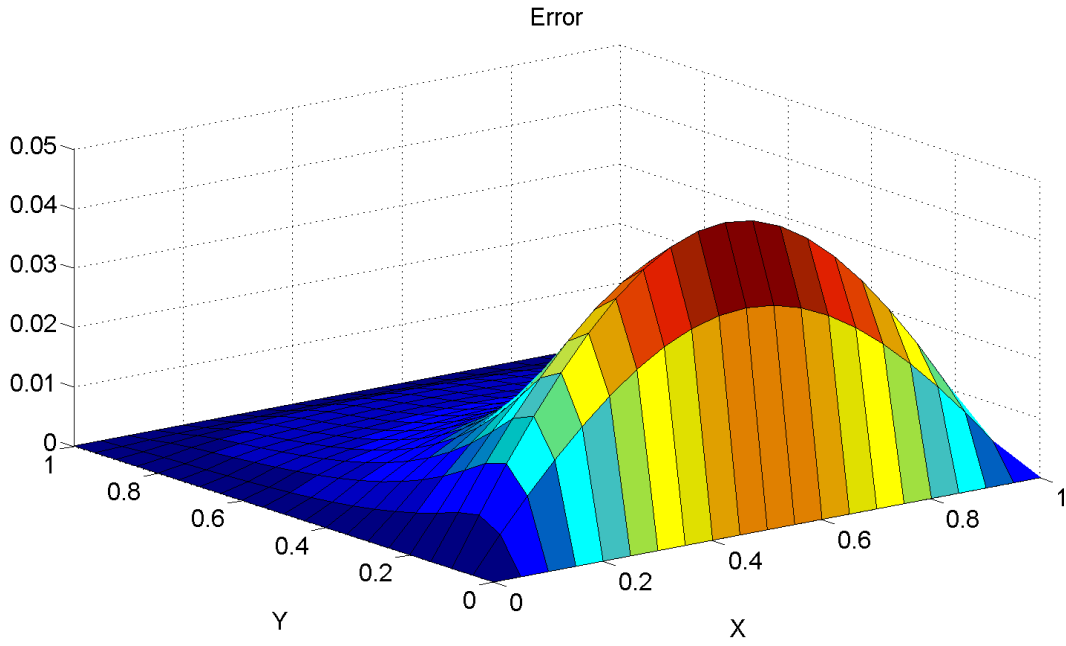


Figure B.8: Test 1a - Exact boundary conditions (q is not extended outside of Ω), exact BCE integral

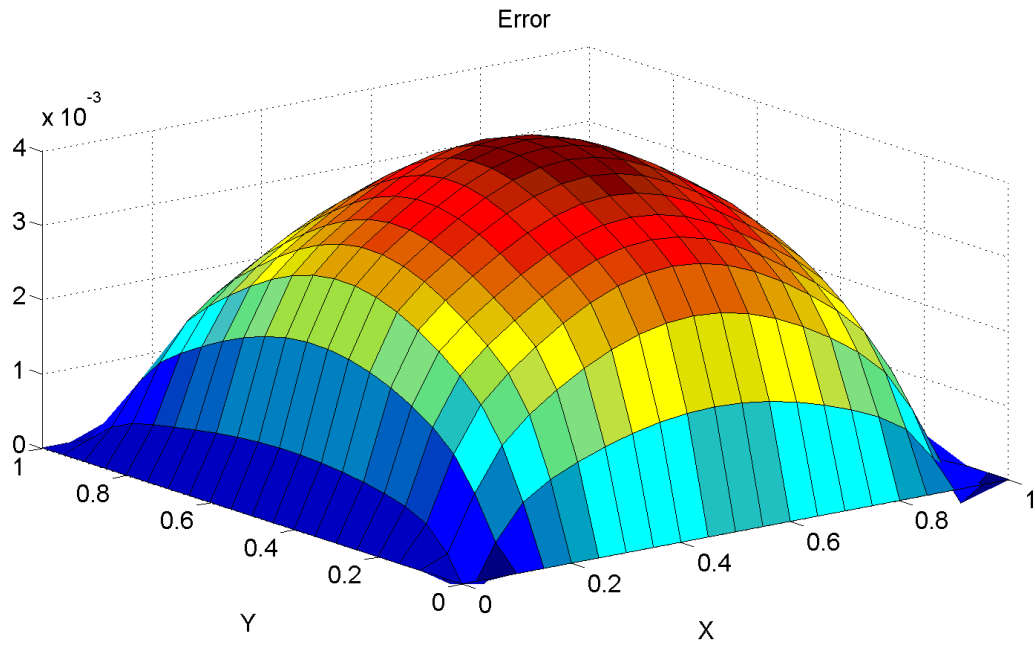


Figure B.9: Test 1b - Exact boundary conditions (q is extended outside of Ω), exact BCE integral

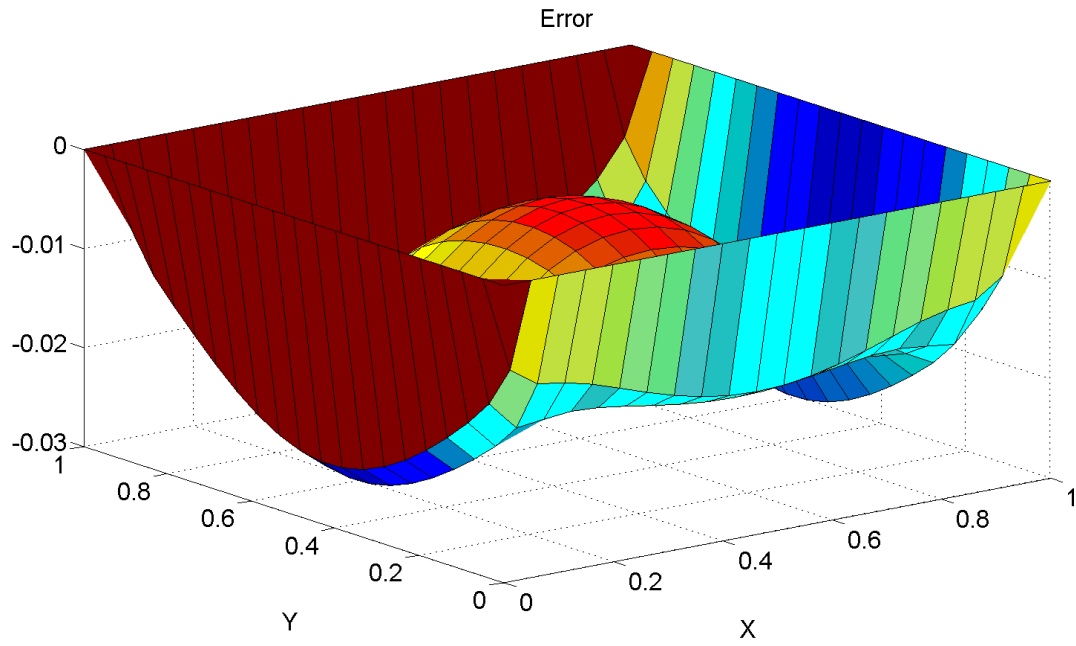


Figure B.10: Test 2 - Exact boundary conditions, no BCE integral

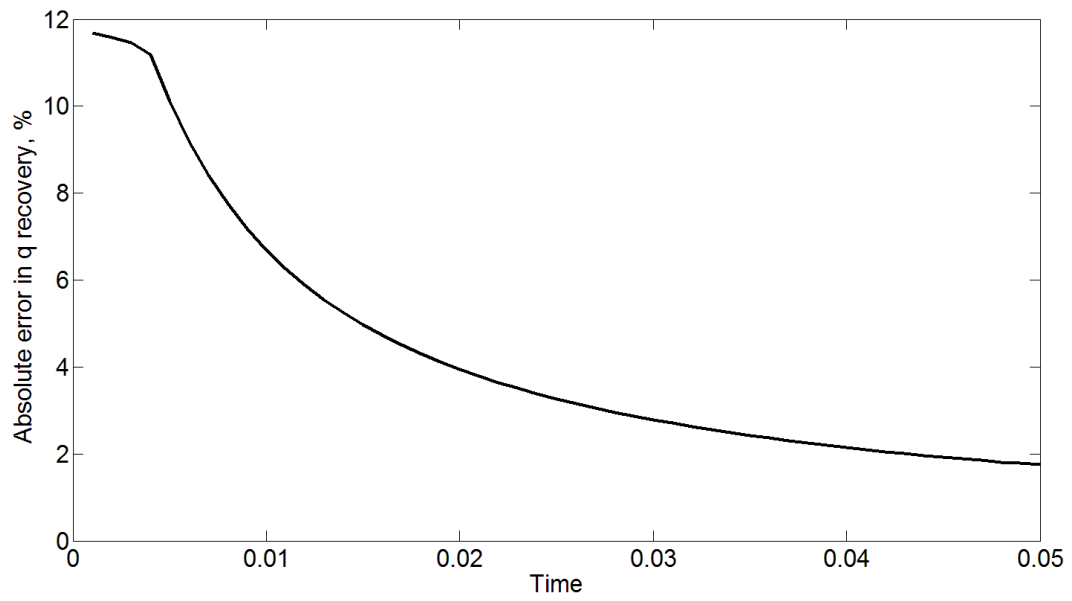


Figure B.11: Test 1b - Absolute error in approximating q using the AD formula

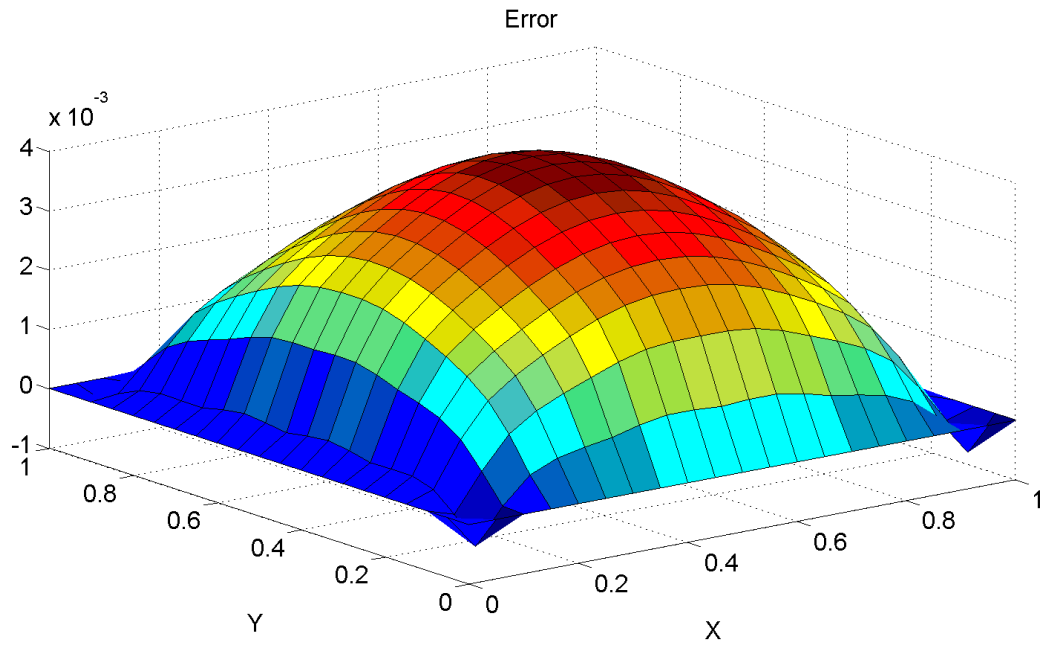


Figure B.12: Test 3 - Exact boundary conditions, approximate BCE integral

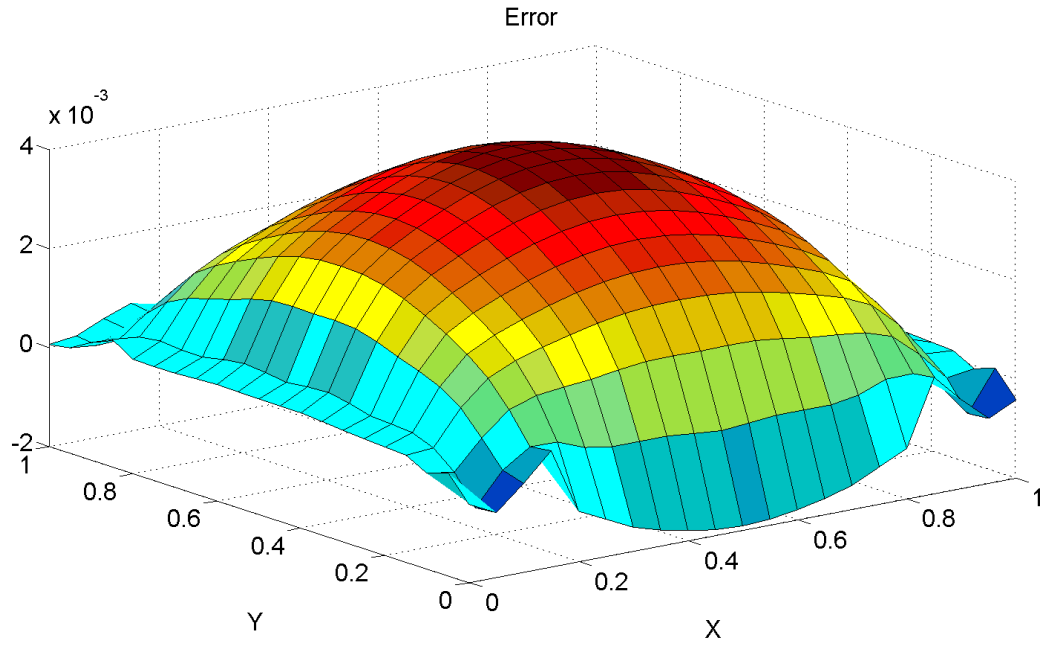


Figure B.13: Test4 - Approximate boundary conditions, approximate BCE integral

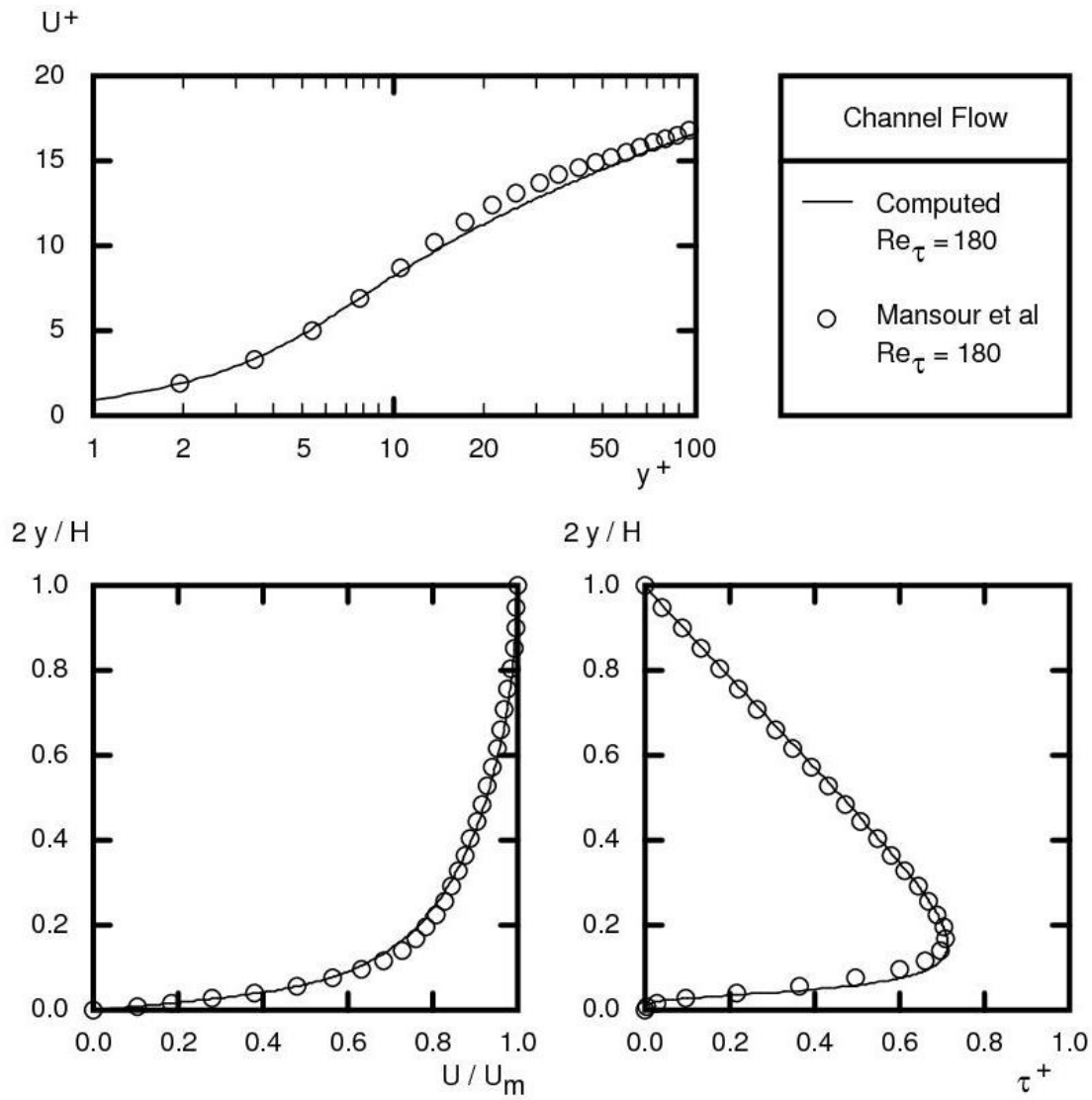


Figure B.14: Comparison of the computed and DNS solutions for $Re^+ = 180$

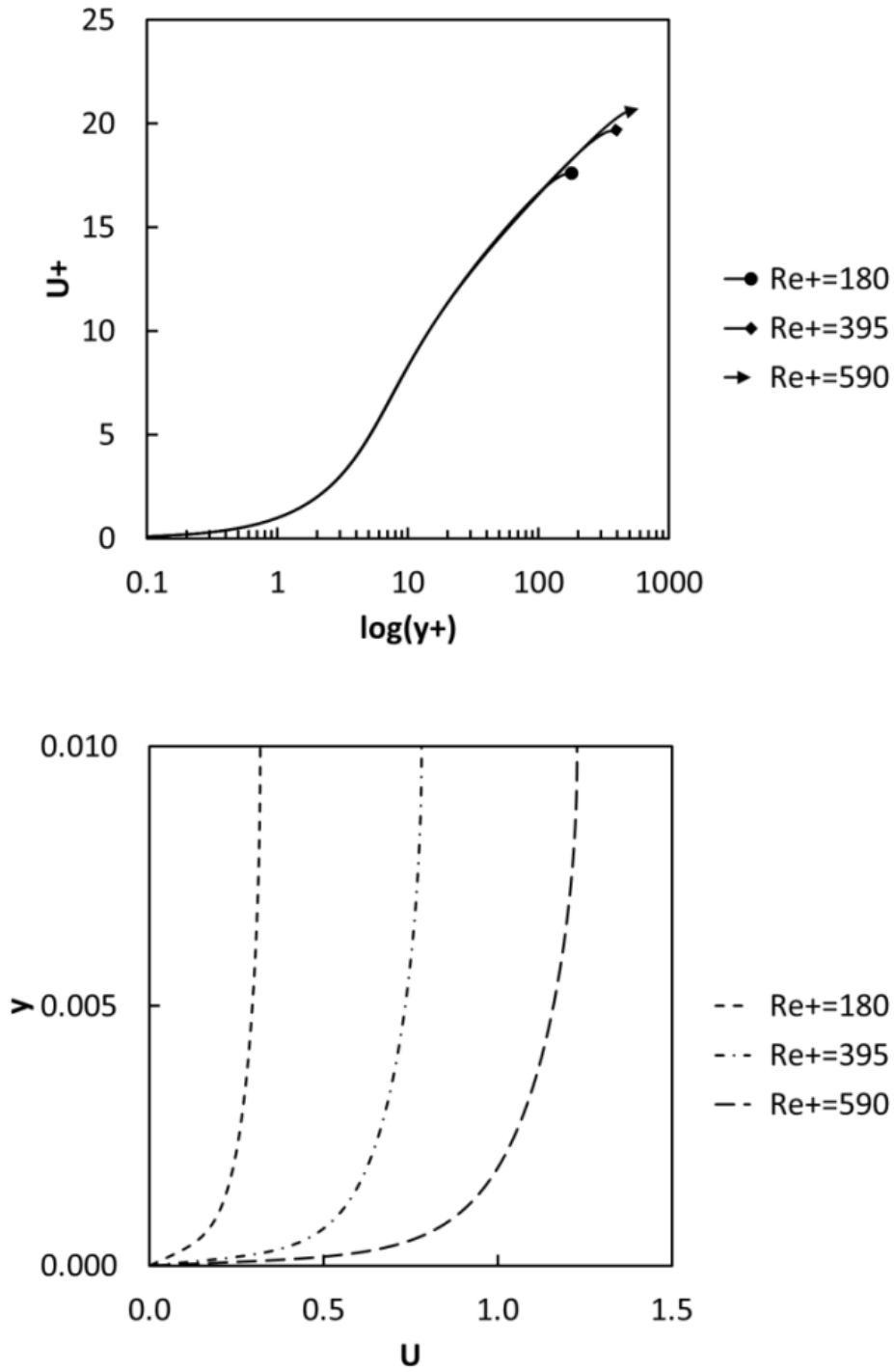


Figure B.15: Similarity space (top) and physical space (bottom) velocity profiles

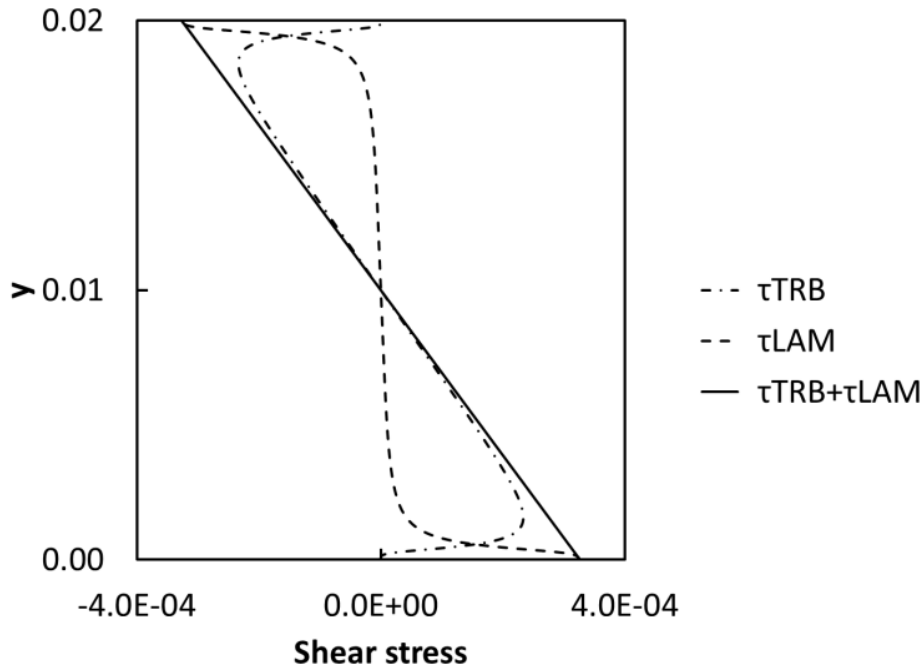


Figure B.16: Shear stress profiles for $Re^+ = 180$

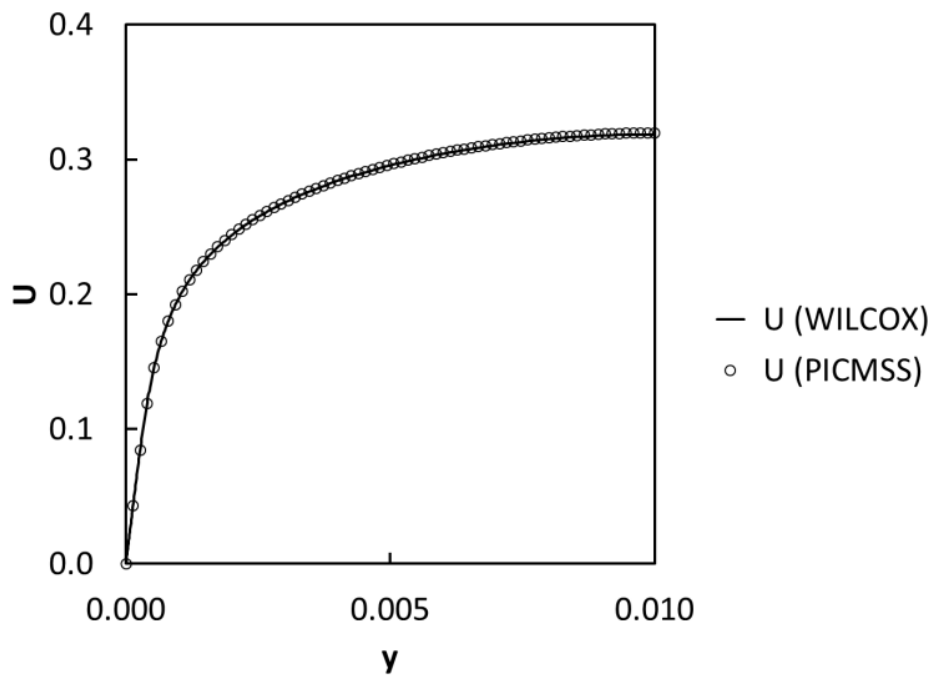
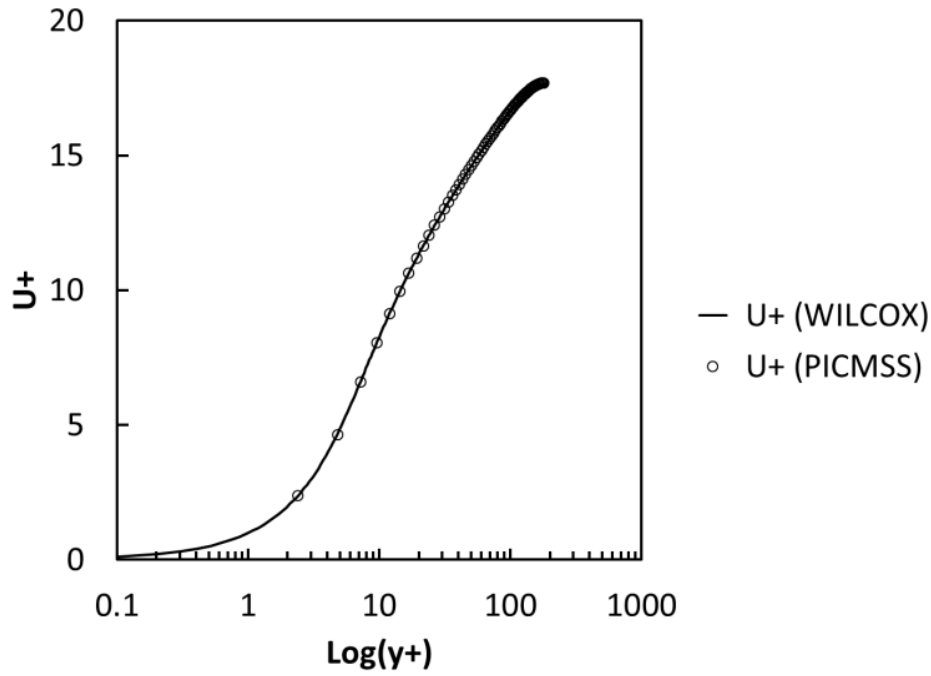


Figure B.17: Comparison of computed (PICMSS) and reference (WILCOX) velocity profiles in similarity space (top) and physical space (bottom)

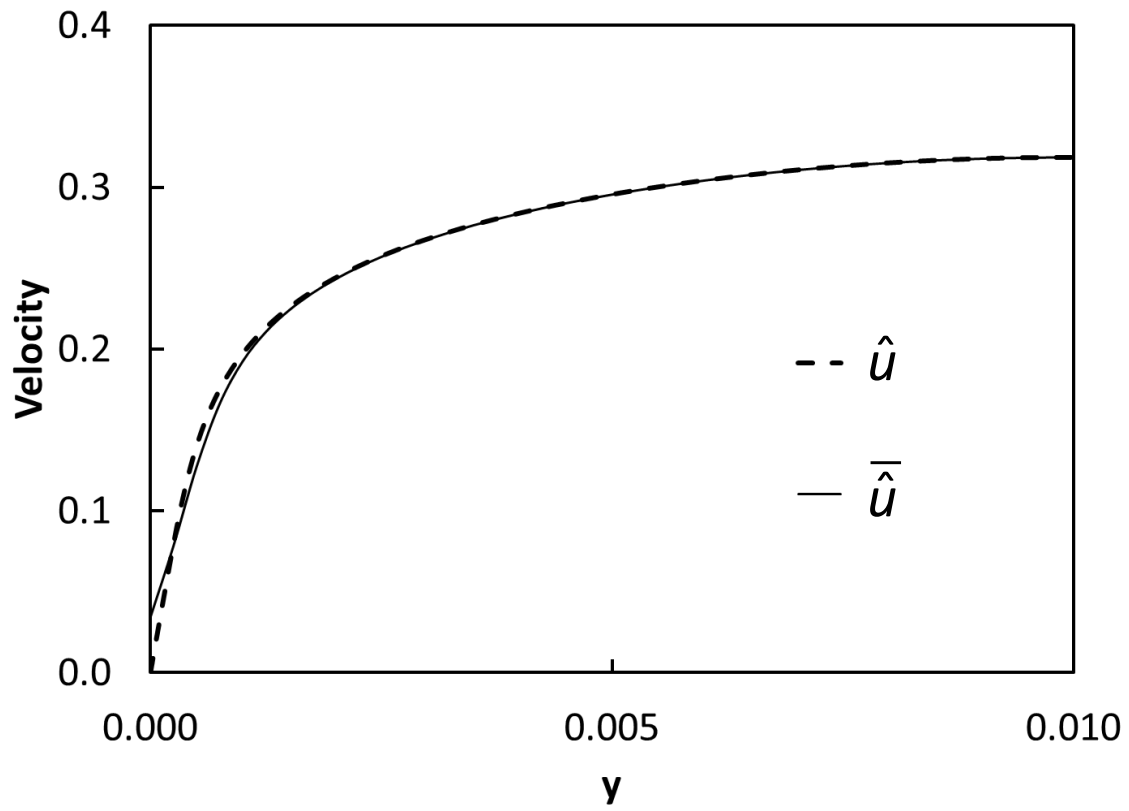


Figure B.18: Action of space filtering on the velocity profile with $\delta = 0.001$

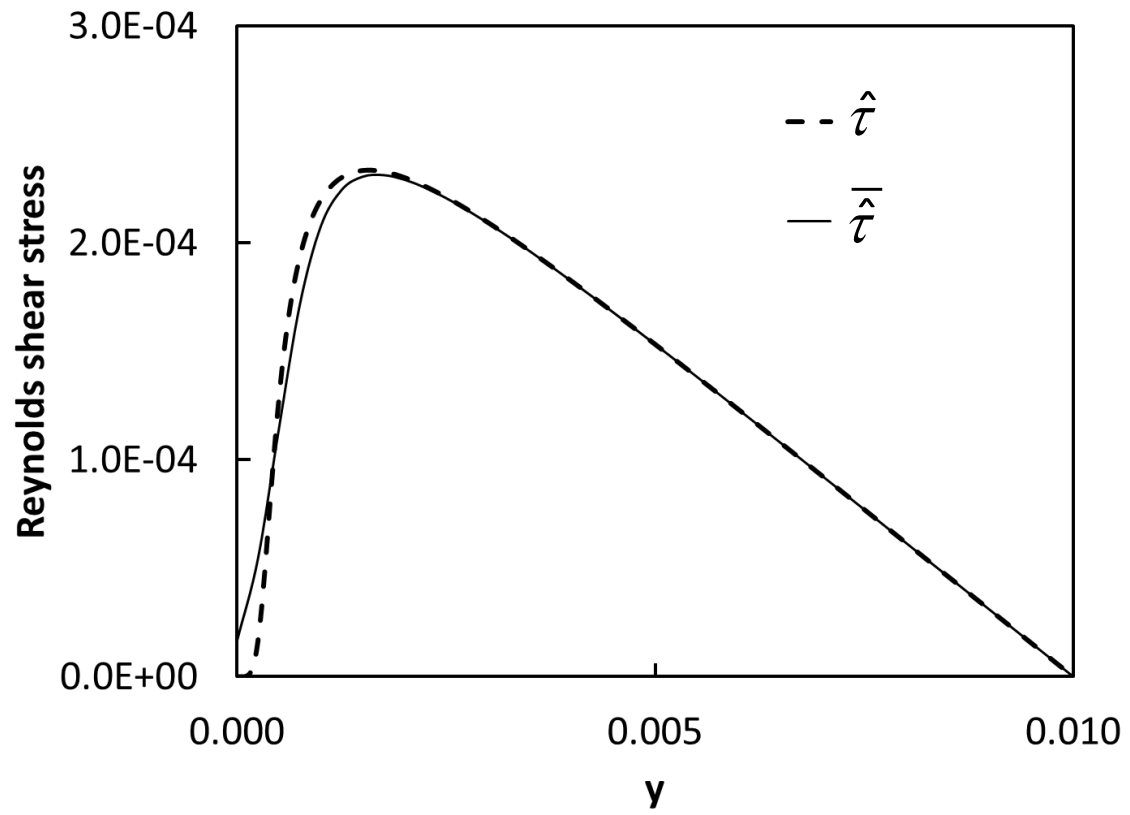


Figure B.19: Action of space filtering on the Reynolds stress profile with $\delta = 0.001$

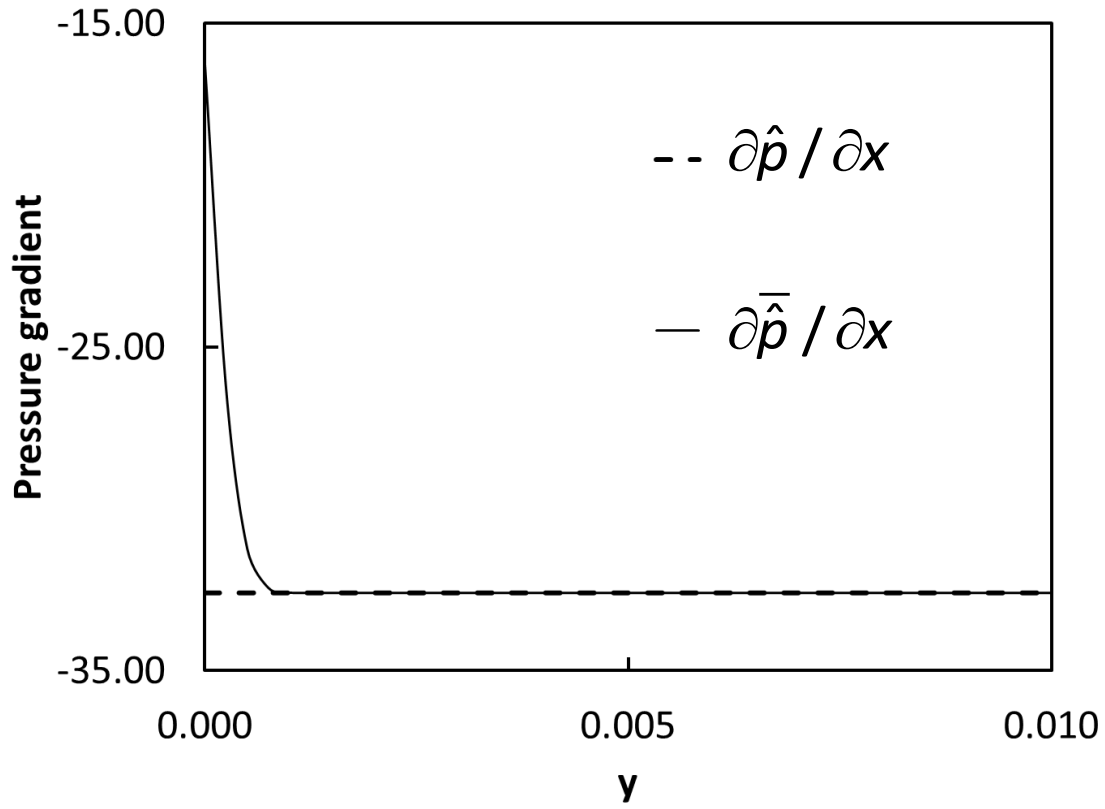


Figure B.20: Action of space filtering on the constant pressure gradient profile, $\partial p / \partial x = -32.595$, with $\delta = 0.001$

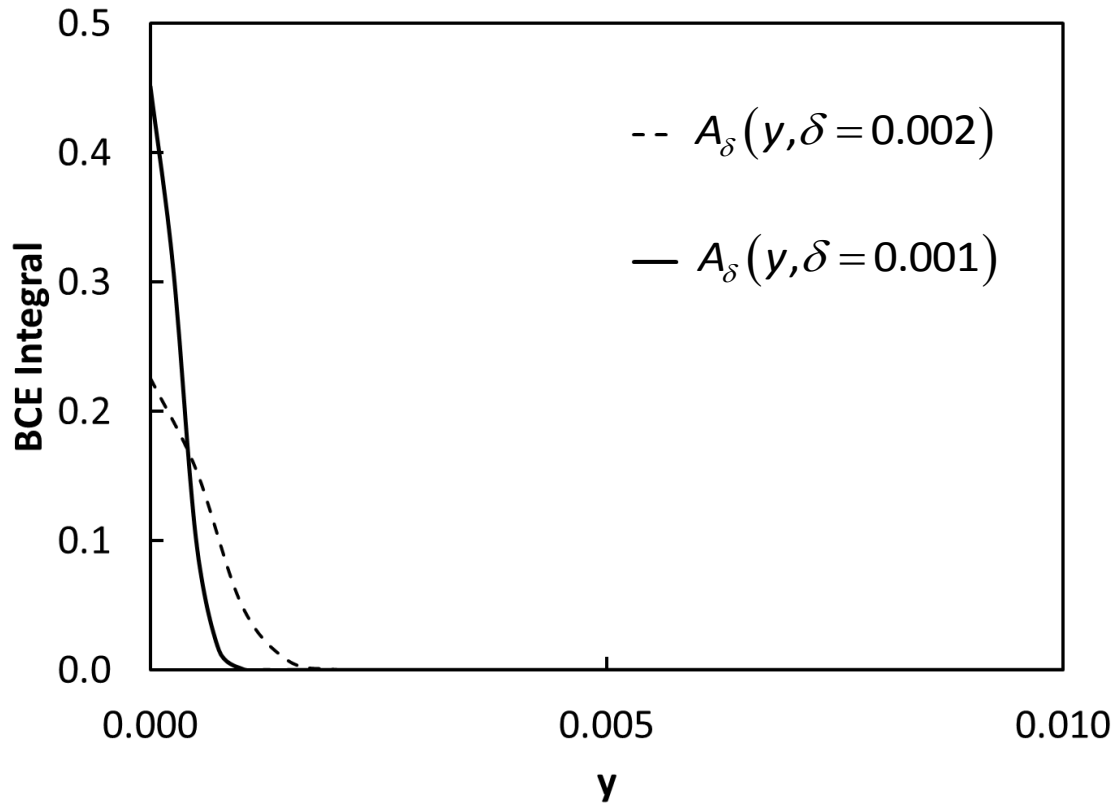


Figure B.21: The BCE integral as a function of filter measure

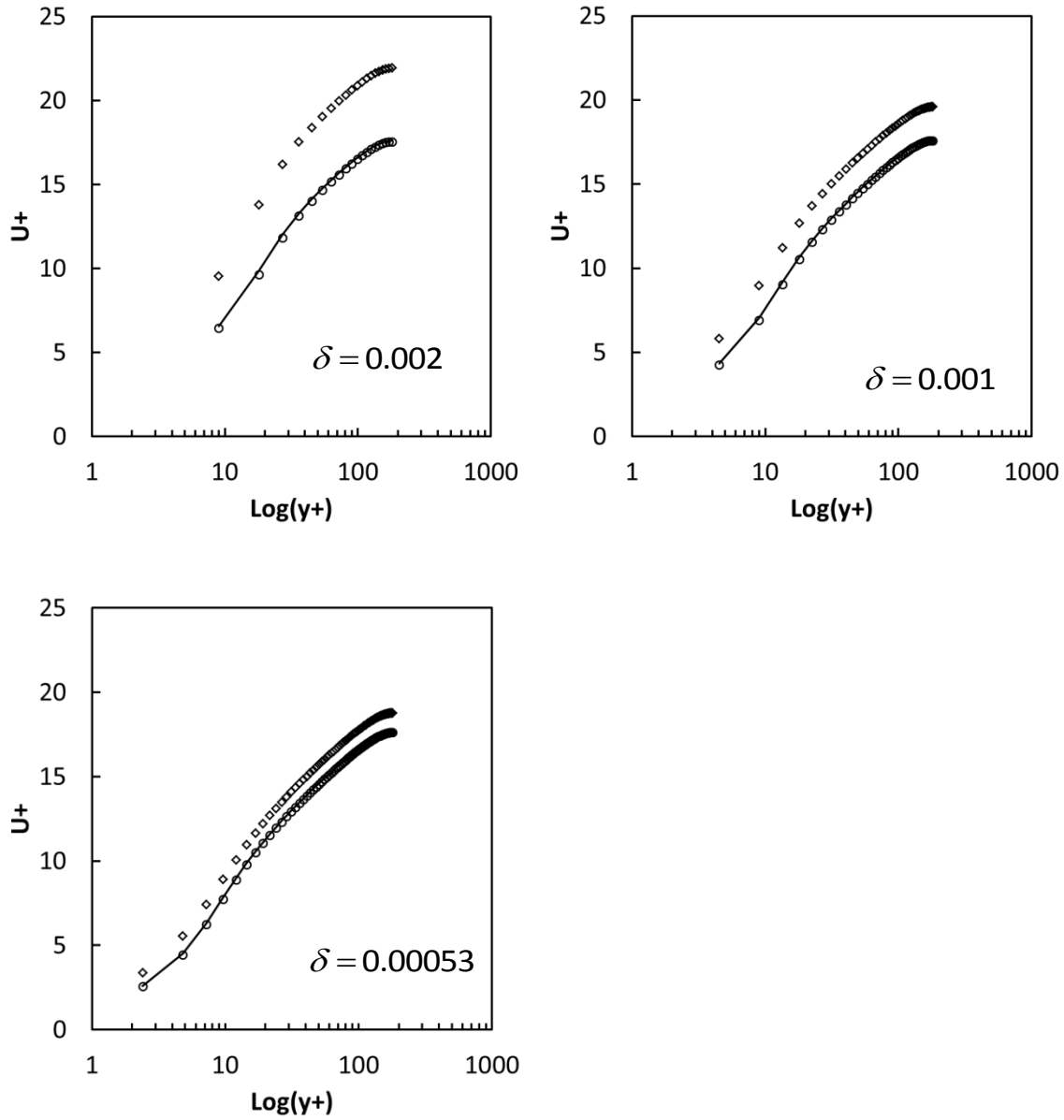


Figure B.22: The importance of the BCE term. Solid line – analytical \bar{u}^+ , circle – computed \bar{u}^+ with BCE term, diamond – computed \bar{u}^+ without BCE term

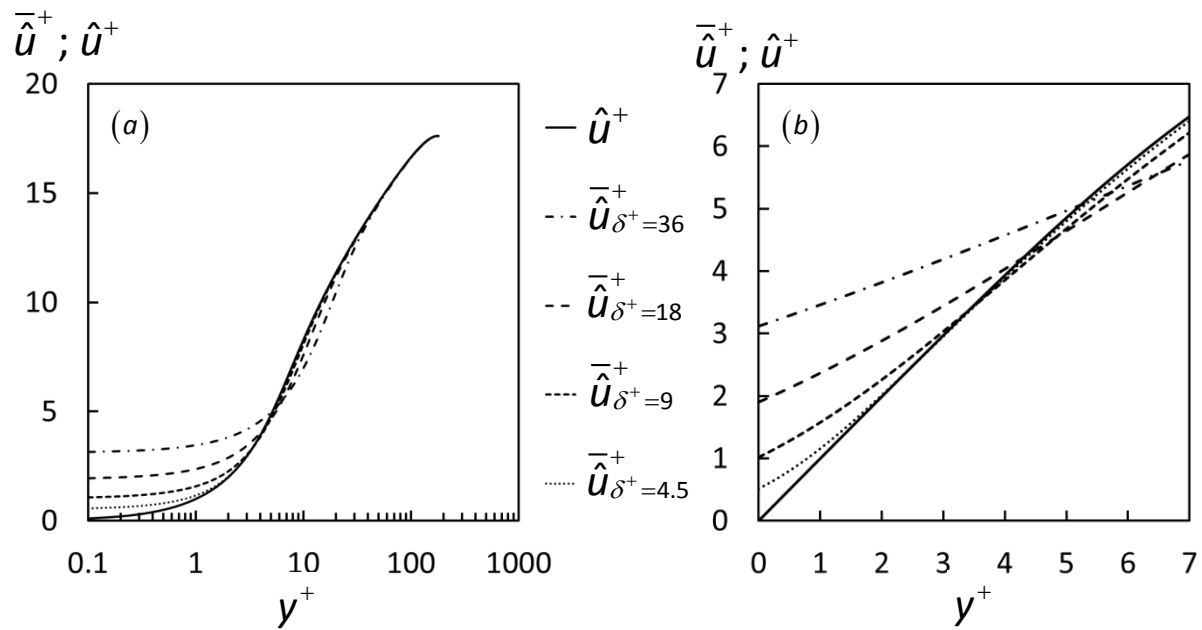


Figure B.23: Comparison of a time-averaged velocity profile with four space-filtered velocity profiles for different filter measures: (a) full-size profile with logarithmic scale; (b) close-up of the viscous sublayer without the logarithmic scale.

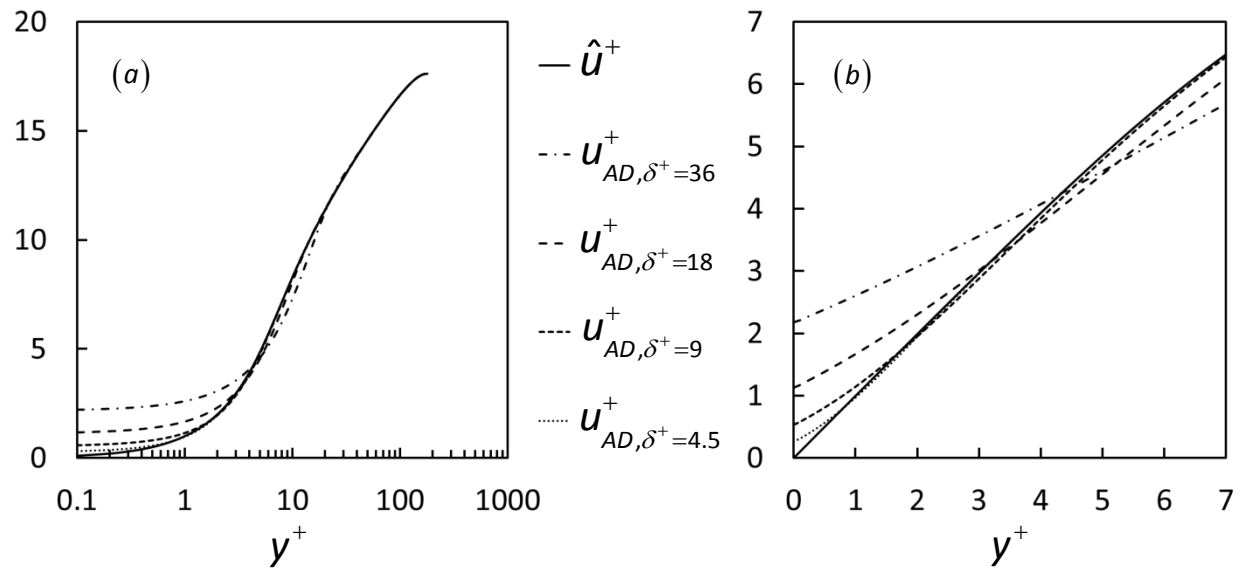


Figure B.24: Comparison of a time-averaged velocity profile with the unfiltered velocity profiles for different filter measures: (a) full-size profile with logarithmic scale; (b) close-up of the viscous sublayer without a logarithmic scale

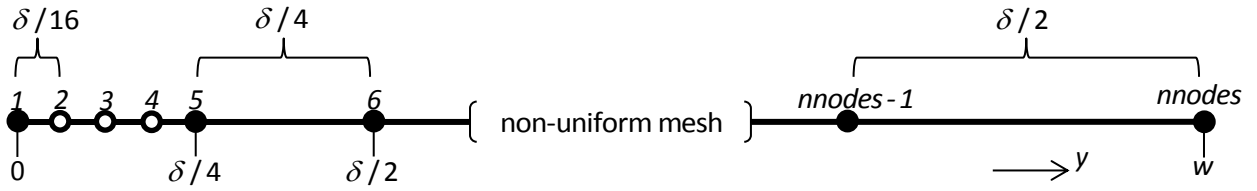


Figure B.25: Optimal mesh construction

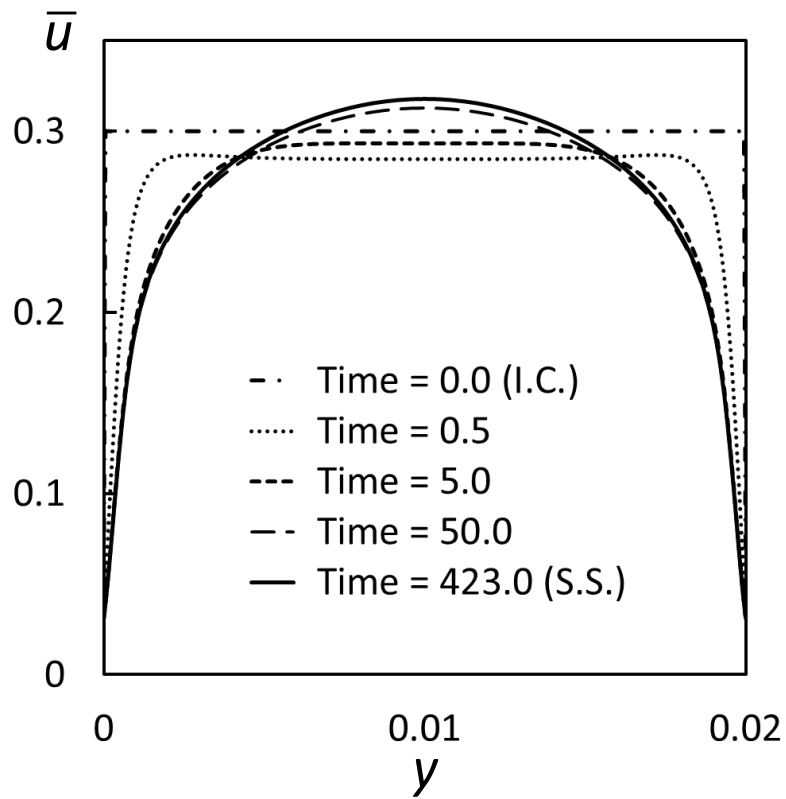


Figure B.26: Evolution of the space-filtered velocity profile for $Re^+ = 180$ (exact BCs, exact BCE)

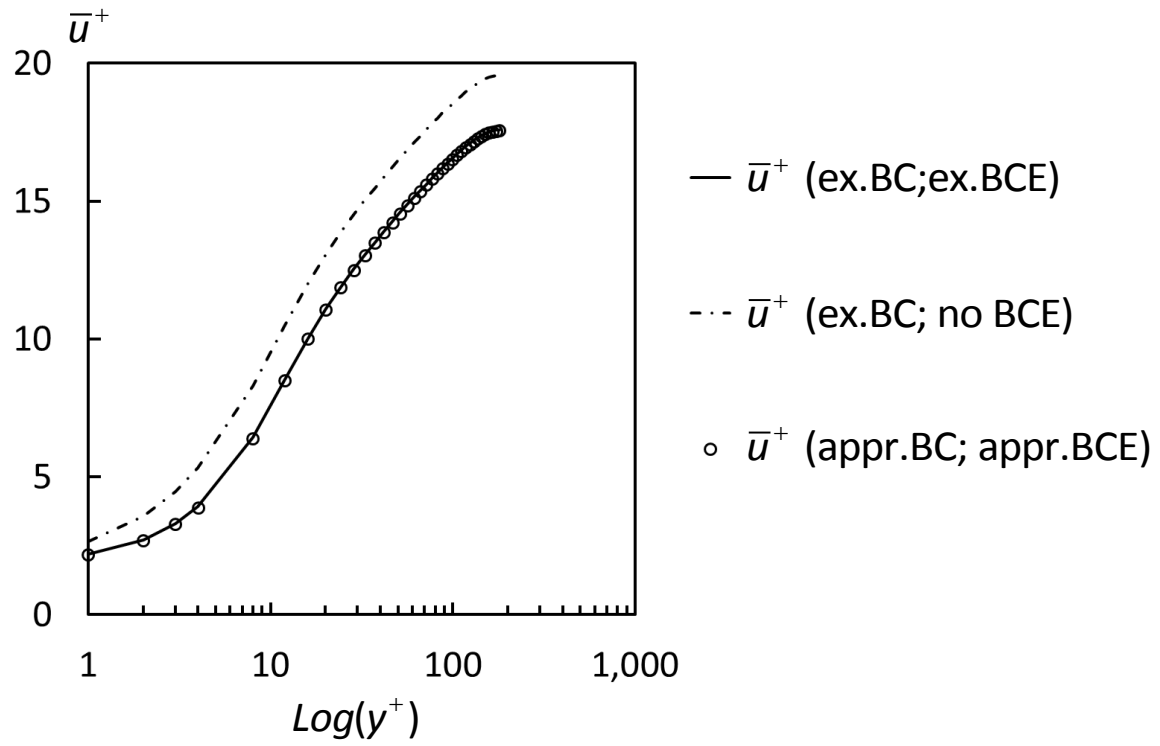


Figure B.27: Computed solutions for three case studies

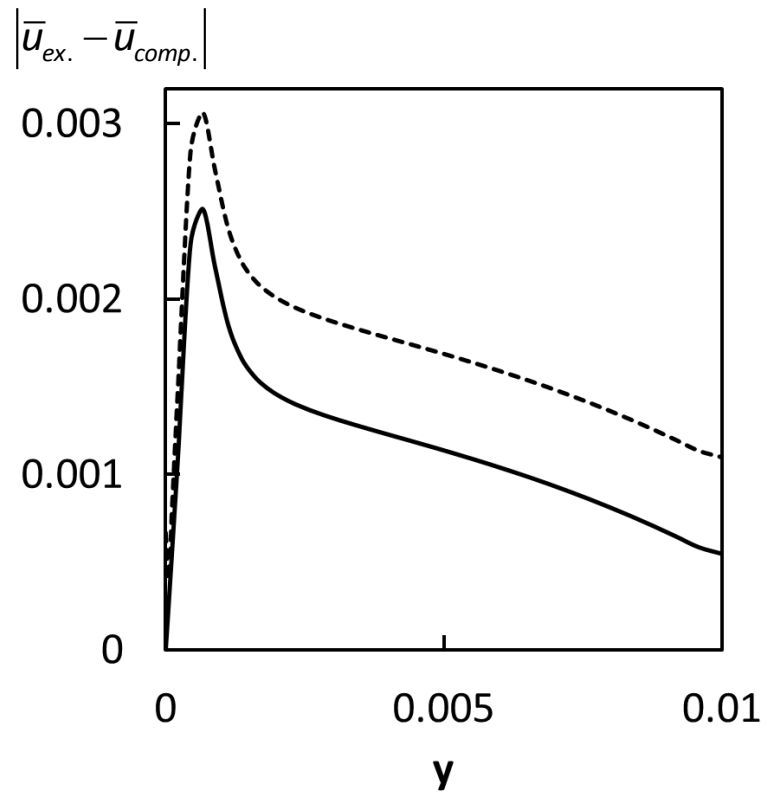


Figure B.28: Error analysis: solid line – exact BCs and BCE; dashed line – approximate BCs and BCE

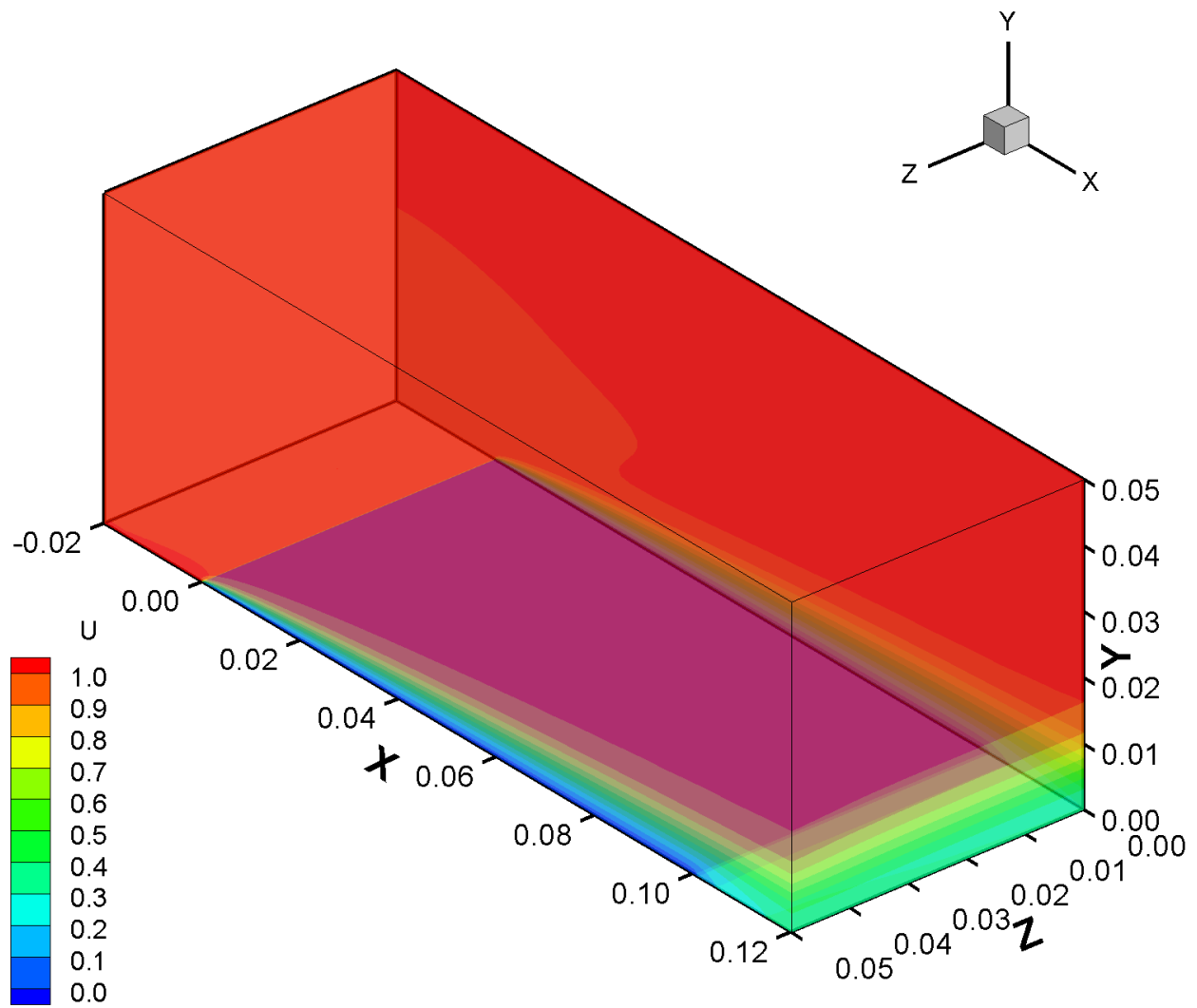
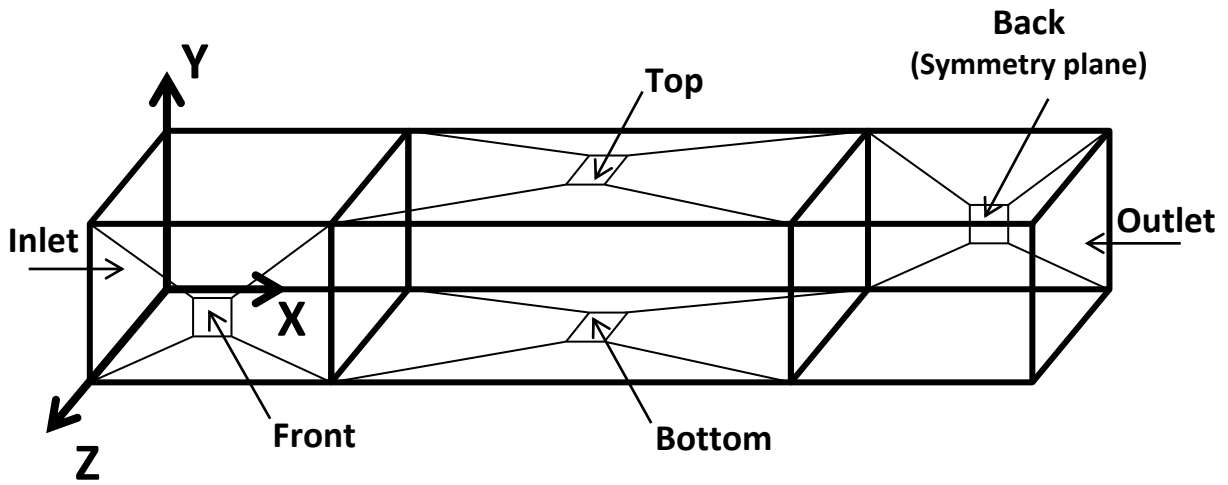


Figure B.29: Boundary layer development for flow over a flat plate. Free stream velocity $u = 1$ m/s



	u	v	w	φ
Front 1			$w = 0$	
Front 2				$\varphi = 0$
Front 3				$\varphi = 0$
Bottom 1		$v = 0$		
Bottom 2	$u = 0$	$v = 0$	$w = 0$	
Bottom 3		$v = 0$		
Back 1			$w = 0$	
Back 2			$w = 0$	
Back 3			$w = 0$	
Top 1		$v = 0$		
Top 2				$\varphi = 0$
Top 3				$\varphi = 0$
Inlet	$u = 1$	$v = 0$	$w = 0$	
Outlet				$\varphi = 0$

Figure B.30: Dirichlet boundary conditions for a flat plate with symmetry plane. Empty cells in the table imply zero Neumann, or do-nothing BCs

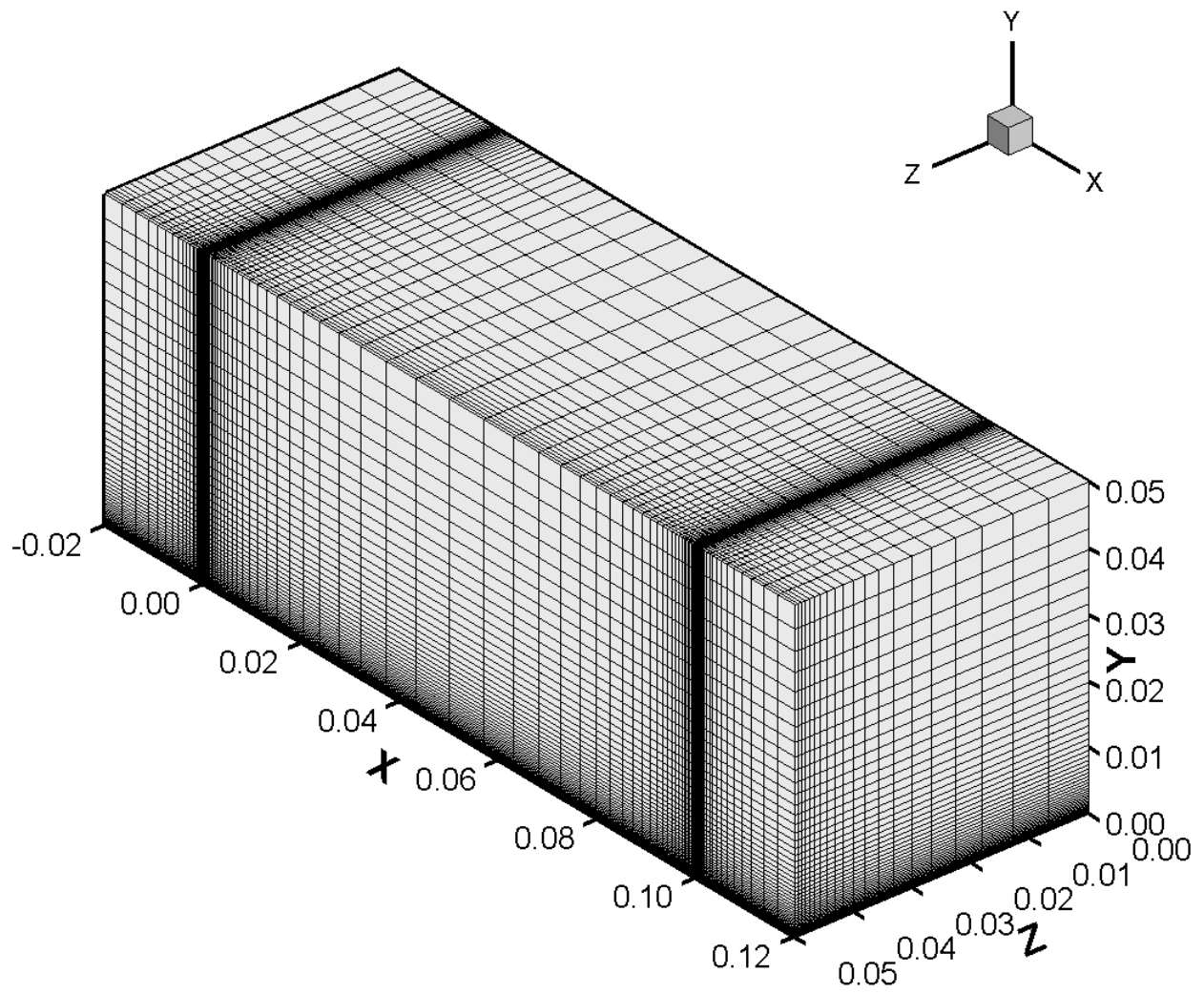


Figure B.31: Computational mesh for flow over a flat plate

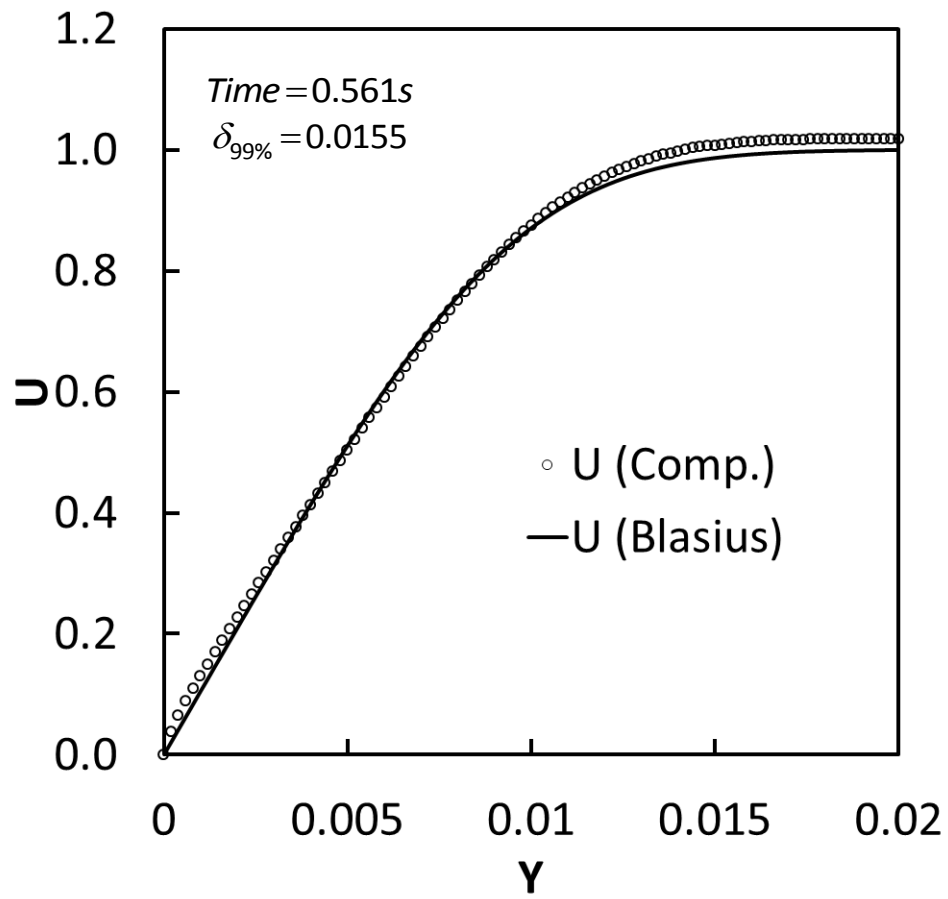


Figure B.32: Flat-plate computed and similarity solutions for $Re = 1E3$

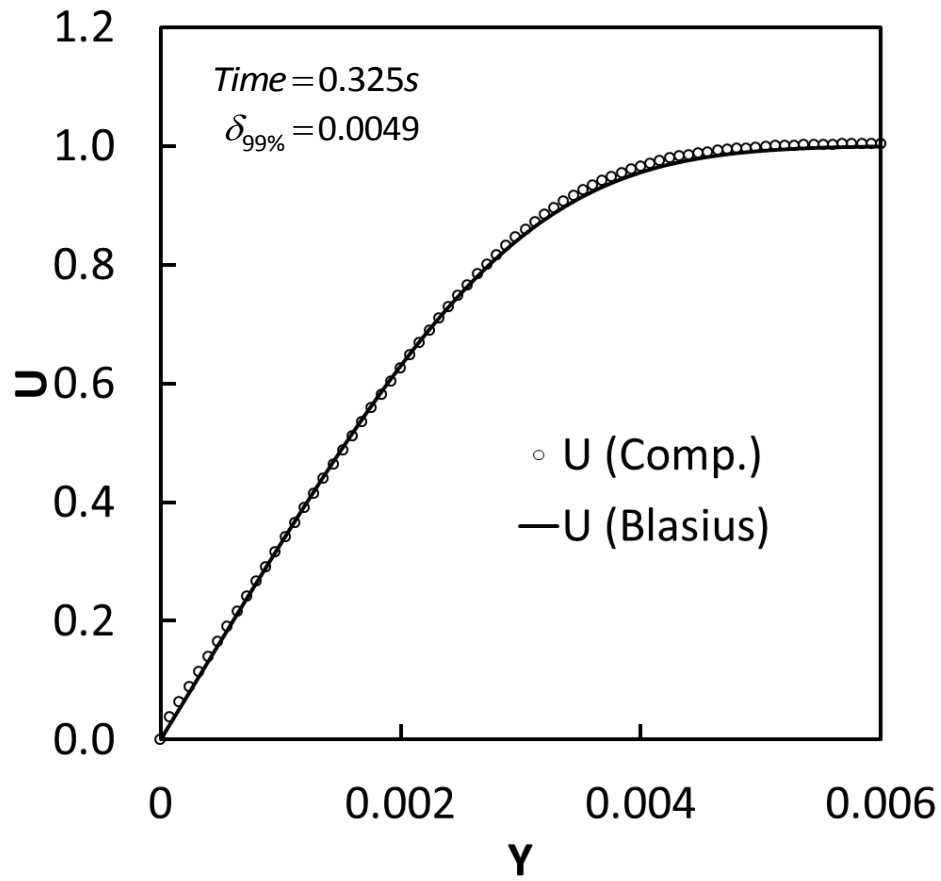


Figure B.33: Flat-plate computed and similarity solutions for $Re = 1E4$

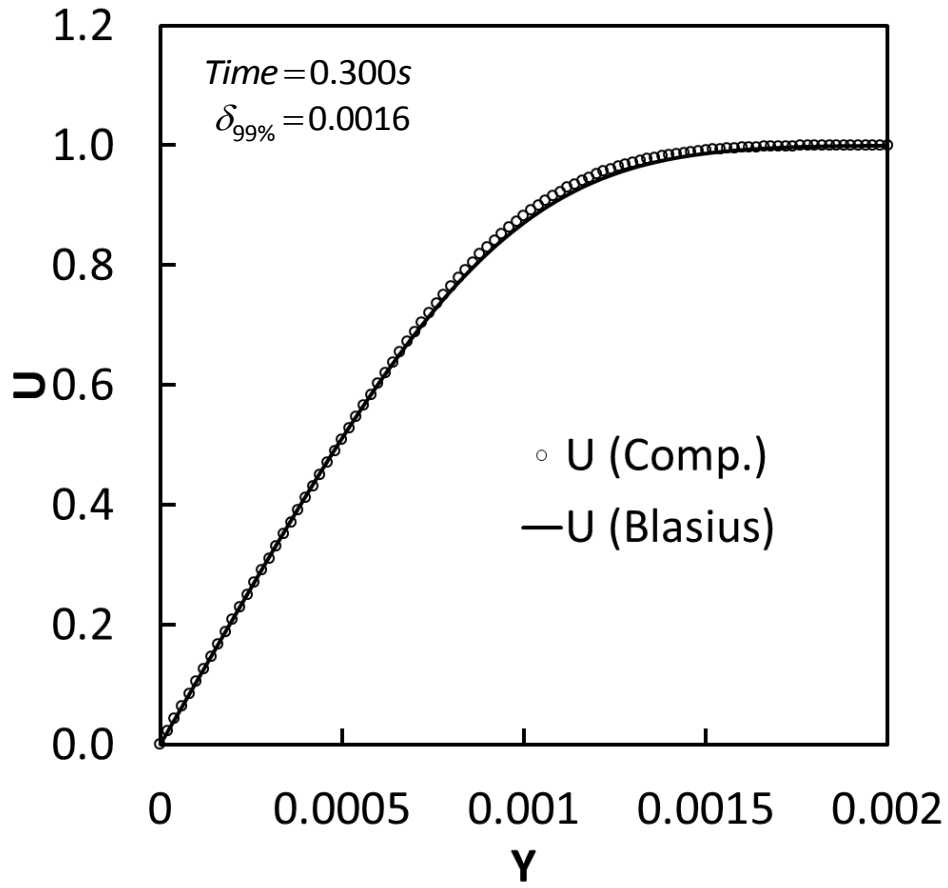


Figure B.34: Flat-plate computed and similarity solutions for $Re = 1E5$

Flow over a flat plate
(V velocity component)

Re = 1,000
x-y plane at z=0.0
Time = 0.561

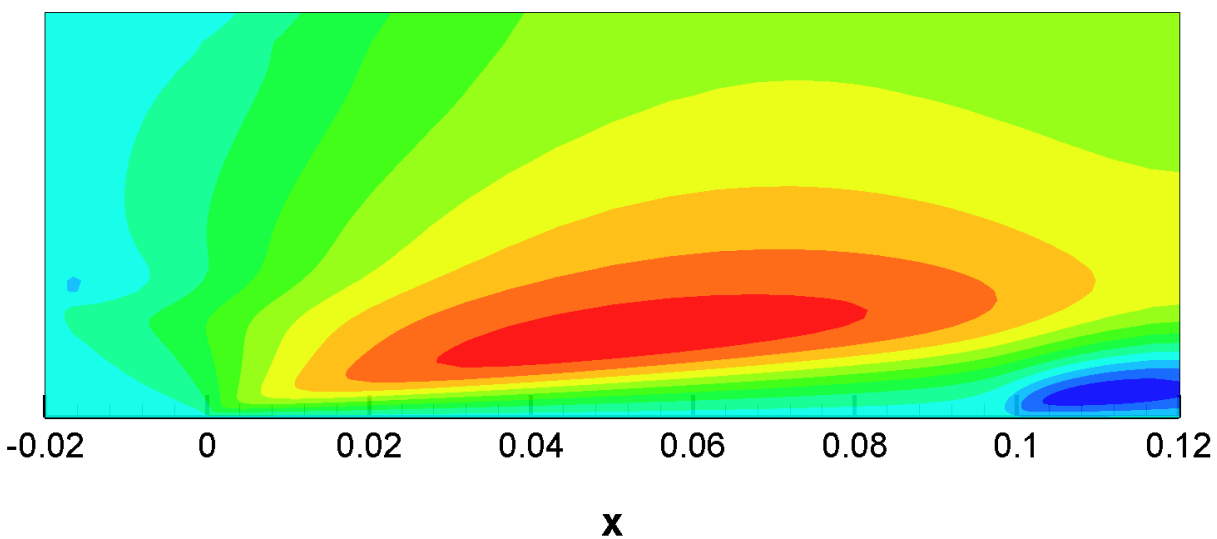
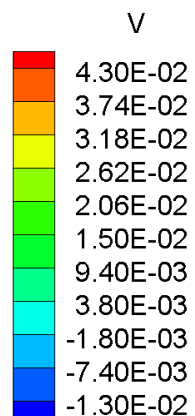
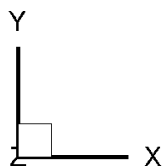


Figure B.35: Flat-plate second velocity component distribution for Re = 1E3

Flow over a flat plate
(V velocity component)

Re = 10,000
x-y plane at z=0.0
Time = 0.325

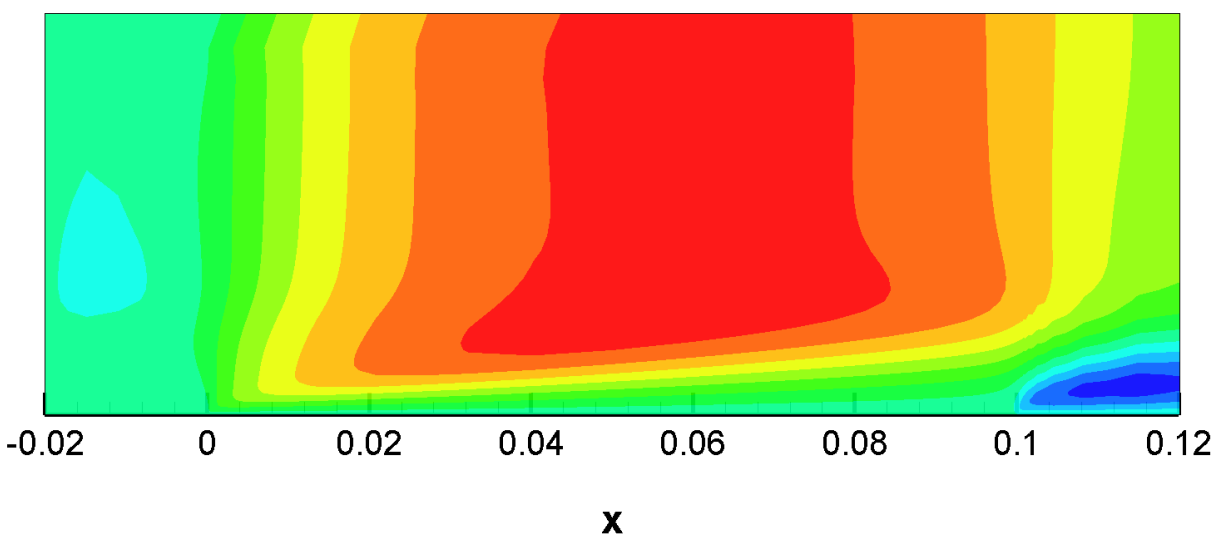
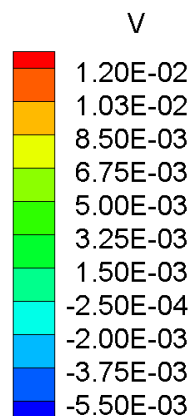
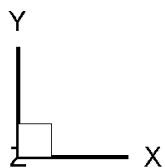


Figure B.36: Flat-plate second velocity component distribution for Re=1E4

Flow over a flat plate
(V velocity component)

Re = 100,000
x-y plane at z=0.0
Time = 0.300

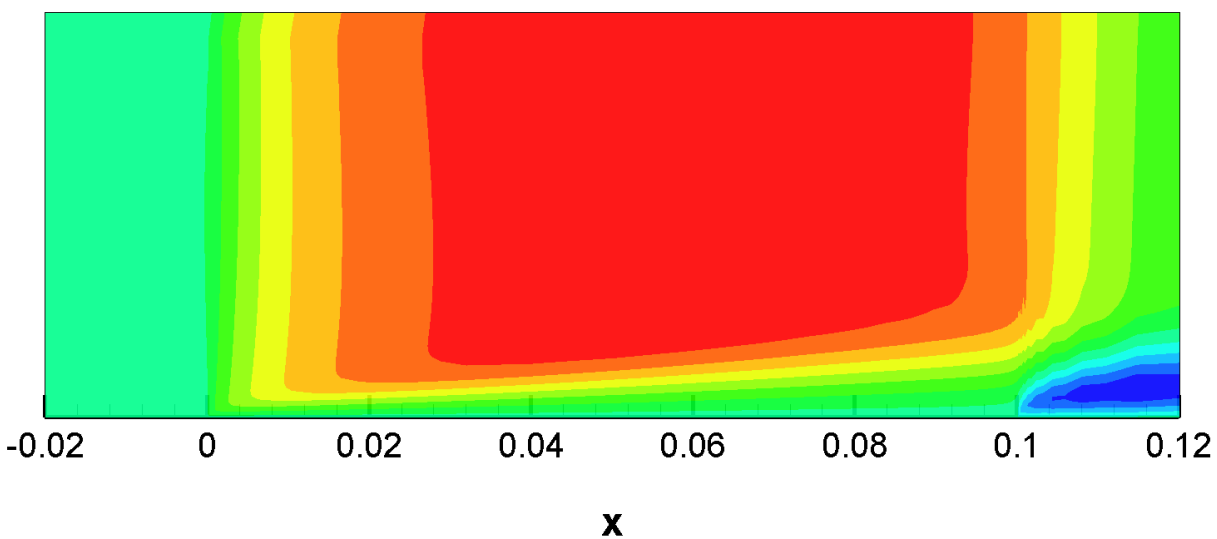
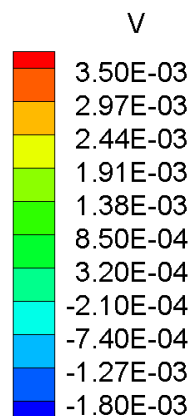
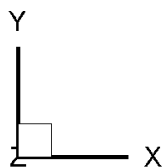


Figure B.37: Flat-plate second velocity component distribution for Re = 1E5

Flow over a flat plate
(W velocity component)

Re = 1,000
x-y plane at z=0.05
Time = 0.561

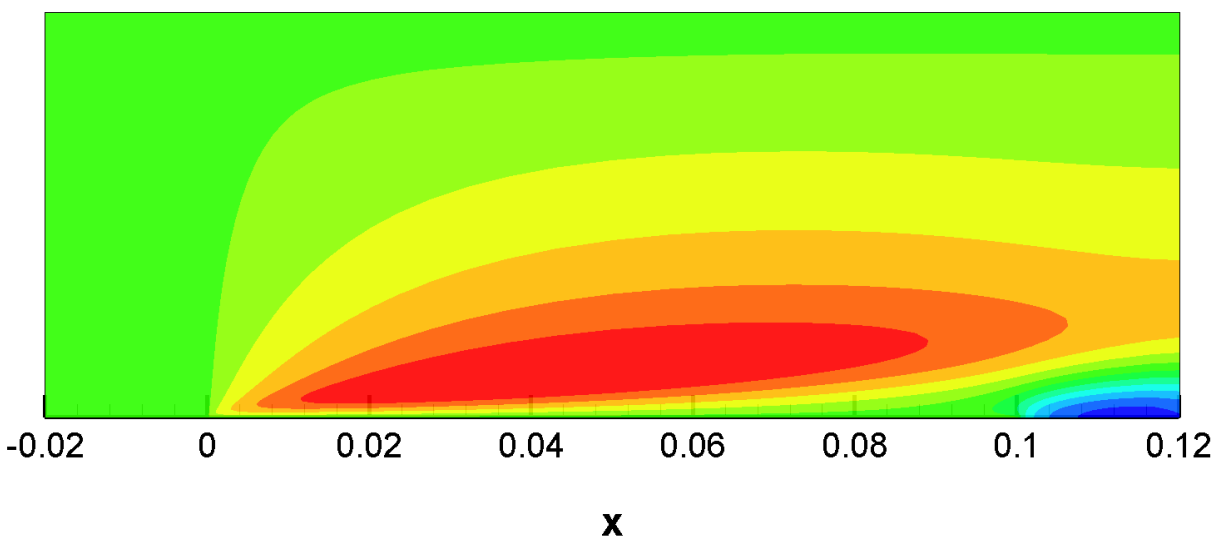
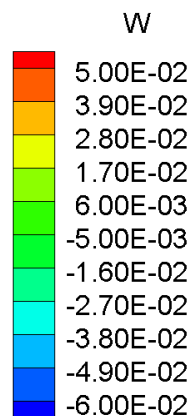
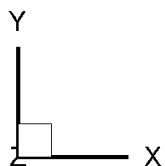


Figure B.38: Flat-plate third velocity component distribution for Re = 1E3

Flow over a flat plate
(W velocity component)

Re = 10,000
x-y plane at z=0.05
Time = 0.325

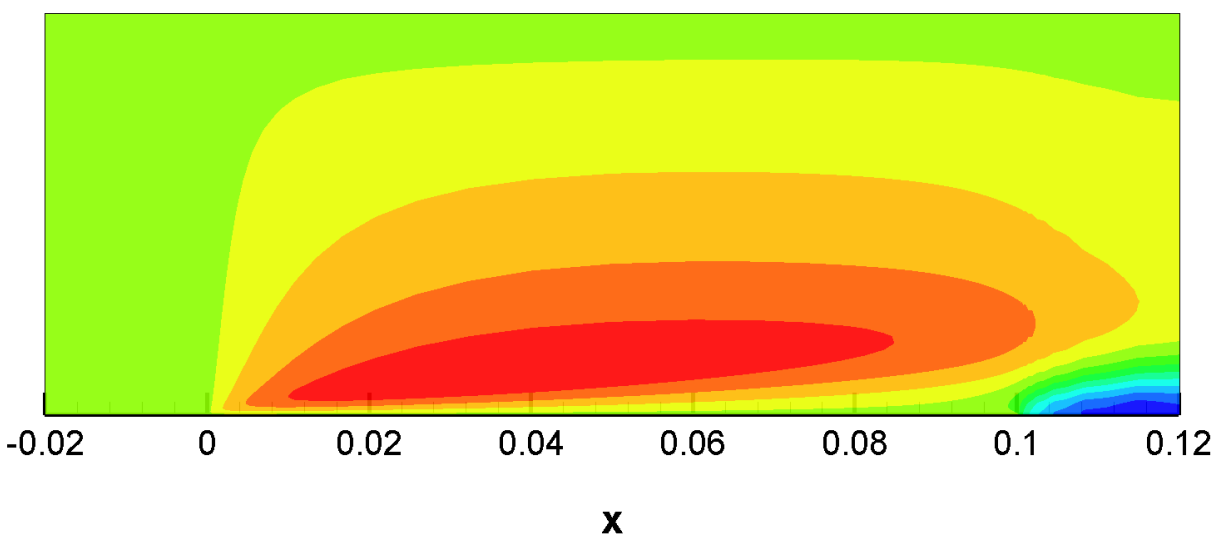
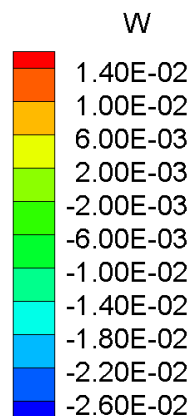
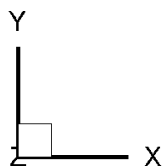


Figure B.39: Flat-plate third velocity component distribution for $Re = 1E4$

Flow over a flat plate
(W velocity component)

Re = 100,000
x-y plane at z=0.05
Time = 0.300

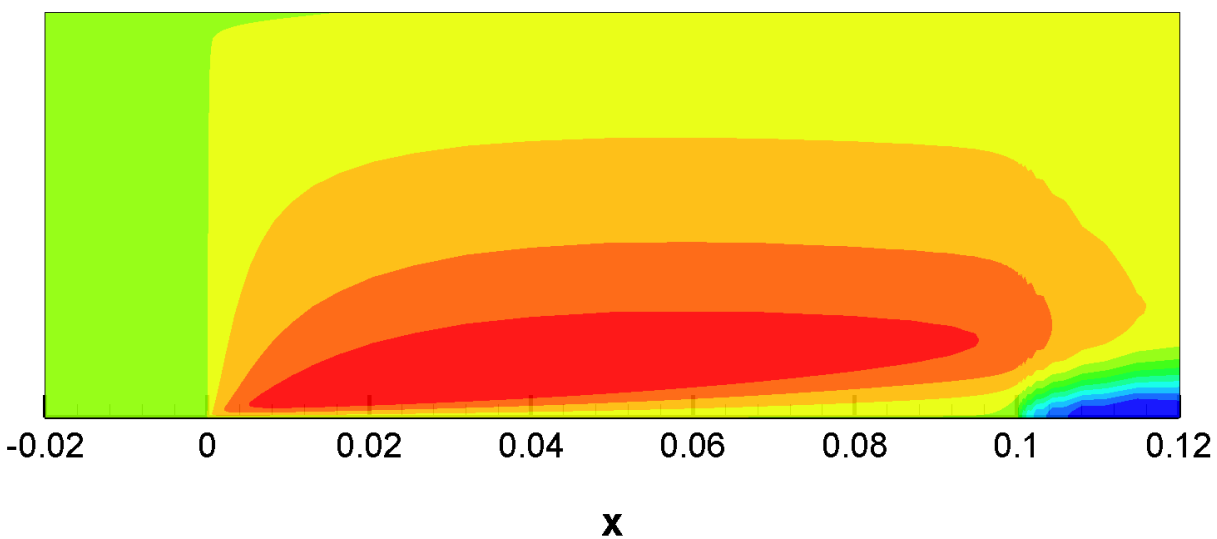
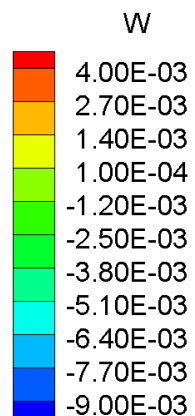
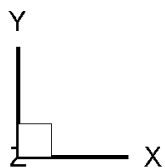


Figure B.40: Flat-plate third velocity component distribution for Re = 1E5

Flow over a flat plate
(U velocity component)

Re = 100,000

x-y plane at z=0.0 (back)

x-z plane at y=0.0 (bottom)

Time = 0.300

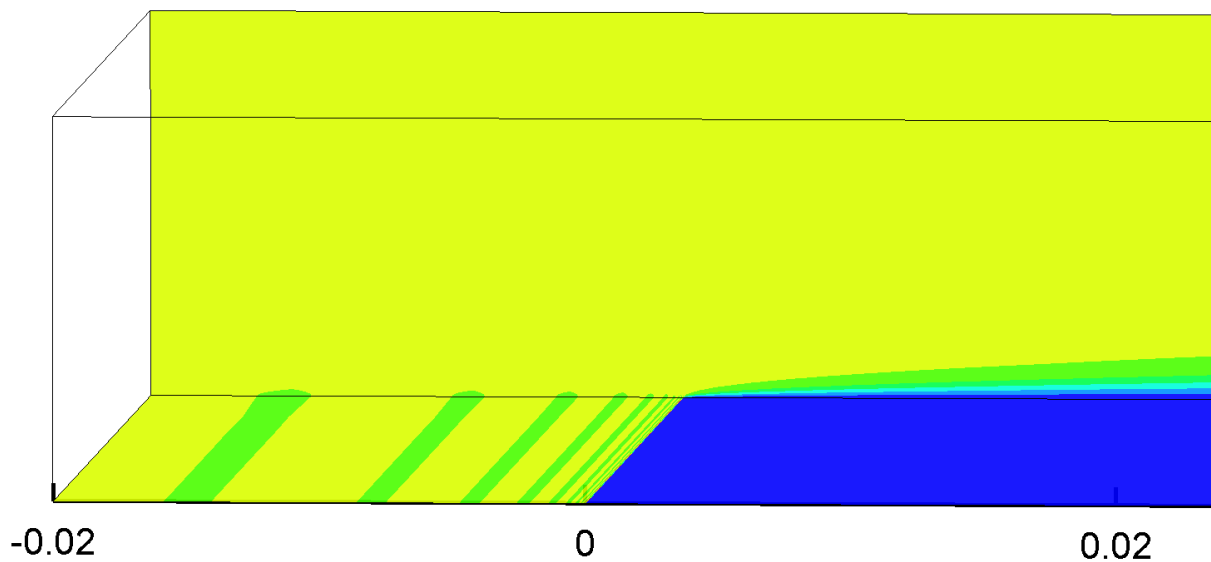
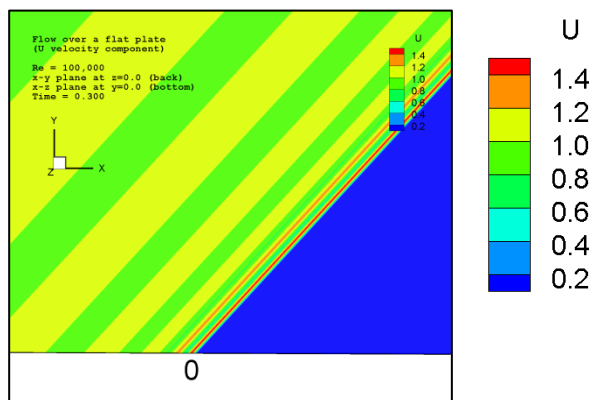
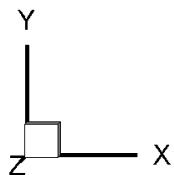


Figure B.41: Dispersion error distribution caused by the leading edge BC singularity, Re = 1E5

Flow over a flat plate
(U velocity component)

Re = 100,000 (with Kolesnikov)
x-y plane at z=0.0 (back)
x-z plane at y=0.0 (bottom)
Time = 0.300

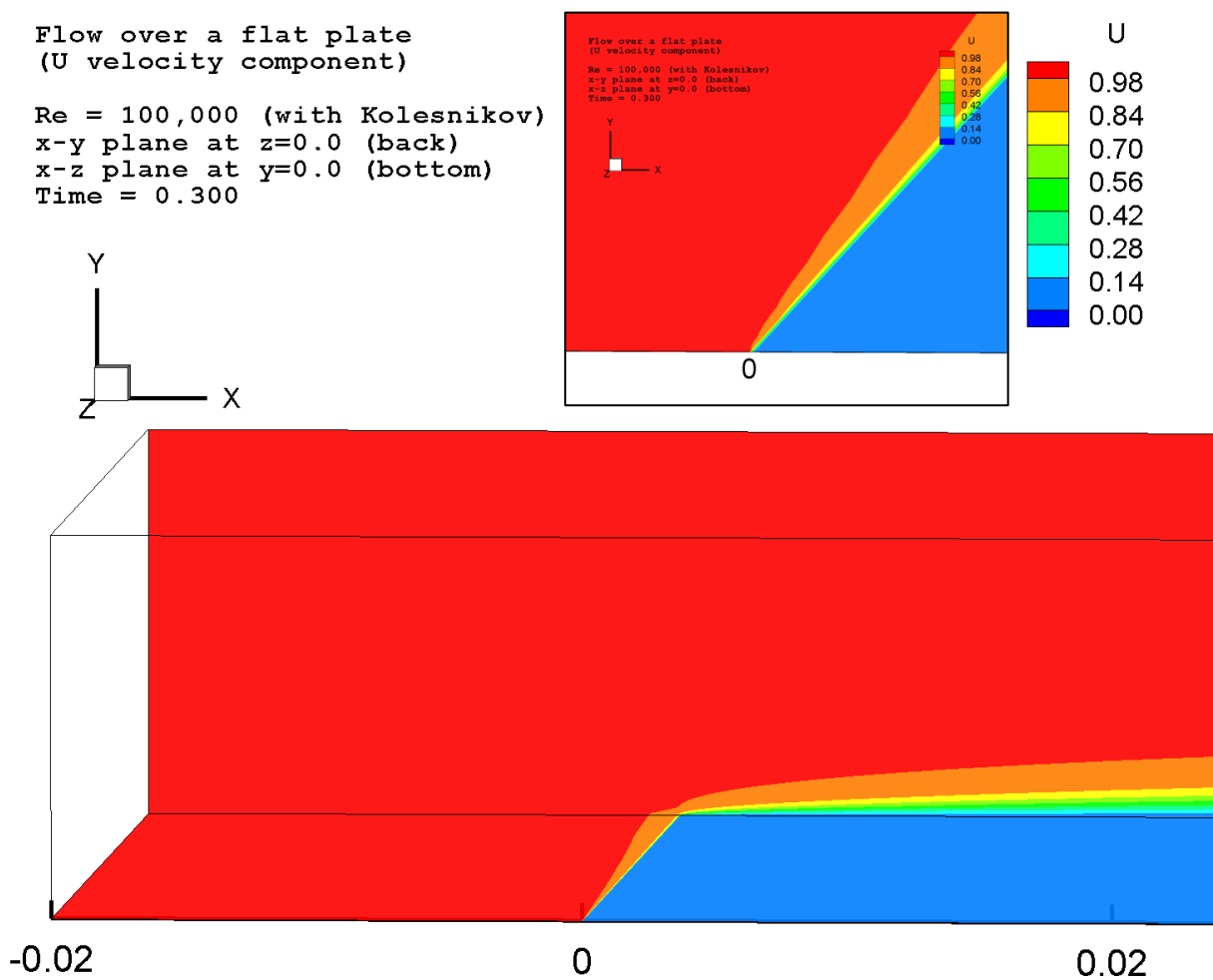


Figure B.42: Dispersion error control using Kolesnikov's theory, Re = 1E5

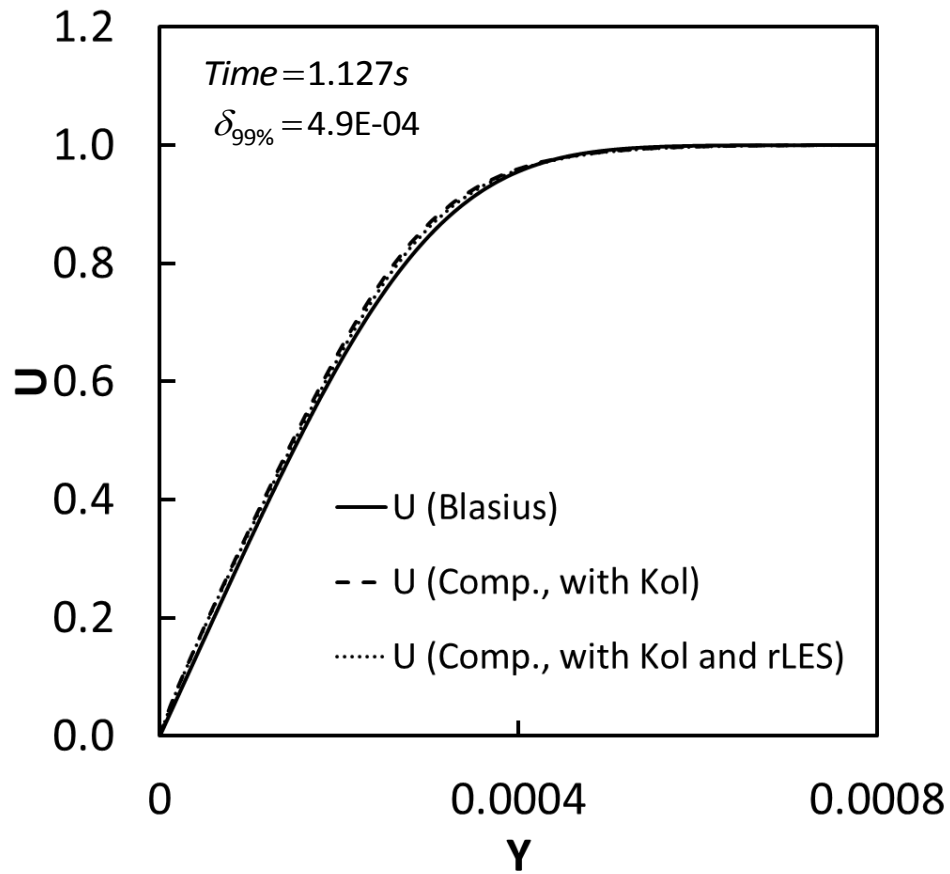


Figure B.43: Comparison of the Blasius and two computed solutions for $Re=1E6$. The profiles are extracted from the trailing edge of the flat plate ($x=0.01, y=0$)

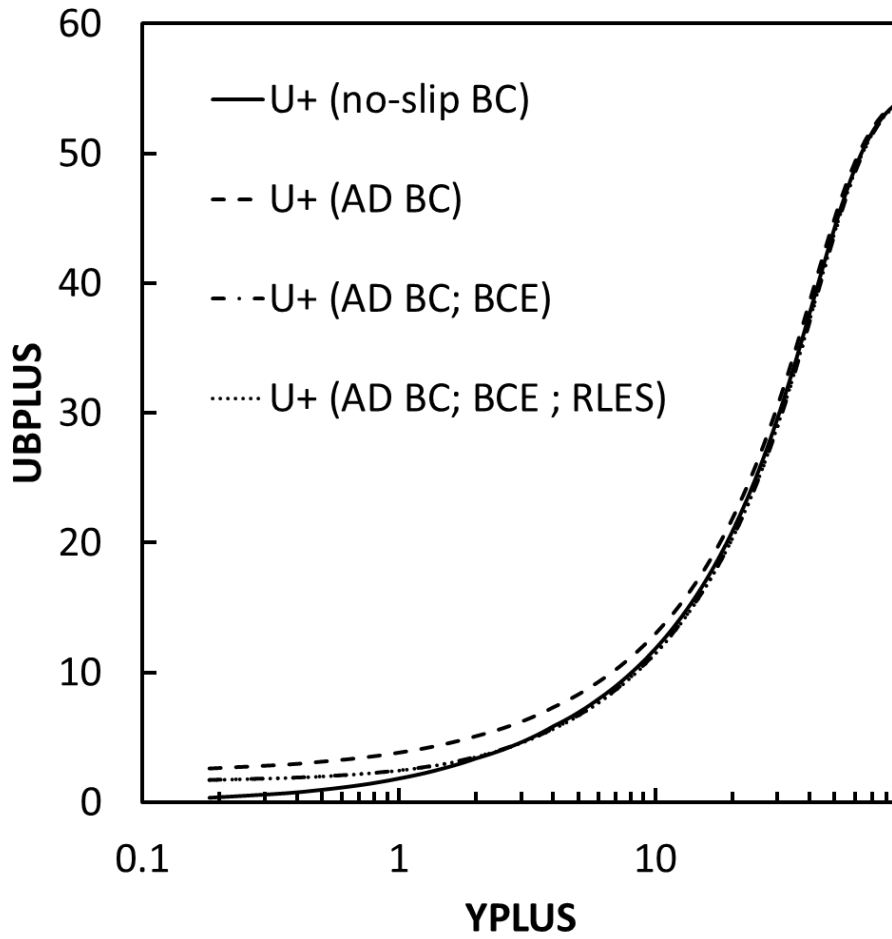


Figure B.44: Computed velocity profiles with and without ADBC formulation

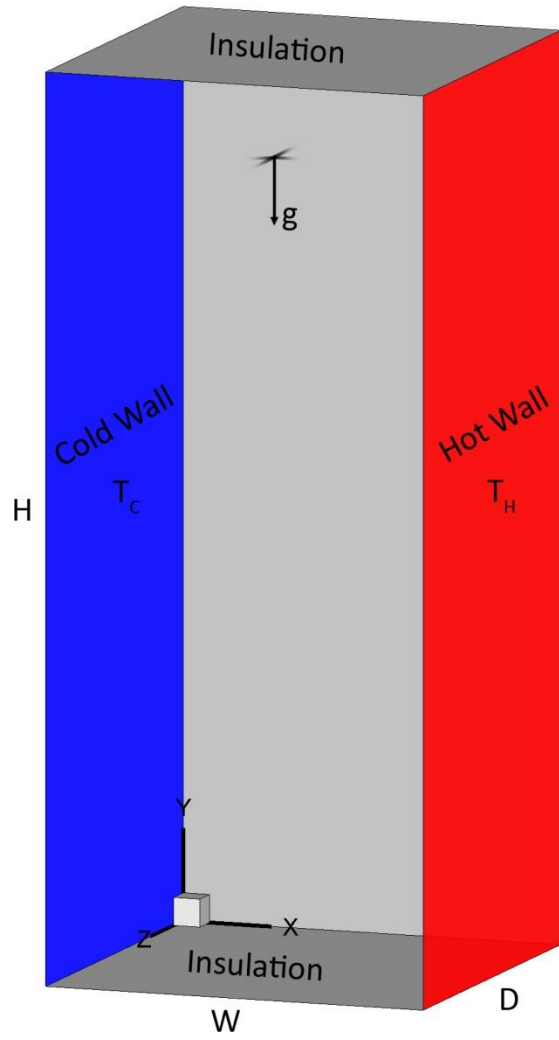


Figure B.45: Differentially heated enclosure with 1:8:8 aspect ratio (not to scale)

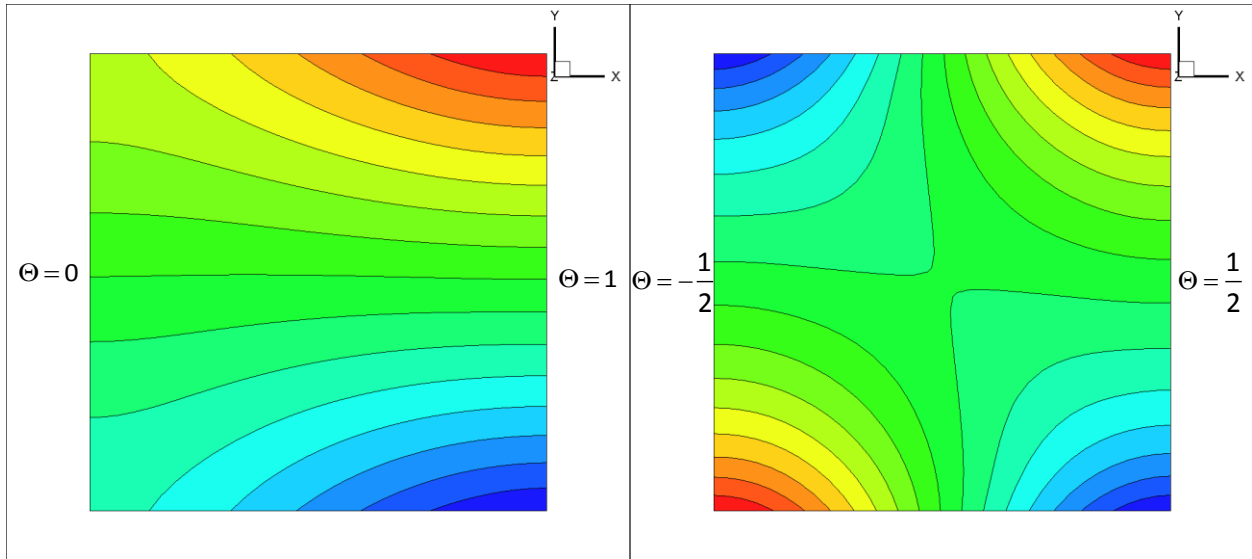


Figure B.46: Pressure contours for square thermal cavity at $Ra = 10^4$. The choice of reference temperature, i.e. $T_{ref} = T_c$ (left) and $T_{ref} = (T_h + T_c)/2$ (right), significantly affects the pressure distribution.

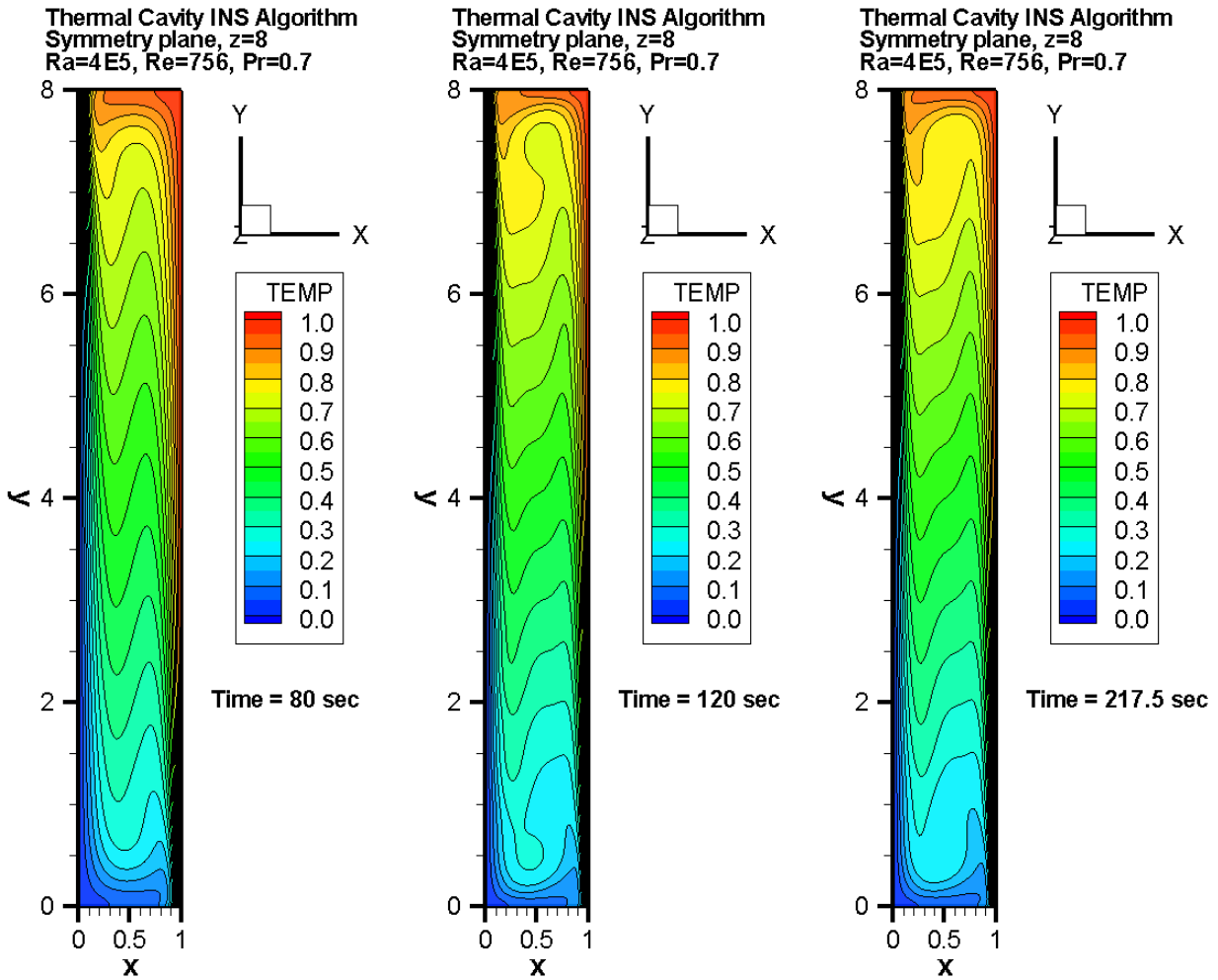


Figure B.47: Temperature distribution at t=80, 120 and 217.5 seconds for an incipient non-steady laminar flow at $Ra = 4 \times 10^5$, $Re = 756$.

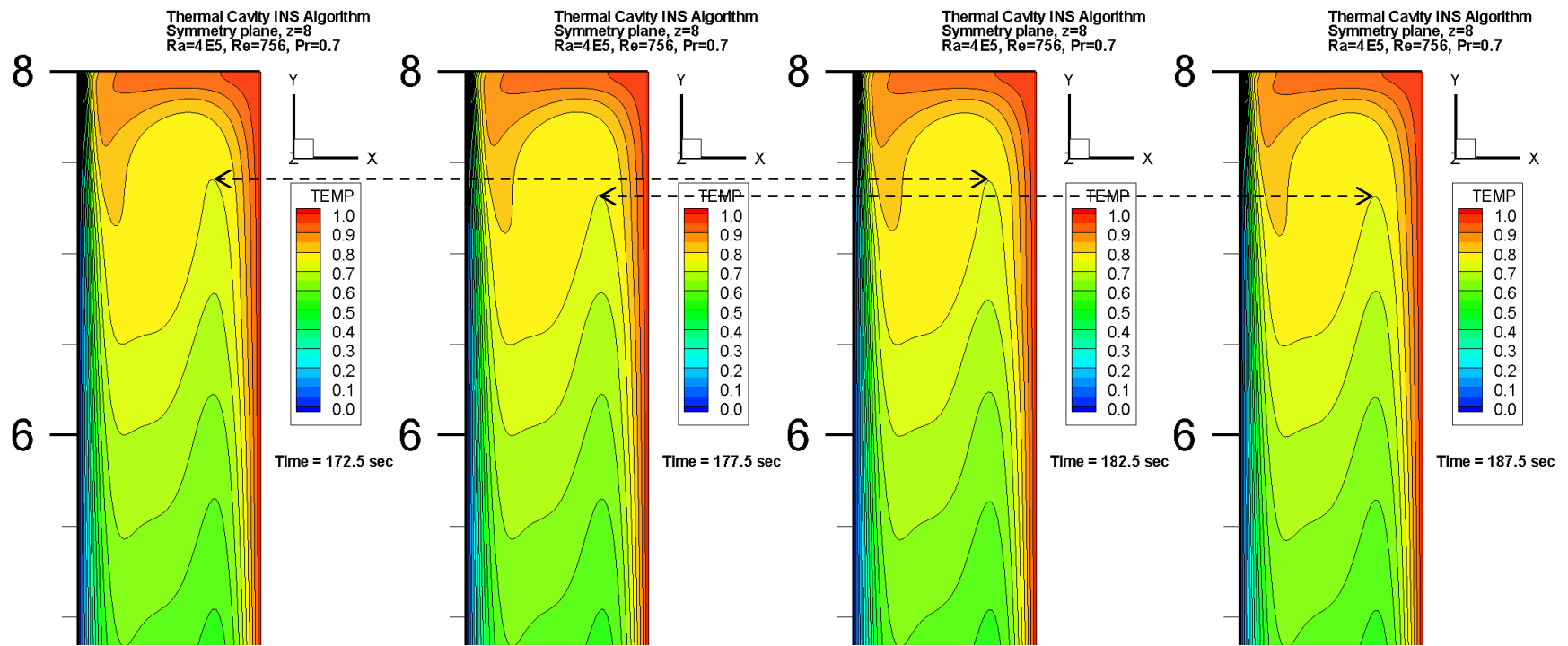


Figure B.48: Temperature samples in the upper-right corner of the cavity at $t=172.5, 177.5, 182.5$ and 187.5 seconds indicating an incipient non-steady laminar flow at $Ra = 4 \times 10^5$, $Re = 756$.

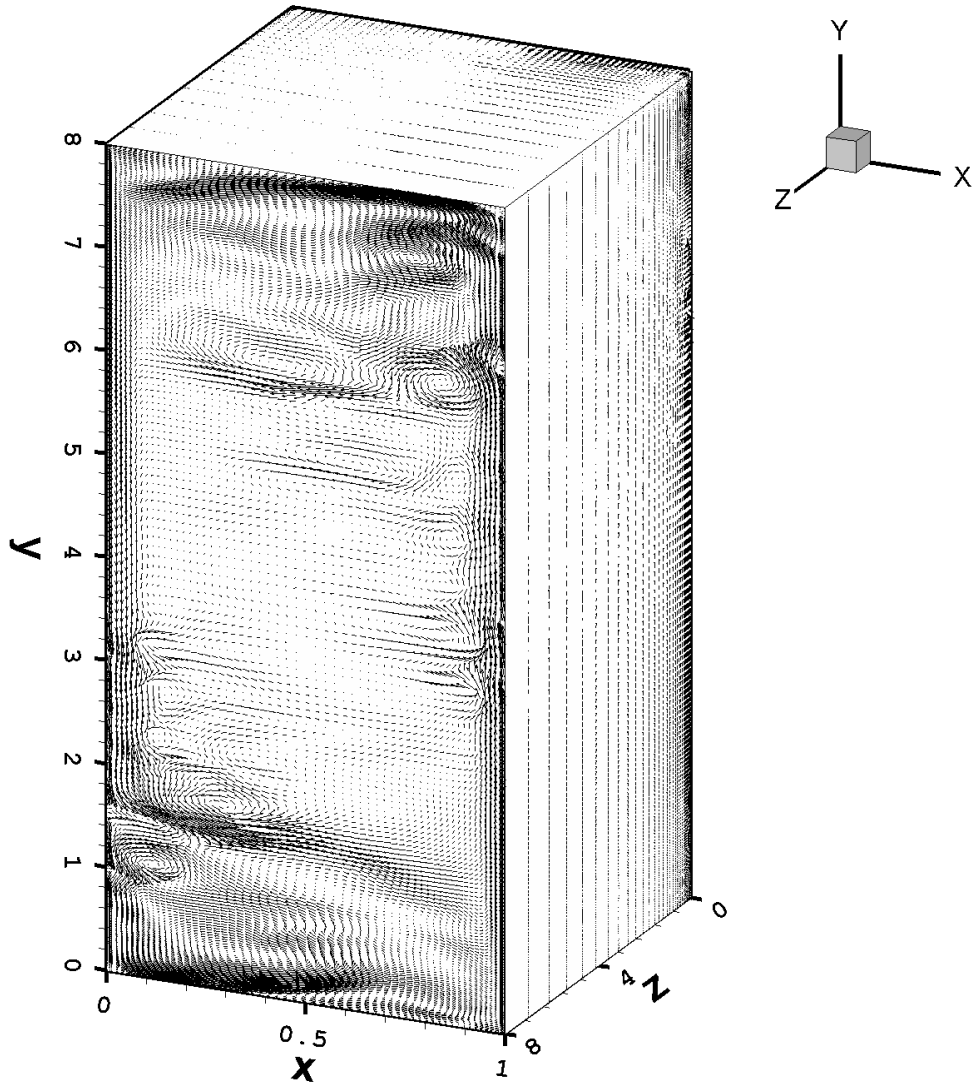


Figure B.49: Velocity vectors directly on the surface (top and right planes). Symmetry plane is shown in front ($z=8$)

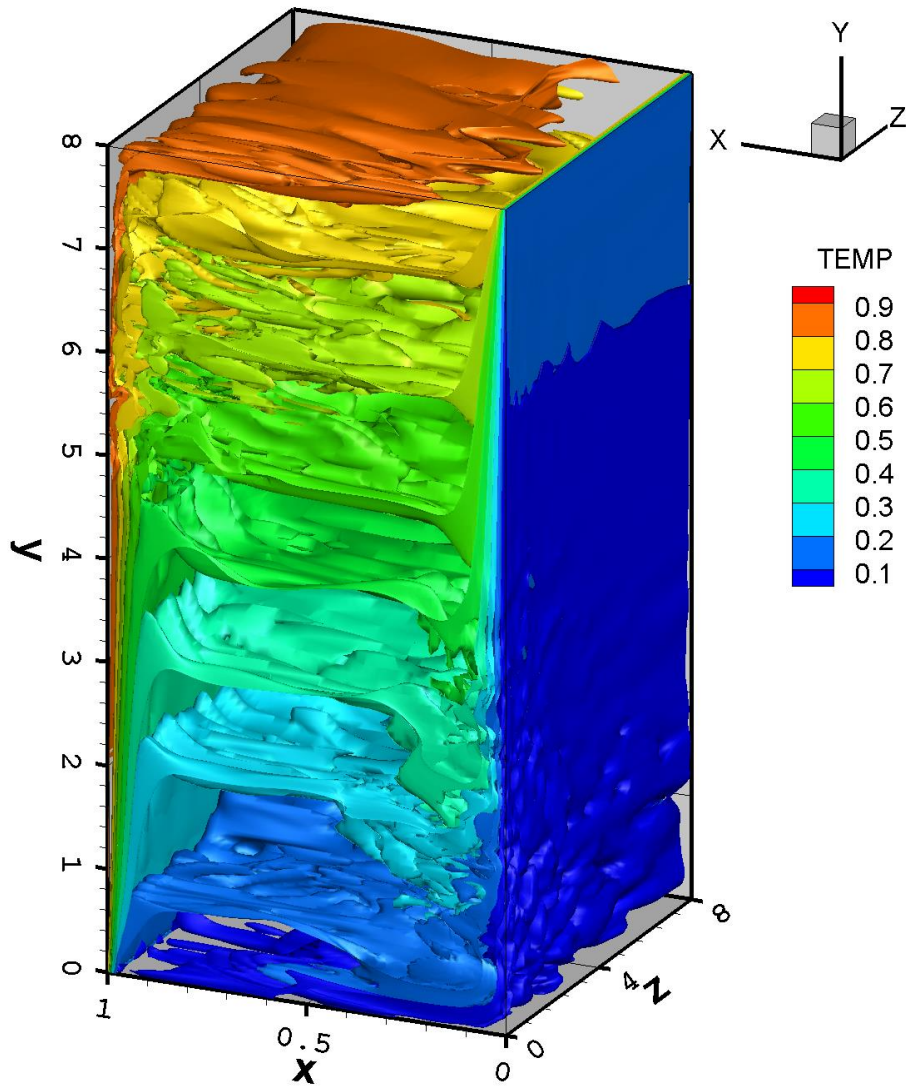


Figure B.50: Iso-surfaces of temperature. Solid wall is shown in front ($z=0$)

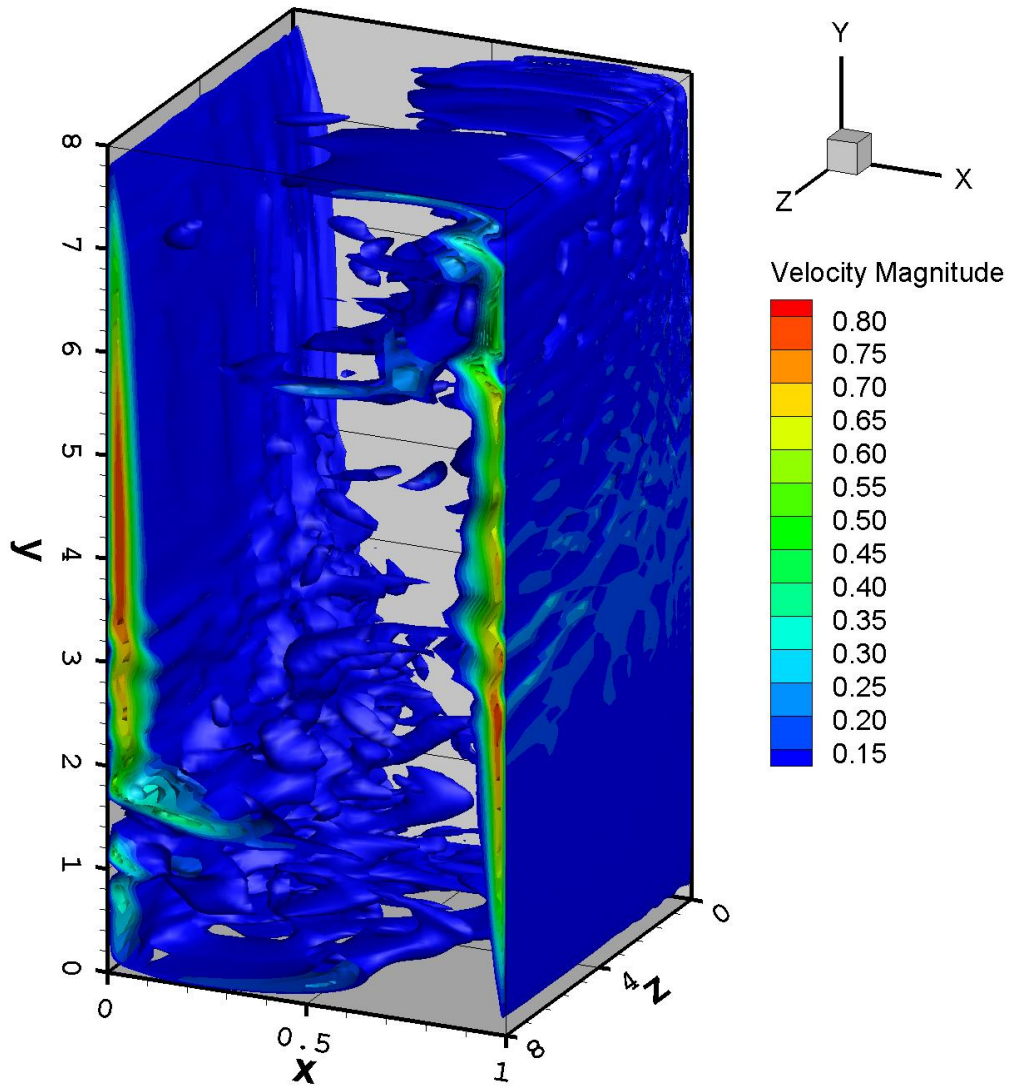


Figure B.51: Iso-surfaces of velocity magnitude. Symmetry plane is shown in front ($z=8$)

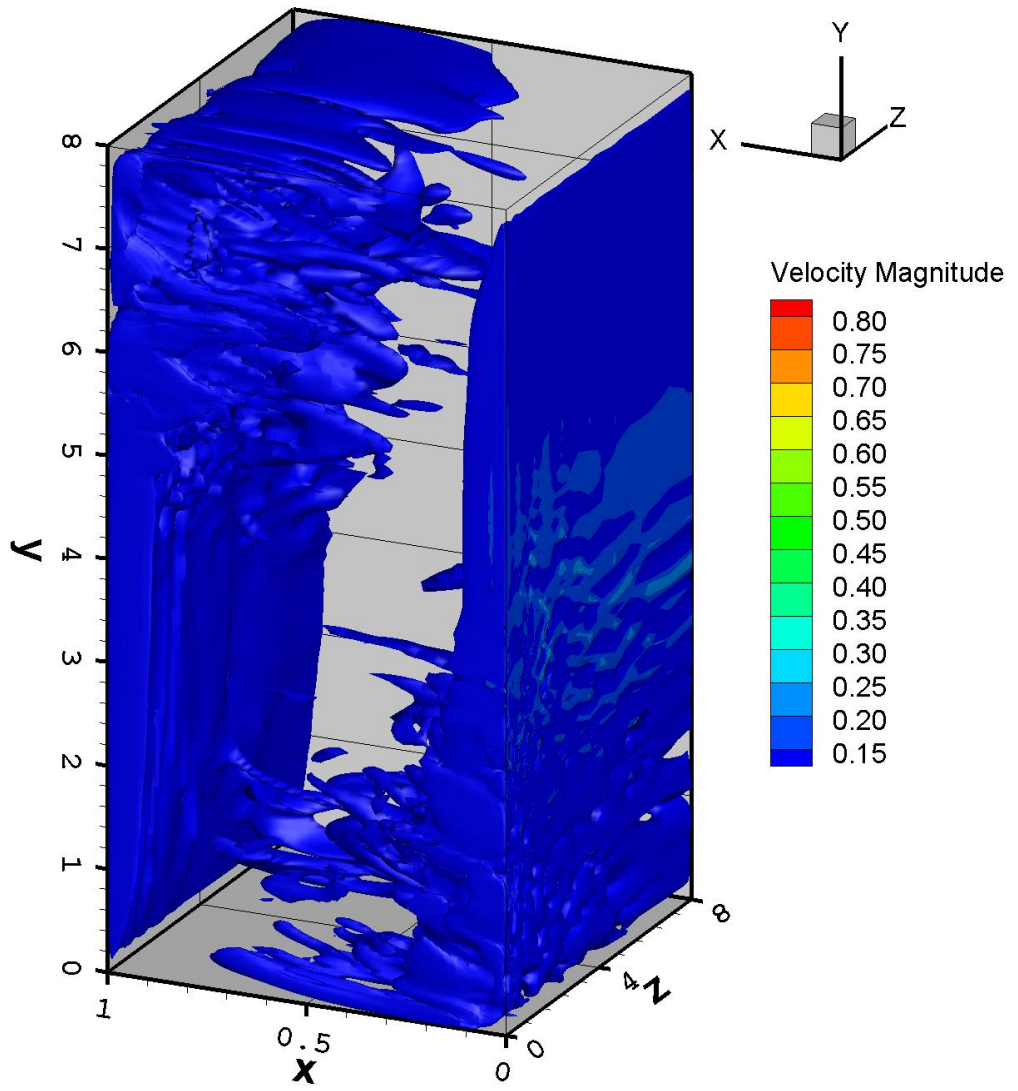


Figure B.52: Iso-surfaces of velocity magnitude. Solid wall is shown in front ($z=0$)

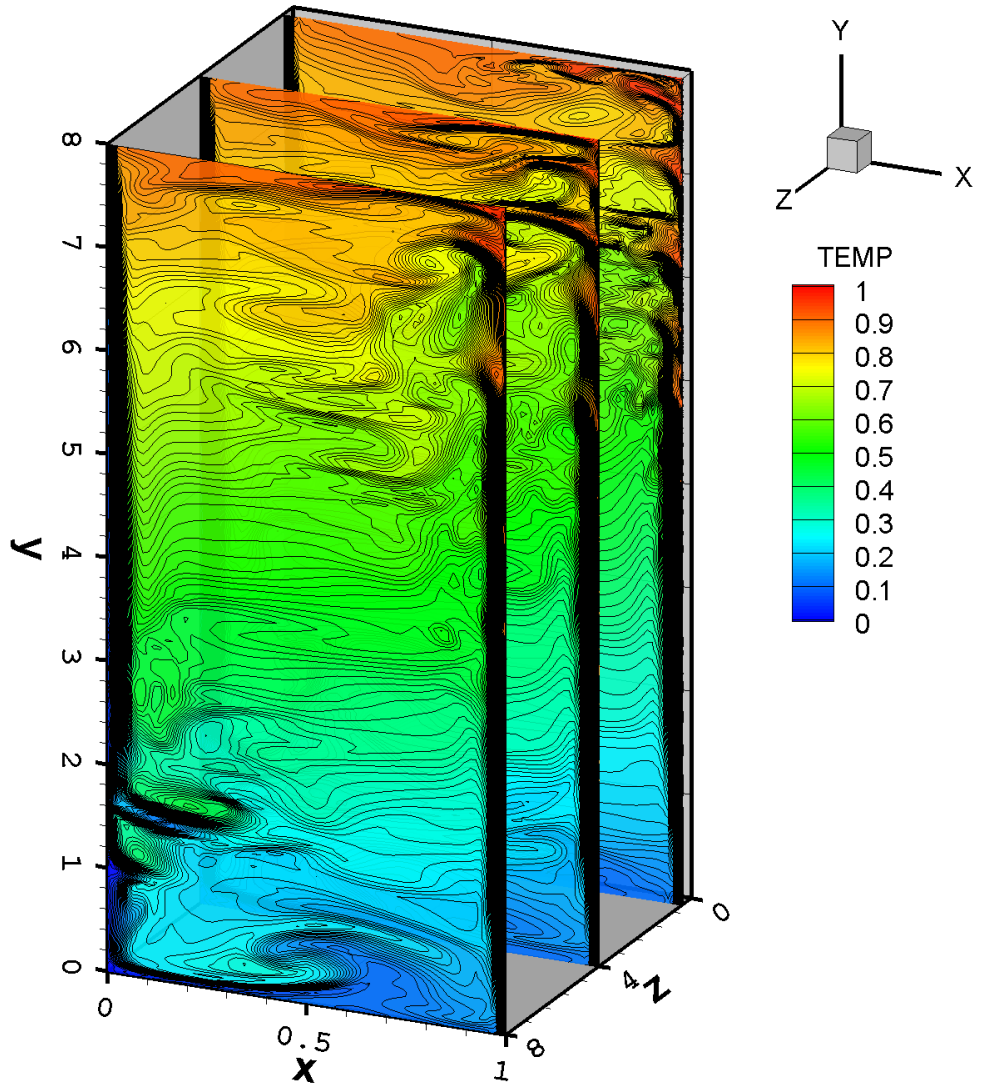


Figure B.53: Temperature contours

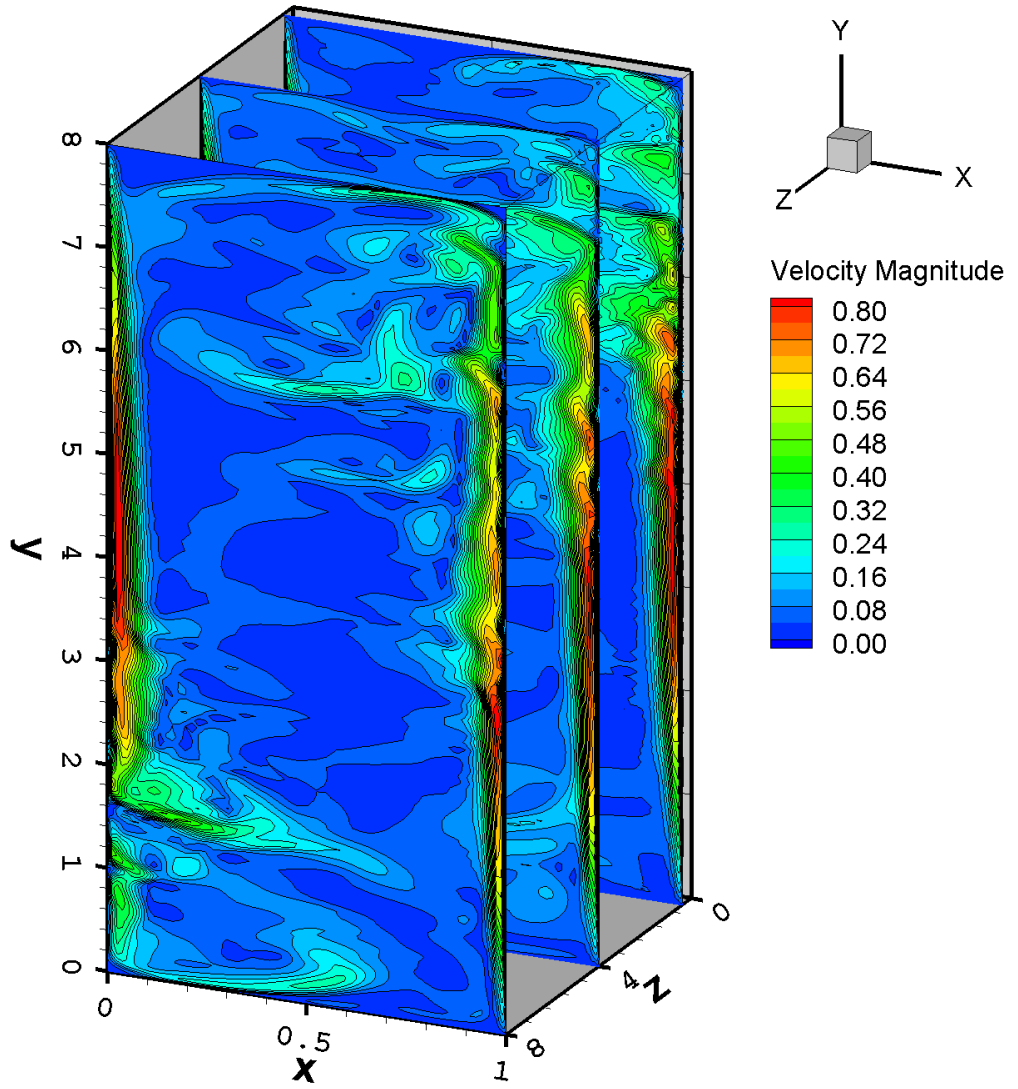


Figure B.54: Velocity magnitude contours

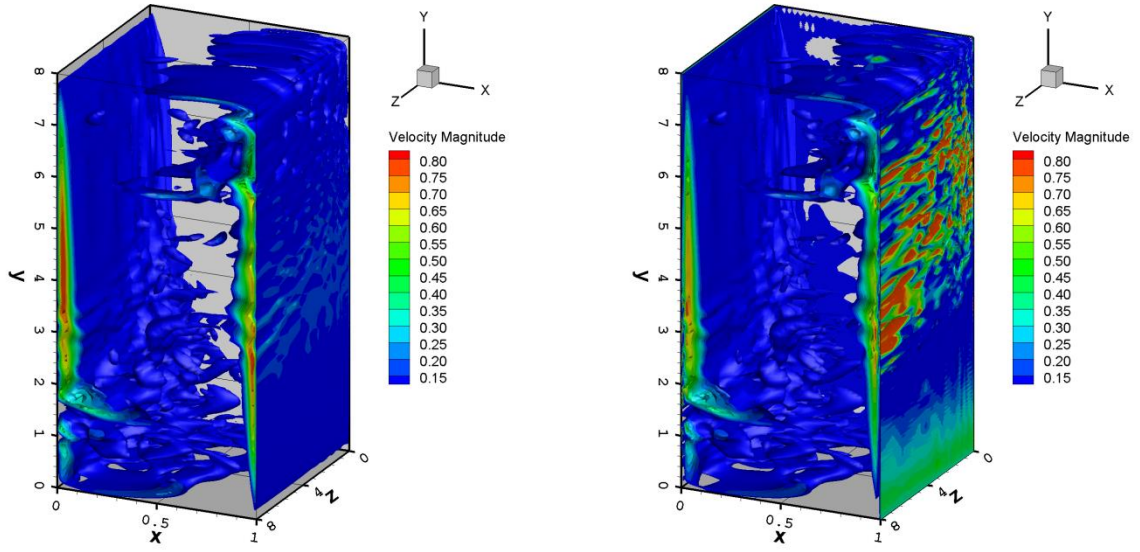


Figure B.55: Iso-surfaces of velocity magnitude. Comparison of the filtered (left) and AD (right) velocity fields. Symmetry plane is shown in front ($z=8$)

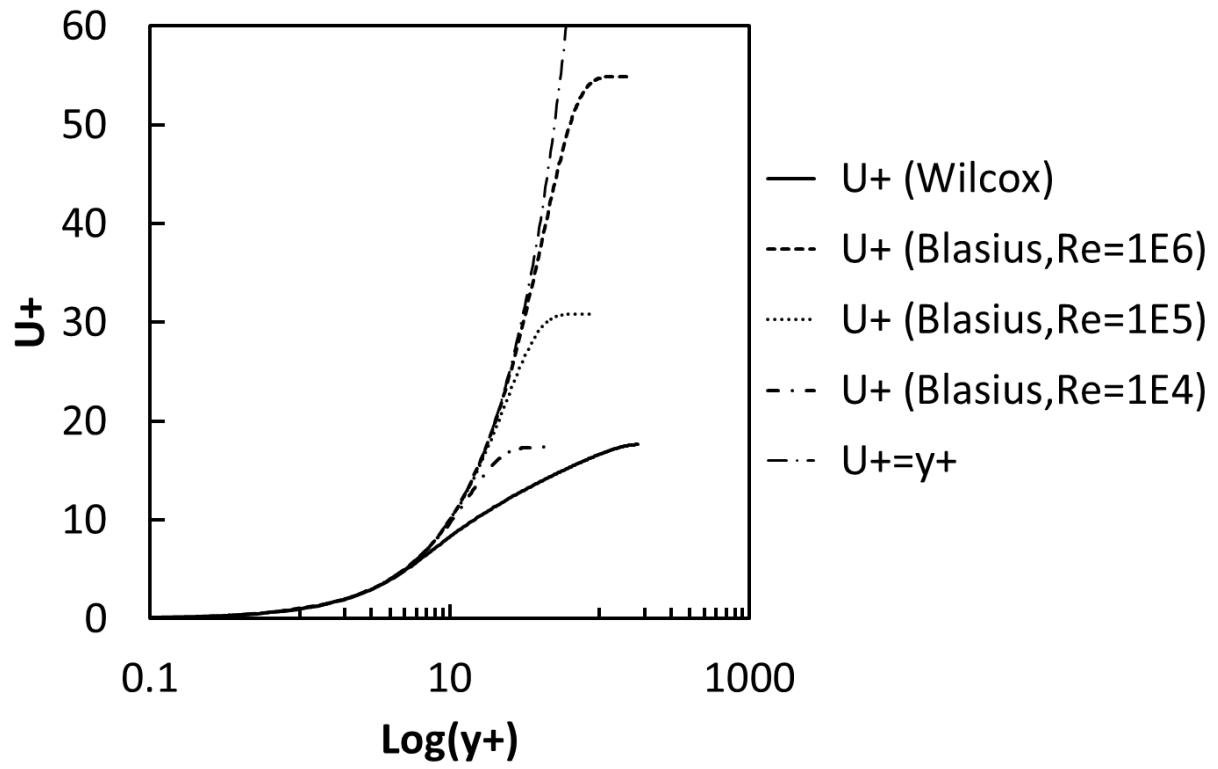


Figure B.56: Comparison of laminar and turbulent velocity profiles

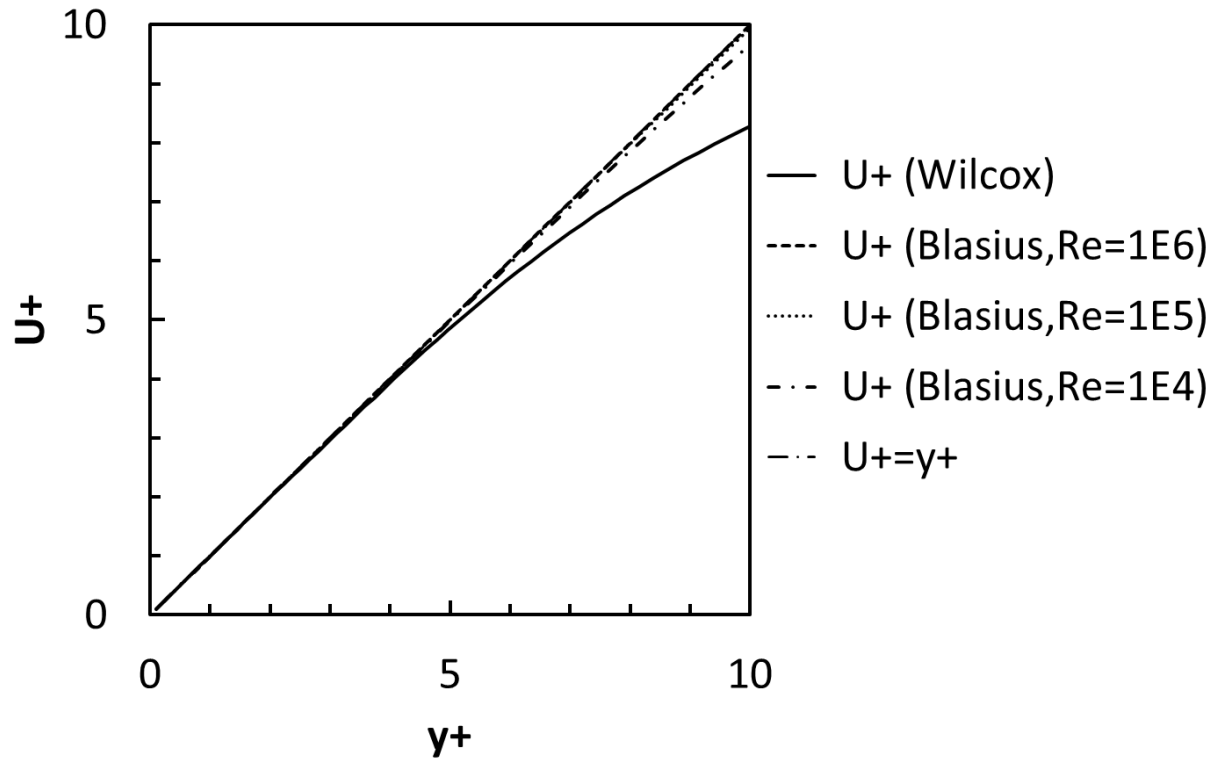


Figure B.57: Comparison of laminar and turbulent velocity profiles (viscous sublayer)

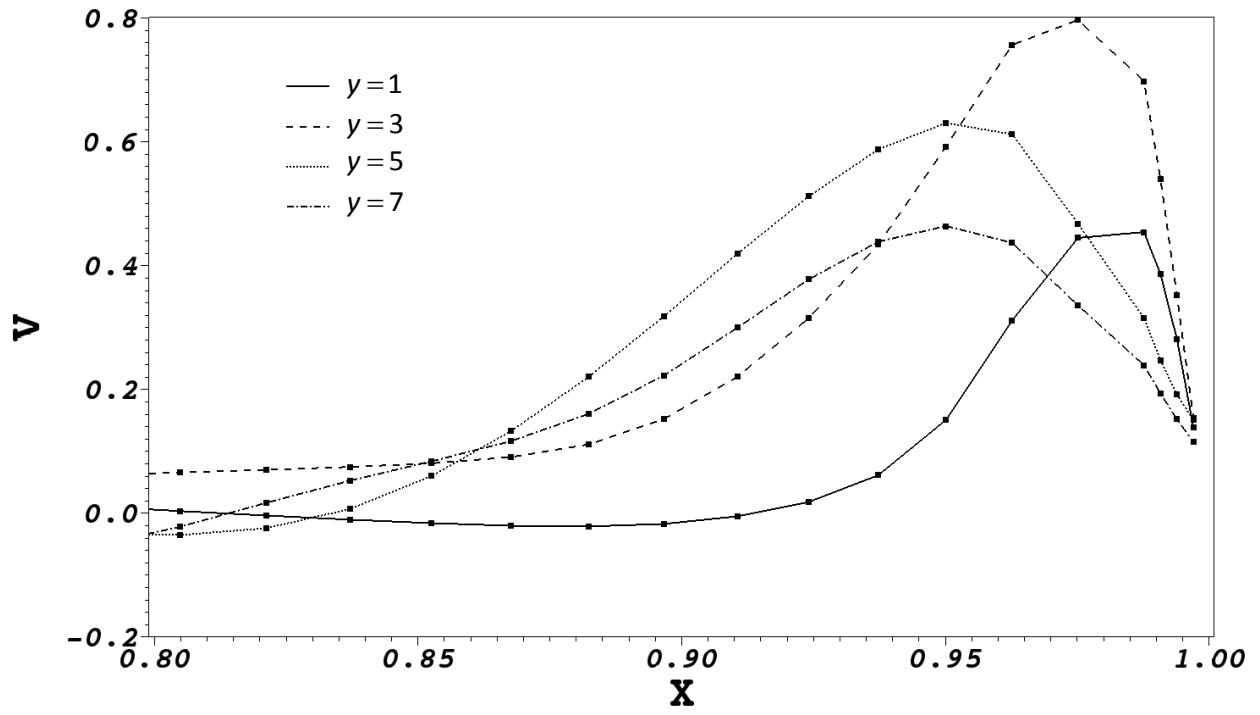


Figure B.58: Thermal cavity V-velocity profiles extracted from the symmetry plane (z-8) at different heights

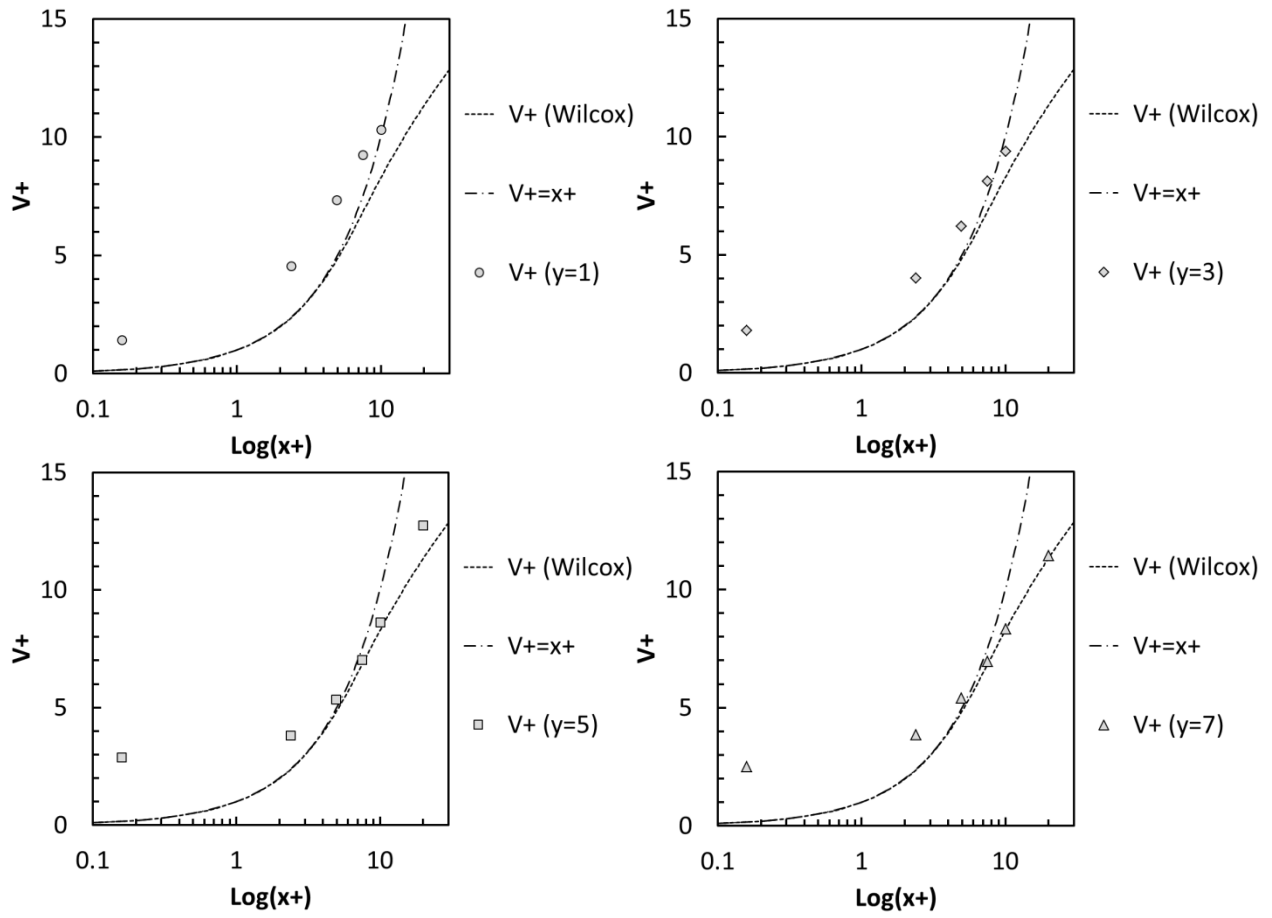


Figure B.59: Thermal cavity V-velocity profiles extracted from the symmetry plane ($z=8$) at different heights

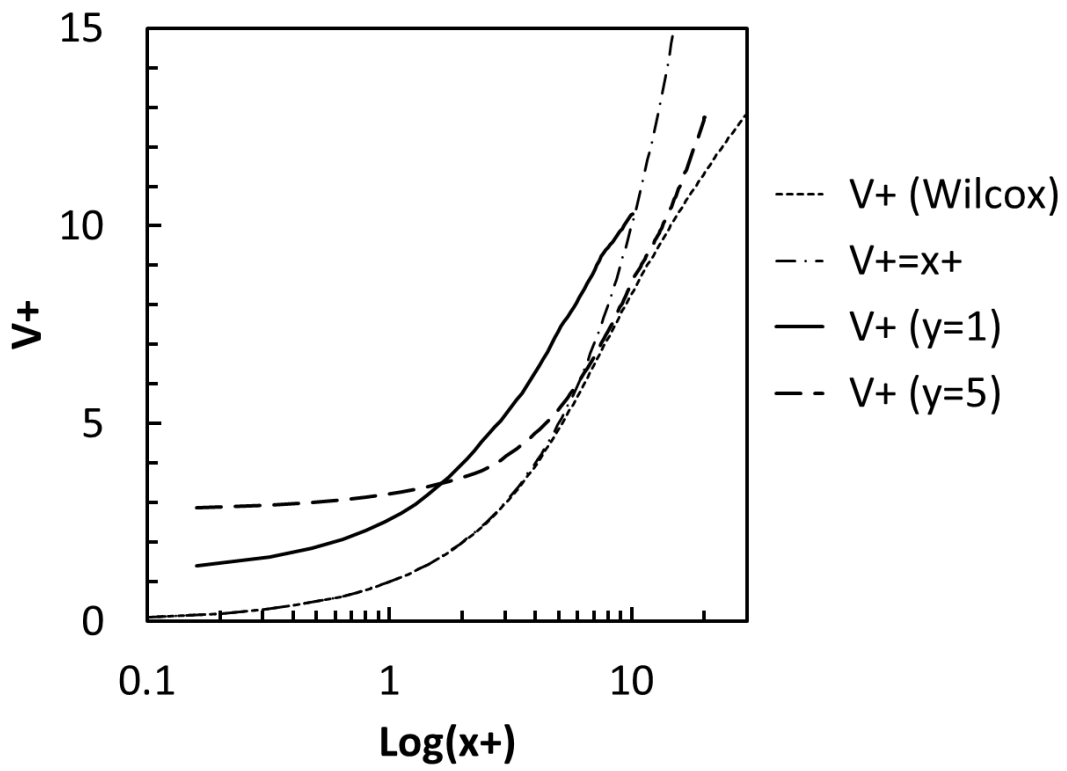


Figure B.60: Interpolated thermal cavity V -velocity profiles extracted from the symmetry plane ($z=8$) at $y=1$ and $y=5$.

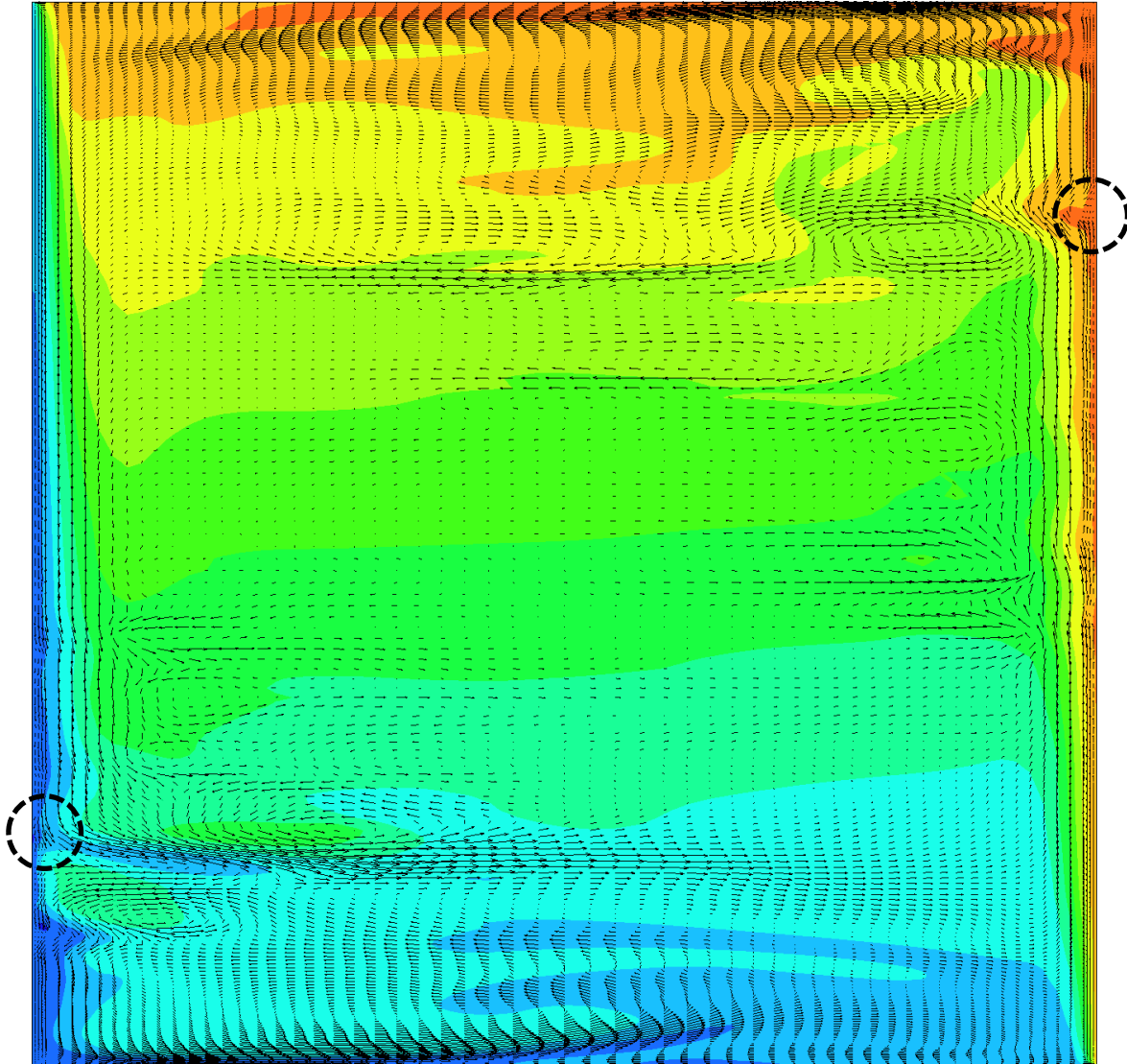


Figure B.61: Thermal cavity symmetry plane unitized scale temperature flood with velocity vector overlay. Dashed circles highlight the traversing vortex entities at hot/cold walls

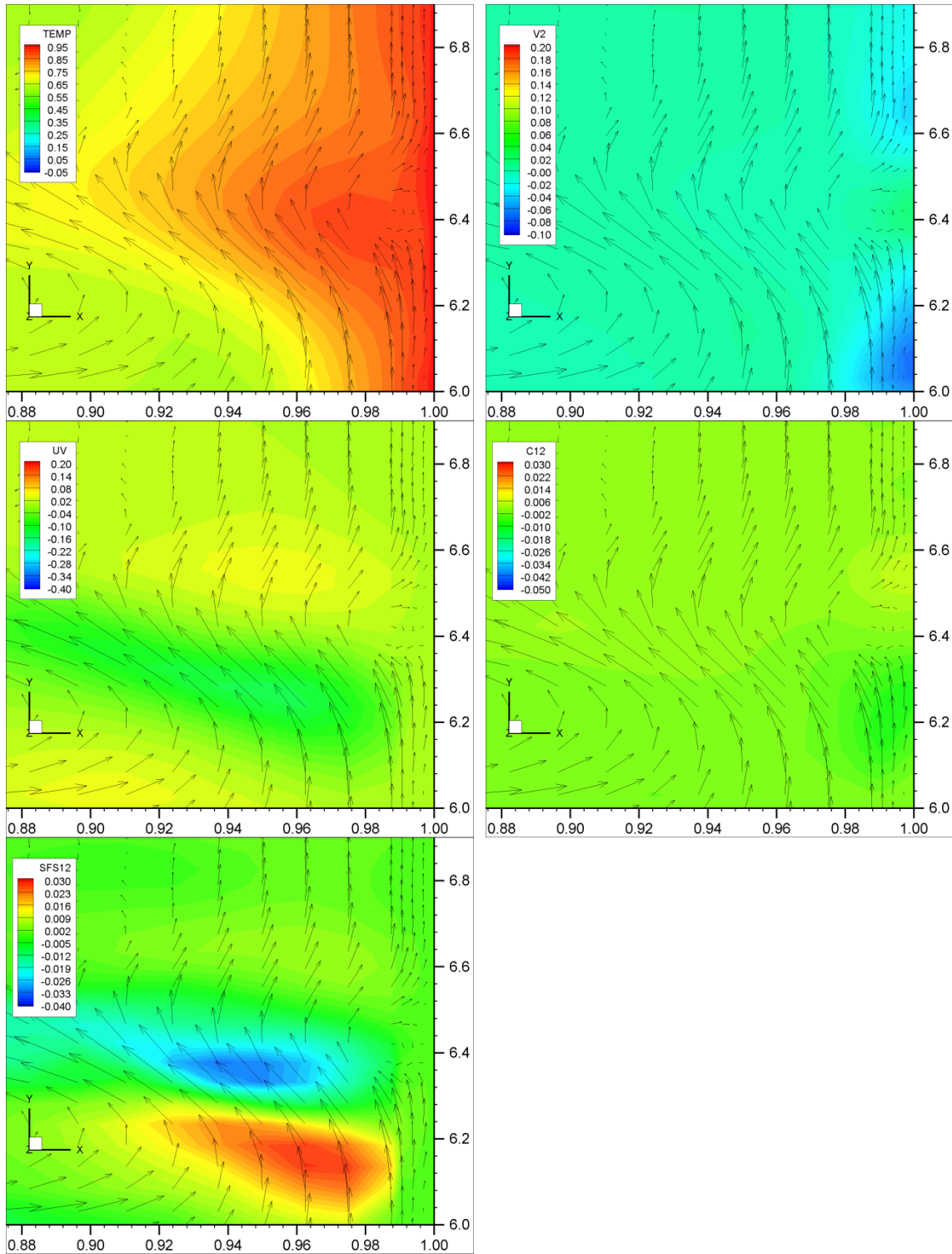


Figure B.62: Thermal cavity symmetry plane *arLES* theory close-up flood with velocity vector overlay, $Ra = 10^8$, $t = 382.1s$. Left to right, top to bottom: $\overline{\Theta}$, $\overline{u_2 \Theta'} + \overline{u_2' \Theta}$, $\overline{u_1 u_2}$, $\overline{u_1 u_2} + \overline{u_1' u_2'}$, $\overline{u_1' u_2'}$

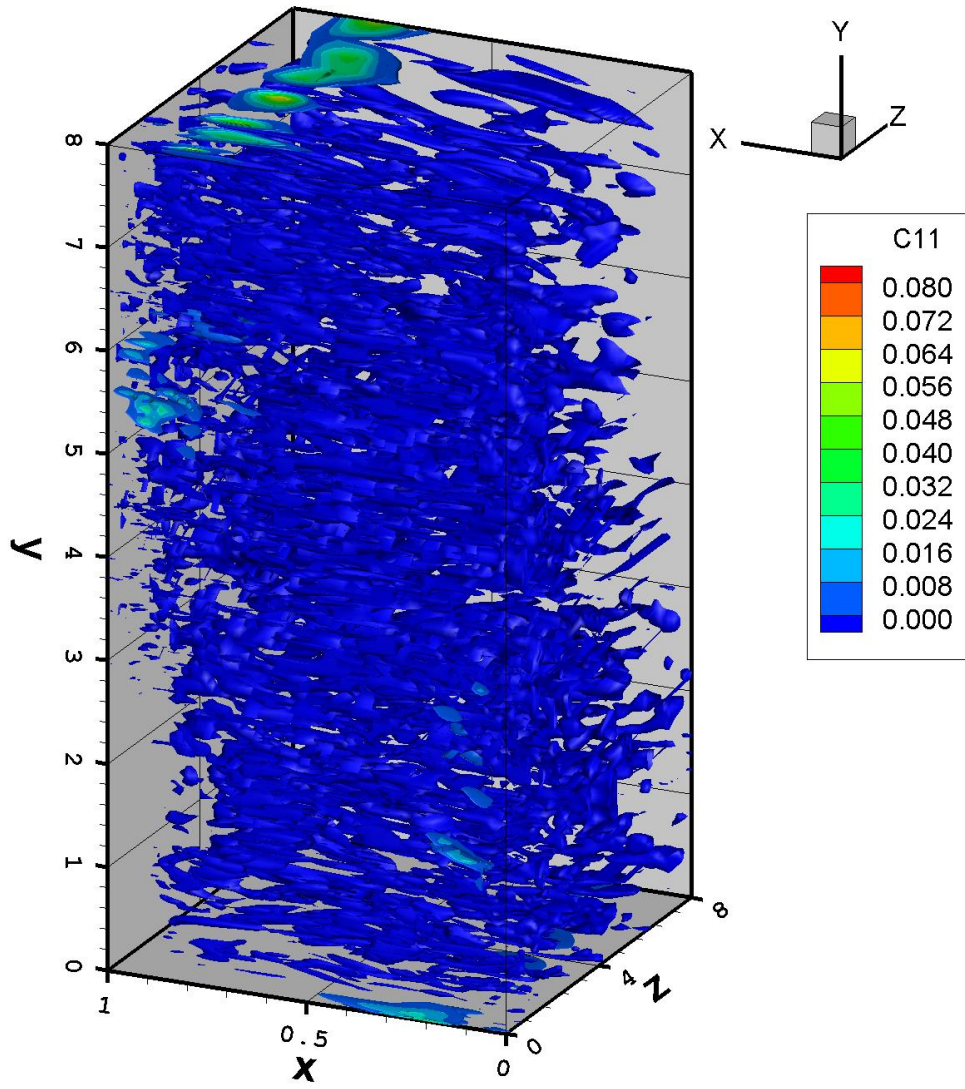


Figure B.63: The *arLES* statistics – C_{11} component

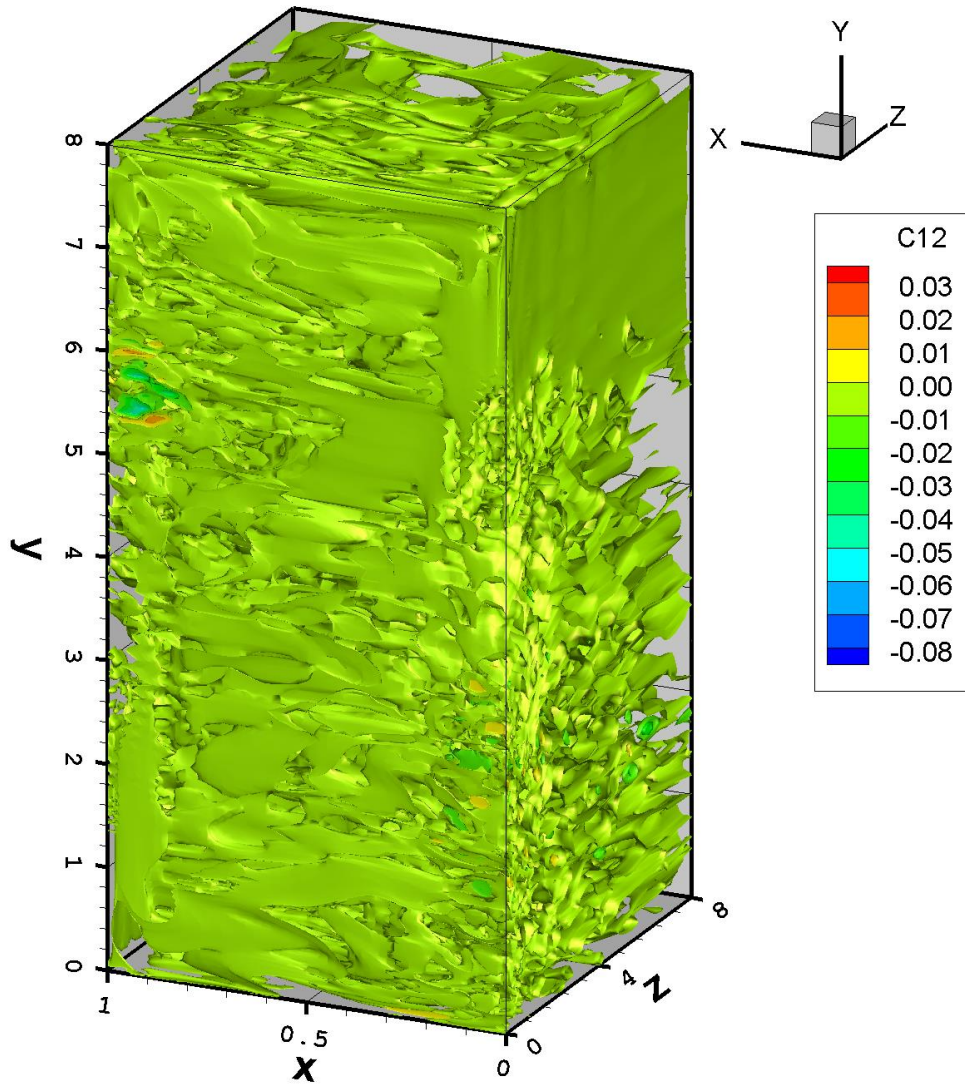


Figure B.64: The *arLES* statistics – C_{12} component

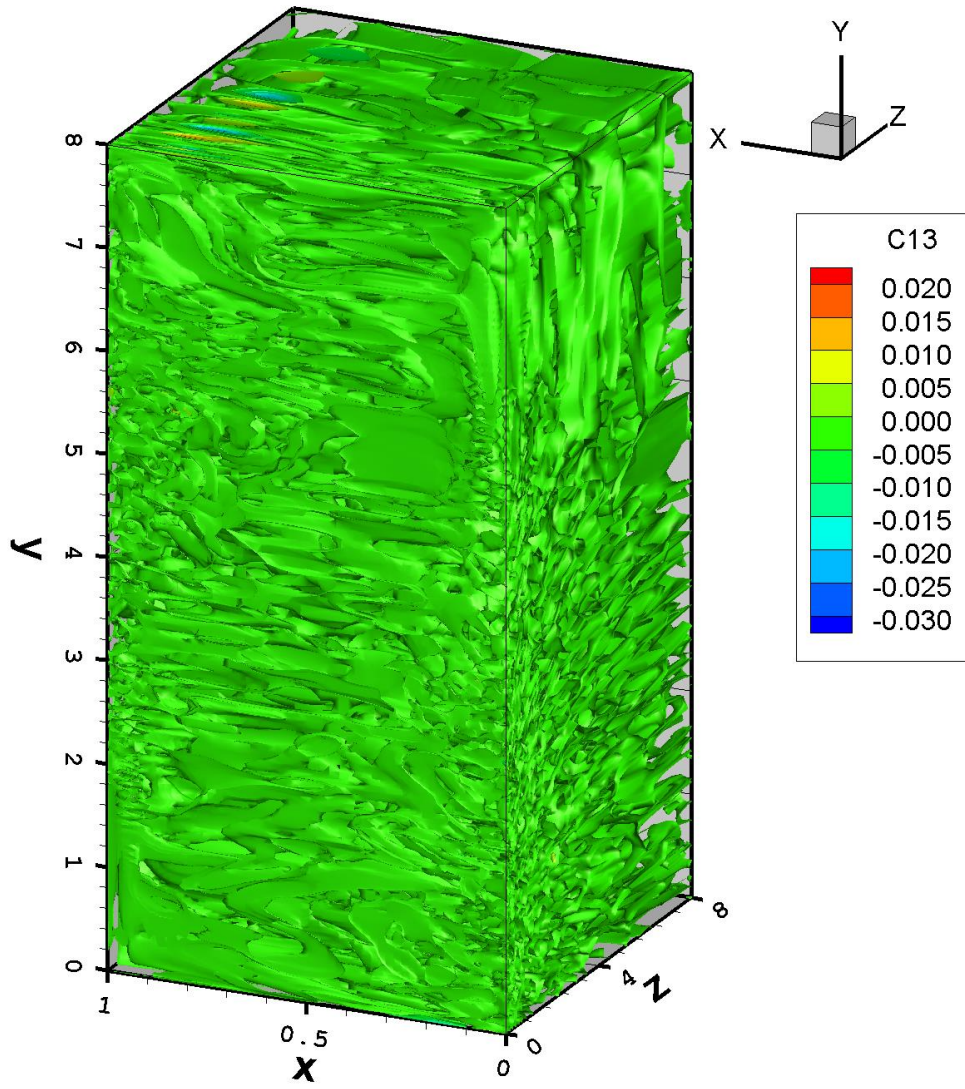


Figure B.65: The *arLES* statistics – C_{13} component

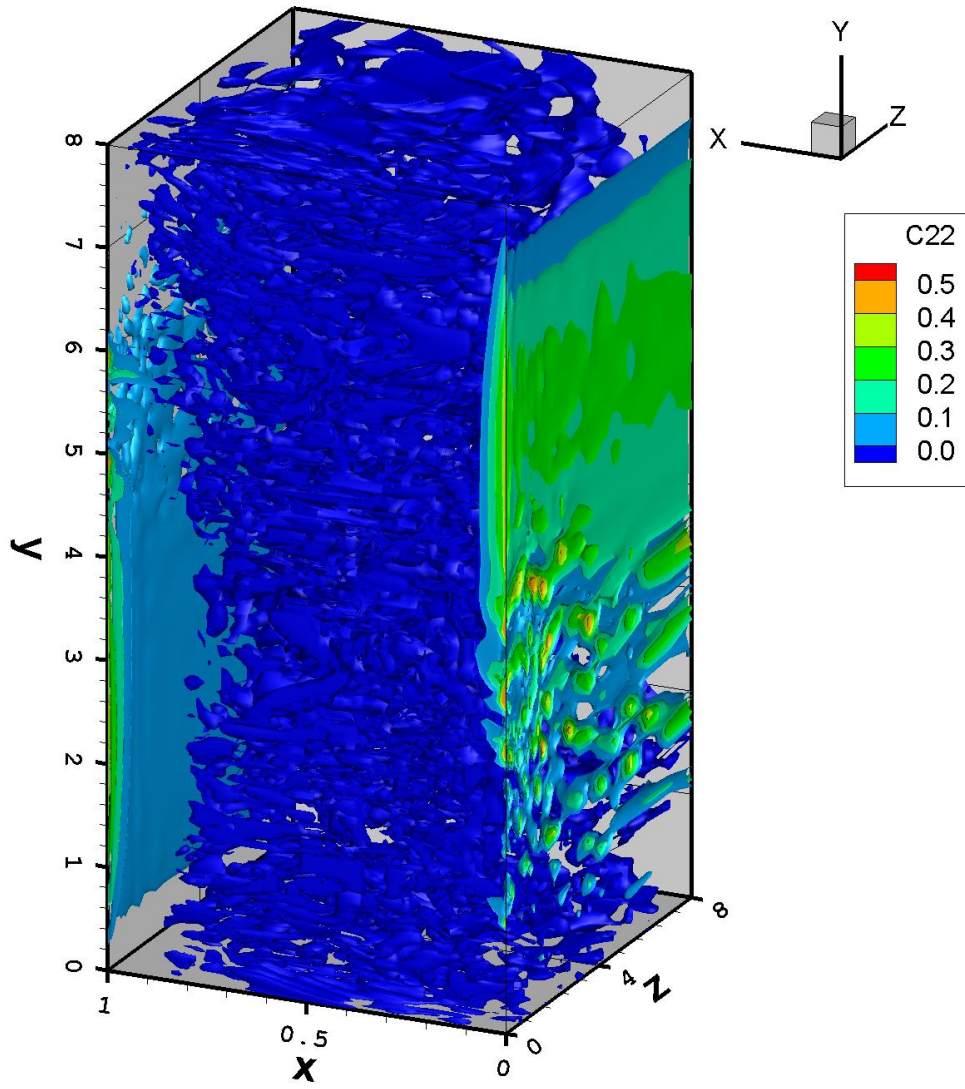


Figure B.66: The *arLES* statistics – C_{22} component

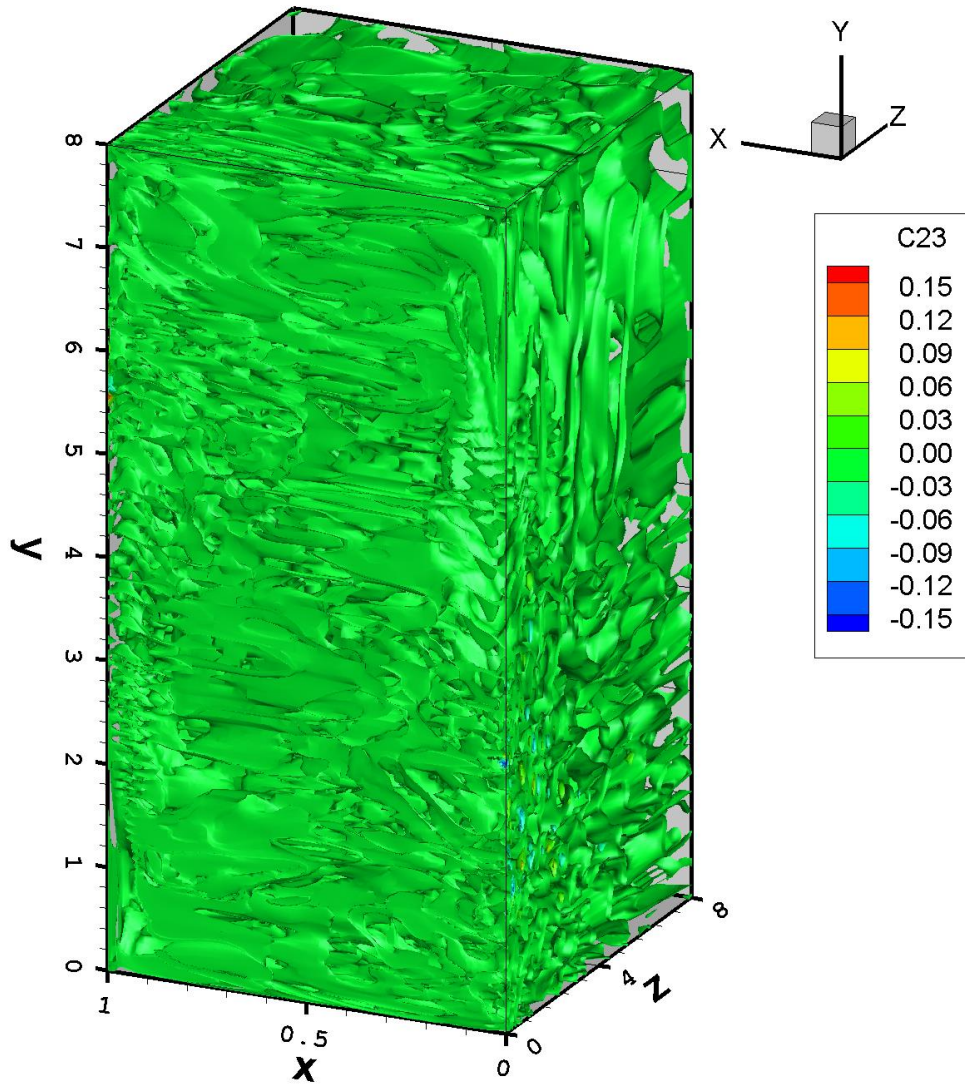


Figure B.67: The *arLES* statistics – C_{23} component

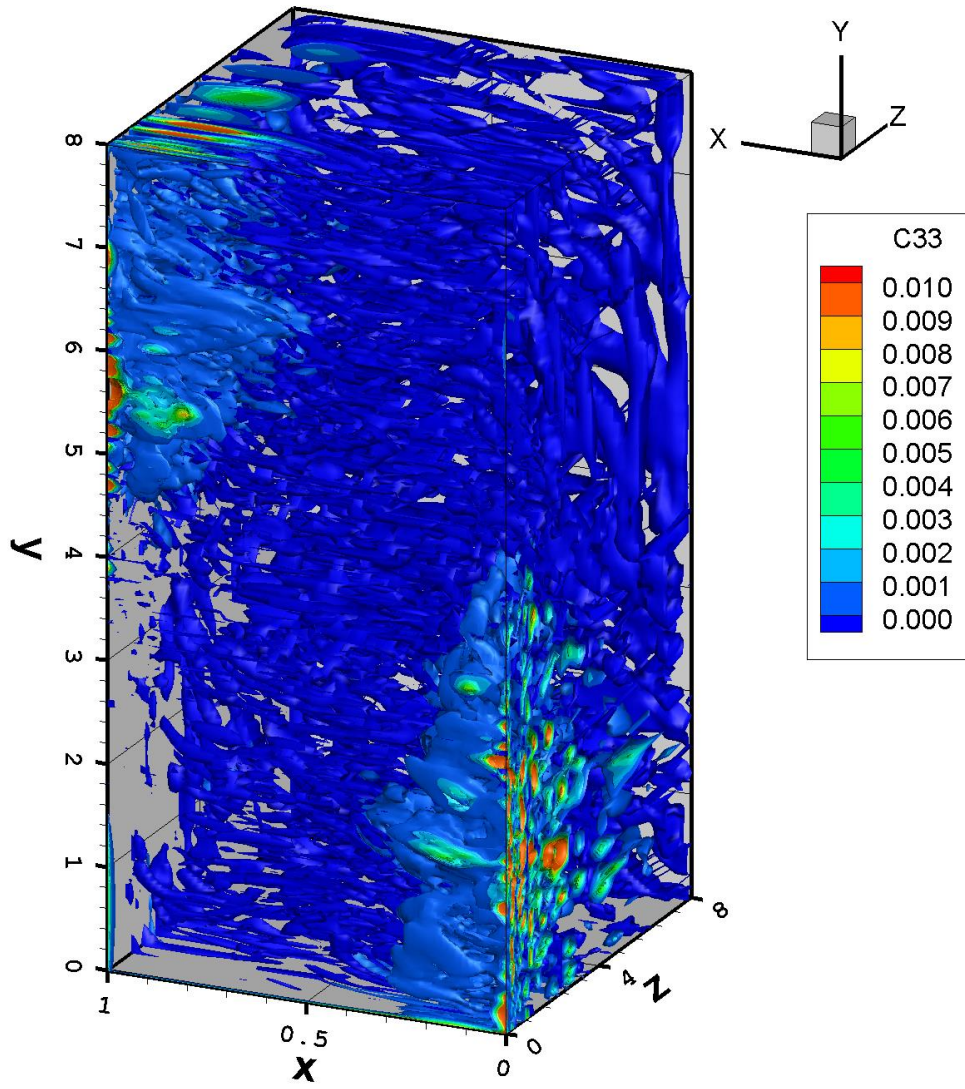


Figure B.68: The *arLES* statistics – C_{33} component

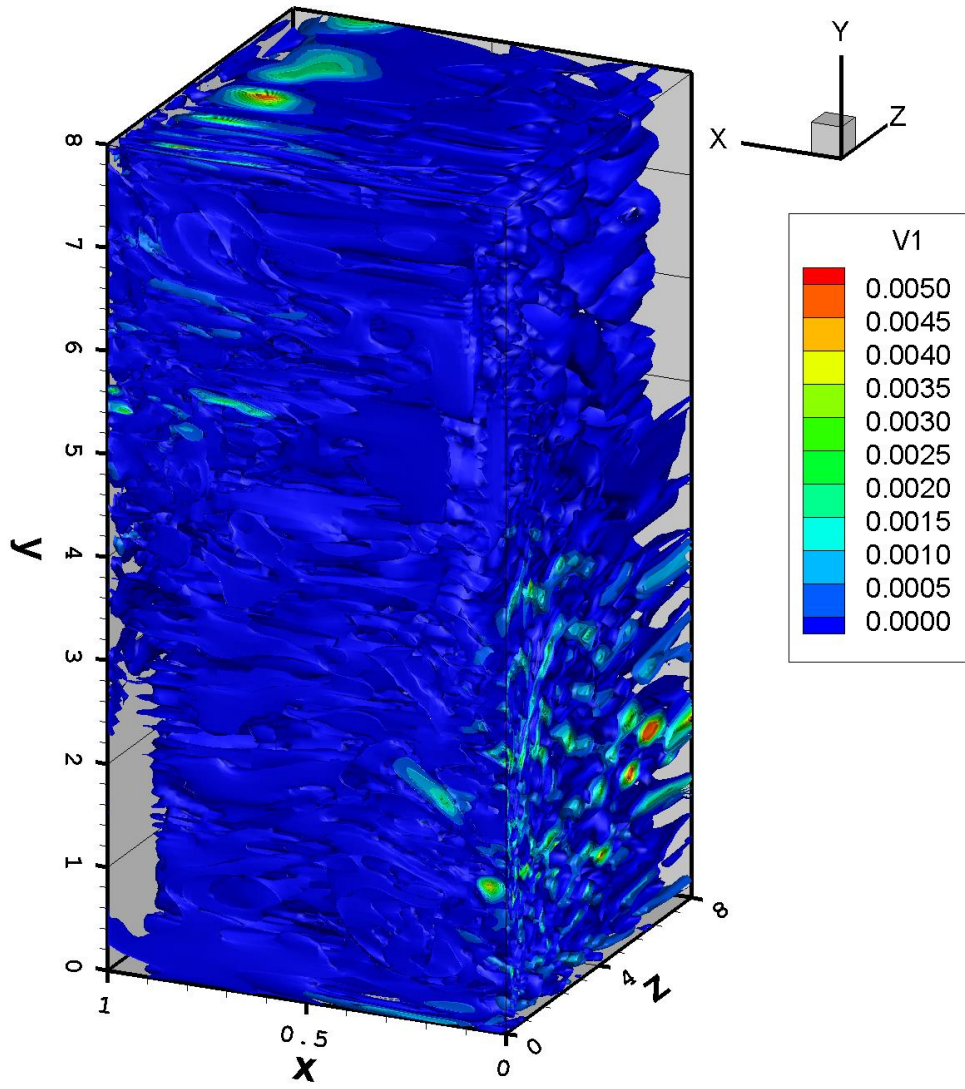


Figure B.69: The *arLES* statistics – V_1^\ominus component

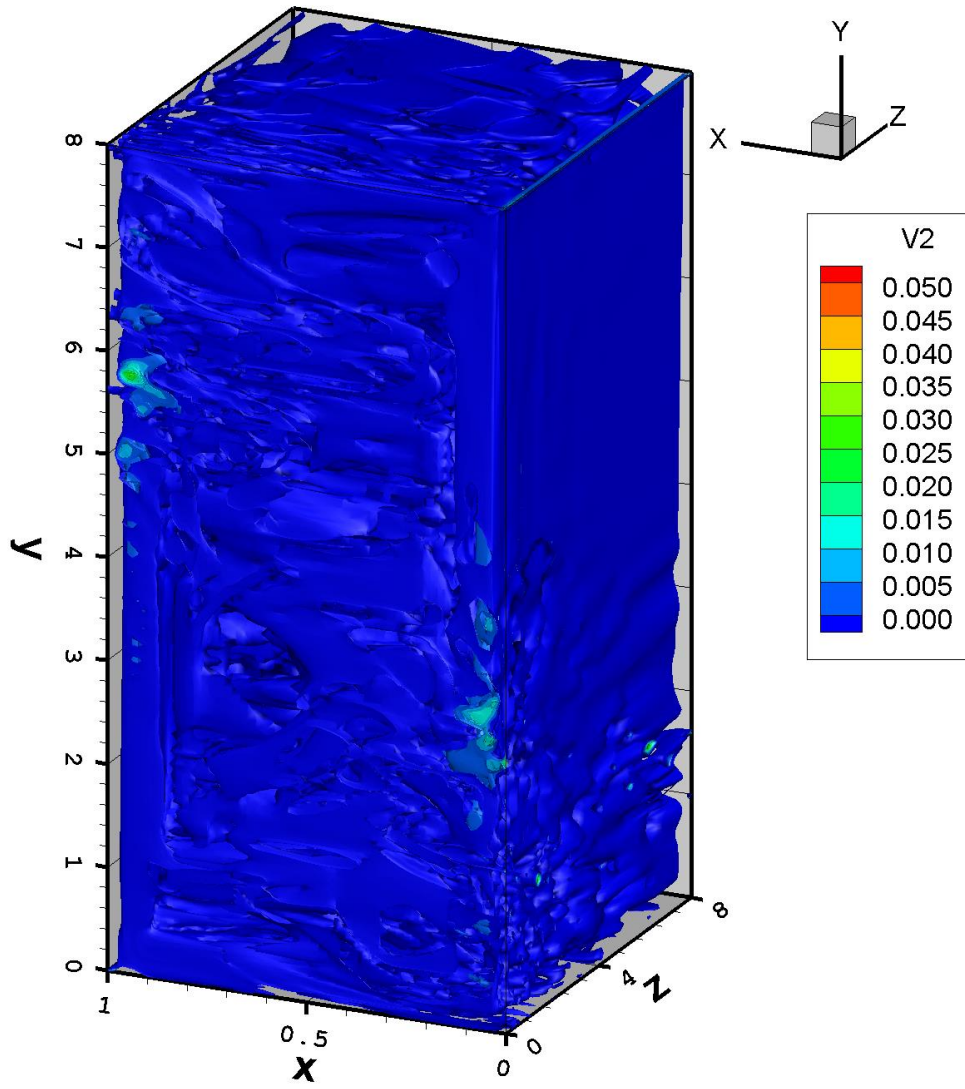


Figure B.70: The *arLES* statistics – V_2^\ominus component

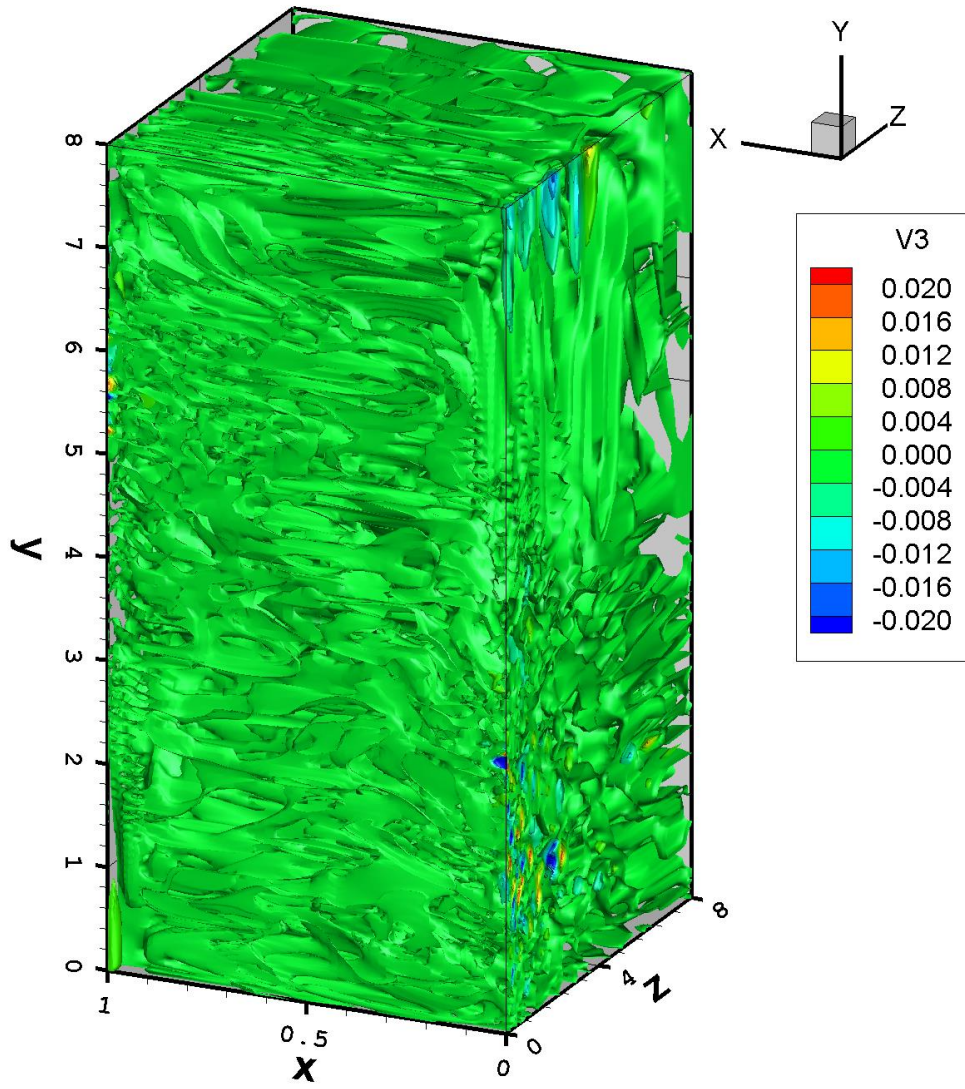


Figure B.71: The *arLES* statistics – V_3^\ominus component

APPENDIX C

PICMSS THERMAL CAVITY FE TEMPLATE

```

PRIMARY_VARIABLES 27
U V W TEMP PHI
SPHI
C11 C12 C13 C22 C23 C33
T1 T2 T3
DUBDY DVBDY DWBDY DTBDY
UAD VAD WAD TAD
UBCE VBCE WBCE TBCE *

SECONDARY_VARIABLES 0
*

FIXED_VARIABLES 5
DCONST XCVAl YCVAl ZCVAl TCVAL *

INVERSE_VARIABLES 0
*

DERIVED_VARIABLES 6
UU 2 U U
UV 2 U V
UW 2 U W
VV 2 V V
VW 2 V W
WW 2 W W
*

OPERATORS 93
OP_1 * c200t *
OP_2 * c20x *
OP_3 * c20y *
OP_4 * c20z *
OP_5 U c300x *
OP_6 V c300y *
OP_7 W c300z *
OP_8 * c2kk *
OP_9 U c3x00 *
OP_10 U c3y00 *
OP_11 U c3z00 *
OP_12 V c3x00 *
OP_13 V c3y00 *
OP_14 V c3z00 *
OP_15 W c3x00 *
OP_16 W c3y00 *
OP_17 W c3z00 *
OP_18 UU c30xxh *
OP_19 UV c30xyh *
OP_20 UW c30xzh *
OP_21 UV c30yxh *
OP_22 VV c30yyh *
OP_23 VW c30yzh *
OP_24 UW c30zxh *
OP_25 VW c30zyh *
OP_26 WW c30zzh *
OP_27 TEMP c3x00 *
OP_28 TEMP c3y00 *
OP_29 TEMP c3z00 *
OP_30 * c200 *
OP_31 UU c30xxt *
OP_32 UV c30xyt *
OP_33 UW c30xzt *
OP_34 UV c30yxt *

```

```

OP_35 VV c30yyt *
OP_36 VW c30yzt *
OP_37 UW c30zxt *
OP_38 VW c30zyt *
OP_39 WW c30zzt *
OP_40 U c30xx *
OP_41 U c30yx *
OP_42 U c30zx *
OP_43 V c30xy *
OP_44 V c30yy *
OP_45 V c30zy *
OP_46 W c30xz *
OP_47 W c30yz *
OP_48 W c30zz *
OP_49 * c2y0 *
OP_50 U c3x0x *
OP_51 U c3y0y *
OP_52 U c3z0z *
OP_53 V c3x0x *
OP_54 V c3y0x *
OP_55 V c3z0z *
OP_56 W c3x0x *
OP_57 W c3y0y *
OP_58 W c3z0z *
OP_59 TEMP c3x0x *
OP_60 TEMP c3y0y *
OP_61 TEMP c3z0z *
OP_62 UV c30xxh *
OP_63 UW c30xxh *
OP_64 VV c30yxh *
OP_65 VW c30yxh *
OP_66 VW c30zxh *
OP_67 WW c30zxh *
OP_68 VV c30xyh *
OP_69 VW c30xzh *
OP_70 VW c30xyh *
OP_71 WW c30xzh *
OP_72 UU c30yxh *
OP_73 UV c30yyh *
OP_74 UW c30yzh *
OP_75 UW c30yxh *
OP_76 VW c30yyh *
OP_77 WW c30yzh *
OP_78 UU c30zxh *
OP_79 UV c30zyh *
OP_80 UW c30zzh *
OP_81 UV c30zxh *
OP_82 VV c30zyh *
OP_83 VW c30zzh *
OP_84 VV c30xxh *
OP_85 VW c30xxh *
OP_86 WW c30xxh *
OP_87 UU c30yyh *
OP_88 UW c30yyh *
OP_89 WW c30yyh *
OP_90 UU c30zzh *
OP_91 UV c30zzh *
OP_92 VV c30zzh *
OP_93 * cn200 *

```

NUMBER_OF_SETS 7

UVWPHI_EQUATION_SET 0:

OPERATORS 61

OP_1 OP_2 OP_3 OP_4 OP_5 OP_6
 OP_7 OP_8 OP_9 OP_10
 OP_11 OP_12 OP_13 OP_14 OP_15 OP_16
 OP_17 OP_18 OP_19 OP_20
 OP_21 OP_22 OP_23 OP_24 OP_25 OP_26
 OP_27 OP_28 OP_29 OP_30
 OP_62 OP_63 OP_64 OP_65 OP_66 OP_67
 OP_68 OP_69 OP_70 OP_71
 OP_72 OP_73 OP_74 OP_75 OP_76 OP_77
 OP_78 OP_79 OP_80 OP_81
 OP_82 OP_83 OP_84 OP_85 OP_86 OP_87
 OP_88 OP_89 OP_90 OP_91
 OP_92

EQUATIONS 5

RHS_U 29

ONE OP_1 U
 ONE OP_5 U
 ONE OP_6 U
 ONE OP_7 U
 ONE OP_2 C11
 ONE OP_3 C12
 ONE OP_4 C13
 ITDELT OP_2 PHI
 ITDELT OP_2 SPHI
 ONE OP_30 UBCE
 TTTT47 OP_8 U
 TTTT58 OP_18 U
 TTTT58 OP_19 U
 TTTT58 OP_20 U
 TTTT58 OP_21 U
 TTTT58 OP_22 U
 TTTT58 OP_23 U
 TTTT58 OP_24 U
 TTTT58 OP_25 U
 TTTT58 OP_26 U
 TTTT58 OP_18 U
 TTTT58 OP_19 U
 TTTT58 OP_20 U
 TTTT58 OP_72 V
 TTTT58 OP_73 V
 TTTT58 OP_74 V
 TTTT58 OP_78 W
 TTTT58 OP_79 W
 TTTT58 OP_80 W

RHS_V 30

ONE OP_1 V
 ONE OP_5 V
 ONE OP_6 V
 ONE OP_7 V
 ONE OP_2 C12
 ONE OP_3 C22
 ONE OP_4 C23
 ITDELT OP_3 PHI
 ITDELT OP_3 SPHI

ONE OP_30 VBCE

TTTT47 OP_8 V
 MONE OP_30 TEMP
 TTTT58 OP_18 V
 TTTT58 OP_19 V
 TTTT58 OP_20 V
 TTTT58 OP_21 V
 TTTT58 OP_22 V
 TTTT58 OP_23 V
 TTTT58 OP_24 V
 TTTT58 OP_25 V
 TTTT58 OP_26 V
 TTTT58 OP_62 U
 TTTT58 OP_68 U
 TTTT58 OP_69 U
 TTTT58 OP_21 V
 TTTT58 OP_22 V
 TTTT58 OP_23 V
 TTTT58 OP_81 W
 TTTT58 OP_82 W
 TTTT58 OP_83 W

RHS_W 29

ONE OP_1 W
 ONE OP_5 W
 ONE OP_6 W
 ONE OP_7 W
 ONE OP_2 C13
 ONE OP_3 C23
 ONE OP_4 C33
 ITDELT OP_4 PHI
 ITDELT OP_4 SPHI
 ONE OP_30 WBCE
 TTTT47 OP_8 W
 TTTT58 OP_18 W
 TTTT58 OP_19 W
 TTTT58 OP_20 W
 TTTT58 OP_21 W
 TTTT58 OP_22 W
 TTTT58 OP_23 W
 TTTT58 OP_24 W
 TTTT58 OP_25 W
 TTTT58 OP_26 W
 TTTT58 OP_63 U
 TTTT58 OP_70 U
 TTTT58 OP_71 U
 TTTT58 OP_75 V
 TTTT58 OP_76 V
 TTTT58 OP_77 V
 TTTT58 OP_24 W
 TTTT58 OP_25 W
 TTTT58 OP_26 W

RHS_TEMP 18

ONE OP_1 TEMP
 ONE OP_5 TEMP
 ONE OP_6 TEMP
 ONE OP_7 TEMP
 ONE OP_2 T1
 ONE OP_3 T2
 ONE OP_4 T3
 TTTT29 OP_8 TEMP

ONE OP_30 TBCE	MONE OP_5
TTTT88 OP_18 TEMP	MONE OP_6
TTTT88 OP_19 TEMP	MONE OP_7
TTTT88 OP_20 TEMP	MONE OP_13
TTTT88 OP_21 TEMP	TTTT48 OP_8
TTTT88 OP_22 TEMP	TTTT59 OP_18
TTTT88 OP_23 TEMP	TTTT59 OP_19
TTTT88 OP_24 TEMP	TTTT59 OP_20
TTTT88 OP_25 TEMP	TTTT59 OP_21
TTTT88 OP_26 TEMP	TTTT59 OP_22
	TTTT59 OP_23
RHS_PHI 4	TTTT59 OP_24
ITDELT OP_2 U	TTTT59 OP_25
ITDELT OP_3 V	TTTT59 OP_26
ITDELT OP_4 W	TTTT59 OP_21
ITDELT OP_8 PHI	TTTT59 OP_22
	TTTT59 OP_23
JAC_U_by_U 18	JAC_V_by_W 4
MONE OP_1	MONE OP_14
MONE OP_5	TTTT59 OP_81
MONE OP_6	TTTT59 OP_82
MONE OP_7	TTTT59 OP_83
MONE OP_9	
TTTT48 OP_8	JAC_V_by_TEMP 1
TTTT59 OP_18	ONE OP_30
TTTT59 OP_19	
TTTT59 OP_20	JAC_V_by_PHI 1
TTTT59 OP_21	MITDELT OP_3
TTTT59 OP_22	
TTTT59 OP_23	JAC_W_by_U 4
TTTT59 OP_24	MONE OP_15
TTTT59 OP_25	TTTT59 OP_63
TTTT59 OP_26	TTTT59 OP_70
TTTT59 OP_18	TTTT59 OP_71
TTTT59 OP_19	
TTTT59 OP_20	JAC_W_by_V 4
	MONE OP_16
JAC_U_by_V 4	TTTT59 OP_75
MONE OP_10	TTTT59 OP_76
TTTT59 OP_72	TTTT59 OP_77
TTTT59 OP_73	
TTTT59 OP_74	JAC_W_by_W 18
	MONE OP_1
JAC_U_by_W 4	MONE OP_5
MONE OP_11	MONE OP_6
TTTT59 OP_78	MONE OP_7
TTTT59 OP_79	MONE OP_17
TTTT59 OP_80	TTTT48 OP_8
	TTTT59 OP_18
JAC_U_by_TEMP 0	TTTT59 OP_19
	TTTT59 OP_20
JAC_U_by_PHI 1	TTTT59 OP_21
MITDELT OP_2	TTTT59 OP_22
	TTTT59 OP_23
JAC_V_by_U 4	TTTT59 OP_24
MONE OP_12	TTTT59 OP_25
TTTT59 OP_62	TTTT59 OP_26
TTTT59 OP_68	TTTT59 OP_24
TTTT59 OP_69	TTTT59 OP_25
	TTTT59 OP_26
JAC_V_by_V 18	
MONE OP_1	

```

JAC_W_by_TEMP 0
JAC_W_by_PHI 1
  MITDELT OP_4
JAC_TEMP_by_U 1
  MONE OP_27
JAC_TEMP_by_V 1
  MONE OP_28
JAC_TEMP_by_W 1
  MONE OP_29
JAC_TEMP_by_TEMP 14
  MONE OP_1
  MONE OP_5
  MONE OP_6
  MONE OP_7
  TTTT30 OP_8
  TTTT89 OP_18
  TTTT89 OP_19
  TTTT89 OP_20
  TTTT89 OP_21
  TTTT89 OP_22
  TTTT89 OP_23
  TTTT89 OP_24
  TTTT89 OP_25
  TTTT89 OP_26
JAC_TEMP_by_PHI 0
JAC_PHI_by_U 1
  MITDELT OP_2
JAC_PHI_by_V 1
  MITDELT OP_3
JAC_PHI_by_W 1
  MITDELT OP_4
JAC_PHI_by_TEMP 0
JAC_PHI_by_PHI 1
  MITDELT OP_8
NO_NEU_BC_TYPE_U 0
NO_NEU_BC_TYPE_V 0
NO_NEU_BC_TYPE_W 0
NO_NEU_BC_TYPE_TEMP 0
NO_NEU_BC_TYPE_PHI 0
SPHI_EQUATION_SET 1:
OPERATORS 0
EQUATIONS 1

RHS_SPHI SPHI 2
  ONE 1 SPHI
  ONE 1 PHI
CIJ_EQUATION_SET 2:
OPERATORS 11
  OP_8 OP_30 OP_50 OP_51 OP_52 OP_53
  OP_54 OP_55 OP_56 OP_57 OP_58
EQUATIONS 6
RHS_C11 5
  ONE OP_8 C11
  TTTT54 OP_30 C11
  TTTT56 OP_50 U
  TTTT56 OP_51 U
  TTTT56 OP_52 U
RHS_C12 5
  ONE OP_8 C12
  TTTT54 OP_30 C12
  TTTT56 OP_50 V
  TTTT56 OP_51 V
  TTTT56 OP_52 V
RHS_C13 5
  ONE OP_8 C13
  TTTT54 OP_30 C13
  TTTT56 OP_50 W
  TTTT56 OP_51 W
  TTTT56 OP_52 W
RHS_C22 5
  ONE OP_8 C22
  TTTT54 OP_30 C22
  TTTT56 OP_53 V
  TTTT56 OP_54 V
  TTTT56 OP_55 V
RHS_C23 5
  ONE OP_8 C23
  TTTT54 OP_30 C23
  TTTT56 OP_53 W
  TTTT56 OP_54 W
  TTTT56 OP_55 W
RHS_C33 5
  ONE OP_8 C33
  TTTT54 OP_30 C33
  TTTT56 OP_56 W
  TTTT56 OP_57 W
  TTTT56 OP_58 W
JAC_C11_by_C11 2
  MONE OP_8
  TTTT55 OP_30
JAC_C11_by_C12 0
JAC_C11_by_C13 0
JAC_C11_by_C22 0
JAC_C11_by_C23 0
JAC_C11_by_C33 0

```

JAC_C12_by_C11 0
 JAC_C12_by_C12 2
 MONE OP_8
 TTTT55 OP_30
 JAC_C12_by_C13 0
 JAC_C12_by_C22 0
 JAC_C12_by_C23 0
 JAC_C12_by_C33 0

 JAC_C13_by_C11 0
 JAC_C13_by_C12 0
 JAC_C13_by_C13 2
 MONE OP_8
 TTTT55 OP_30
 JAC_C13_by_C22 0
 JAC_C13_by_C23 0
 JAC_C13_by_C33 0

 JAC_C22_by_C11 0
 JAC_C22_by_C12 0
 JAC_C22_by_C13 0
 JAC_C22_by_C22 2
 MONE OP_8
 TTTT55 OP_30
 JAC_C22_by_C23 0
 JAC_C22_by_C33 0

 JAC_C23_by_C11 0
 JAC_C23_by_C12 0
 JAC_C23_by_C13 0
 JAC_C23_by_C22 0
 JAC_C23_by_C23 2
 MONE OP_8
 TTTT55 OP_30
 JAC_C23_by_C33 0

 JAC_C33_by_C11 0
 JAC_C33_by_C12 0
 JAC_C33_by_C13 0
 JAC_C33_by_C22 0
 JAC_C33_by_C23 0
 JAC_C33_by_C33 2
 MONE OP_8
 TTTT55 OP_30

 NO_NEU_BC_TYPE_C11 0

 NO_NEU_BC_TYPE_C12 0

 NO_NEU_BC_TYPE_C13 0

 NO_NEU_BC_TYPE_C22 0

 NO_NEU_BC_TYPE_C23 0

 NO_NEU_BC_TYPE_C33 0

 TJ_EQUATION_SET 3:

 OPERATORS 5
 OP_8 OP_30 OP_59 OP_60 OP_61

EQUATIONS 3

 RHS_T1 5
 ONE OP_8 T1
 TTTT54 OP_30 T1
 TTTT56 OP_59 U
 TTTT56 OP_60 U
 TTTT56 OP_61 U

 RHS_T2 5
 ONE OP_8 T2
 TTTT54 OP_30 T2
 TTTT56 OP_59 V
 TTTT56 OP_60 V
 TTTT56 OP_61 V

 RHS_T3 5
 ONE OP_8 T3
 TTTT54 OP_30 T3
 TTTT56 OP_59 W
 TTTT56 OP_60 W
 TTTT56 OP_61 W

 JAC_T1_by_T1 2
 MONE OP_8
 TTTT55 OP_30
 JAC_T1_by_T2 0
 JAC_T1_by_T3 0

 JAC_T2_by_T1 0
 JAC_T2_by_T2 2
 MONE OP_8
 TTTT55 OP_30
 JAC_T2_by_T3 0

 JAC_T3_by_T1 0
 JAC_T3_by_T2 0
 JAC_T3_by_T3 2
 MONE OP_8
 TTTT55 OP_30

 NO_NEU_BC_TYPE_T1 0

 NO_NEU_BC_TYPE_T2 0

 NO_NEU_BC_TYPE_T3 0

 DUBDY_EQUATION_SET 4:

 OPERATORS 0

 EQUATIONS 4

 RHS_DUBDY DUBDY -222
 U

 RHS_DVBDY DVBDY -222
 V

 RHS_DWBDY DWBDY -222
 W

RHS_DTBDY DTBDY -222
TEMP

UVWTAD_EQUATION_SET 5:

OPERATORS 3
OP_8 OP_30 OP_93

EQUATIONS 4

RHS_UAD 3
ONE OP_30 UAD
MONE OP_30 U
CE1 OP_8 U

RHS_VAD 3
ONE OP_30 VAD
MONE OP_30 V
CE1 OP_8 V

RHS_WAD 3
ONE OP_30 WAD
MONE OP_30 W
CE1 OP_8 W

RHS_TAD 3
ONE OP_30 TAD
MONE OP_30 TEMP
CE1 OP_8 TEMP

JAC_UAD_by_UAD 1
MONE OP_30
JAC_UAD_by_VAD 0
JAC_UAD_by_WAD 0
JAC_UAD_by_TAD 0

JAC_VAD_by_UAD 0
JAC_VAD_by_VAD 1
MONE OP_30
JAC_VAD_by_WAD 0
JAC_VAD_by_TAD 0

JAC_WAD_by_UAD 0
JAC_WAD_by_VAD 0
JAC_WAD_by_WAD 1
MONE OP_30
JAC_WAD_by_TAD 0

JAC_TAD_by_UAD 0
JAC_TAD_by_VAD 0
JAC_TAD_by_WAD 0
JAC_TAD_by_TAD 1
MONE OP_30

NO_NEU_BC_TYPE_UAD 1

NEU_RHS_UAD 1

CE1 OP_93 DUBDY

NEU_JAC_UADUAD 0
NEU_JAC_UADVAD 0
NEU_JAC_UADWAD 0
NEU_JAC_UADTAD 0

NO_NEU_BC_TYPE_VAD 1

NEU_RHS_VAD 1
CE1 OP_93 DVBDY

NEU_JAC_VADUAD 0
NEU_JAC_VADVAD 0
NEU_JAC_VADWAD 0
NEU_JAC_VADTAD 0

NO_NEU_BC_TYPE_WAD 1

NEU_RHS_WAD 1
CE1 OP_93 DWBDY

NEU_JAC_WADUAD 0
NEU_JAC_WADVAD 0
NEU_JAC_WADWAD 0
NEU_JAC_WADTAD 0

NO_NEU_BC_TYPE_TAD 1

NEU_RHS_TAD 1
CE1 OP_93 DTBDY

NEU_JAC_TADUAD 0
NEU_JAC_TADVAD 0
NEU_JAC_TADWAD 0
NEU_JAC_TADTAD 0

UBCE_EQUATION_SET 6:

OPERATORS 0

EQUATIONS 4

RHS_UBCE UBCE -444
UAD

RHS_VBCE VBCE -444
VAD

RHS_WBCE WBCE -444
WAD

RHS_TBCE TBCE -444
TAD

END SYSTEM

VITA

Mikhail Sekachev was born in Kokchetav, Kazakhstan on December 26, 1983 where he obtained his primary and secondary education graduating from the Multidisciplinary Gymnasium “Tandau” in 2001 with specialization in physics and mathematics. In pursuit of high-quality education he then entered the Tomsk State University in the Siberian town of Tomsk, Russia where he obtained his bachelor’s degree in engineering and technology in 2005. He stayed another two years to obtain his master’s degree focusing on computational fluid dynamics of free-surface flows. In 2007 he relocated to his third country of studies, the USA, where he began his PhD in Mechanical Engineering at the University of Tennessee in Knoxville, TN. He successfully completed his doctoral studies in August of 2013.